NANOMATERIALS FOR REGULATING CANCER AND STEM CELL FATE

BY BIRJU P. SHAH

A dissertation submitted to the

Graduate School—New Brunswick

Rutgers, The State University of New Jersey

in partial fulfillment of the requirements

for the degree of

Doctor of Philosophy

Graduate Program in Chemistry and Chemical Biology

Written under the direction of

Professor Ki-Bum Lee

and approved by

_____

_____

_____

_____

New Brunswick, New Jersey

May, 2014

ABSTRACT OF THE DISSERTATION

Nanomaterials for regulating cancer and stem cell fate

by BIRJU P. SHAH

Dissertation Director: Professor Ki-Bum Lee

The realm of nanomedicine has grown exponentially over the past few decades. However, there are several obstacles that need to be overcome, prior to the wide-spread clinical applications of these nanoparticles, such as (i) developing well-defined nanoparticles of varying size, morphology and composition to enable various clinical applications; (ii) overcome various physiological barriers encountered in order to deliver the therapeutics to the target location; and (iii) real-time monitoring of the nano-therapeutics within the human body for tracking their uptake, localization and effect. Hence, this dissertation focuses on developing multimodal nanotechnology-based approaches to overcome the above-mentioned challenges and thus enable regulation of cancer and stem cell fate.

The initial part of this dissertation describes the development of multimodal magnetic core-shell nanoparticles (MCNPs), comprised of a highly magnetic core surrounded by a thin gold shell, thus combining magnetic and plasmonic properties. These nanoparticles were utilized for mainly two applications: (i) Magnetically-facilitated delivery of siRNA and plasmid DNA for effective stem cell differentiation and imaging and (ii) Combined hyperthermia and targeted delivery of a mitochondria-targeting peptide for enhancing apoptosis in cancer cells. The following part of this dissertation presents

the generation of a multi-functional cyclodextrin-conjugated polymeric delivery platform (known as DexAMs), for co-delivery of anticancer drugs and siRNAs in a target-specific manner to brain tumor cells. This combined delivery of chemotherapeutics and siRNA resulted in a synergistic effect on the apoptosis of brain tumor cells, as compared to the individual treatments. The final part of this thesis presents development of stimuli-responsive fluorescence resonance energy transfer (FRET)-based mesoporous silica nanoparticles for real-time monitoring of drug release in cells. The stimuli-responsive behavior of these nanoparticles resulted in change in the FRET signal, thus allowing for real time monitoring of drug release.

Taken together, these nanomaterial-based approaches combine therapeutic and imaging modalities within a single nanoplatform and as a result have the potential for regulating cancer and stem cell fate such as proliferation, differentiation and apoptosis as well as allowing for real-time monitoring of these events in a non-invasive manner.

Acknowledgements

This doctoral thesis would remain incomplete without acknowledging those who have played an integral role in shaping this thesis and my life.

First and foremost, I would like to sincerely thank my advisor, Dr. Ki-Bum Lee for motivating me to expand my horizons, for silently encouraging me to go beyond my capabilities and for inspiring me with his own sincerity and passion towards science. I will always be indebted to him for his scientific suggestions and feedback, his keen sense of perfection as well as his high standards that he set for all of us, for those made me a better scientist. Above all, he always encouraged and supported me whenever there were setbacks in my research, making sure that I rise above these failures. I know that he will always support me irrespective of the path I choose from here on.

I would next like to express my deepest gratitude to my committee members, Prof. Kathryn Uhrich, Dr. Ralf Warmuth and Dr. Nanjoo Suh. Right from her class in my second semester as a graduate student at Rutgers, to the end of my graduate studies, Prof. Uhrich has been extremely supportive and encouraging and I greatly value her opinions and feedback for my career. I would also like to thank Dr. Ralf Warmuth for his feedback, advice and support during and after my qualifying exams. I would also like to thank Dr. Nanjoo Suh, who has also been our collaborator for projects and grants for her advice, generous help and support.

I would also like to appreciate the help and support that I have received from all my past and current colleagues in Dr. Ki-Bum Lee's lab. I consider myself privileged to have worked with such intelligent and diverse group of people, who have impacted my life in one way or the other. Specifically, I would like to Dr. Aniruddh Solanki and Dr. Prasad Subramaniam, for their kindness, support and illuminating discussions throughout my stay at Rutgers. I will always cherish those memories (and laugh at

them too) and I wish them both all the success and happiness in their lives. I would also like to thank Shraboni Ghoshal, who has been a great friend both in and out of Rutgers. I would specially thank Dr. Jinping Lai, a post-doc in our lab, whom I have worked with on several projects and have also co-authored a paper; for his guidance and scientific feedback. Perry Yin and Nicholas Pasquale also deserve a special mention for their support and contributions to my work. I would also like to thank the remaining KBLee group members for their support and wish for everyone to attain great heights in their chosen career.

Last but not the least, I would like to express my gratitude to my family for their never-ending love and support, for I would not be here without them. My parents, Shraddha and Pankaj Shah, have been the most wonderful and supportive parents that I could ever ask for, and there are no words to describe what they have done for me. My brother, Parth Shah, who, in spite for being younger to me, has shown me that it is ok to sometimes not follow the oft-beaten track in life and create your own unique path. My husband, Dr. Chintan Oza has always inspired me with his passion and dedication to science and his support to all my dreams. I am sure at times he must have felt that he was doing a second PhD, but his love and support has always been unwavering. I would also like to thank my in-laws for their love and support. Finally, my friends deserve kudos for their exceptional support and for providing me the much needed respite from graduate life.

Dedication

I would like to dedicate this dissertation to my parents, Shraddha Shah and Pankaj Shah for giving me everything that I wished for and more, and for their unconditional love and support. I would also like to dedicate this dissertation to my husband, Chintan Oza, for his unwavering love and support, ever since we met.

Table of Contents

List of Figures

Chapter 1

Introduction

The earliest mention of nanomedicine or nanotechnology can be found in the Richard P. Feynman's seminal lecture at Caltech in 1959 [1], where he spoke about the possibilities of designing atomically precise microscopic tools which could be maneuvered at the cellular level for various medical applications. Such nanorobots or nanodevices, as Feynman called them, were expected to bring about enormous benefits in the research and practice of medicine, such as improved accuracy, precision, versatility, cost and time benefits, to eventually result in enhanced quality of life [2, 3]. Since then, nanotechnology has encompassed the entire gamut of applications, especially in clinical medicine, by branching out in different directions [4]. The term nanotechnology (derived from the Latin word, nanus; meaning dwarf) [5], in general is used to describe any matter with at least one dimension sized between 1 to 100 nanometers following the definition set by National Nanotechnology Initiative (NNI) in the US. A more specific definition, again given by NNI states that " Nanotechnology is concerned with materials and systems whose structures and components exhibit novel and significantly improved physical, chemical and biological properties, phenomena and processes due to their nanoscale size". Two main subfields of nanotechnology or nanofabrication, are either top-down approach, which involves miniaturization of surface features to the nanoscale level, or the bottom-up approach, which involves building up nanoscale systems from atomic or molecular level components [6].

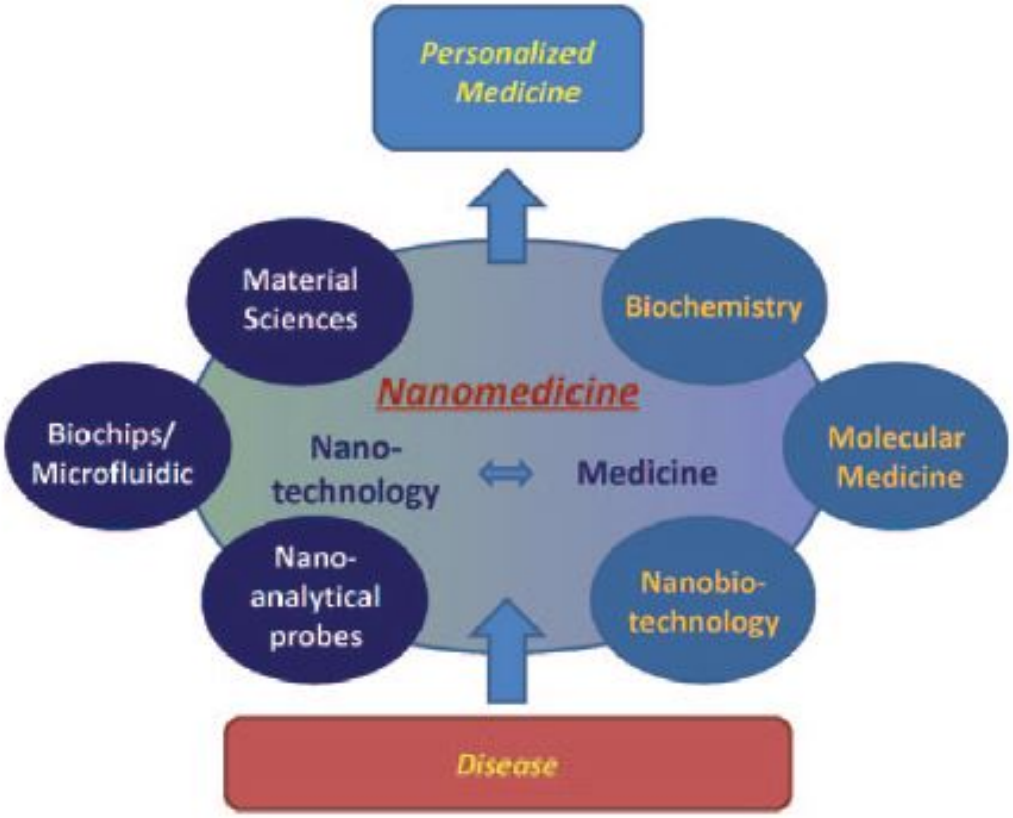

Figure 1.1: Technology or science fields associated with nanotechnology.Reprinted from Ref [5]. Copyright 2009 John Wiley and Sons, Inc

The application of nanotechnology to healthcare, also referred to as nanomedicine (Figure 1.1), requires the intersection of orthogonal disciplines including, but not limited to biology, chemistry, physics, chemical and mechanical engineering, material science and clinical medicine [7]. Over the past few decades, nanomedicine has seen a enormous surge in research activity (Figure 1.2), with patent and publication numbers increasing exponentially, as more and more federal agencies as well as private companies invest in this area of research.

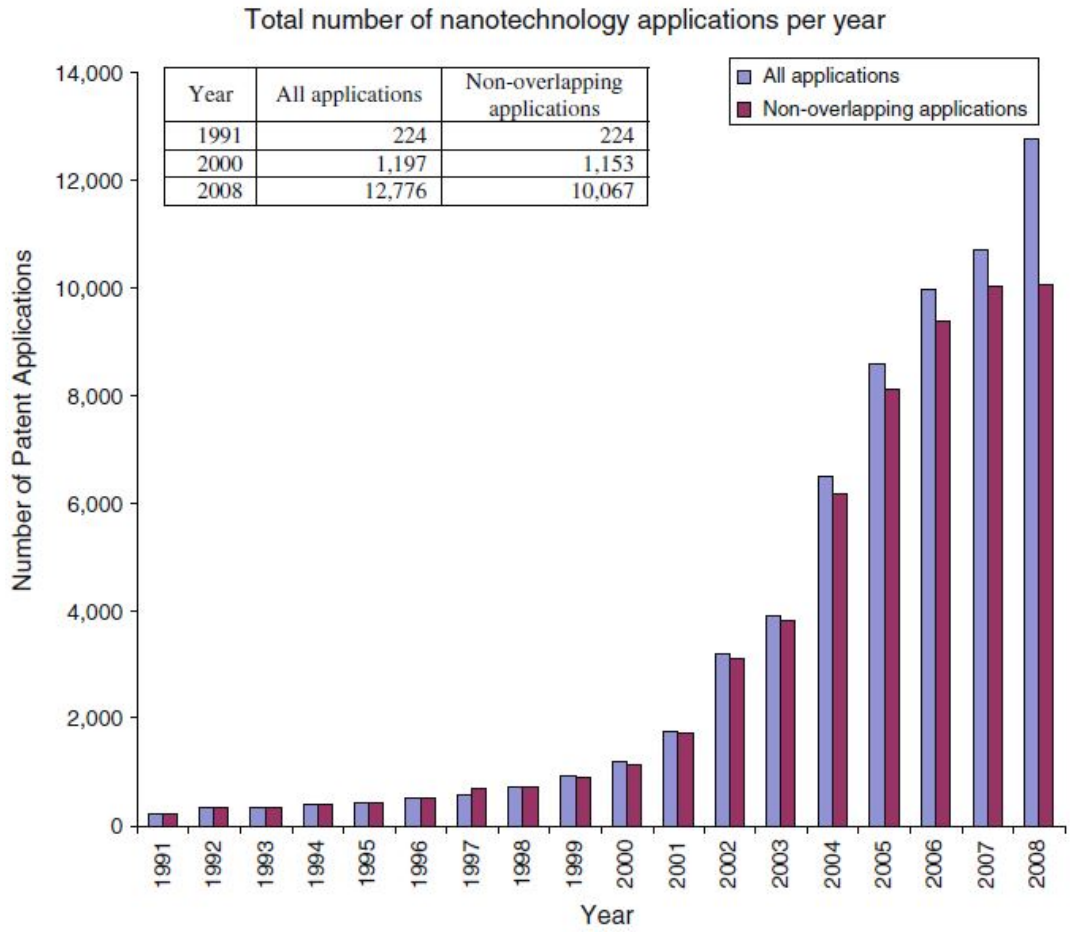

Figure 1.2: Longitudinal evolution of the percentage of patent publications on nanotechnology versus all topics, in the repositories of leading 15 countries/regions and USA from 1991 to 2008 using keyword title abstract search. Reprinted from Ref. [8]. Copyright 2010 Springer

What can be expected in the future, however, is a continuous influx of novel nanotechnology platforms that can positively impact clinical medicine at various levels (Figure 1.3), such as (i) elucidation of changes occurring at molecular level, which are responsible for disease pathogenesis and progression [9–11], (ii) diagnosis and imaging of diseases [12–14], (iii) targeted delivery of various therapeutics such as small molecules, nucleic acids and proteins/peptides [15–17], (iv) real-time monitoring of localization and in-vivo efficacy of therapeutics [12, 18], and (v) multifunctional systems which combine imaging, diagnosis and therapy in one singular platform [19–21].

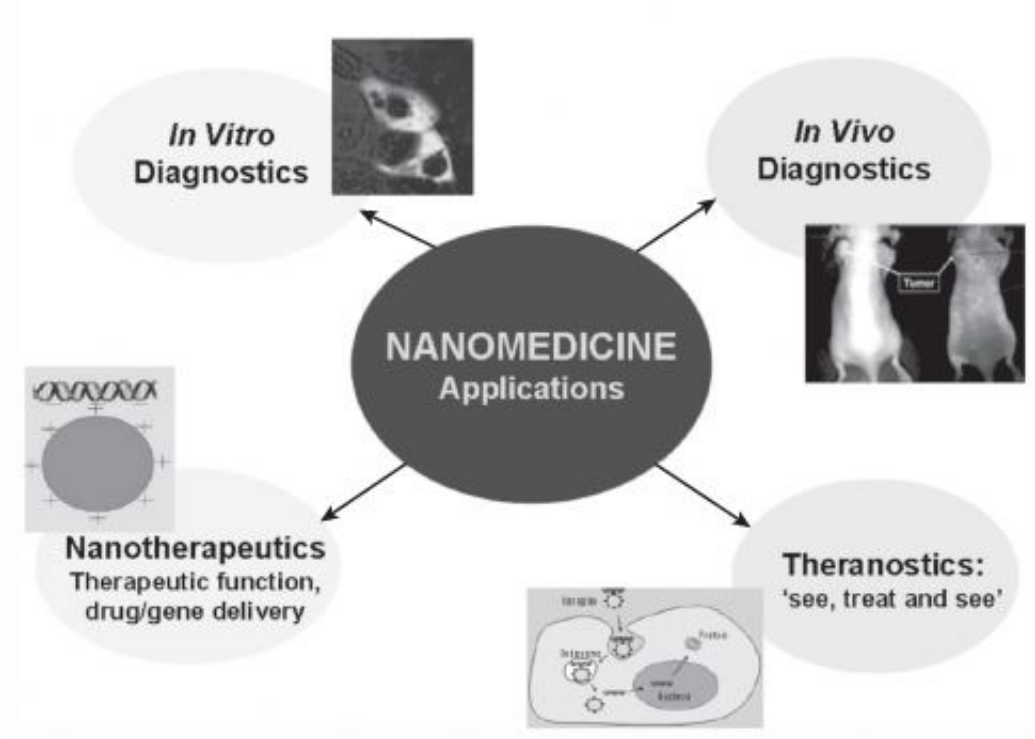

Figure 1.3: The broad scope of applications for nanomedicine. Reprinted from Ref. [4]. Copyright 2005 Elsevier, Inc.

1.1 Cancer nanomedicine

The outstanding progress seen in fundamental cancer biology has not yet translated into ground-breaking clinical advances, and this has been mainly attributed to the inability to administer the therapeutics such that they reach the desired target region, i.e. tumor(s), with minimal damage or off-target effects [22,23].Using conventional strategies, less than 10 ppm of the various therapeutics actually reach their parenchymal targets, when administered systemically. This is also true for contrast agents used for imaging and diagnostic applications [24]. Hence, an ideal therapeutic system (Figure 1.4) for increasing the efficacy of cancer therapeutics or imaging agents, should comprise of the following features: (i) capability to selectively deliver various therapeutics, such as drugs, nucleic acids or proteins/peptides in its most potent form to the tumors [25] and (ii) possess the means or features to overcome the various physiological barriers preventing it from reaching its target [26]. However, in order to develop such a system,

there are several challenges that must be first overcome, such as identification of early markers of malignancy and understanding their evolution as the disease progresses, utilizing these markers as probes for screening and detecting tumors; and developing therapeutic platforms that combine both delivery and imaging capabilities, which can not only target the above-mentioned tumor biomarkers but can also overcome the various physiological and biological barriers that impede efficient delivery [27].

It can thus be expected that nanomedicine can overcome the above-mentioned challenges and make essential breakthroughs in the fight against cancer, due to the unique capabilities and properties of nanomedicine [2,27]. For instance, the dimensions of nanomaterials can match the size scale of the tumor cells as well as interendothelial junctions and hence could potentially allow for efficient tumor localization [28]. Additionally, the facile surface chemistry and tunable surface-to-volume ratios of nanoparticles allow for high drug loading efficiencies, thus improving solubility, stability and potency of such drugs. Also, the ability to attach multiple functionalities, such as targeting ligands, drug payloads and imaging agents, on a single nanoplatform enables the synthesis of multifunctional complexes that can simultaneously provide efficient and specific delivery of therapeutics [26], and also highly sensitive imaging capabilities that can be used to monitor the overall progress of the treatment [3, 19, 29].

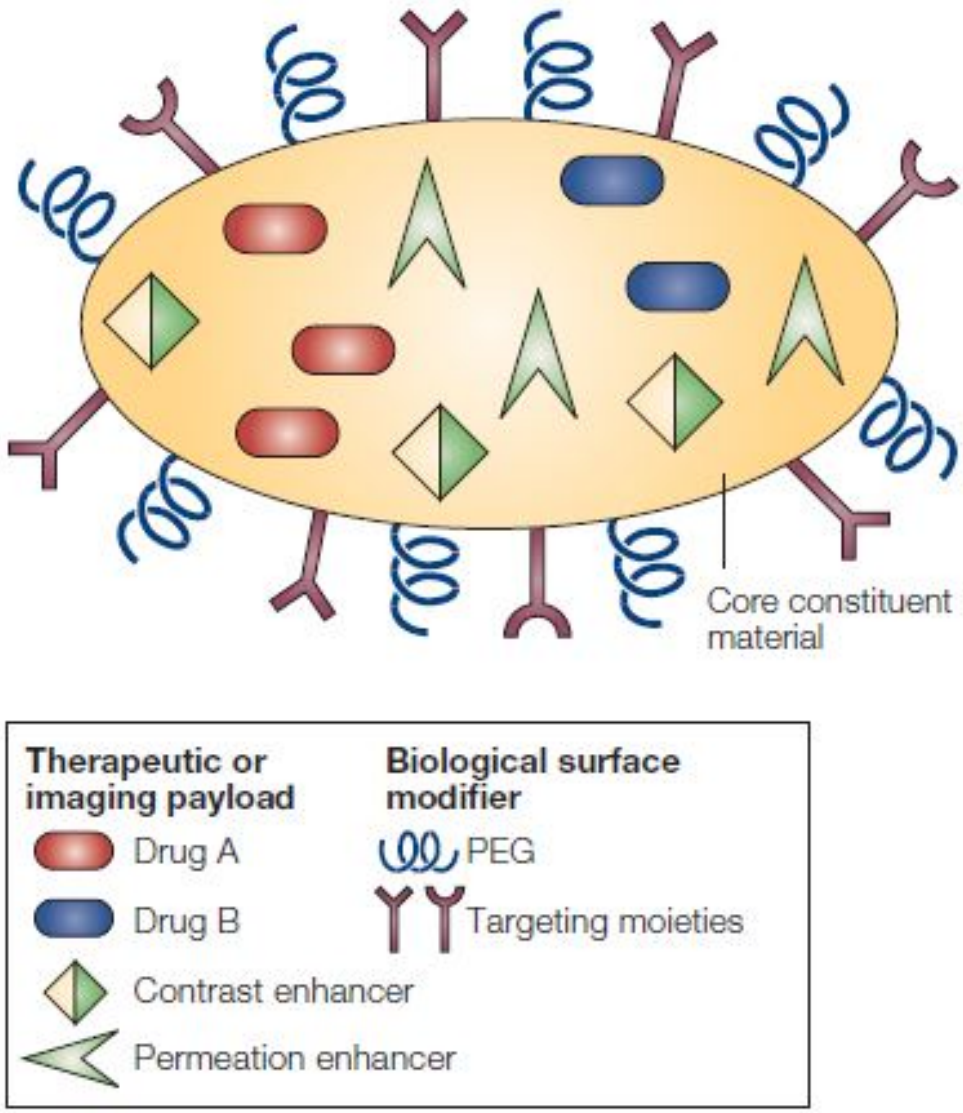

Figure 1.4: The following are illustrated: the ability to carry one or more therapeutic agents; biomolecular targeting through one or more conjugated antibodies or other recognition agents; imaging signal amplification, by way of co-encapsulated contrast agents; and biobarrier avoidance, exemplified by an endothelial tight-junction opening permeation enhancer, and by polyethylene glycol (PEG) for the avoidance of macrophage uptake by macrophages. Reprinted from Ref. [27]. Copyright 2005 Nature Publishing Group.

In this regard, several nanoparticle-based approaches have been developed, including lipid-based vehicles (liposomes, micelles and solid lipid nanoparticles) [30]; polymeric systems (dendrimers, hydrogels, and nanofibers) [31]; metallic nanoparticles (quantum

dots, magnetic, gold, silver and titanium) [31–33]; carbon nanostructures (carbon nanotubes, graphene) [34, 35] and inorganic nanoparticles (silica) [36]. (Figure 1.5)

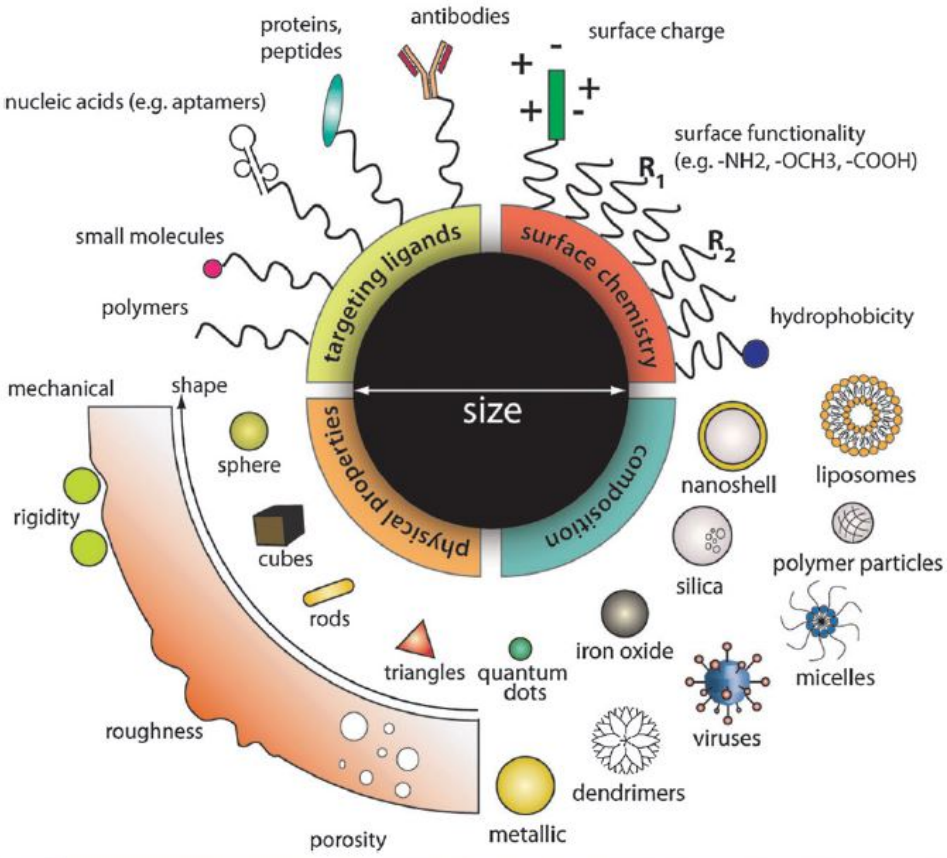

Figure 1.5: Nanoparticles can be modularly assembled from different materials composition with different physical and chemical properties and functionalized with a myriad of ligands for biological targeting. Such flexibility in design freedom enables researchers to tailor nanoparticle for specific intracellular applications as contrast agents, drug delivery vehicles, and therapeutics. Reprinted from Ref. [37]. Copyright 2011 The Royal Society of Chemistry.

1.2 Nanotechnology in regenerative medicine

In addition to its pivotal role in cancer diagnosis and therapy, nanotechnology also plays a very important role in the field of regenerative medicine and stem cell biology. Stem cells are characterized by their unlimited self-renewal ability and pluripotency (i.e. capability to differentiate into several different kinds of cells), and as a result have gained much attention for the treatment of degenerative diseases. However, it is

imperative to consider several obstacles that limit their widespread clinical applications. These obstacles include: (i) development of advanced techniques to control the stem cell fate such as proliferation and differentiation in order to generate engraftable sources of specialized cells; and (ii) imaging modalities which would allow tracking and monitoring of the transplanted stem cells within the human body. To this end, nanomaterials and nanostructures can be particularly useful as they have been shown to interact with the biological systems at molecular and cellular level with high specificity, owing to their nanoscale dimensions. Such behavior, combined with the unique physical, chemical and electronic properties of the nanomaterials, can enable controlling stem cell behavior as well as help dissect the underlying mechanisms (Figure 1.5).

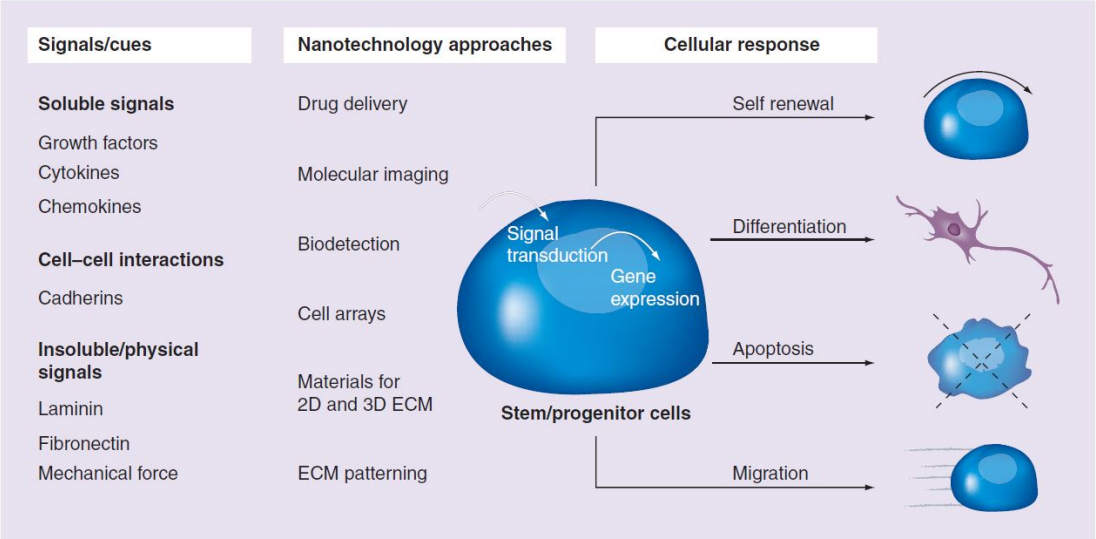

Figure 1.6: Regulation of stem cell fate by microenvironmental signals and corresponding applications of nanotechnology. Reprinted from Ref. [6]. Copyright 2008 Nanomedicine.

Examples of different nanotechnology-based approaches in stem cell research include organic and inorganic nanoparticles, quantum dots, carbon nanotubes, nanofibers and nanoscale-engineered substrates. Potential applications of such nanomaterials in stem-cell research include, but are not limited to (i) tracking of stem cell motility at molecular level without photobleaching, (ii) noninvasive tracking of the transplanted stem cells in vivo, (iii) optimized delivery vehicles for small molecules or genetic materials to control stem cell differentiation, and (iv) nanopatterned substrates which present topographical

features and covalently tethered biologically active moieties that can enhance stem cell differentiation and transplantation. Although the above mentioned nanomaterials have been widely used in other research areas, but their application to stem cell research is relatively new. This is likely due to the advances made in the development of safer and more effective nanomaterials which have been successfully applied in the field of medicine, as well as growing awareness amongst the material scientists of the potential of stem cells for regenerative medicine. Nanotechnologies clearly possess the potential to enhance stem cell biology and stem cell-based therapeutics. But at the same time, it is important to advance our ability to further understand and control the stem cell-fate decisions, by engineering better nanomaterials and nanotechnologies with the ultimate goal of prevention, diagnosis and treatment of human diseases.

1.3 Nanomaterials as imaging agents

Molecular imaging modalities such as optical bioluminescence, optical fluorescence, targeted ultrasound, magnetic resonance imaging (MRI), magnetic resonance spectroscopy (MRS), single-photon emission computed tomography (SPECT) and positron-emission tomography (PET) have been widely utilized for detection and diagnosis of diseases in patients. To this end, using a molecularly targeted nanoplatform affords several advantages as compared to the conventional imaging probes. Firstly, multiple imaging modalities (same or different kinds) can be attached to a single nanoparticle thus leading to dramatic signal amplification. Secondly, these nanoparticles can be decorated with different targeting ligands to allow for enhanced binding affinity and specificity. Thirdly, since these nanoparticles possess the capability of overcoming the various physical and physiological barriers, they can further enhance targeting efficacy and localization. Finally, the combination of the imaging and therapeutic modalities on the same nanoplatform may enable effective and controlled delivery of therapeutic agents in patients, which can be monitored non-invasively in real-time. In the following sections, various nanomaterials that have been employed for molecular imaging at cellular and whole-body level are described here.

1.3.1 Magnetic nanoparticles

Magnetic nanoparticles (MNPs) are a major class of nanoscale materials with the potential to revolutionize current clinical diagnostic and therapeutic techniques [38]. Due to their unique physical properties and ability to function at the cellular and molecular level of biological interactions, MNPs are being actively investigated as the next generation of magnetic resonance imaging (MRI) contrast agents [39] and as carriers for targeted drug delivery [40] (Figure 1.7).Although early research in the field can be dated back several decades, the recent surge of interest in nanotechnology has significantly expanded the breadth and depth of MNP research. With a wide range of applications in the detection, diagnosis, and treatment of illnesses, such as cancer [27], cardiovascular disease, and neurological disease [41], MNPs may soon play a significant role in meeting the healthcare needs of tomorrow.

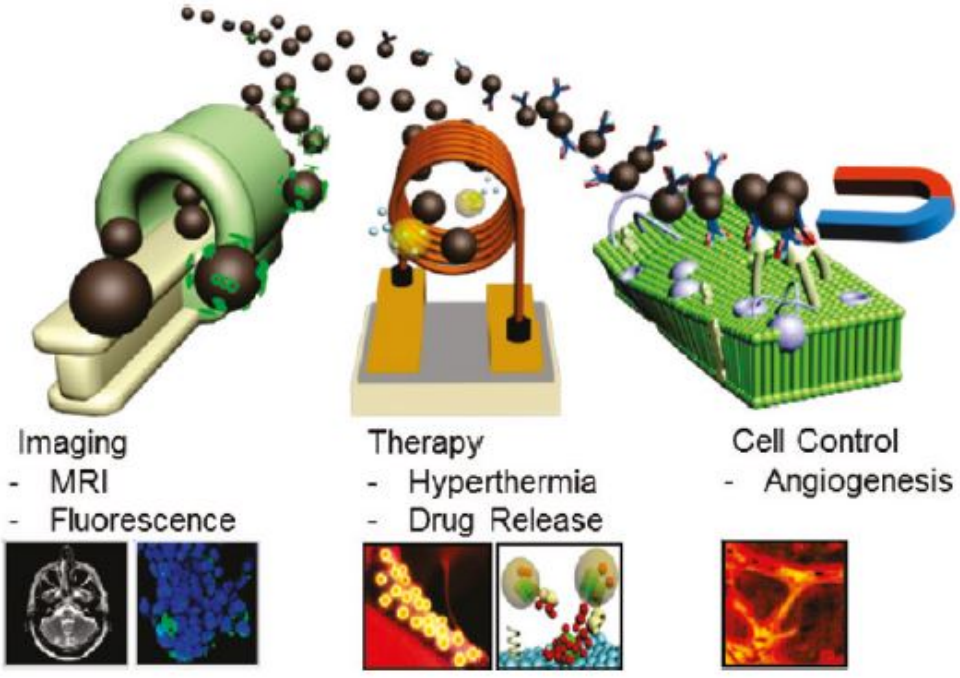

Figure 1.7: Magnetic nanoparticles are versatile platform materials suitable for theranostics. Targeted imaging, thermal therapy, precise drug release and cell signaling controls are all possible. Reprinted from Ref. [42]. Copyright 2011 American Chemical Society.

Numerous forms of MNPs with various chemical compositions have been proposed and evaluated for biomedical applications to exploit nanoscale magnetic phenomena, such as enhanced magnetic moments and superparamagnetism. Like other nanomaterial-based systems, advances in nanotechnology now allow for precise engineering of the critical features of these fine particles [38]. Composition, size, morphology and surface chemistry can now be tailored by various processes to not only improve magnetic properties but also affect the behavior of nanoparticles *in vivo* [43, 44]. In its simplest form, a biomedical MNP platform is comprised of an inorganic nanoparticle core and a biocompatible surface coating that provides stabilization under physiological conditions (Figure 1.8). Additionally, the application of suitable surface chemistry allows for the integration of functional ligands [45]. This modular design enables MNPs to perform multiple functions simultaneously, such as in multimodal imaging, drug delivery and real-time monitoring, as well as combined therapeutic approaches [42, 46].

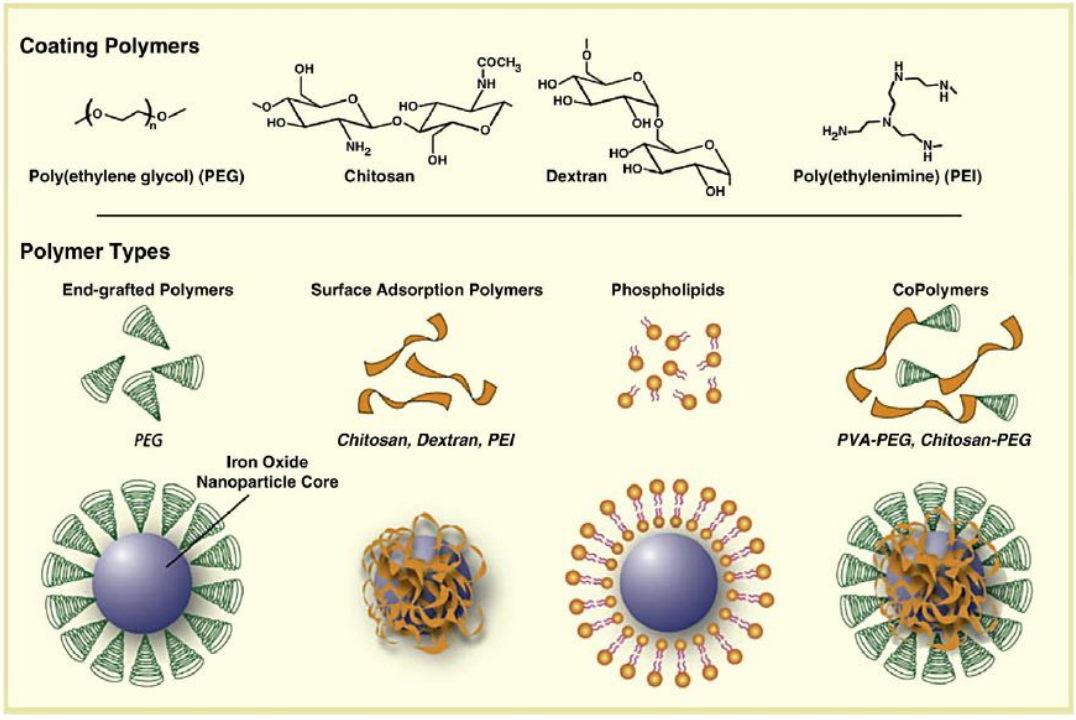

Figure 1.8: Illustration depicting the assembly of polymers onto the surface of magnetic nanoparticle cores. Reprinted from Ref. [47]. Copyright 2010 Elsevier, Inc.

The characteristics of magnetic nanoparticles are usually measured by magnetization

(M), coercivity (Hc), and magnetocrystalline anisotropy constant (K) [42]. Saturation magnetization (Ms) is the maximum magnetization value of a nanoparticle under a high magnetic field. Coercivity (Hc) is the strength of the external magnetic field to make the magnetization value of subjective nanoparticles zero. The zero coercivity of a superparamagnetic nanoparticle is essential for biomedical studies where no residual magnetization is critical in preventing their coagulation and sustaining a long period of circulation in the body. Magnetocrystalline anisotropy is the tendency of the magnetization to align itself along a preferred crystallographic direction of easy axis. The magnetocrystalline anisotropy constant (K) is a physical constant which reflects the energy required to change the direction of magnetization from easy to hard axis. Figure 1.9 summarizes the relationship of magnetic parameters to magnetic resonance imaging (MRI) sensitivity, heat generation, and magnetic attraction force. Under external magnetic field, magnetic nanoparticles generate a secondary magnetic field, which can cause a faster relaxation time (T2) of the protons in the water molecules. Graphs (a) and (b) predict that a high Ms and large particle size (r) are necessary for a higher R2 [42].

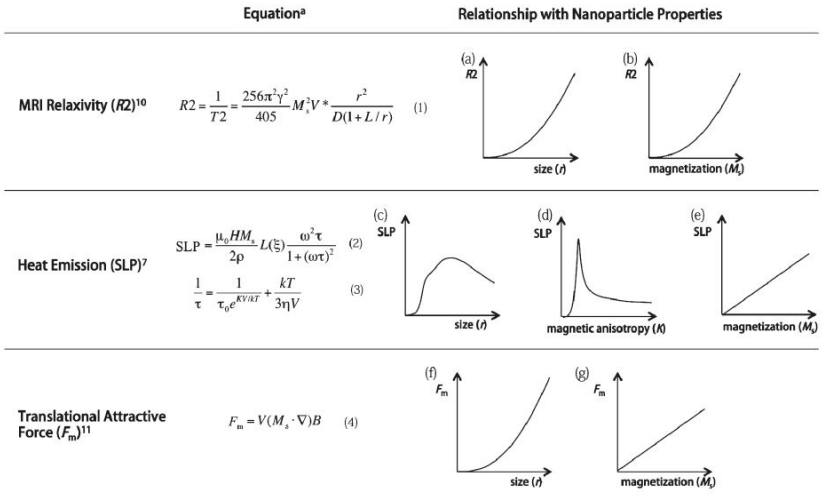

[a] T2, transverse relaxation time; γ, proton gyromagnetic ratio; M_s, saturation magnetization; V^*, nanoparticle volume fraction; r, nanoparticle core radius; D, diffusivity of water molecule; L, thickness of surface coating; SLP, specific loss power; μ_0, vacuum permeability; H, magnetic field strength; ρ, density of particle; $L(\xi)$, Langevin function; ω, angular frequency; τ, relaxation time; K, magnetic anisotropy constant; k, Boltzmann constant; V, particle volume; η, viscosity of solution; F_m, force experienced by a particle; B, magnetic field intensity.

Figure 1.9: Functional properties of magnetic nanoparticles. Reprinted from Ref. [42]. Copyright 2011 American Chemical Society

Iron oxide nanoparticles have been produced by a variety of synthesis processes ranging from traditional wet chemistry solution based methods to more exotic techniques such as laser pyrolysis or chemical vapor deposition [48]. Currently, super-paramagnetic iron oxide (SPIO) and ultrasmall super-paramagnetic iron oxide (USPIO) utilized or under investigation for clinical application as MRI contrast agents are predominately synthesized by an aqueous co-precipitation process in the presence of the coating material [49]. In these hydrolytic processes, the control of the solution pH value and the presence of the coating material serving as a surfactant are critical to particle formation and properties. Unfortunately, magnetization can vary vastly among synthesis methods even within particles of similar size due to incorporation of impurities disrupting the crystal structure, as well as the surface effects described previously. Typically, Ms values of magnetite nanoparticles obtained by these methods are in the range of 3050 emu/g, which is lower than the 90 emu/g reported for their bulk form [44]. Recently, the use of high-temperature decomposition of organometallic precursors has been examined to produce iron oxide nanoparticles with marked improvements in size control, size distributions, and crystallinity [50]. In this process, the size of the nanoparticle is controlled by varying the reaction temperature or changing the metal precursor. Sizes could be further tuned by a seed-mediated growth process to obtain larger particles. Utilizing this process, Sun et al. demonstrated the ability to synthesize highly uniform spherical Fe_3O_4 particles with size variation within 2 nm and mean diameters from 4 to 20 nm [51]. One drawback of this approach is the use of hydrophobic oleic acid and oleylamine surfactants in the process which results in a hydrophobic coating on the particle surface necessitating additional modification to achieve nanoparticle solubility in aqueous media. Approaches such as the addition of an amphiphilic polymer or surface surfactant exchange have been utilized to overcome this problem [52].

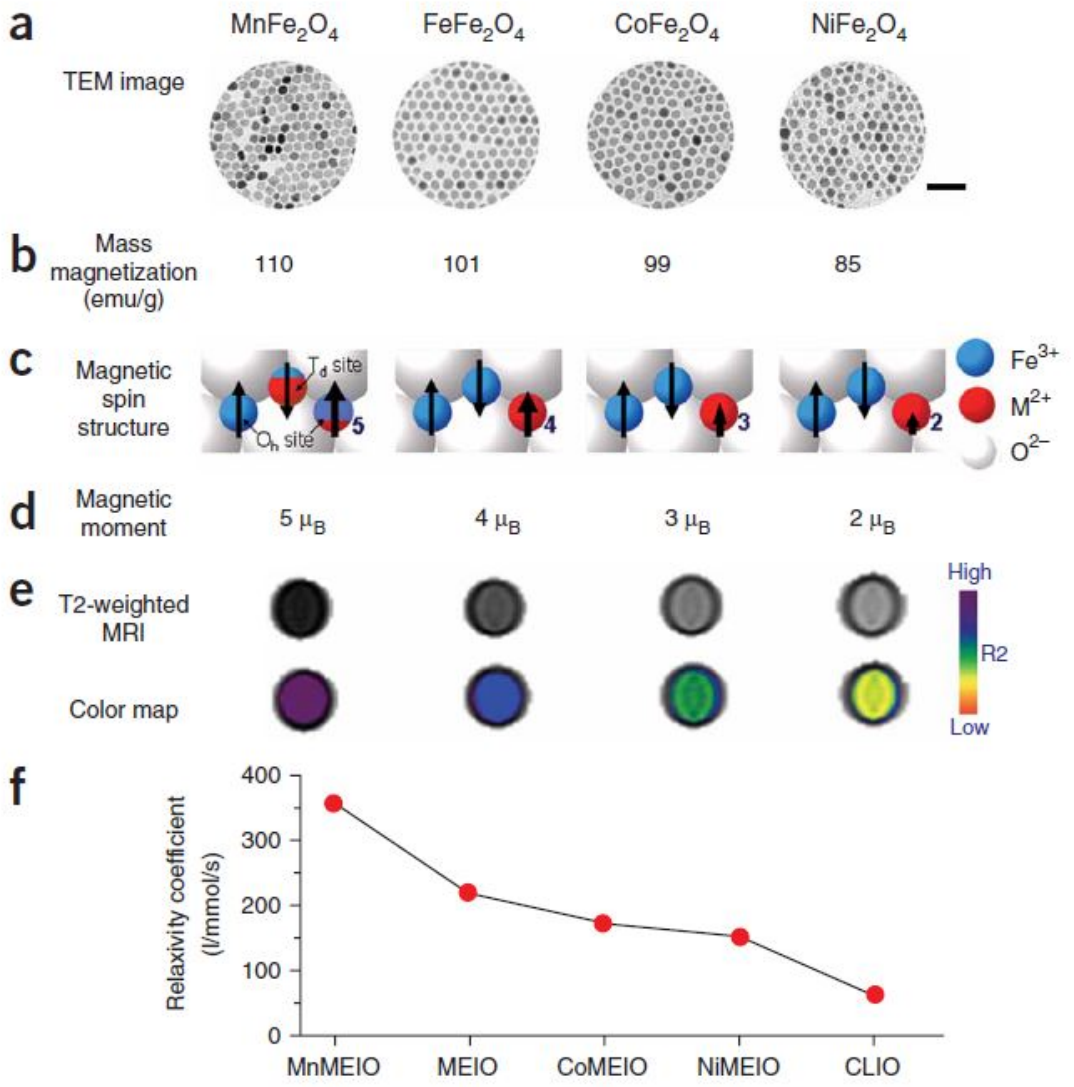

Figure 1.10: (a) TEM images of $MnFe_2O_4$, $FeFe_2O_4$, $CoFe_2O_4$, and $NiFe_2O_4$. All nanoparticles were synthesized to be 12 nm with narrow size distributions. Scale bar, 50 nm. (b) Mass magnetization values of MFe_2O_4, where M = Mn, Fe, Co or Ni. (c,d) Schematics of spin alignments of magnetic ions in spinel structures under external magnetic field and magnetic spin moment of MFe_2O_4 nanoparticles. In face-centered cubic lattices of oxygen, the magnetic spins at Oh sites aligned in parallel with the direction of the external magnetic field whereas those at the tetrahedral (Td) sites aligned antiparallel. $MnFe_2O_4$ has the highest magnetization value, with a magnetic spin magnitude of 5 μ_B. (e,f) T2-weighted spin echo MR images, their color maps and relaxivity (R2) of a series of MEIO nanoparticles at 1.5 T. In f, the R2 of CLIO is also presented for comparison. Consistent with the mass magnetization results, MnMEIO showed the strongest MR contrast effect and had the highest R2 coefficient. Mass magnetization value, MR contrast and R2 coefficient gradually decreased as M^{2+} changed from Mn^{2+} to Fe^{2+}, to Co^{2+} and to Ni^{2+}. Reprinted from Ref. [53]. Copyright 2007 Nature Publishing group.

The need to improve magnetic properties for applications, such as molecular imaging, has generated interest in the development of metal-doped iron oxides due to their enhanced magnetic properties. These spinel metal ferrites with a composition of MFe2O4, where M is +2 cation of Mn, Fe, Co or Ni, have been fabricated by various methods to tune specific magnetic properties [54]. Recently, Lee et al. reported the synthesis and characterization of $MnFe_2O_4$, $FeFe_2O_4$, $CoFe_2O_4$, and $NiFe_2O_4$ by high-temperature reaction between divalent metal chloride and iron tris-2,4-pentadioate [50, 53]. Through comparison of various metal-doped ferrite nanoparticles, this group has demonstrated that $MnFe_2O_4$ nanoparticles are nontoxic in vitro and possess higher magnetic susceptibility than magnetite nanoparticles, suggesting that they may be used as an ultrasensitive MR imaging probe (Figure 1.10).

The ability of MNPs to enhance proton relaxation of specific tissues and serve as MR imaging contrast agents is one of the most promising applications of nanomedicine. MNPs in the form of superparamagnetic iron oxides (SPIO) have been actively investigated as MR imaging contrast agents for over two decades [55]. With applications, such as bowel contrast agents (i.e., Lumiren and Gastromark) and liver/spleen imaging (i.e., Endorem and Feridex IV), already on the market, SPIOs have led the way for MNPs into the clinic. Several forms of ultrasmall superparamagnetic iron oxides (USPIO) have undergone clinical trials with one of the most notable being Combidex which is in late stage clinical trials for use in the detection of lymph node metastases [9]. Currently, clinical imaging of liver tumors and metastases through Reticulo-endothelial system (RES)-mediated uptake of SPIOs has been capable of distinguishing lesions as small as 23 mm [39]. In addition, USPIOs have been shown to be effective in identification of lymph node metastases with a diameter of 5-10 mm under MRI [9]. This non-invasive approach has broad implications as identification of lymphatic dissemination is an essential component of staging and determining the approaches to treatment of diseases such as prostate, breast, and colon cancers [56].

Another clinical application of USPIO MNPs under evaluation is their use in improving the delineation of brain tumor boundaries and quantify tumor volume [57]. Current approaches utilizing gadolinium chelate-based contrast agents are typically limited by

edema surrounding tumor and diffusion of these small molecules from the tumor vasculature. In comparison, MNP-based contrast agents offer prolonged delineation of tumor margins due to enhanced cellular internalization and slower clearance from the tumor site [57, 58]. Although it has been shown that these USPIOs will not replace gadolinium chelates, they have been demonstrated to be helpful in distinguishing neoplastic tissue from areas of radiation necrosis [59]. The next generation of active targeting MNPs currently being investigated have the potential to offer significantly improved tumor detection and localization by exploiting the unique molecular signatures of these diseases [60]. For example, Xhang group have recently demonstrated the specific accumulation of chlorotoxin (CTX)-targeted iron oxide nanoparticles in 9L glioma flank xenografts resulting in more thorough contrast enhancement of tumors in comparison to nontargeted control nanoparticles [38] (Figure 1.11).

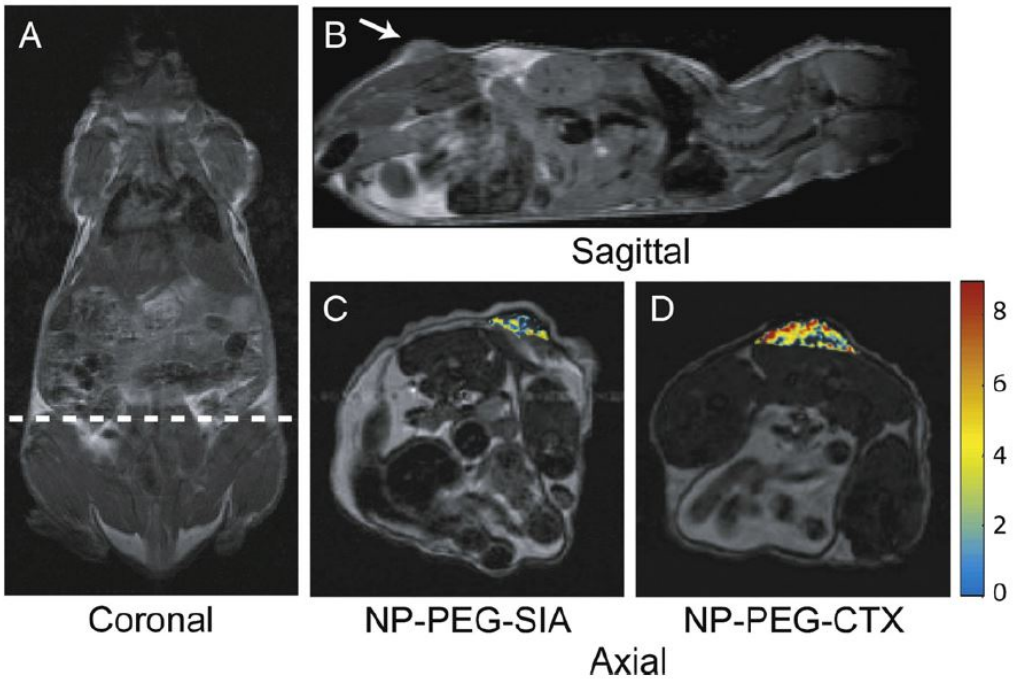

Figure 1.11: MRI anatomical image of a mouse in the (A) coronal plane with the dotted line displaying the approximate location of the axial cross sections displayed in (C) and (D). Anatomical image in the (B) sagittal plane displaying the location of the 9L xenograft tumor. Change in the R2 relaxation values for the tumor regions (superimposed over anatomical MR images) for mouse receiving (C) non-targeting PEG-coated iron oxide nanoparticles and (D) CTX-targeted PEG-coated iron oxide nanoparticles 3 h post nanoparticle injection. Reprinted from Ref. [38]. Copyright 2008 Elsevier, Inc.

In addition to their use as MR imaging probes, iron oxide nanoparticles have been used as both diagnostic and therapeutic nanoscale materials to treat deep tissue tumors [61]. Oscillating magnetic fields (kHz-MHz) applied to magnetic nanoparticles such as iron oxide nanoparticles (Fe_3O_4) results in the generation of heat due to two mechanisms (Neel and Brownian relaxation) that are size dependent (Figure 1.12a). For single domain nanoparticles (¡100 nm) the greatest relaxation losses are due either to Brownian modes (heat due to friction arising from total particle oscillations) or Neel modes (heat due to rotation of the magnetic moment with each field oscillation).

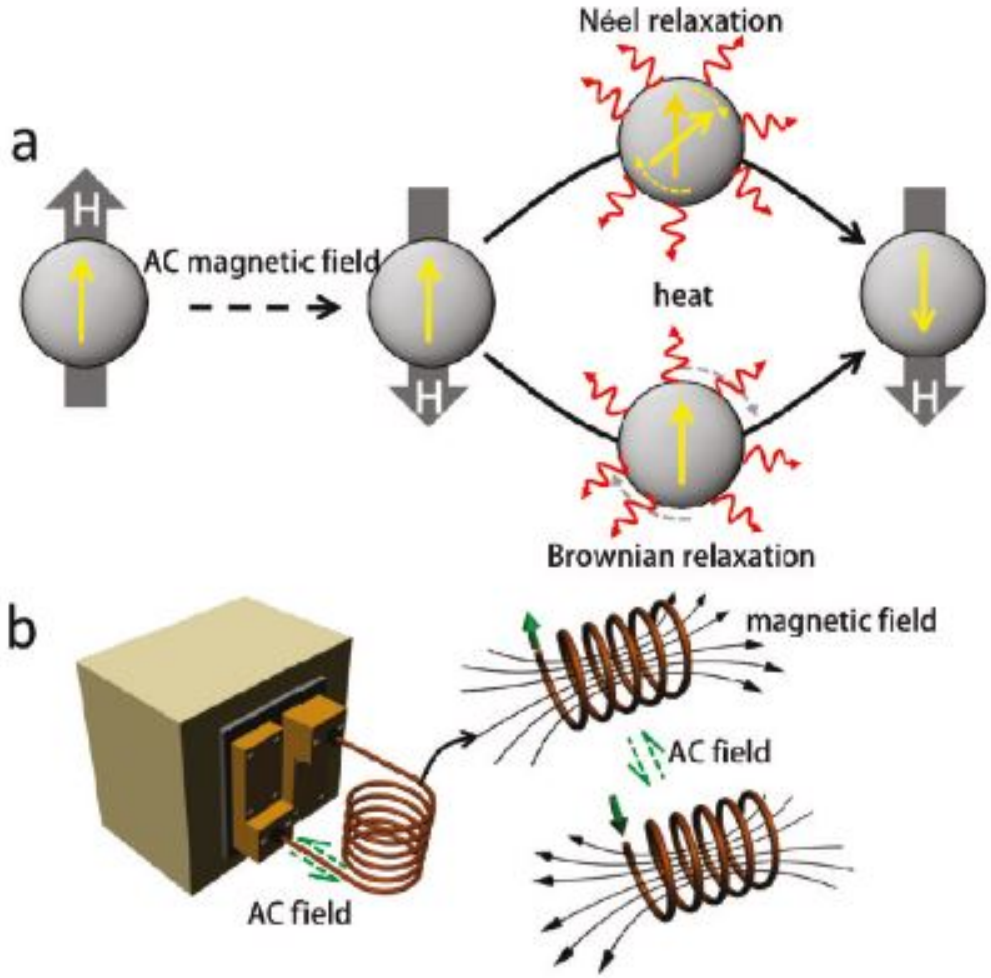

Figure 1.12: (a) Neel and Brownian relaxation processes. (b) Experimental apparatus. Reprinted from Ref. [42]. Copyright 2011 American Chemical Society.

For example, the Zn ion doped magnetic nanoparticles $(Zn_{0.4}Mn_{0.6})Fe_2O_4$ have a high Ms value of 175 emu/g and hence are considered to be promising candidates for

hyperthermia. When these MNPs were used to induce hyperthermia in HeLa cells, it was found that 84.4% cells were dead 10 min following the application of magnetic field, as compared to the 15% cell death seen in case of Fe_3O_4 MNPs. As shown in Figure 1.13, the viability of the cells treated with hyperthermia is examined using fluorescence microscope, wherein the live cells are stained with calcein emitting green fluorescence.

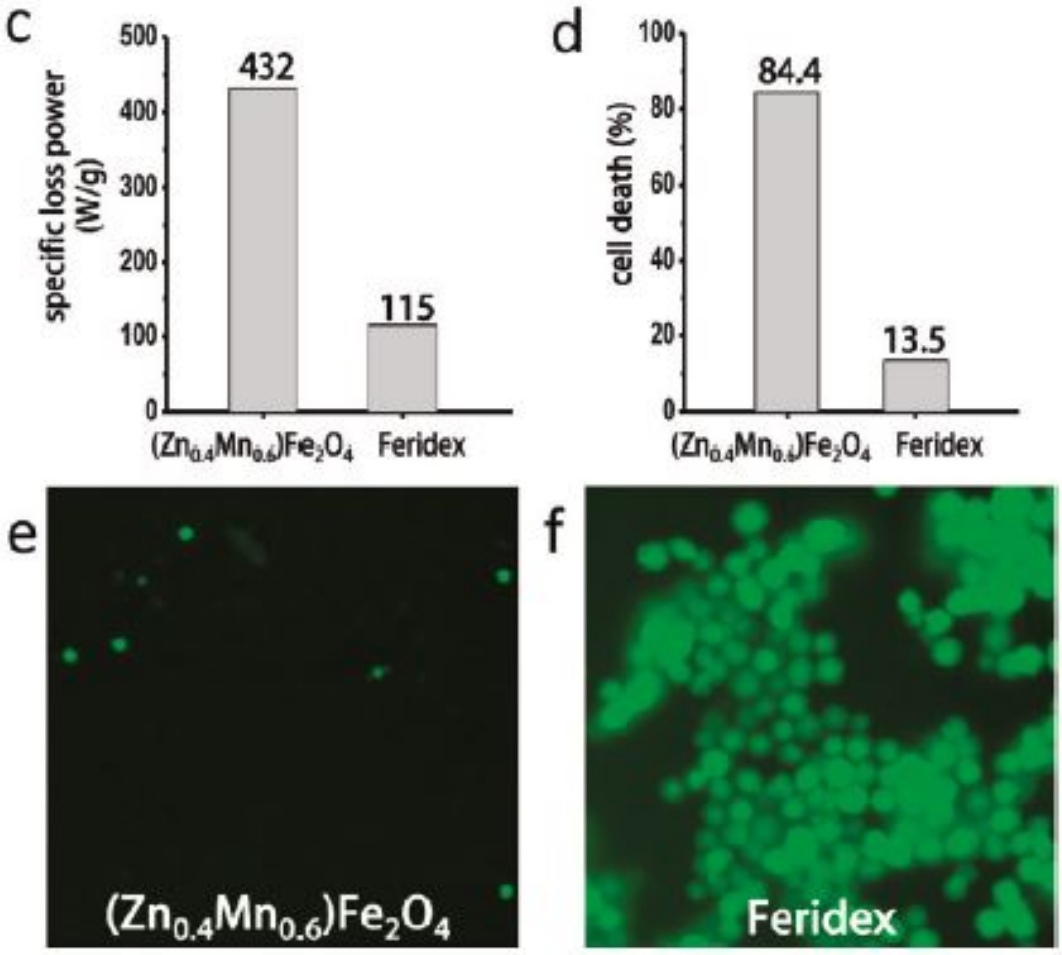

Figure 1.13: (c) SLP values for $(Zn_{0.4}Mn_{0.6})Fe_2O_4$ and Feridex in a 500 KHz AC magnetic field with an amplitude of 37 kA/m. (d) Percentage of HeLa cells killed after hyperthermic treatment with $(Zn_{0.4}Mn_{0.6})Fe_2O_4$ and Feridex. Fluorescence microscopy images of HeLa cells treated with (e) $(Zn_{0.4}Mn_{0.6})Fe_2O_4$ and (f) Feridex. Reprinted from Ref. [42]. Copyright 2011 American Chemical Society.

Commercially available iron nanoparticles such as Feridex are coated with sugars (e.g. dextran) for biocompatibility and aqueous stability in the saline environment of biological tissues. The dextran coating facilitates chemical derivatization and provides

a basis for targeting magnetic nanoparticles to regions of diagnostic and therapeutic interest. Feridex has the benefit of being both a hyperthermic agent and a magnetic resonance imaging (MRI) contrast material. However, heat produced using inductively-coupled magnetic fields results in limited thermal enhancement requiring extremely high concentrations of iron oxide [62]. These high concentrations and the difficulty targeting the iron oxide nanoparticles to only cancer cells can lead to destruction of normal (nonmalignant) cells surrounding the tumor. Nonetheless, iron nanoparticles continue to be investigated actively because of minimal toxicities and the potential for rapid heating of tumor tissue [63].

1.3.2 Gold nanoparticles

In 1857, Faraday reported the first scientific article on AuNPs, attributing the red color to the colloidal nature of AuNPs [64], and in 1908 Mie rationalized their visible absorption using Maxwells electromagnetic equations. AuNPs can be synthesized in various sizes ranging from 1 nm to 120 nm, with sizes above 3 nm showing their characterisitic plasmon band in the visible region. As a result, they have the potential for various applications in optics, catalysis, materials science and nanotechnology, including biology and nanomedicine [32, 65] (Figure 1.14).

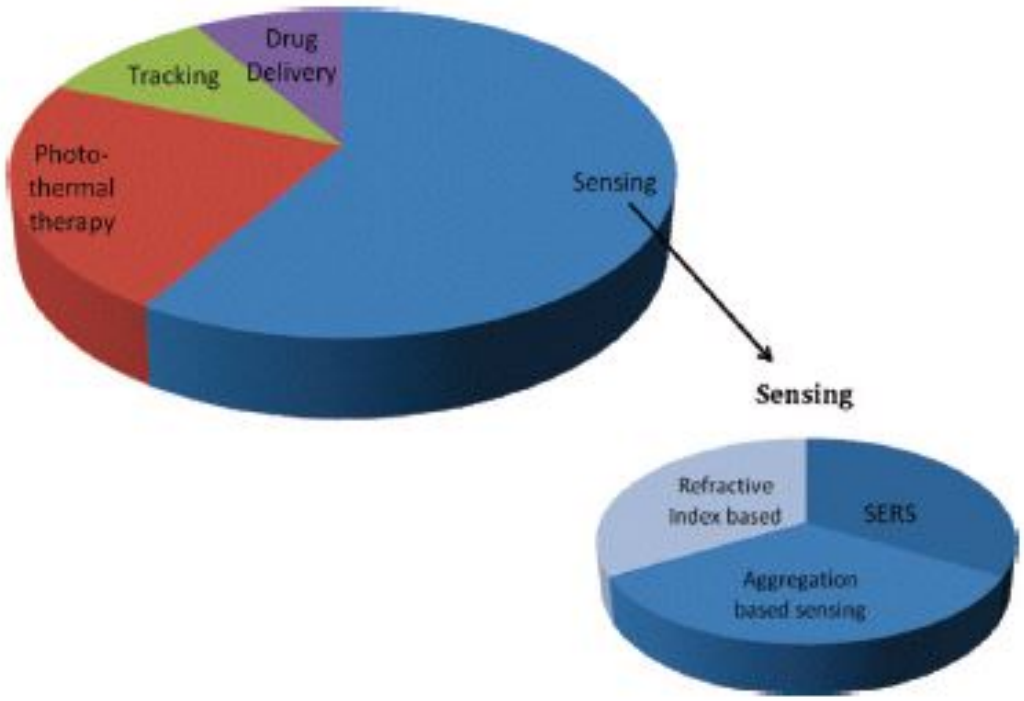

Figure 1.14: (A) Chemical sensing can be based on particle aggregation, changes in local refractive index due to chemical binding, or surface-enhanced Raman scattering (SERS) due to inelastic scattering of light from vibrations in molecules near the surface. Tracking of nanoparticles in a complex biological system is possible using dark-field microscopy or two-photon luminescence microscopy. Therapeutic applications of gold nanoparticles include drug delivery and photothermal therapy, wherein the gold nanoparticles rapidly release heat into their local environment upon light absorption. Pie slice sizes roughly correspond to the length of time that there is literature in the area. Reprinted from Ref. [32]. Copyright 2008 American Chemical Society.

Several methods have been developed for synthesizing discrete and monodisperse gold nanoparticles, including citrate reduction and Brust-Schiffrin method biphasic

method. In addition to different sizes, the morphology of the AuNPs can be varied using appropriate techniques (Figure 1.15). In particular, Au nanorods (AuNRs) with controlled aspect ratio (i.e. the ratio of the length along the long axis to the short axis) in the range of 26 have been synthesized using the micelle-templated seed and feed technique developed by the groups of Murphy [32] and El Sayed [66–68], while the Halas group has developed the synthesis of Au nanoshells (AuNSs) composed of a silica core (100-200 nm in diameter) surrounded by a thin Au layer (5-20 nm) [69].

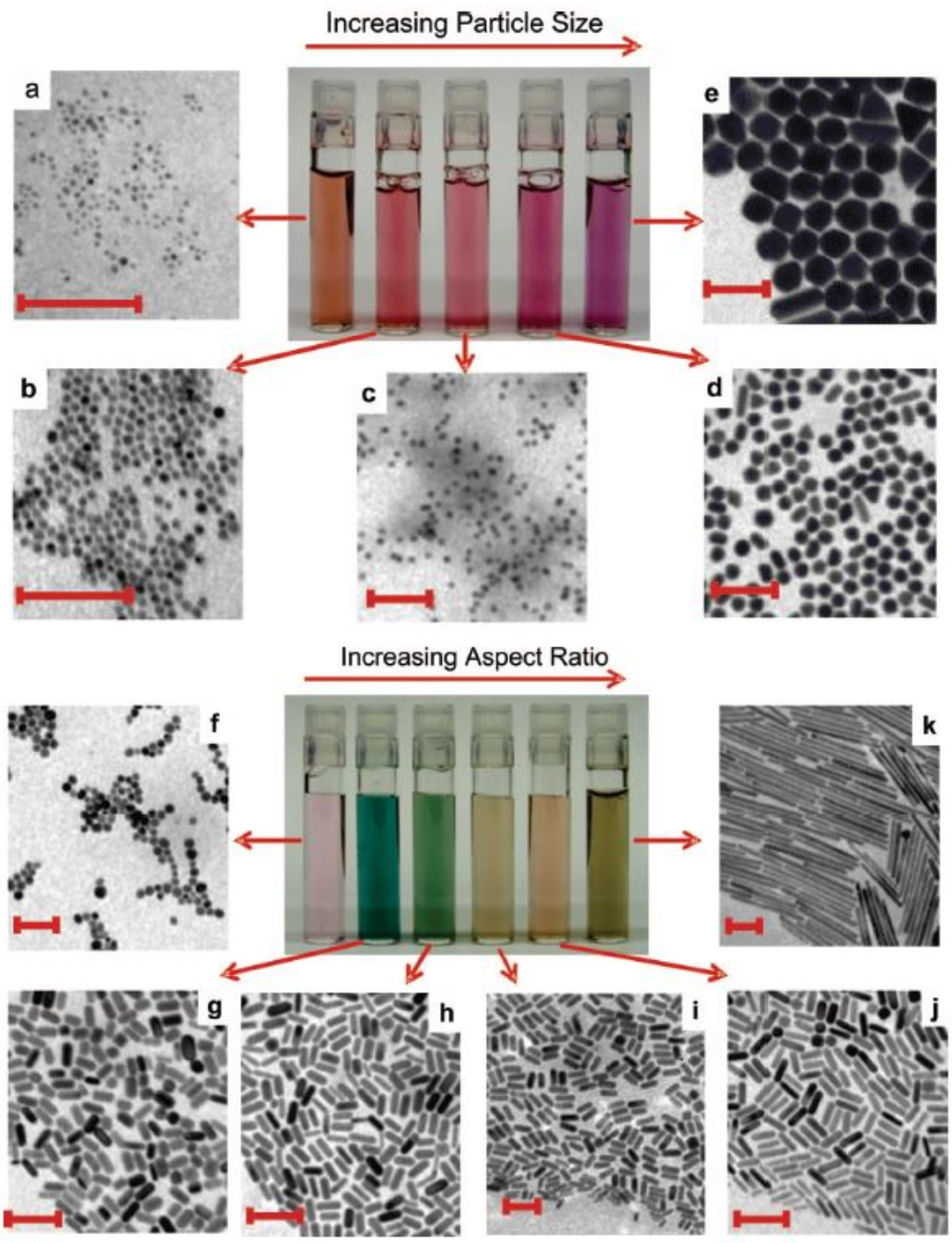

Figure 1.15: Photographs of aqueous solutions of gold nanospheres (upper panels) and gold nanorods (lower panels) as a function of increasing dimensions. Corresponding transmission electron microscopy images of the nanoparticles are shown, all scale bars = 100 nm. The difference in color of the particle solutions is more dramatic for rods than for spheres. This is due to the nature of plasmon bands (one for spheres and two for rods) that are more sensitive to size for rods than for spheres. For spheres, the size varies from 4 to 40 nm (TEM a-e) whereas for rods, the aspect ratio varies from 1.3 to 5 for short rods (TEMs f-j) and 20 (TEM k) for long rods. Reprinted from Ref. [32]. Copyright 2008 American Chemical Society.

The sizes and shapes of the gold nanostructures have a profound effect on their absorption properties, as seen in Figure 1.16. Thus, it is possible to synthesize gold nanoparticles, such that they could absorb a particular wavelength. Additionally, anisotropic nanoparticles such gold nanorods may also have different chemical reactivity for different crystal faces [32]. According to the Mie theory, an electromagnetic frequency induces a resonant coherent oscillation of the free electrons, called the surface plasmon resonance (SPR), at the surface of aspherical NP if it is much smaller than the light wavelength. This absorption lies in the visible region for Au, Ag and Cu. For metal nanoparticles, the localized surface plasmon resonance results in an enhanced electromagnetic field at the metal nanoparticle surface. The plasmon resonance of AuNPs is observed down to 3 nm diameter, below which the AuNP can no longer be considered as a piece of metal with a conduction band but becomes a molecule depicted by molecular orbitals (then the term cluster should be used rather than nanoparticle) [66]. As a result, an enhanced electromagnetic field appears at the AuNP surface above this size allowing surface-enhanced optical properties revealed using spectroscopic techniques. Thus, the extinction coefficients of the SPR bands are extremely high, up to 10^{11} M^{-1} cm^{-1}, which is several orders of magnitude larger than those or all the organic dyes.

AuNPs give rise to both absorption and scattering whose proportions depend on the AuNP size. AuNPs with a diameter smaller than 20 nm essentially show absorption, but size increase to 80 nm also increases the ratio of scattering to absorption. A high scattering cross section is indeed required for biological imaging based on light scattering. For spherical AuNPs of 5 nm diameter, the surface plasmon band is located at 520 nm in ethanol, but it is very sensitive to the composition, size, shape, interparticle distance and environment (dielectric properties) of the AuNPs. It is the high sensitivity to these factors that makes the basis of their use for biological labeling, detection, diagnostic and sensing [70, 71].

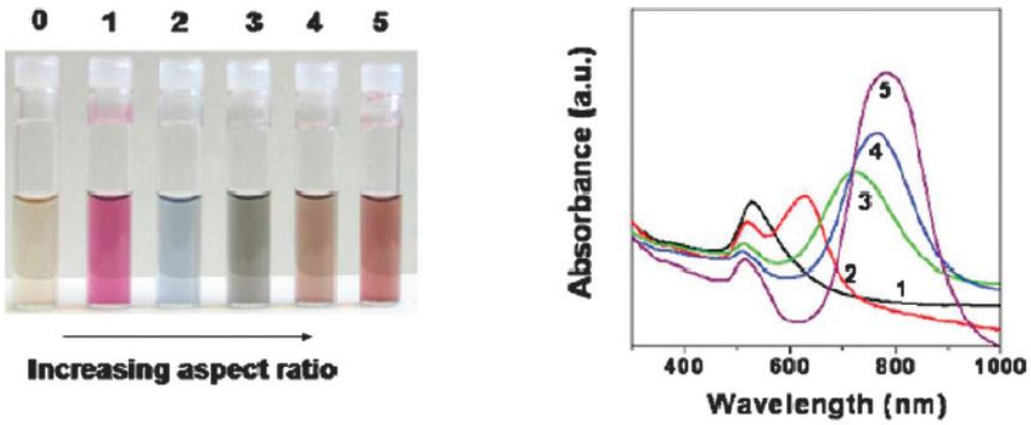

Figure 1.16: The optical properties of gold nanoparticles change drastically with nanoparticle shape. The photograph shows aqueous solutions of 4 nm gold nanospheres (vial 0) and progressively higher aspect ratio gold nanorods (1-5). The optical spectra for the particles in vials 1-5 is also shown. Reprinted from Ref. [72]. Copyright 2009 The Royal Society of Chemistry.

The commonly used techniques for AuNP-based imaging include: (i) Transmission electron microscopy which uses the high atomic weight of Au, (ii) Optical microscopy, such as dark-field microscopy (Figure 1.17), which utilizes the surface plasmon resonance properties of the AuNPs, (iii) photothermal imaging, which records local variations of the refractive index due to generation of heat in the environment, (iv) fluorescence microscopy, that allows for detection at single particle level, (v) photothermal coherence tomography, (vi) multiphoton SPR microscopy, (vii) X-ray scattering and (viii) Gamma radiation using neutron activation [73, 74]. Among the different spectroscopic techniques that characterize the electromagnetic field resulting from the plasmon resonance of AuNPs (surface-enhanced fluorescence, surface-enhanced Rayleigh scattering, surface-enhanced absorption and surface-enhanced Raman scattering, SERS), SERS is most attractive, because of the huge enhancement of the SERS signal, by a factor of ca. 10^{14}-10^{15}, which improves the detection limit from ensembles of molecules to the single-molecule level [65]. Molecules located on the AuNP surface are submitted to the large field caused by the plasmon resonance of the AuNP up to a distance of approximately 10 nm at most from the AuNP surface.

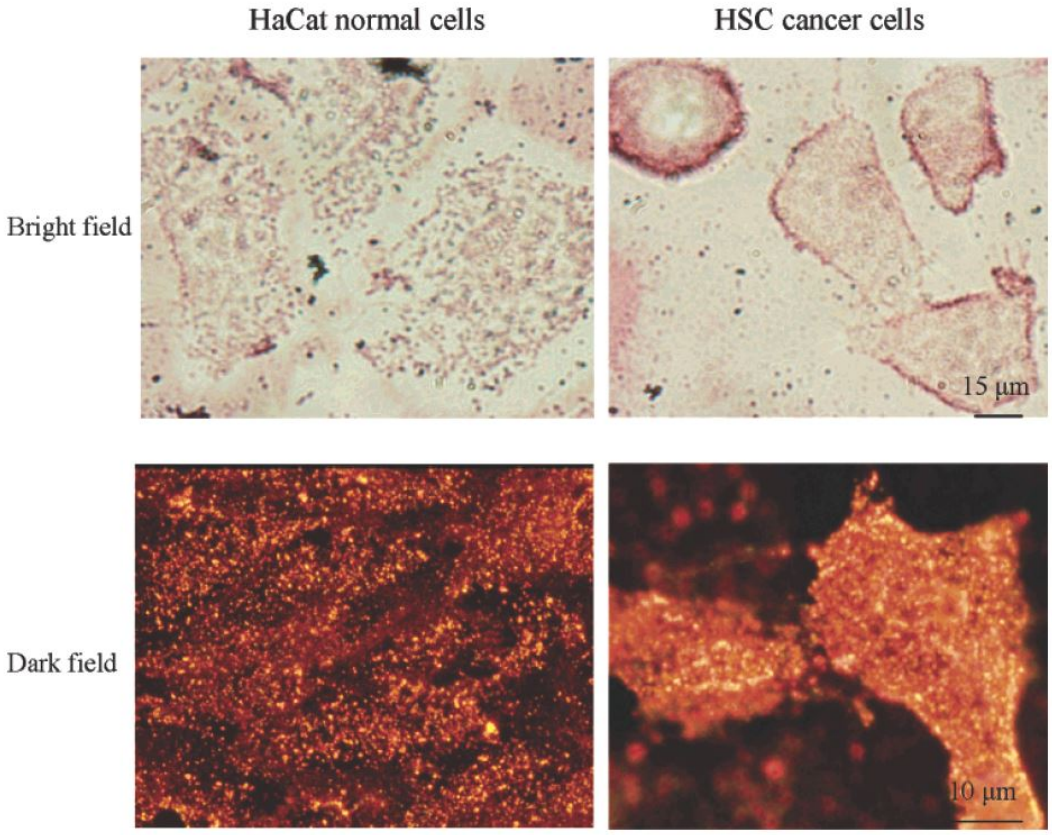

Figure 1.17: Bright and dark field images of anti-EGFR antibody conjugated gold nanorods on HaCat normal and HSC cancer cells. Reprinted from Ref. [66]. Copyright 2007 American Chemical Society.

A number of studies have optimized the SERS of small AuNP-adsorbed molecules with non-spherical AuNPs. For example, El-Sayed et al. have recently shown that oral cancer cells can align AuNRs that have been conjugated with anti-epidermal growth factor receptor antibodies on the cell surface, leading to a SERS fingerprint specific of the cancer cells [66]. The Halas group has discriminated between cancer cells and healthy cells by monitoring changes in the Raman spectrum induced by pH changes over a suitable range with carboxy groups of a mercaptobenzoic acid layer on AuNSs that were active in the NIR region where blood and tissues are less absorbing [75] (Figure 1.18). Mammalian cell surfaces were imaged using SERS with nitrilefunctionalized AuNPs. SERS hot sites correlate well with small aggregated AuNPs oriented preferentially in the direction of incident laser polarization [76]. Spatially resolved probing

and imaging of pH in live cells was demonstrated by SERS using 4-mercaptobenzoic acid-AuNP aggregates [77].

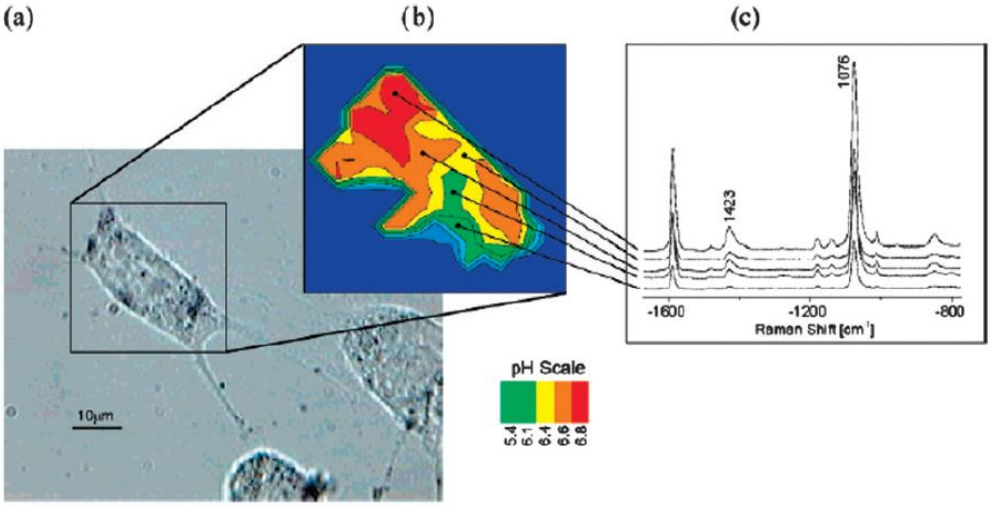

Figure 1.18: (a) Photomicrograph of an NIH/3T3 cell after 4.5 h incubation with the p-mercaptobenzoic acid (pMBA) gold nanosensor. Numerous gold nanoparticles have accumulated in the cell, enabling pH probing in different endosomes over the entire cell based on the SERS signature of pMBA. Lysosomal accumulations can be observed as black spots at the resolution of the light microscope. (b) pH map of the cell displayed as a false color plot of the rations of the SERS lines at 1423 and 1076 cm^{-1}. The values given in the color scale bar determine the upper end value of each respective color. Scattering signals below a defined signal threshold (i.e., where no SERS signal exist) appear in dark blue. (c) Typical SERS spectra collected in the endosomal compartments with different pH. The spectra were collected in 1 s each using 830 nm cw excitation. Reprinted from Ref. [72]. Copyright 2009 The Royal Society of Chemistry.

1.3.3 Semiconductor quantum dots

Quantum dots (QDs) are essentially luminescent semiconductor nanocrystals that have emerged as a new class of fluorescent tags in the field of biology and medicine [12,78].As compared to organic dyes and fluorescent proteins, these tiny light-emitting particles have unique optical and electronic properties, such as size- and composition dependent tunable emission, photostability, large absorption cross-section leading to increased brightness, and a broad absorption spectra, allowing for simultaneous excitation of multiple fluorophores (Figure 1.19) [79]. In addition, upon suitable surface modification with targeting ligands such as antibodies, proteins or small molecules, these QDs can prove to be a versatile scaffold for therapeutic applications [80, 81].

Figure 1.19: Ten distinguishable emission colors of ZnS-capped CdSe QDs excited with a near-UV lamp. From left to right (blue to red), the emission maxima are located at 443, 473, 481, 500, 518, 543, 565, 587, 620, and 655 nm. Reprinted from Ref. [82]. Copyright 2002 Elsevier, Inc.

The most common chemical composition of QDs explored so far for biological applications is cadmium selenide (CdSe) QDs, with other examples including cadmium telluride (CdTe) and cadmium sulfide (CdSe) [83]. Additionally, several strategies have been developed for post-synthetically modifying these QDs for various purposes, such as coating with a protective inorganic shell, surface modification to render colloidal stability and direct linkage to biomolecules [84, 85]. When designing a QD probe, the selection of the QD core composition and size is based upon the desired wavelength of

emission [86]. (Figure 1.20)

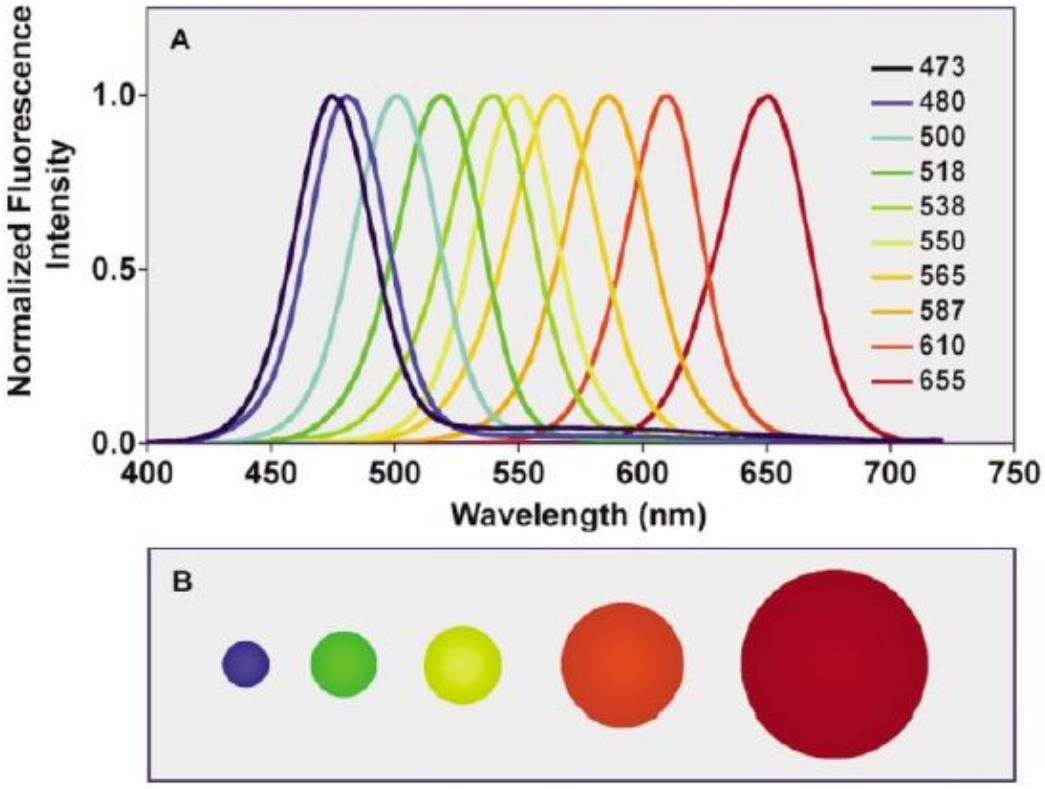

Figure 1.20: (A) Size-tunable fluorescence spectra of CdSe quantum dots and (B) Illustration of relative particle sizes. From left to right, the particle diameters are 2.1 nm, 2.5 nm, 2.9 nm, 4.7 nm and 7.5 nm. Reprinted from Ref. [79]. Copyright 2008 The Royal Society of Chemistry.

Typically, these QDs are synthesized via swift injection of precursor solutions (eg: Cadmium and selenium salts) into a hot solution of coordinating ligands under inert atmosphere, thus forming nanocrystal nuclei which are subsequently stabilized by binding of the coordinating ligands. The interplay between nucleation and crystal growth is dependent on the solution temperature, with the crystal growth being arrested by cooling the reaction mixture to room temperature, once the desired size range of the QDs is achieved [79]. The resulting QDs, however are highly hydrophobic owing to the presence of aliphatic coordinating ligands on their surface and hence require a phase-transfer process to be carried out prior to their use in biological applications. To this end, two main strategies for rendering these hydrophobic QDs soluble in aqueous solutions include: (a) ligand exchange with heterobifunctional ligands, which possess one

functional group that can bind to the surface of the QD and another functional group that is hydrophilic (eg: TOPO); [87] and (b) encapsulation by an amphiphilic polymer or inorganic silica shell(Figure 1.21) [88, 89].

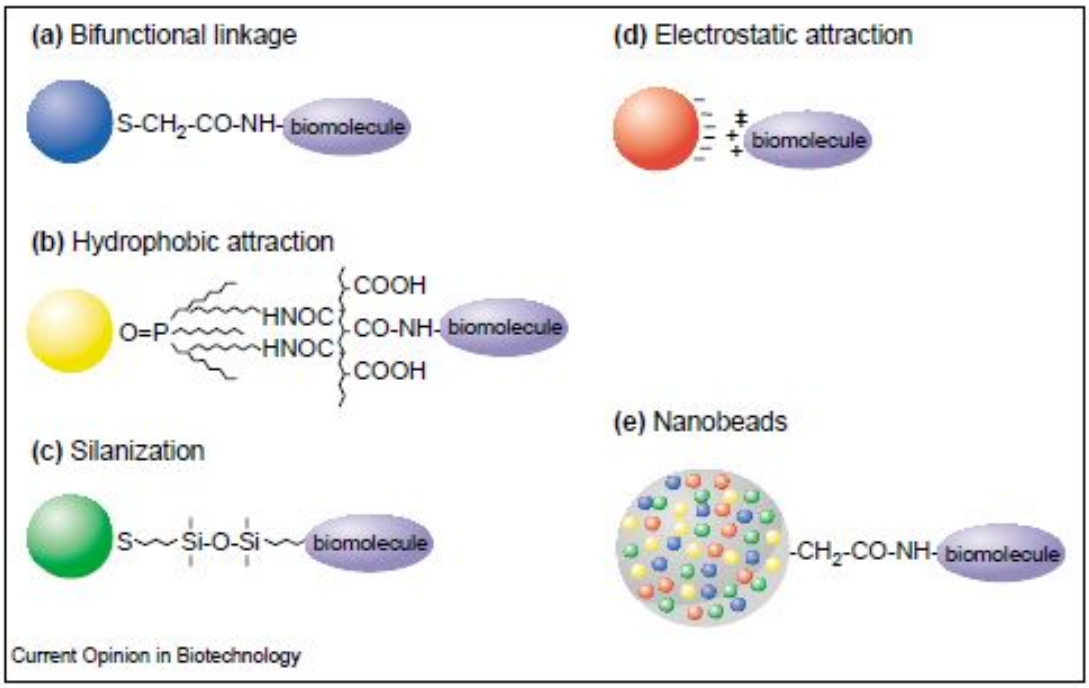

Figure 1.21: (a) Use of a bifunctional ligand such as mercaptoacetic acid for linking QDs to biomolecules. (b) TOPO-capped QDs bound to a modified acrylic polymer by hydrophobic forces. (c) QD solubilization and bioconjugation using a mercaptosilane compound. (d) Positively-charged biomolecules are linked to negatively charged QDs by electrostatic attraction. (e) Incorporation of QDs in microbeads and nanobeads. Reprinted from Ref. [82]. Copyright 2002 Elsevier, Inc.

Such bioconjugated QDs have been used as fluorescent labels for *in vitro* cellular imaging, in DNA hybridization and immunoassays, receptor-mediated endocytosis and time-gated fluorescence imaging of tissue sections. An important advantage of using QDs as fluorescent labels is their photostability which allows for tracking the labeled cells or tissues over a longer period of time as compared to fluorescent dyes. For example, Nie and his coworkers conjugated luminescent QDs to transferrin and folic acid, ligands which are known to be recognized by cancer cells and used these QDs to visualize the cancer cells, when these QDs were taken up by the cells via receptor-mediated endocytosis [82]. (Figure 1.22)

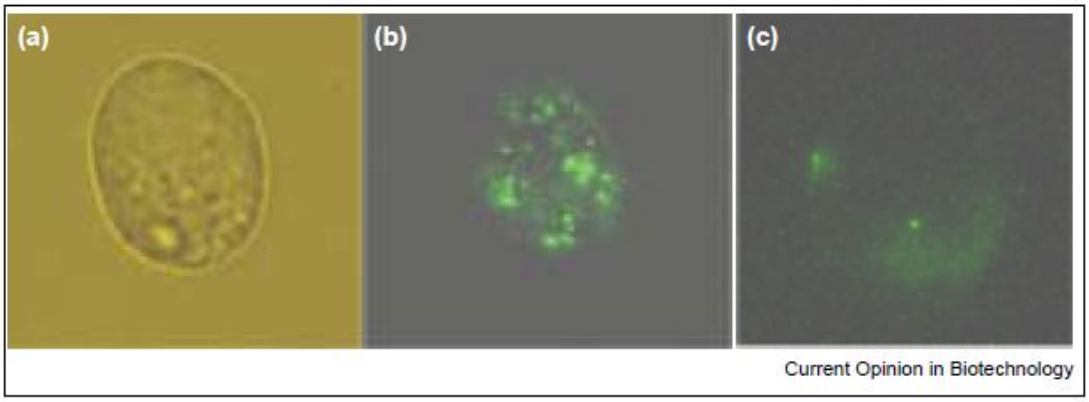

Figure 1.22: (a) Bright field image of control KB cell (without QDs), (b) KB cell incubated with folate-conjugated QDs and (c) KB cell incubated with bovine-serum albumin-conjugated QDs. Receptor-mediated endocytosis only occurs when the QDs are conjugated to folic acid, which recognized by folate receptors overexpressed on the surface of cancer cells. Reprinted from Ref. [82]. Copyright 2002 Elsevier, Inc.

Similarly, Lee and his coworkers also demonstrated the use of CdSe/ZnS QDs for simultaneous imaging and delivery of siRNA in glioblastoma cells (Figure 1.23). By using different bioconjugation strategies, they were able to track the siRNA delivered to the cells as well as release the siRNA in a stimuli-responsive manner to induce apoptosis in glioblastoma cells.

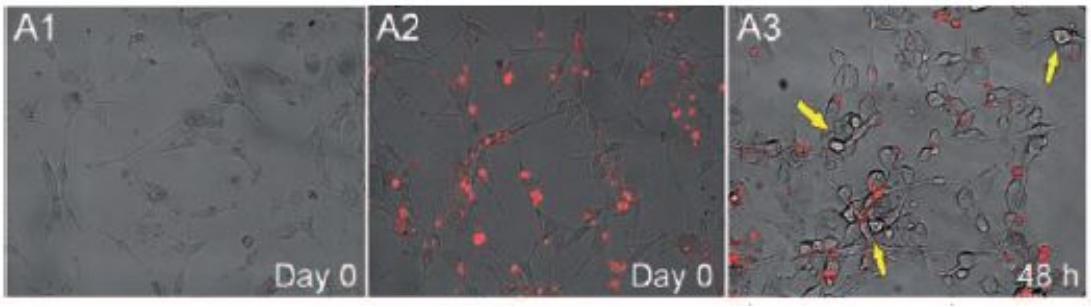

Figure 1.23: (A1) Morphology of U87-EGFRvIII cells before incubation with siRNAQDs on Day 0. A2) U87-EGFRvIII cells after incubation with siRNAQDs (red) on Day 0. A3) Morphology of U87-EGFRvIII cells 48 h after incubation with siRNAQDs. Note that effect of the EGFRvIII knockdown by the siRNAQDs can be clearly seen as the cells have clearly shrunk (yellow arrows) and appear to have collapsed (cf. Day 0), marking the onset of apoptosis. Reprinted from Ref. [80]. Copyright 2010 John Wiley and Sons.

However, *in vivo* targeting and imaging is very challenging due to the relatively large overall size (typically greater than 20 nm in hydrodynamic diameter) and short

circulation half lives of QD conjugates [90] and as a result there are very few reports of such studies in literature [91,92]. Specific targeting of QD conjugates in living subjects was first reported using peptides as the targeting ligands [93]. In this pioneering study, *ex vivo* histological analysis showed that QDs were specifically directed to the tumor vasculature and other targets by different peptides. Although no *in vivo* imaging was achieved, this study demonstrated the feasibility of using QD as a nanoplatform for *in vivo* specific targeting, which opened up a new field of QD-based research. Recently, Cai *et al.* reported the *in vivo* targeted imaging of tumor vasculature using QDs conjugated to RGD containing peptides which are known to target $\alpha_v\beta_3$ integrins present on tumor cells and vasculature [94] (Figure 1.24). In this study, in vivo NIR fluorescence (NIRF) imaging was successfully achieved in nude mice bearing subcutaneous $\alpha_v\beta_3$ integrin-positive U87MG human glioblastoma tumors, where tumor fluorescence intensity reached maximum at 6 h post injection (Figure 1.24). Owing to the size of QD705-RGD (20 nm in diameter), QD705-RGD did not penetrate the tumor and mainly targeted tumor vasculature as confirmed by ex vivo immunofluorescence staining. Such QDs which target tumor vasculature has immense potential as an imaging modality, as it is known the sprouting neovasculature in many tumor types overexpresses $\alpha_v\beta_3$ integrin [94].

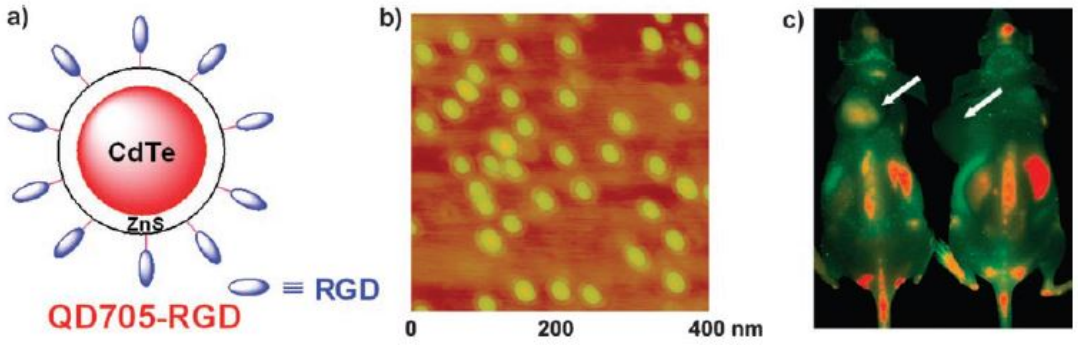

Figure 1.24: (A) A schematic illustration of QD705-RGD probe. B) An atomic force microscopy image of QD705-RGD deposited on a silicon wafer. C) In vivo NIRFimaging of tumor vasculature in U87MG human glioblastoma-tumor-bearing mice. The mouse on the left was injected with QD705-RGD and the mouse on the right was injected with QD705. Arrows indicate tumors. Reprinted from Ref. [94]. Copyright 2006 John Wiley and Sons.

In addition to tumor imaging, the unique photophysical properties of QDs also make them attractive candidates for investigating stem cell behavior. For example, Selvan and coworkers reported a highly efficient method of mimicking the micro-tubule mediated protein transport using biotinylated peptides containing a microtubule-associated sequence (MTAS) and a nuclear localization signaling (NLS) sequence, which were then conjugated to streptavidin-coated CdSe/ZnS quantum dots. They showed that these peptide-conjugated QDs were able to escape the acidic endosomal environment and be delivered into the nucleus of human mesenchymal cells (hMSCs) via microtubules (Figure 1.25)

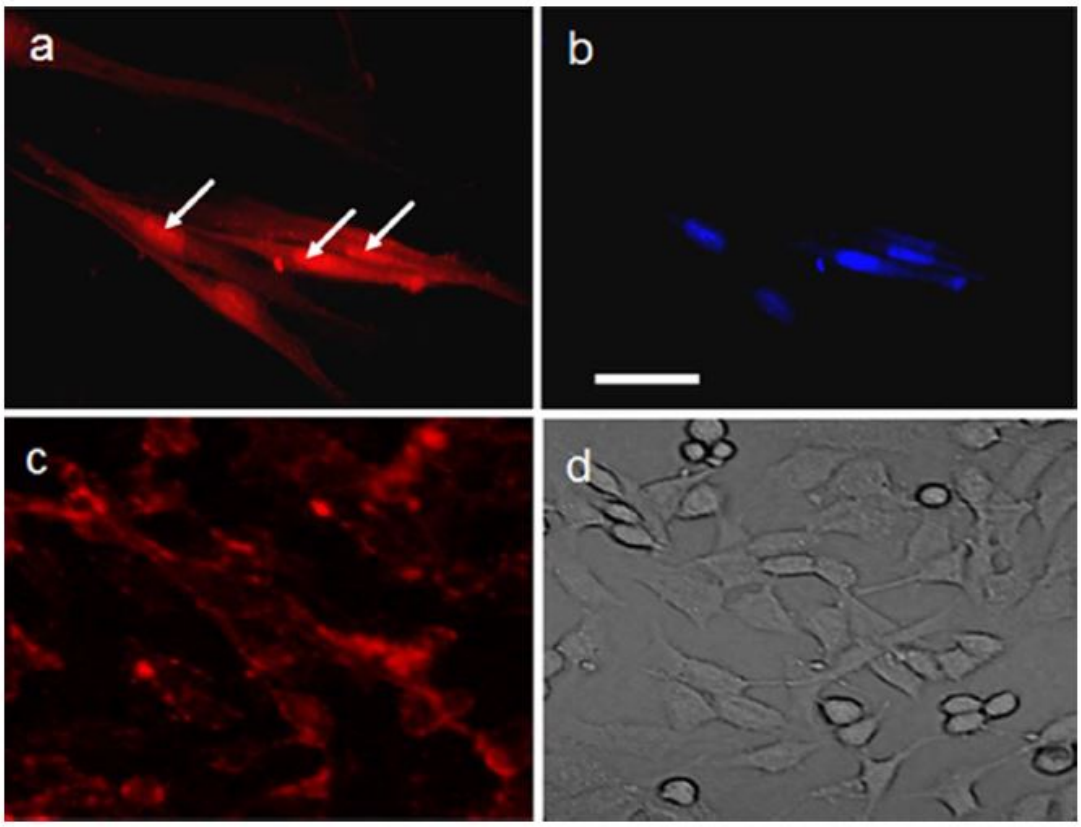

Figure 1.25: (a,b) SV40-NLS-TP and (c,d) SV40-NLS peptide coated red-emitting CdSe/ZnS QDs. (a,c) hMSCs under fluorescence microscope, (b) DAPI staining indicating nucleus of the cells. White arrows in (a) point out the accumulation of QDs in the nucleus. (d) Light microscope image. It is clear from (c) that SV40-NLS-peptide peptide-coated QDs are present on the cell membrane and endosomes without nuclear targeting. Scale bar: 100 μm. Reprinted from Ref. [95]. Copyright 2013 Nature Publishing group.

However, QD-based fluorescence imaging in small animals cannot be directly scaled up to in vivo imaging in patients due to the limited optical signal penetration depth. Hence it is important to first overcome the major roadblocks for clinical translation of QDs, such as inefficient delivery, potential toxicity, and lack of quantification. However, with the development of biocompatible and multifunctional quantum dots and further improvement of the conjugation strategy, it is expected that QDs may achieve optimal tumor targeting efficacy with acceptable toxicity profile for clinical translation in the near future [96].

1.3.4 Upconversion nanoparticles

In recent years lanthanide-doped upconversion nanocrystals (UCNPs) have emerged as a new class of luminescent optical labels that have become promising alternatives to organic fluorophores and quantum dots for applications in biological assays and medical imaging [97, 98]. These lanthanide and other rare-earth upconversion nanophosphors, when excited by continuous-wave near-infrared light, emit higher-energy light through the sequential absorption of multiple photons or energy transfers. As a result, they exhibit low autofluorescence background, large anti-Stokes shifts, sharp emission bandwidths, high resistance to photobleaching, and high penetration depth and temporal resolution. Such special luminescence properties make UCNPs attractive candidates as bioimaging probes (Figure 1.26).

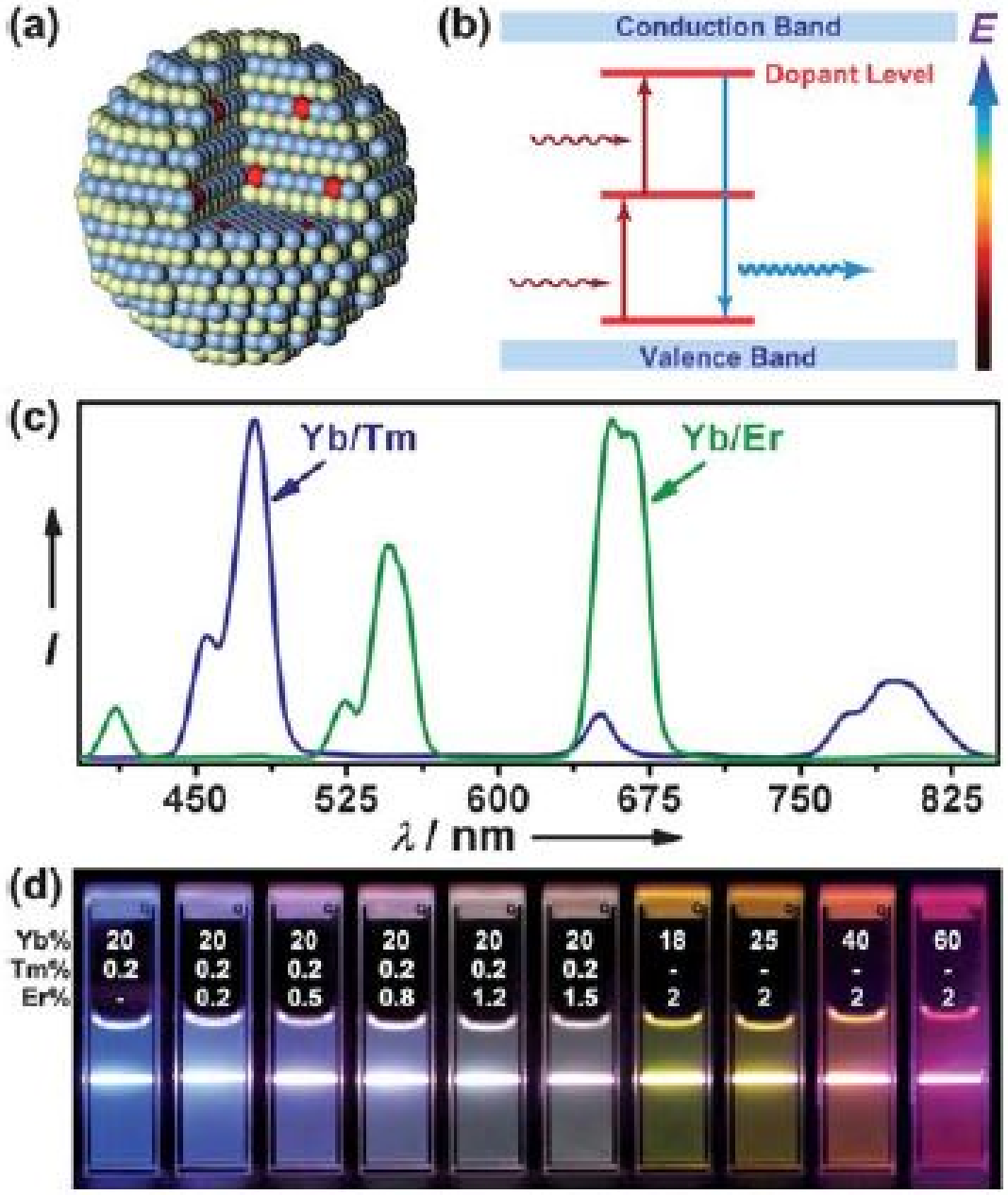

Figure 1.26: (A) Schematic illustration of UCNPs composed of a crystalline host and lanthanide dopant ions embedded in the host lattice. (B) Schematic energy level diagram showing that UC luminescence primarily originates from electron transitions between energy levels of localized dopant ions. (C) Typical emission spectra showing multiple narrow and well-separated emissions (Intensities, I)produced by cubic $NaYF_4$:Yb/Tm (20/0.2 mol%) and $NaYF_4$: Yb/Er (18/2 mol%) nanoparticles. (D) UC multicolor fine-tuning through the use of lanthanide-doped $NaYF_4$ nanoparticles with varied dopant ratios. Note that the emission spectra and colors are associated with the host composition, particle size, and particle surface properties. Reprinted from Ref. [98]. Copyright 2010 The Royal Society of Chemistry.

A variety of chemical techniques, including coprecipitation, thermal decomposition, hydro(solvo)thermal synthesis, solgel processing and combustion synthesis, have been demonstrated to synthesize lanthanide-doped UCNPs [99,100]. Most of the UCNPs prepared using high-temperature routes described above have no intrinsic aqueous solubility and lack functional moieties. Surface modification of lanthanide-doped nanocrystals not only improves photostability of the nanocrystals with desirable interfacial properties, but also provides a potential platform for attaching biological macromolecules for various biomedical applications [98, 101] (Figure 1.27).

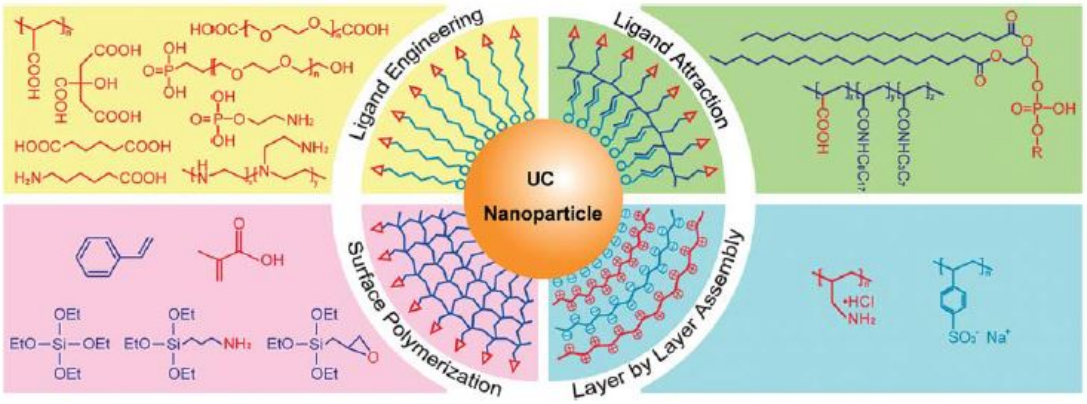

Figure 1.27: Ligand engineering involves a ligand exchange reaction with hydrophilic bifunctional molecules or involves a direct oxidation of the terminal group of native ligands to generate a pendant carboxylic functional group. Some bifunctional molecules may be employed in a one-pot synthetic procedure to directly yield hydrophilic UCNPs with additional functional groups and further bioconjugation capabilities. Ligand attraction involves absorption of an additional amphiphilic polymer onto the nanoparticle surface through the hydrophobic van der Waals attraction between the original ligand and hydrocarbon chain of the polymer. Layer-by-layer assembly involves electrostatic absorption of alternately charged polyions on the nanoparticle surface. Surface polymerization involves growing a dense cross-linked shell on the nanoparticle core by condensation of small monomers. Reprinted from Ref. [98]. Copyright 2010 The Royal Society of Chemistry.

For small animal bioimaging, UCNPs have attractive features (i) infrared excitation is less harmful to small animals; (ii) Upconversion luminescence (UCL)-based bioimaging offers no autofluorescence from biosamples [102], because no biosamples show UCL properties under CW excitation at 980 nm; (iii) Tm^{3+} provides NIR UCL emission at 800 nm, that is, the excitation (980 nm) and emission wavelengths are both in the range of the NIR window. Using UCL emission of Tm^{3+} as the output signal, UCNPs can

be successfully used as probes for the visualization of biological samples even at high penetration depth. To date, UCNPs have successfully been applied to small-animal imaging, including tumor targeted imaging, lymphatic imaging, vascular imaging, cell tracking and multimodal imaging [97] (Figure1.28).

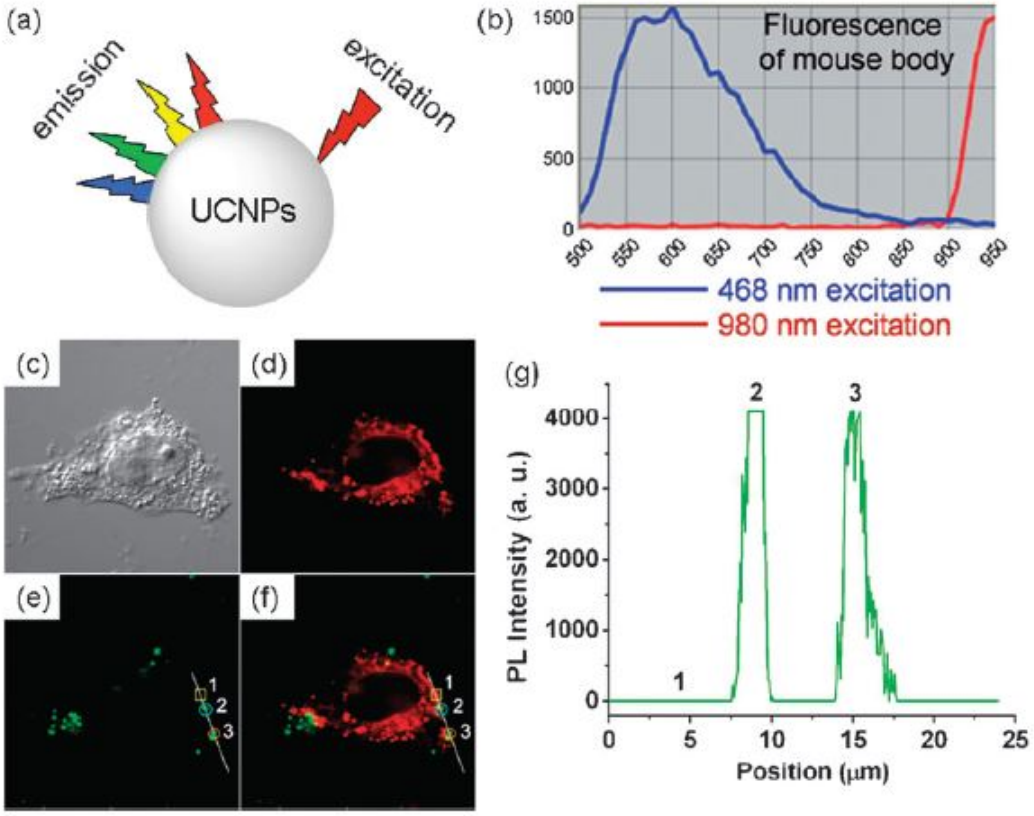

Figure 1.28: (a) A scheme of the excitation/emission profiles of UCNPs. (b) A comparison of autofluorescence emission spectra from the mouse abdomen excited with 468 nm blue (blue line) and 980 nm near infrared (red line). Images of a live HeLa cell dual-labeled with DiI and UCNPs. (c) Differential interference contrast brightfield image. (d) Image of DiI when emission was collected at 560600 nm (λex = 543 nm). (e) UCL image of UCNPs when emission was collected at 500600 nm (λex = 980 nm). The overlay of panels d and e is shown in panel f. (g) UCL intensity profile along the lines shown in panels e and f (the output power of the laser was 400 mW, corresponding to approximately 19 mW in the focal planes; image size, 800 x 800 pixel; sampling speed, 2.0 μs/pixel; pinhole, 197 mm; 60x oil-immersion objective lens; NA 1.35; zoom, x3.5). Reprinted from Ref. [97]. Copyright 2012 The Royal Society of Chemistry.

The first example of targeted UCL imaging *in vivo* is using FA-modified UCNPs as probes. FA as a targeting agent has attracted wide attention, due to its high stability,

non-immunogenic character, and ability to conjugate with a wide variety of molecules. Moreover, folate receptors (FR) are over-expressed in many of the human cancerous cells, and are only minimally distributed in normal tissues. On the basis of the high affinity of FA and FR, several FA-modified UCNPs have been developed for targeted imaging *in vitro* [103–105]. However, only one case of FA-targeted UCL imaging of small animal has been reported by Huang group [106]. After intravenous injection of FA-modified UCNPs into HeLa tumor-bearing athymic nude mouse for 24 h, a significant UCL signal at 600-700 nm was observed in the tumor, whereas no significant luminescence signal was observed in the tumor for the mouse which was injected amine-functionalized UCNPs (as a control) (Figure 1.29). Moreover, the successful targeted recognition of FA-modified UCNPs was confirmed by *ex vivo* UCL imaging. In particular, such UCL signal in the tumor was inhibited in the presence of a blocking dose of FA (10 mg kg^{-1}), proving the specificity of the targeting *in vivo* of FA-modified UCNPs [106].

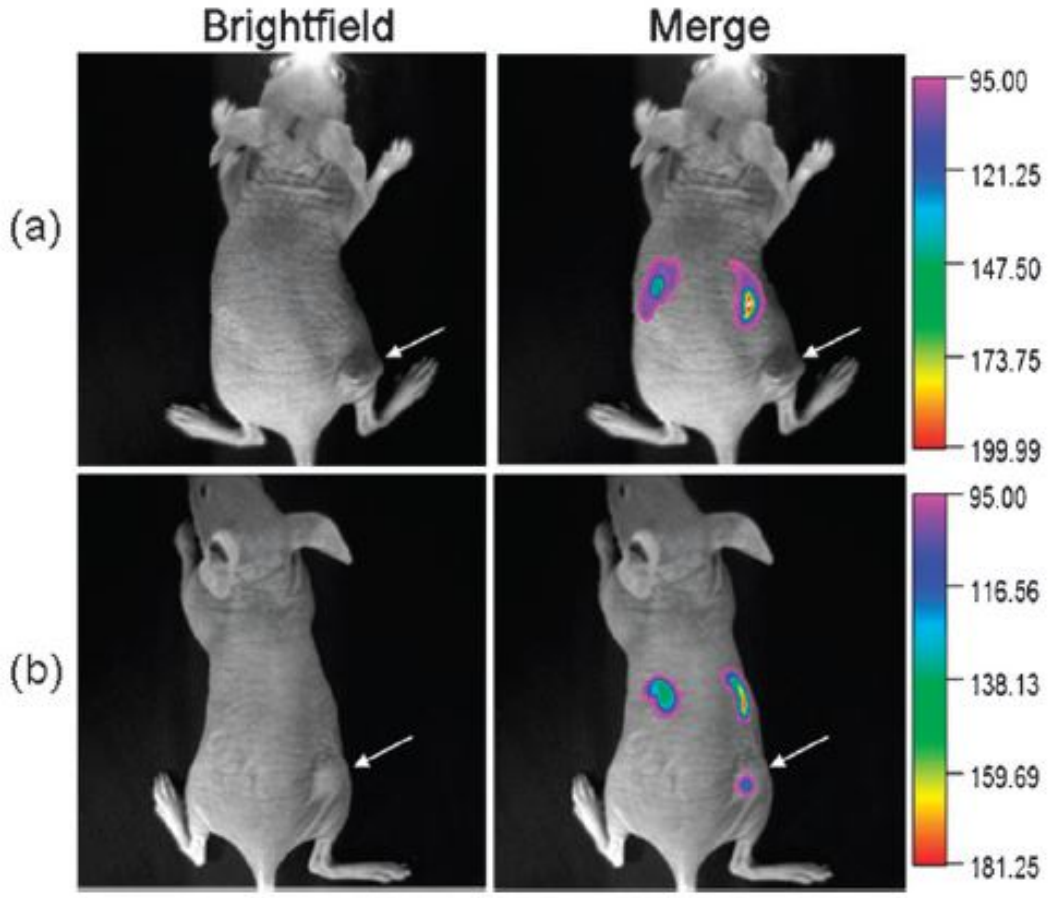

Figure 1.29: In vivo upconversion luminescence imaging of subcutaneous HeLa tumor-bearing athymic nude mice (right hind leg, pointed by white arrows) after intravenous injection of UCNPs-NH_2 (a) and UCNPs-FA (b), respectively. All images were acquired under the same instrumental conditions (power density E120 mW cm^2 on the surface of mouse). Reprinted from Ref. [97]. Copyright 2012 The Royal Society of Chemistry.

Small peptides provide better cellular uptake and tissue penetration when introduced to animals. The arginine-glycine-aspartic acid (RGD) peptide has a high affinity for the $\alpha_v\beta_3$ integrin receptor which plays a pivotal role in tumor angiogenesis [107,108]. Recently, it was reported that cyclopeptide c(RGDFK)-modified $NaYF_4$:Yb,Er,Tm nanoparticles with the PEG linkage (UCNP-RGD) can be used for targeted imaging of small animals bearing $\alpha_v\beta_3$ -overexpressing tumors (human glioblastoma U87MG) (Figure 1.30) [109]. The sequence of UCL *in vivo* images of the tumor-bearing mice injected with UCNP-RGD showed that the maximum U87MG tumor binding for the

UCNP-RGD appeared at about 4 h postinjection and was retained for 24 h. In particular, the UCL targeted in vivo images achieved high SNR between the tumor and the background, using UCL emission at 800 nm as the output signal. Such high SNR of UCL imaging of small animals can be compared with bioluminescence imaging. High-affinity polypeptide neurotoxins have been shown to be effective agents for probing biological systems with high specify. Li et al. [110] reported that CTX peptide-mediated $NaYF_4$: Yb,Er/Ce nanoprobes could directly target, visualize tumors in living animals and produce high-contrast images based on highly specific tumor binding. These studies provide a foundation for the development of advanced whole-body targeted UCL imaging, based on the UCNPs as biological luminescent labels, which are useful in tumor recognition.

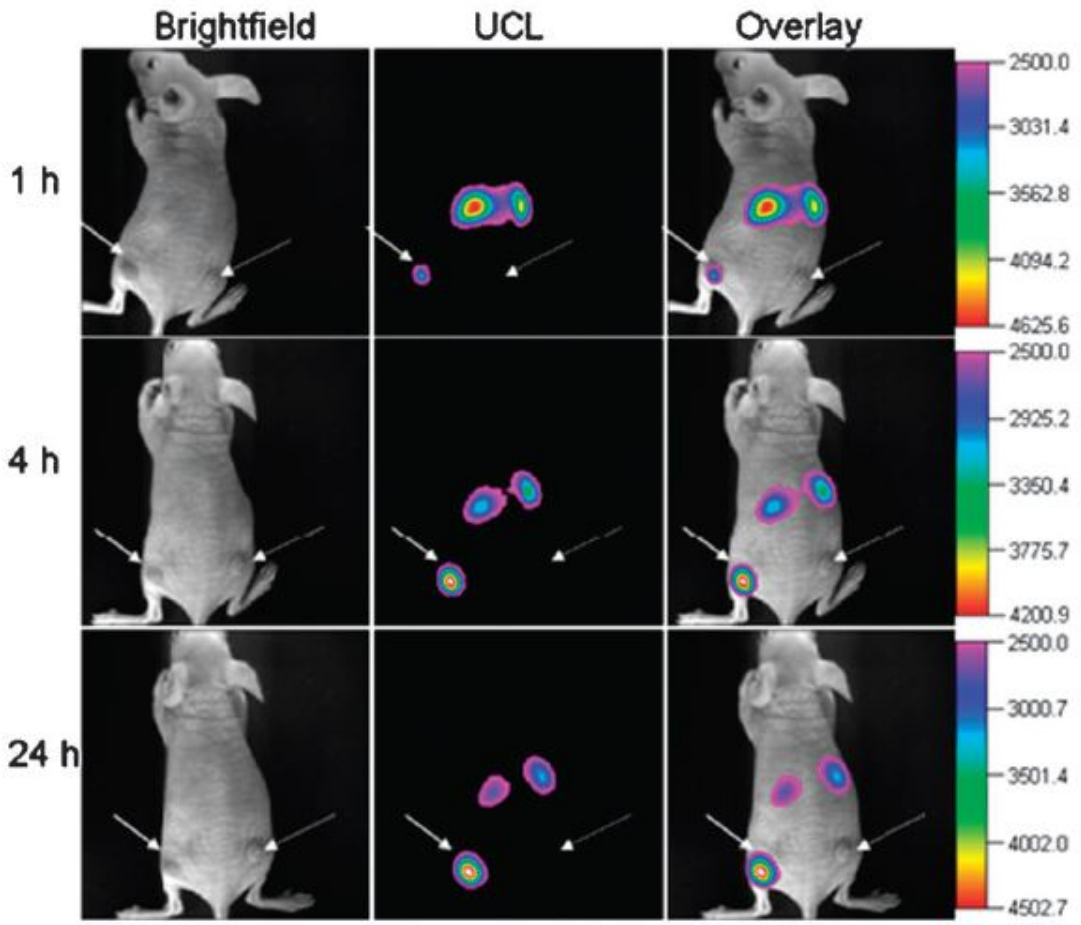

Figure 1.30: Time-dependent *in vivo* upconversion luminescence imaging of subcutaneous U87MG tumor (left hind leg, indicated by short arrows) and MCF-7 tumor (right hind leg, indicated by long arrows) borne by athymic nude mice after intravenous injection of UCNP-RGD over a 24 h period. All images were acquired under the same instrumental conditions (power 80 mW cm−2 and temperature 21.5°C on the surface of the mouse). Reprinted from Ref. [97]. Copyright 2012 The Royal Society of Chemistry.

In addition to tumor imaging, UCNPs have also been explored for stem cell applications such as tracking the transplanted stem cells *in vivo*. For example, Liu and his coworkers [111] developed multifunctional upconversion nanoparticles (MFNPs) for labeling mouse mesenchymal stem cells (mMSCs). Varying numbers of mMSCs labeled with MFNPs were then injected into the back of a nude mouse and imaged using a modified Maestro *in vivo* imaging system using an external 980 nm laser as the excitation source. Strong upconversion luminescence (UCL) was detected at sites where

MFNPs-labeled mMSCs were injected (Figure 1.31a). Quantification of the UCL emission intensities demonstrated a concomittant increase in UCL intensity with an increase in cell number (Figure 1.31b). Remarkably, as low as 10 MFNP-labeled mMSCs were enough to generate a positive signal, thus demonstrating a significantly higher sensitivity than other imaging modalities, like QDs and fluorescent proteins.

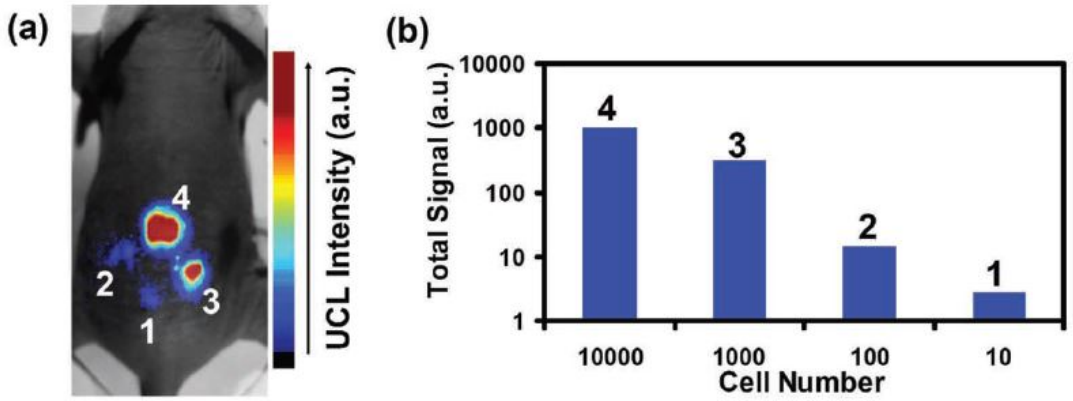

Figure 1.31: (a) A UCL image of a mouse subcutaneously injected with various numbers of mMSCs (10 to 10^4) labeled with MFNP-PEG. (b) Quantification of UCL signals in (A). Reprinted from Ref. [97]. Copyright 2012 The Royal Society of Chemistry.

1.4 Nanomaterials as delivery vehicles

Therapeutic moieties such as proteins, peptides, small molecule drugs and nucleic acids face several transport barriers on their tortous journey from their site of introduction to their molecular site of action. Critical barriers include (i) rapid clearance through the kidney and reticulo-endothelial system (RES); (ii) transport from the bloodstream to target cells within tissues; (iii) translocation across the plasma membrane of the cellular targets; (iv) endosomal escape, (v) multi-drug resistance mechanisms present in cells [112]. Recent studies have illustrated that nano-scale delivery vehicles such as polymers, lipids, inorganic and metal nanoparticles can be used to surmount these barriers faced by the therapeutic moieties and thus improve the overall efficacy of the drugs as well as minimize the deletarious side effects. The following section will focus on some examples of such nanomaterials used for drug delivery to cancer and stem cells, more specifically on the two most commonly employed strategies - polymers and silica nanoparticles.

1.4.1 Polymeric dendrimers

Development of efficient drug delivery systems has attracted tremendous attention during the last two decades. The principal reason for the incredible growth of drug delivery technology is the realization that the best prospect for achieving substantial improvements over current therapies will occur through improved delivery of both existing drugs and yet undiscovered drugs. This necessity arises primarily due to the enormous barriers that a drug molecule must overcome before it reaches its target site within the body, where it can perform its biological role. In addition, delivery systems can address and correct problems related to the physical characteristic of a drug, including solubility and stability. Consequently, the technologies currently under development for drug delivery and drug targeting systems will have a tremendous impact on the improvement of novel drug therapies. A major subset of existing drug delivery systems, are those based on polymers, referred to as polymer therapeutics, which have attracted significant attention, as they appear particularly promising [23] (Figure 1.32).

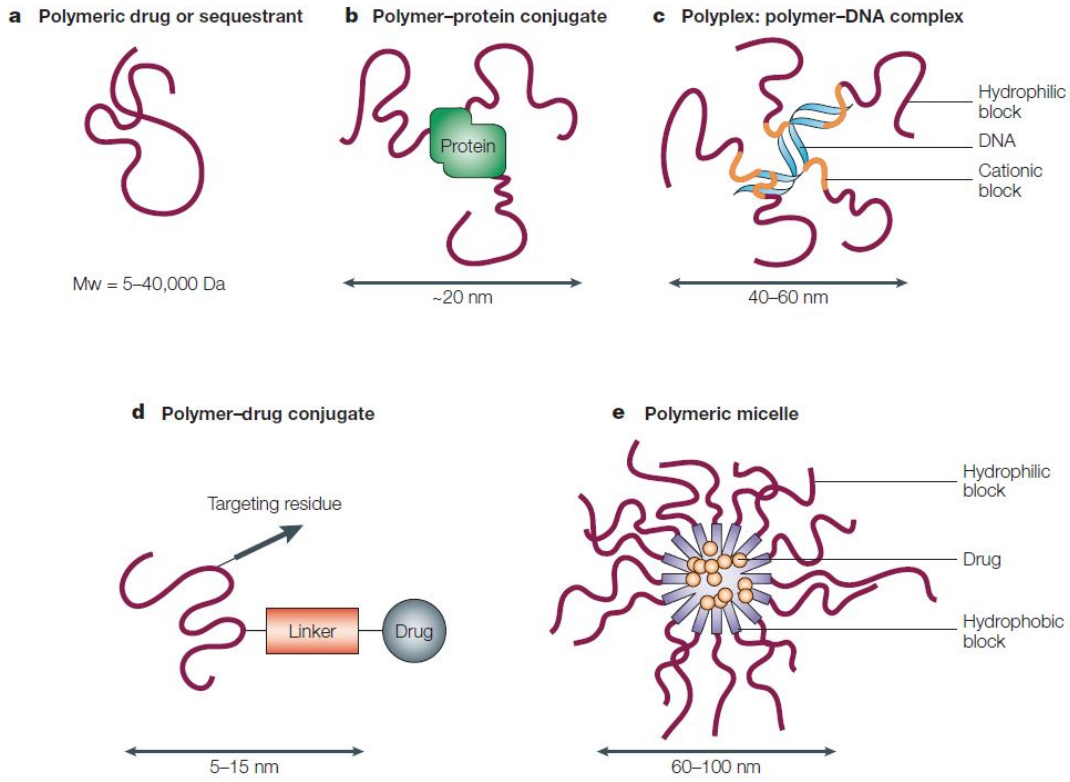

Figure 1.32: Schematic representation of polymer therapeutics now in, or progressing towards, clinical development. The nano-sized and frequrently multicomponent nature of these structures is visible. Reprinted from Ref. [23]. Copyright 2003 Nature Publishing Group.

Generally, polymer therapeutics refer to any polymer that is used as a component of a drug product for the purpose of eliciting or modifying drug action. This includes polymers, which are inherently biologically active, polymer-drug conjugates, polymeric micelles, nanoparticles and polymer-coated liposomes. The polymers themselves comprise linear, branched and dendritic structures (Figure 1.33). Because of the flexibility of polymer chemistries, it might be possible to provide the multiple functions required for efficient gene and drug delivery while maintaining biocompatibility, facile manufacturing, and robust and stable formulation [113].

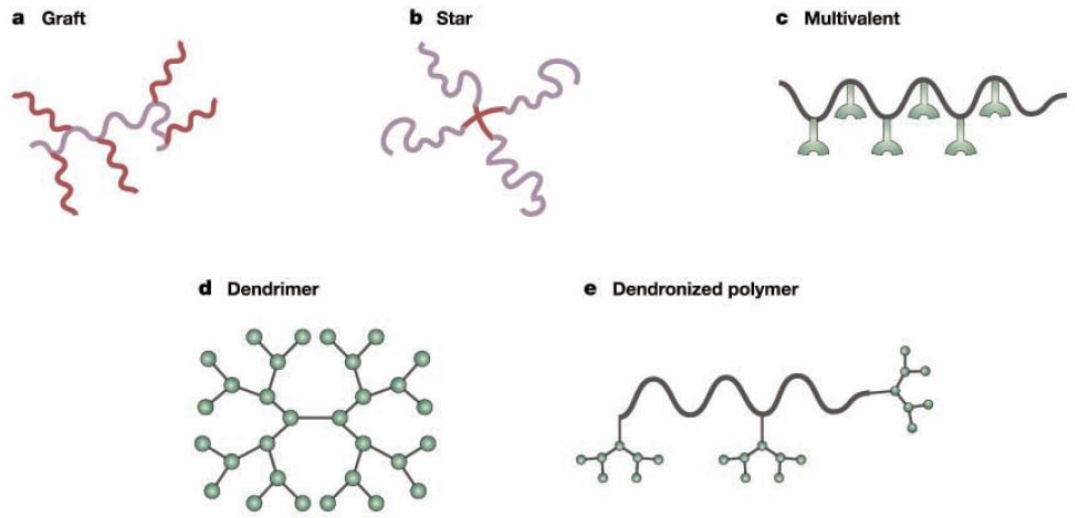

Figure 1.33: Novel polymeric architectures now being explored as the polymer therapeutics of the future. The trend at present is towards more complex star-shaped and graft block-copolymer systems (a and b), tailored multivalent polymers providing improved opportunities for biorecognition (c) and three dimensional biomimetic architectures, including dendrimers and dendronized polymers. Reprinted from Ref. [23]. Copyright 2003 Nature Publishing Group.

Dendrimers are highly branched, globular macromolecules with many arms emanating from a central core. The stepwise synthesis of dendrimers affords molecules with a highly regular branching pattern, a unique molecular weight or a low polydispersity index, and a well-defined number of peripheral groups. Therefore, dendrimers with perfect branching resulting from stepwise synthetic processes are distinct from the more readily accessed but less well-defined hyperbranched polymers with irregular branching obtained by polymerization processes [114]. The rapid emergence of dendrimers in biological applications has been accompanied by a growth in the number of dendrimer backbones designed to be water soluble and biocompatible. Commercially available polyamidoamine (PAMAM) dendrimers (Figure 1.34), prepared by the divergent growth approach of Tomalia et al. [115], are one of the most widely used dendrimer scaffolds in biology [116]. Despite their broad applicability, it is generally necessary to modify the surface amine groups of these dendrimers with neutral or anionic moieties to avoid the toxicity and liver accumulation associated with their polycationic surfaces [117]. Polypropyleneimine dendrimers have been commercialized and investigated

for their biological application, but the presence of multiple cationic amine groups leads to significant toxicity [117]. Polyaryl ether dendrimers, developed by Frechet and Hawker [118], have been tested for drug delivery applications, but their poor water solubility necessitates the extensive use of solubilizing groups at their periphery [119].

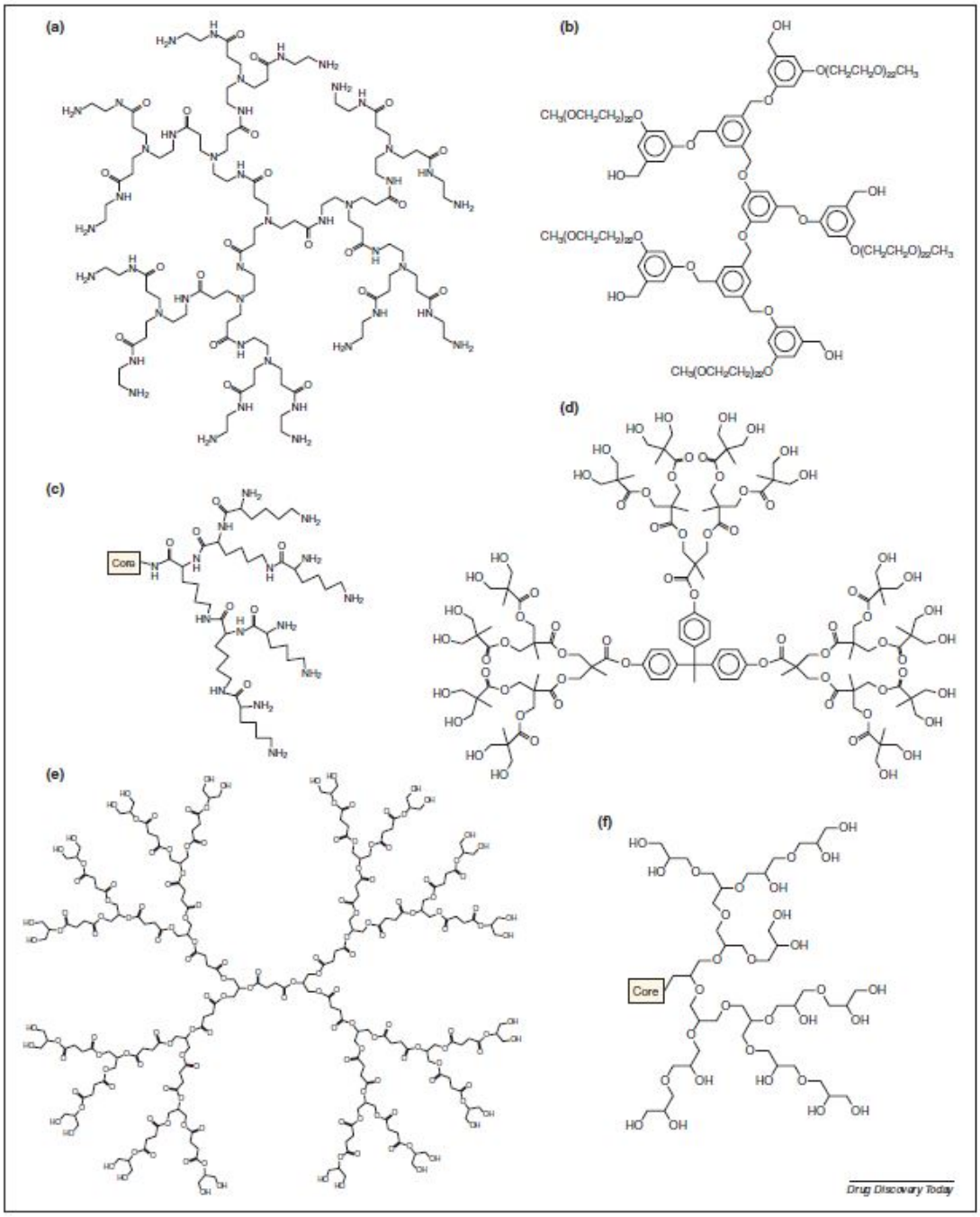

Figure 1.34: (a) PAMAM dendrimer. (b) Polyaryl ether dendrimer. (c) Polylysine dendron. (d) Polyester dendrimer based on 2,2-bis(hydroxymethyl)propionic acid. (e) Polyester dendrimer based on glycerol and succinic acid. (f) Dendritic polyglycerol. Reprinted from Ref. [114]. Copyright 2005 Elsevier, Inc.

Because of the large number of secondary and tertiary amines on the polymer, PAMAM dendrimers are also thought to be proton sponges (Figure 1.35), as they

can undergo protonation in the low pH conditions of the endosome and thereby cause increased influx of protons and counter ions into the endocytic vesicles [113]. This results in increased osmotic pressure within the vesicle, causing it to swell and ultimately rupture, thereby releasing the contents (i.e polymer-gene complexes) into the cytoplasm. Haensler and Szoka originally reported the use of PAMAM dendrimers for gene delivery [120]. They found that the sixth-generation dendrimer was better than higher and lower generations by 10-fold. Due to its relatively high gene-delivery efficiency and good biocompatibility, PAMAM dendrimers have recently been used in several *in vivo* gene delivery studies [121, 122].

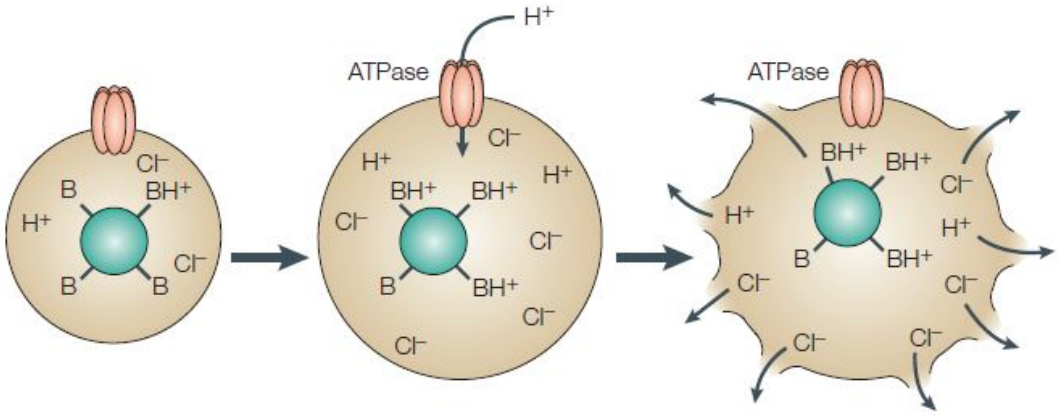

Figure 1.35: Protonation of the proton-sponge polymer (green) causes increased influx of protons (and counter-ions) into endocytic vesicles. Increasing osmotic pressure causes the vesicle to swell and rupture. Reprinted from Ref. [113]. Copyright 2005 Nature Publishing Group.

Additionally, the unique properties of dendrimers, such as improving drug solubility, plasma circulation time and affording passive targeting capabilites due to the enhanced permeation and retention effect; makes them interesting candidate as drug delivery vehicles. Initial studies of dendrimers as potential delivery systems focused on their use as unimolecular micelles and dendritic boxes for the noncovalent encapsulation of drug molecules [123]. For example, in early studies, DNA was complexed with PAMAM dendrimers for gene delivery applications, and hydrophobic drugs and dye molecules were incorporated into various dendrimer cores [124]. An advantage of using dendritic

unimolecular micelles rather than conventional polymeric micelles is that the micellar structure is maintained at all concentrations because the hydrophobic segments are covalently connected. However, this approach suffers from a general drawback in that it is difficult to control the release of molecules from the dendrimer core. In some cases, harsh conditions are required [124], whereas in others the encapsulated drug is not well retained and the molecules are released relatively rapidly [125]. An alternative approach to the development of dendrimers as anticancer drug carriers is to exploit their well-defined multivalency for the covalent attachment of drug molecules to the dendrimer periphery. The drug loading can be tuned by varying the generation number of the dendrimer, and release of the drug can be controlled by incorporating degradable linkages between the drug and dendrimer. For example, Duncan and co-workers [126] have prepared conjugates of PAMAM dendrimers with cisplatin, a potent anticancer drug with nonspecific toxicity and poor water solubility. The conjugates show increased solubility, decreased systemic toxicity and selective accumulation in solid tumors. Furthermore, the dendrimer-platinum complex has been found to show increased efficacy relative to cisplatin in the treatment of subcutaneous B16F10 melanoma.

In addition, Zhou et al. [127] have described the preparation of PAMAM dendrimers from a cyclic tetraamine core and the subsequent attachment of 5-fluorouracil to the dendrimer periphery. These conjugates release free 5-fluorouracil on incubation in phosphate-buffered saline. In early studies directed at developing drug carriers with tumor cell specificity, Frechet and co-workers [128] prepared multivalent conjugates of folic acid or the antitumor drug methotrexate and polyaryl ether dendrimers. Although the presence of several copies of folic acid or the hydrophilic drug molecule on the periphery of the dendrimer renders these conjugates water soluble, the water solubility of the polyaryl ether dendrimers can be increased further by attaching PEO chains to the periphery [119]. By using a careful synthetic strategy with two different chain end functionalities, it is also possible to attach both hydrophobic model drugs and PEO moieties to the dendrimer periphery in a controlled manner. These model studies provided an early demonstration of the advantage of the stepwise synthesis and the controlled multivalency of dendrimers for drug delivery. The preparation of multivalent folic acid

conjugates of dendrimer has important implications for targeting to tumor cells, and the multivalent character of dendrimers facilitates the attachment of various payloads, including targeting, diagnostic and therapeutic molecules, as well as combinations of these agents. Because expression of the folate receptor is amplified in several human cancers and restricted in most normal tissues [129], folic acid is an interesting candidate for the active targeting of dendrimer- drug conjugates to tumors. Inspired by the concepts of Esfand and Tomalia [116], and the multivalent dendrimerfolate and dendrimermethotrexate conjugates of Frechet and co-workers [128], Quintana et al. [130] prepared analogous PAMAM dendrimers with methotrexate conjugated to their periphery via either a stable amide or an ester linkage that could be hydrolyzed under biological conditions. As expected, the introduction of folic acid into these conjugates was found to enhance their cellular uptake, resulting in an increase in cytotoxicity of the methotrexate ester conjugate relative to that of the free drug *in vitro* (Figure 1.36).

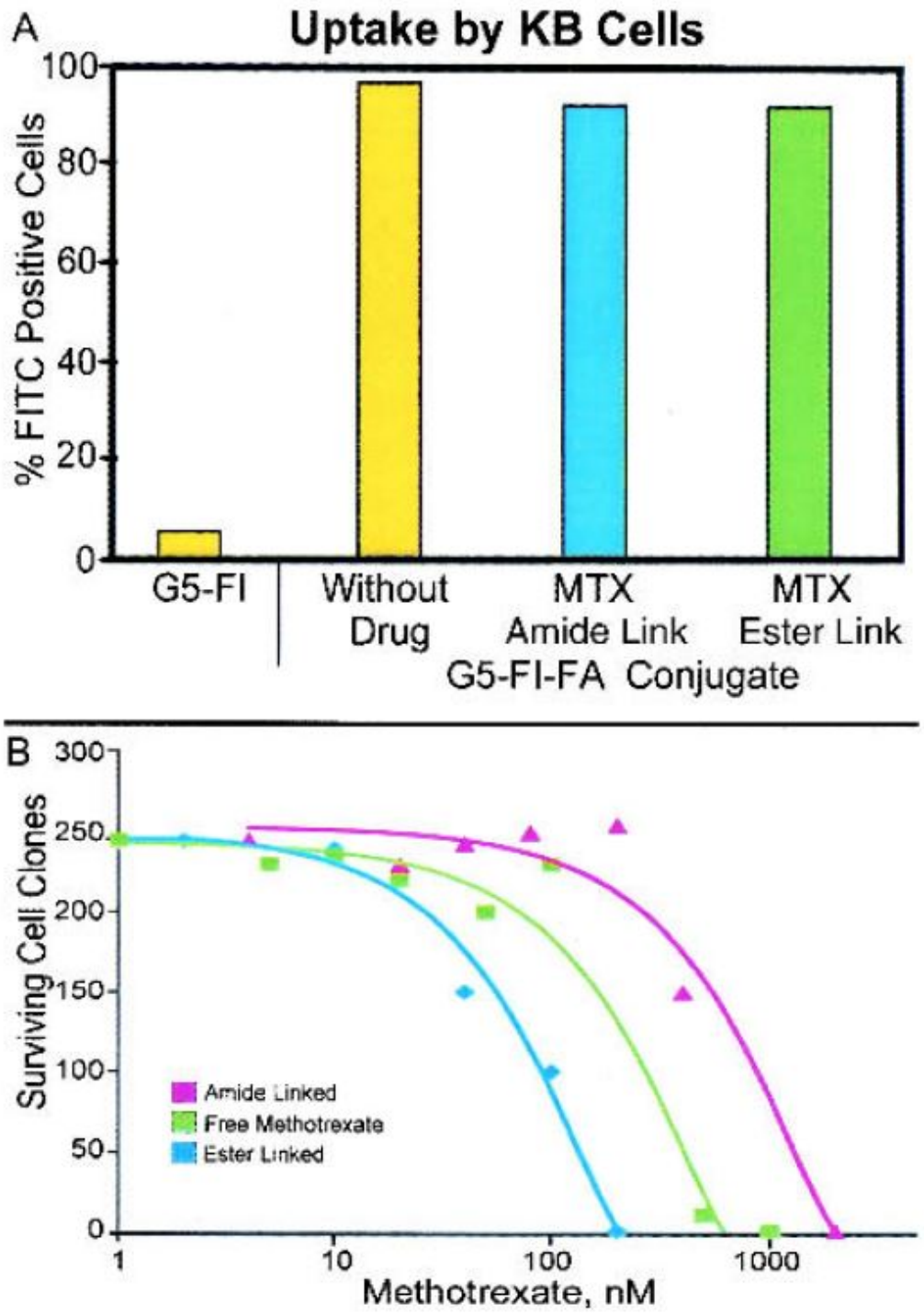

Figure 1.36: (A) Flow cytometry data shows that the PAMAM dendrimer-drug conjugates are readily taken into the cells. (B) A comparision of the efficiency of dendrimer-conjugated drug in killing KB tumor cells. Reprinted from Ref. [130]. Copyright 2002 Springer Science + Business Media.

1.4.2 Porous silicates

Since the first report using MCM-41 type mesoporous silica nanoparticles (MSNs) as drug delivery system in 2001 [131] the last ten years have witnessed an exponential increase in research on biomedical application of MSNs (Figure 1.37). It has been one the hottest areas in nanobiotechnology and nanomedicine for designing biocompatible MSNs and multifunctional counterparts in disease diagnosis and therapy. As nanocarriers, mesoporous silica nanoparticles with unique mesoporous structure have been explored as effective drug delivery systems for a variety of therapeutic agents to fight against various kinds of diseases including bone/tendon tissue engineering [132] diabetes [133], inflammation [134], and cancer [135]. Through much effort MSNs have been proven to possess unprecedented advantages over traditional nano-based formulations, especially for cancer therapy [136]. Mesoporous silica nanoparticles have a tailorable mesoporous structure, high specific surface area, and large pore volume. These properties endow them with unique advantages to encapsulate a variety of therapeutic agents and deliver these agents to the desired location. Importantly, the fabrication of MSNs is simple, scalable, cost-effective, and controllable. Being abundantly distributed in nature, silica has good compatibility and is accepted as Generally Recognized As Safe (GRAS) by the FDA and has been widely used in cosmetics and as FDA-approved food additives [137]. Thereby, MSNs hold the promise to be developed as versatile drug delivery systems arming toward clinical production. Furthermore, it provides unique opportunities for simultaneous diagnosis and therapy with the MSN-based multifunctional nanocomposites not only as drug delivery system but also as an imaging modality.

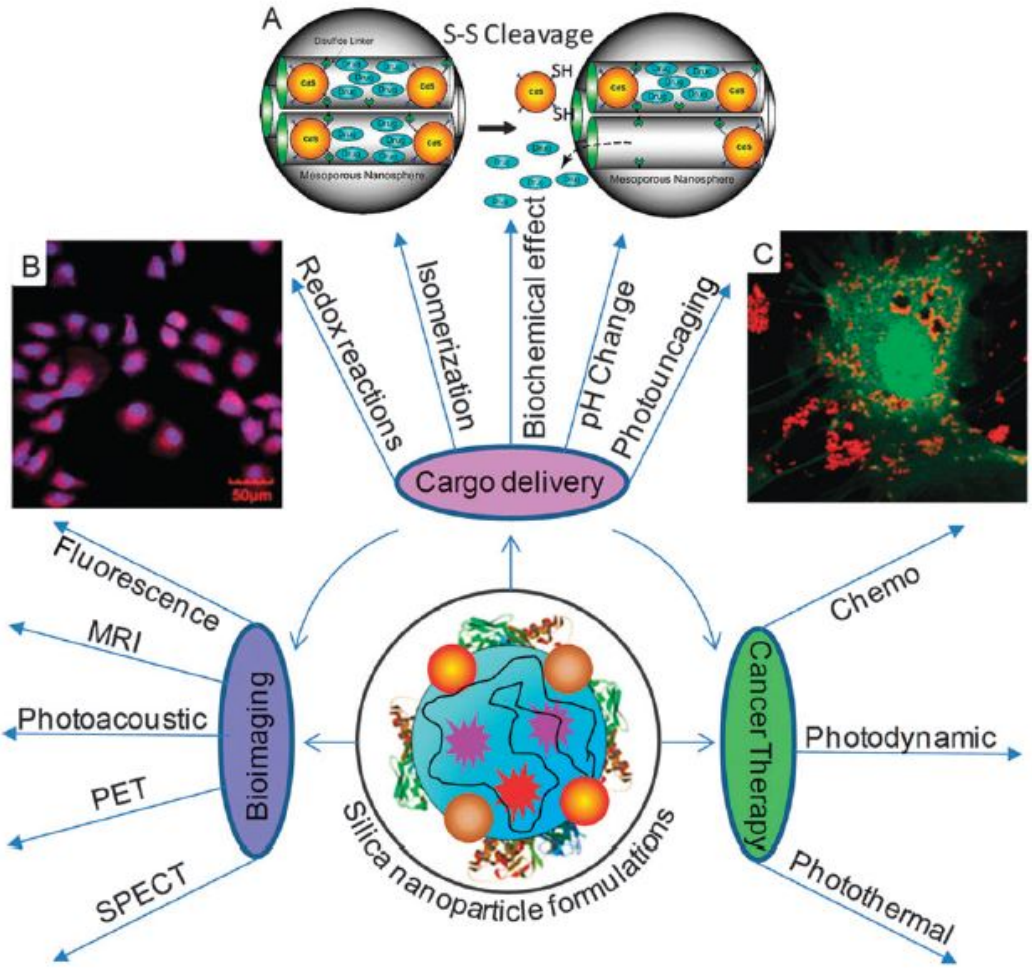

Figure 1.37: (A) Drug delivery by stimuli-responsive removal of molecular valves from the surface of the mesoporous silica nanoparticles. The example shows drug delivery by reductive removal of gate-keeper quantum dots. (B) Bioimaging capabilities of modified mesoporous silica nanoparticles. The example shows fluorescence image of HeLa cells incubated with doxorubicin and iron-oxide conjugated mesoporous silica nanoparticles. (C) Applications of mesoporous silica nanoparticles in cancer therapy. The example shows a fluorescent image of a GFP-expressing rat neural stem cell loaded with Texas-Red containing silica nanoparticles. Reprinted from Ref. [138]. Copyright 2014 The Royal Society of Chemistry.

MCM-41 is the most extensively researched type of MSNs for biomedical applications. With the surfactant of cetyltrimethylammonium bromide (CTAB) as liquid crystal templating, tetraethyl orthosilicate (TEOS) or sodium metasilicate (Na_2SiO_3) as the silica precursor, and alkali as catalyst, MSNs with an ordered arrangement of uniform two-dimensional (2D) hexagonal p6m mesopores were firstly synthesized and

named as MCM-41 (Figure 1.38A) [136, 139]. In the synthesis, when the concentration is above the critical micelle concentration (CMC), the surfactant of CTAB would self-aggregate into micelles. Around the polar head region of the micelles, the silica precursors condensate at the surface of surfactant and form silica wall around the surface of the micelles. After removal of the surfactant, MCM-41 type MSNs could be obtained (Figure 1.38B). The specific surface area is high than 700 m^2/g, and the pore size can be tailored in the range of 1.610 nm. For biomedical applications, precise control over particle size, shape, pore size, and pore geometry is very important. Totally, the pore size and its orientation are mainly determined by the nature of surfactant templates. The particle size and morphology can be controlled from sphere-, rod-, to wormlike structures by tailoring the molar ratio of silica precursors and surfactants, pH control using base catalysts [140], addition of co-solvents or organic swelling agents [141], and introduction of organoalkoxysilane precursors during the co-condensation reaction (Figure 1.38C) [20, 142].

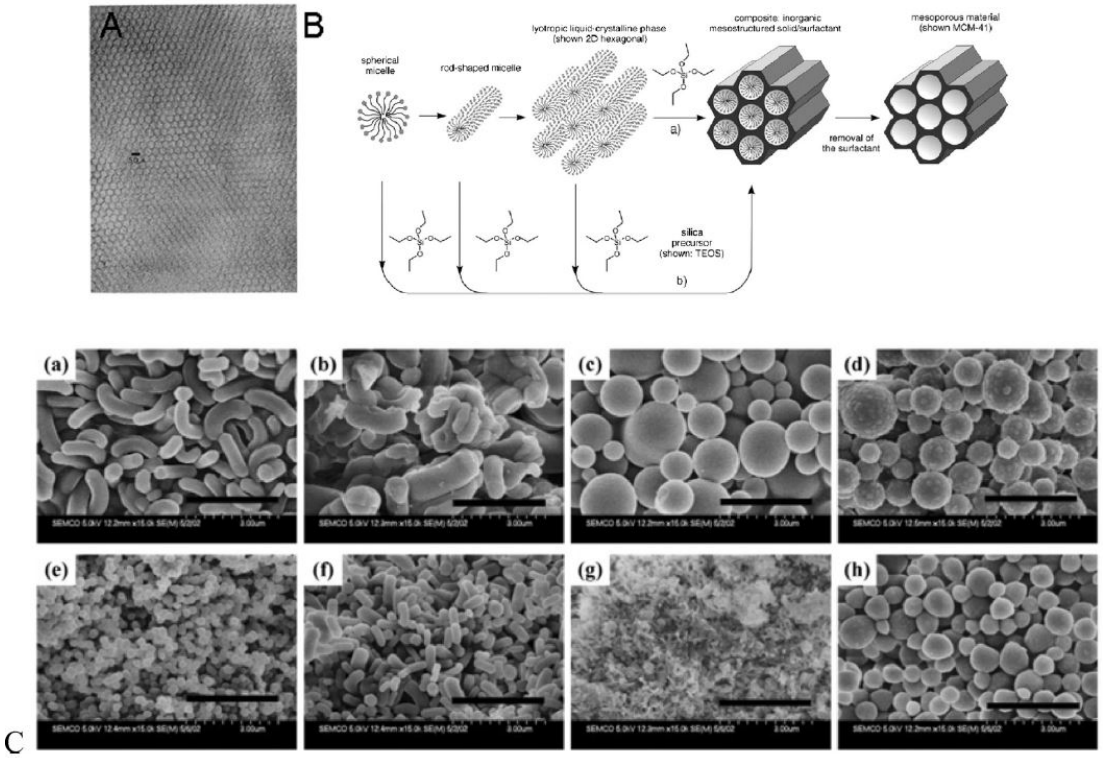

Figure 1.38: (A) High-resolution transmission electron microscopy (HRTEM) showing MCM-41 with ordered arrangement of uniform mesopores. (B) Scheme of synthesis of MCM-41 with CTAB surfactant micelles as template. (C) Transmission electron microscopy (TEM) of MCM-41 with different sizes and structures via a co-condenstation synthesis method. Reprinted from Ref. [136]. Copyright 2012 John Wiley and Sons.

With the versatile and tunable structures, MSNs have been proven to be capable of loading a variety of guest molecules including pharmaceutical drugs, therapeutic peptides and proteins and genes (Figure 1.39). MSNs have been used as drug delivery systems of kinds of pharmaceutical drugs of different hydrophobic/hydrophilic properties, molecule weights, and biomedical effects such as ibuprofen [131], doxorubicin [20], camptothecin [143], cisplatin [144], and alendronate [145]. Peptide and protein drugs have been developed as potent therapeutic agents in many medical applications including cancer therapy, vaccination, and regenerative medicine. However, due to their intrinsic properties of large molecular weight and fragile structure, protein delivery is rather difficult [146]. Due to their porous and stable nature, MSNs can protect these biomacromolecules from premature degradation and as a result can be used for peptide and protein delivery. For most native proteins that are membrane impermeable, MSNs

can escort them to cytosol [147]. In an example, Lin and co-workers used MSNs with 5.4 nm pore diameter to load cytochrome C and deliver the membrane-impermeable protein into Hela cells via cellular uptake [148]. The enzymes released from MSNs were still highly active in catalyzing its substrate. Similarly, MSNs are considered to be promising candidates for gene delivery with high efficiency. The mesoporous structure and tailorable pore provide room to accommodate gene molecules, which deeply hidden in the mesopores can escape from nuclease degradation during delivery [149]. For increasing the loading capacity of electronegative nuclei acid, the well-established surface chemistry allows easy surface modification of MSNs with polycation. Polycation polymers including polyamidoamine (PAMAM) [150], polyethylenimine (PEI), and mannosylated polyethylenimine (MP) [151], have been used to assemble with MSNs for gene delivery. The positive surface can not only increase the electrostatic interaction between MSNs and negatively charged genes, but also facilitate escape from intracellular endosome by proton sponge effect [113]. Nel and co-workers found that noncovalent attachment of PEI to the surface of MSNs could not only generate a cationic surface for DNA/siRNA constructs attachment, but also increase MSN cellular uptake [152]. Recently, Gu and co-workers have directly packaged siRNA or DNA within the mesoporous structure of MSNs without any surface modification [153]. In this case, the main driving forces for siRNA/DNA adsorption into mesopores were the intermolecular hydrogen bonds instead of electrostatic interaction. Similar to delivery of small pharmaceutical drugs, the loading of genes in MSNs also could be controlled by pore size. Min and co-workers synthesized MSNs with very large pores (23 nm) functionalized with amino group for delivering plasmid DNA to human cells. The large pores could protect the plasmid in an intact supercoiled form against degradation by nucleases, whereas plasmid loaded in MSNs with 2 nm pores was completely released or degraded because DNA was mostly on the outer surface of the particles.

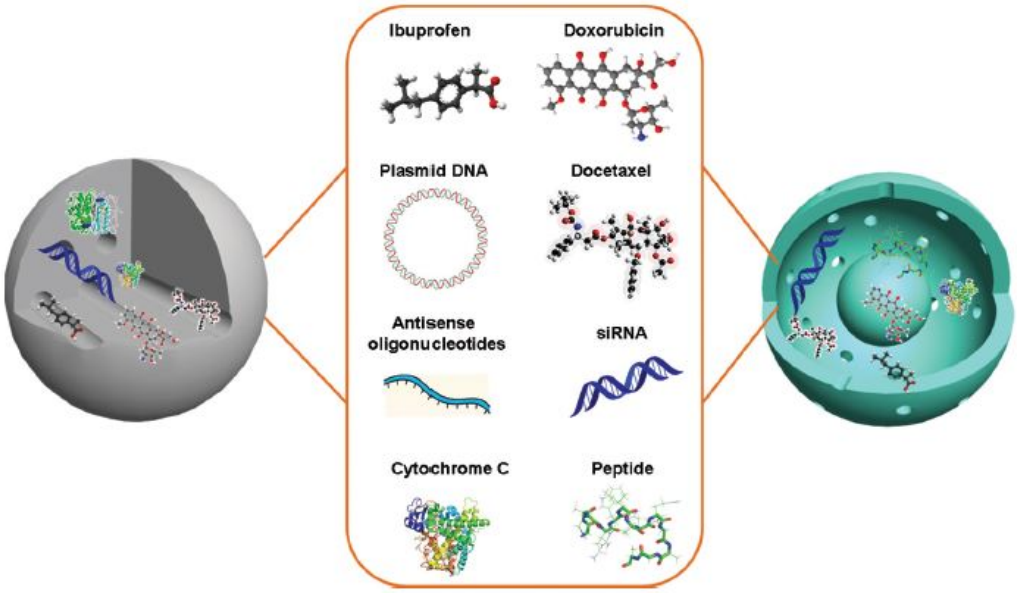

Figure 1.39: (Mesoporous silica nanoparticles as versatile drug delivery systems for a variety of therapeutic agents including pharmaceutical drugs (ibuprofen, doxorubicin, and docetaxel), therapeutic genes (plasmid DNA, antisense oligonucleotides, and siRNA), and therapeutic proteins and peptides (cytochrome C and peptides). Reprinted from Ref. [136]. Copyright 2012 John Wiley and Sons.

Most of the pharmaceutical drugs, especially anti-tumoral cytotoxic drugs, have severe toxicity to normal cells. It is not desired that the delivered drugs would be released from drug delivery systems before reaching the disease foci. The so-called zero premature release can decrease the drug distribution in off-target sites for decreasing the toxicity and increasing the effective drug accumulation. It also facilitates safe dose-escalation. The stimuli-responsive drug delivery system (SRDDS) can realize a zero premature release in response to external stimuli or internal local microenvironment difference and release the encapsulated drugs into designed locations. MSNs have particular advantages to realize spatio-temporal stimuli-responsive and zero premature release due to their unique drug release mechanism [136].

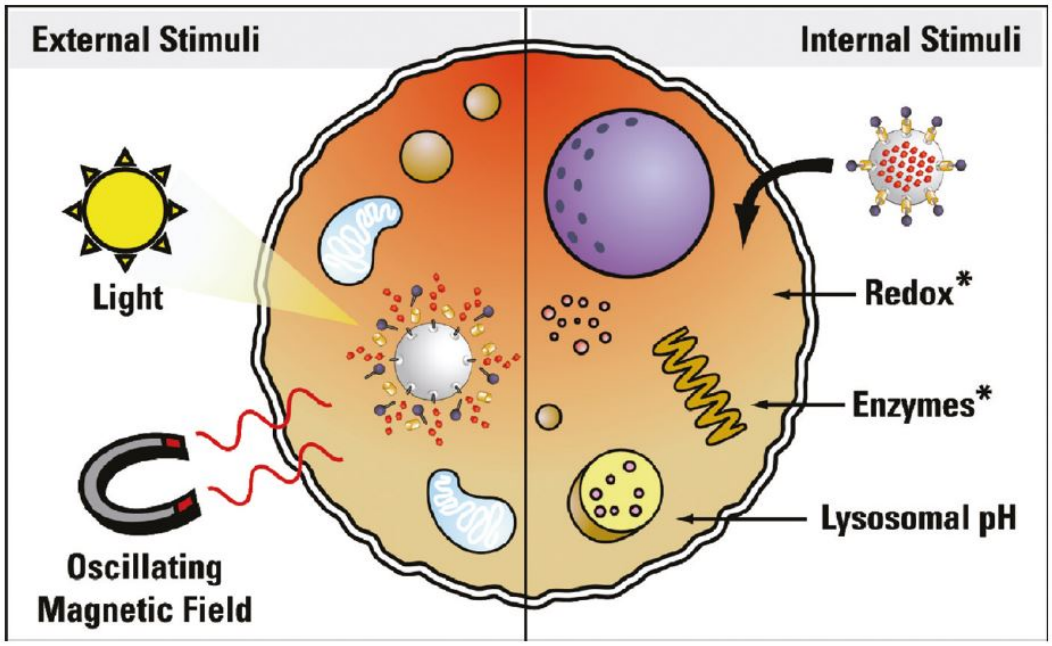

Figure 1.40: Diagram of the different methods employed for controlled release of cargos from mesoporous silica nanoparticles *in vitro*. Cargo can be released in response to external stimuli, such as light or a magnetic field, or by taking advantage of the natural biochemistry inside cells by using redox, enzymes or a pH change in the cellular compartments to release the cargo. Reprinted from Ref. [136]. Copyright 2012 John Wiley and Sons.

These above mentioned mechanized controlled release systems could have a variety of internal and external power supplies (Figure 1.40). The first type of stimuli is provided by chemicals. Systems can be designed to be responsive to external chemical additions, or to the internal chemical changes within organs and cells, such as pH change and cytoplasmic enzymes [136]. Since the addition of chemical stimulants is not always feasible for *in vitro* and *in vivo* experiments, the biological applications of chemical responsive controlled release systems are limited by the types of chemical changes existing in the cells and organisms. The second type of stimuli is electrical, using redox reactions to trigger the release. This can be accomplished by external means, like directly applying electrodes, or by internal means, e.g. using the internal reducing conditions inside cells. Light has been applied as another external power supply for controlled release systems. The *in vivo* application of light stimuli is limited by the tissue penetration ability of the stimulating light. External heating can be used to trigger the release of the mechanized

MSNPs. Heat can also be made an internal stimulus when it is generated by magnetic nanocrystals in an oscillating magnetic field. All of the above-described power supplies trigger the operation of the mechanized MSNPs either by causing structural changes to polymer coatings, or by causing molecular or supramolecular motions of the gatekeeper groups, which in turn leads to the un-blocking of the pore openings. To test the ability of the nanoimpellers to release drug molecules inside cancer cells upon light activation, the azobenzene derivatized particles were loaded with camptothecin (CPT), and *in vitro* studies were carried out on two human cancer cell lines (PANC-1 and SW480). It can thus be seen that such light-activated nanoimpellers can lead to controlled drug release from the mesopores thus enhancing their efficacy. (Figure 1.41) [136].

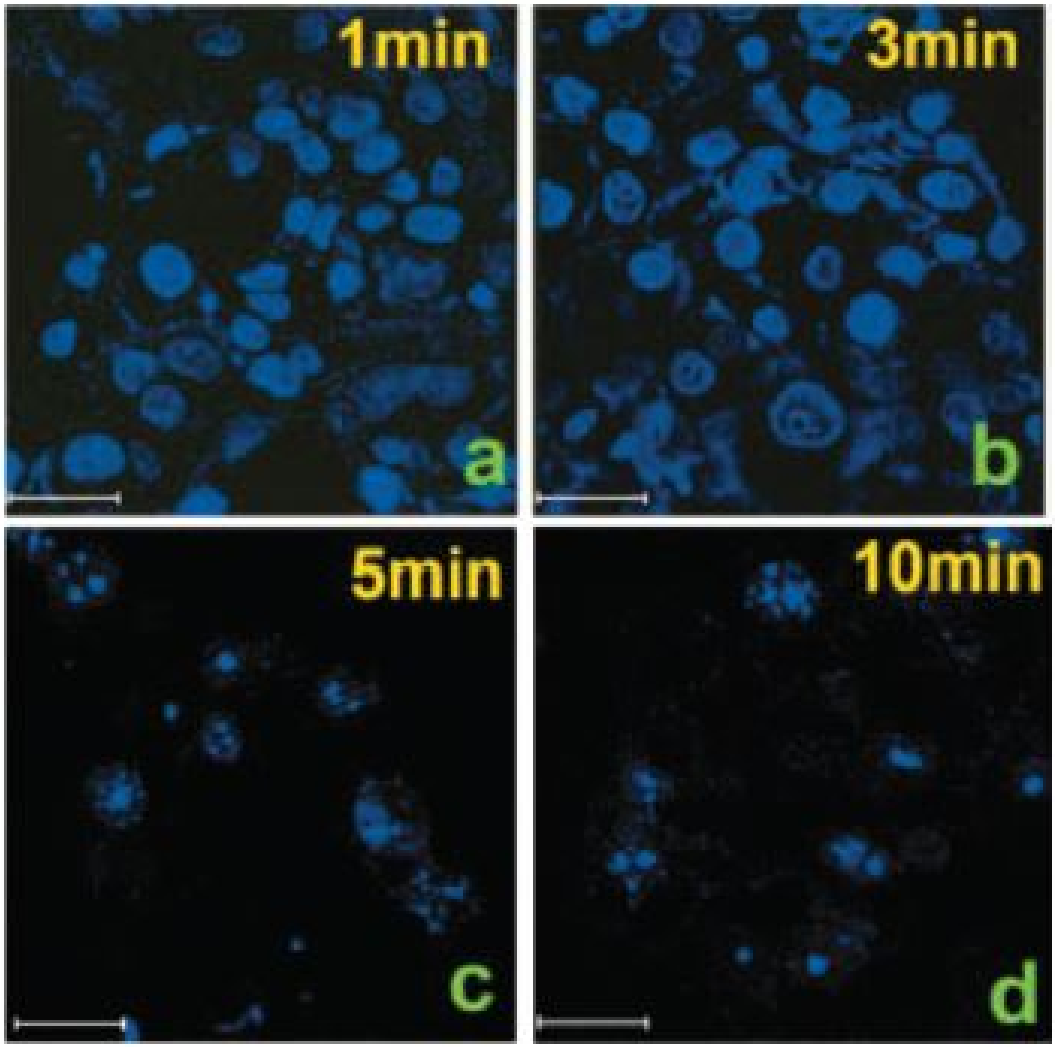

Figure 1.41: Light-triggered in vitro delivery of the anticancer drug camptothecin (CPT) inside PANC-1 cancer cells to induce apoptosis. CPT-loaded nano-impeller controlled MSNPs were incubated with cancer cells and illuminated for 1 (a), 3 (b), 5 (c), or 10 min (d). Reprinted from Ref. [154]. Copyright 2012 The Royal Society of Chemistry.

Another example of stimuli-responsive MSNs are those which are capped by molecular gates that are released upon contact with different pH conditions. For example, the pH-sensitive supramolecular nanovalves with the N-methylbenzimidazole stalks have the ability to bind the β-CD strongly at pH 7.4 (Figure 1.42a), trapping dye or drug molecules inside the mesopores of the MSNPs [155]. Upon entering an acidifying endosomal compartment at pH 6, the stalks become protonated and β-CD cap dissociates, allowing the cargo molecules to be released from the MSNPs. As a proof-of concept,

the nanovalve functionalized MSNPs were loaded with Hoechst 33342 to cause nuclear staining in human differentiated myeloid cells (THP-1), or loaded with anti-cancer drug doxorubicin to induce cell apoptosis in squamous carcinoma (KB-31) cells. The cellular uptake of the particles by the THP-1 and KB-31 cell lines was confirmed by confocal microscopy using FITC labeled MSNPs. The lysosomal pH values of the THP-1 and KB-31 cells are about 4.6 and 5.2 respectively, well below the operating pH of the acid-responsive nanovalve. When the Hoechst-loaded, FITC-labeled MSNPs are taken up by the THP-1 cells, the blue fluorescence from Hoechst is co-localized with the MSNPs in the perinuclear regions, indicating that the Hoechst is well retained in the MSNPs during the endocytosis. As monitored by confocol microscopy, the Hoechst dyes start to be released after 6 h of incubation and stain the nuclei of THP-1. Similarly, when testing the Dox release in KB-31, the red fluorescence of Dox first co-localize with the MSNPs in the perinuclear region, and then slowly release to the nucleus, followed by Dox induced cell apoptosis (Figure 1.42c). This demonstrates the *in vitro* operation of the pH-sensitive nanovalves, and the successful autonomous delivery of anti-cancer drug intracellularly using the mechanized MSNPs.

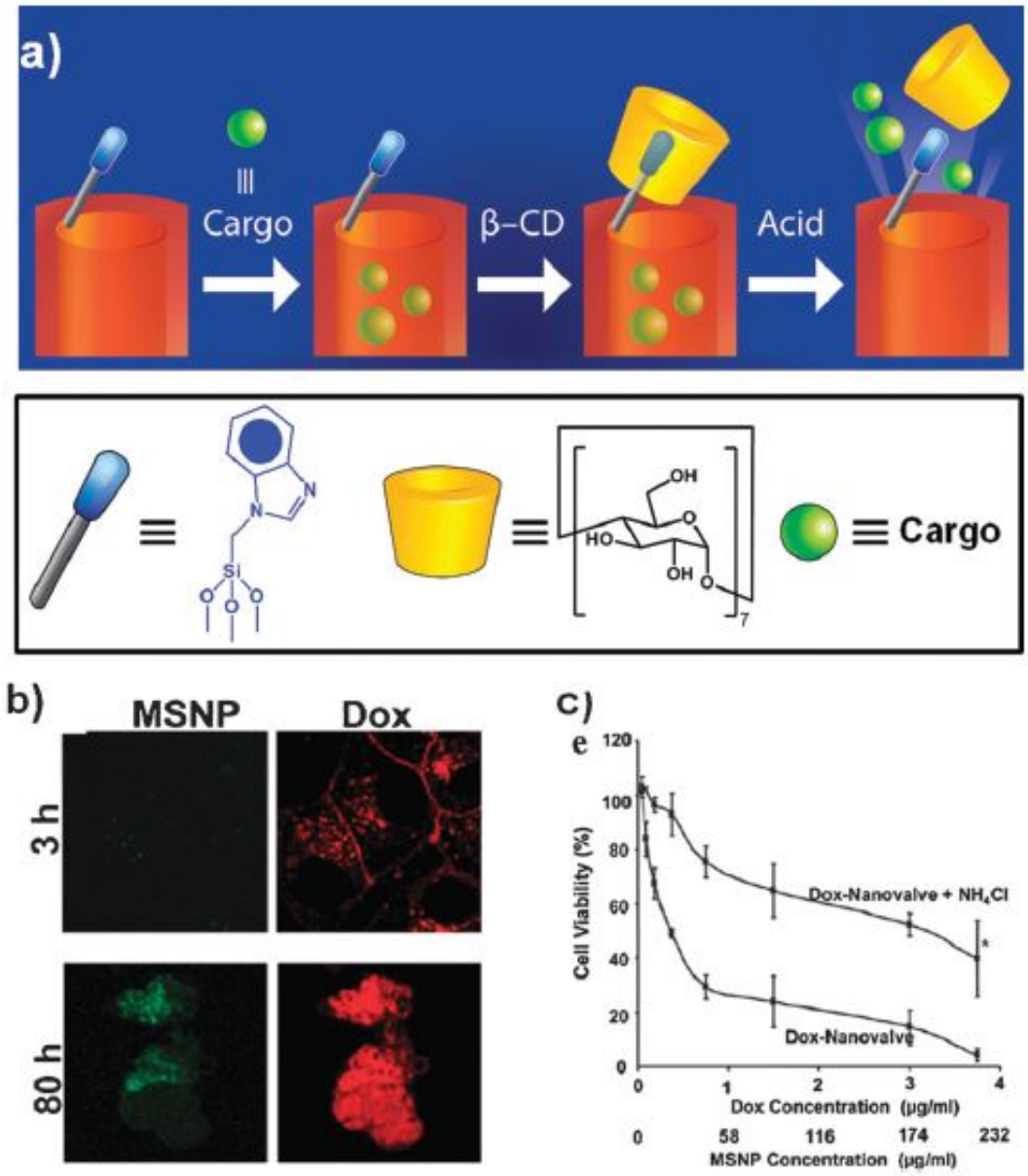

Figure 1.42: In vitro delivery of anticancer drug Doxorubicin by the MSNPs functionalized with the acid-responsive supramolecular nanovalves (a) Scheme of the attachment of the acid-responsive nanovalves to the surface of the MSNPs. (b) Confocal images of KB-31 cells incubated with MSNP containing doxorubicin drug for the indicated times. (c) Doxorubicin-loaded MSNPs, fitted with pH nanovalves, inhbited KB-31 viability efficiently as determined by a MTS assay. Doxorubicin-induced cytotoxicity was partially inhibited by NH_4Cl treatment, which prevents lysosomal acidification. Reprinted from Ref. [154]. Copyright 2012 The Royal Society of Chemistry.

However, external control of nanovalves by a noninvasive tissue-penetrating stimulus still remains a major challenge. An attractive method utilizes an oscillating magnetic

field, wherein local internal heating of the iron oxide core of MSNP was used to activate the nanovalves on the particle surface. The *in vitro* delivery of Dox using this material has been achieved in a breast cancer cell line MDA-MB-231 [156]. The Dox-loaded iron oxide nanocrystal core MSNPs were assembled with a nanovalve that remains closed at physiological temperature and opens when heated. When the loaded particles were taken up by the cells, minimal drug release was observed, indicating that the drug molecules are kept within the particles during the endocytosis. Local heating opens the nanovalves only when an oscillating field is applied and allows the encapsulated Dox to be released. These experiments open the door to the highly desired type of drug delivery; non-invasive, and with spatially selective external control of the time of administration and the dose of anticancer drugs.

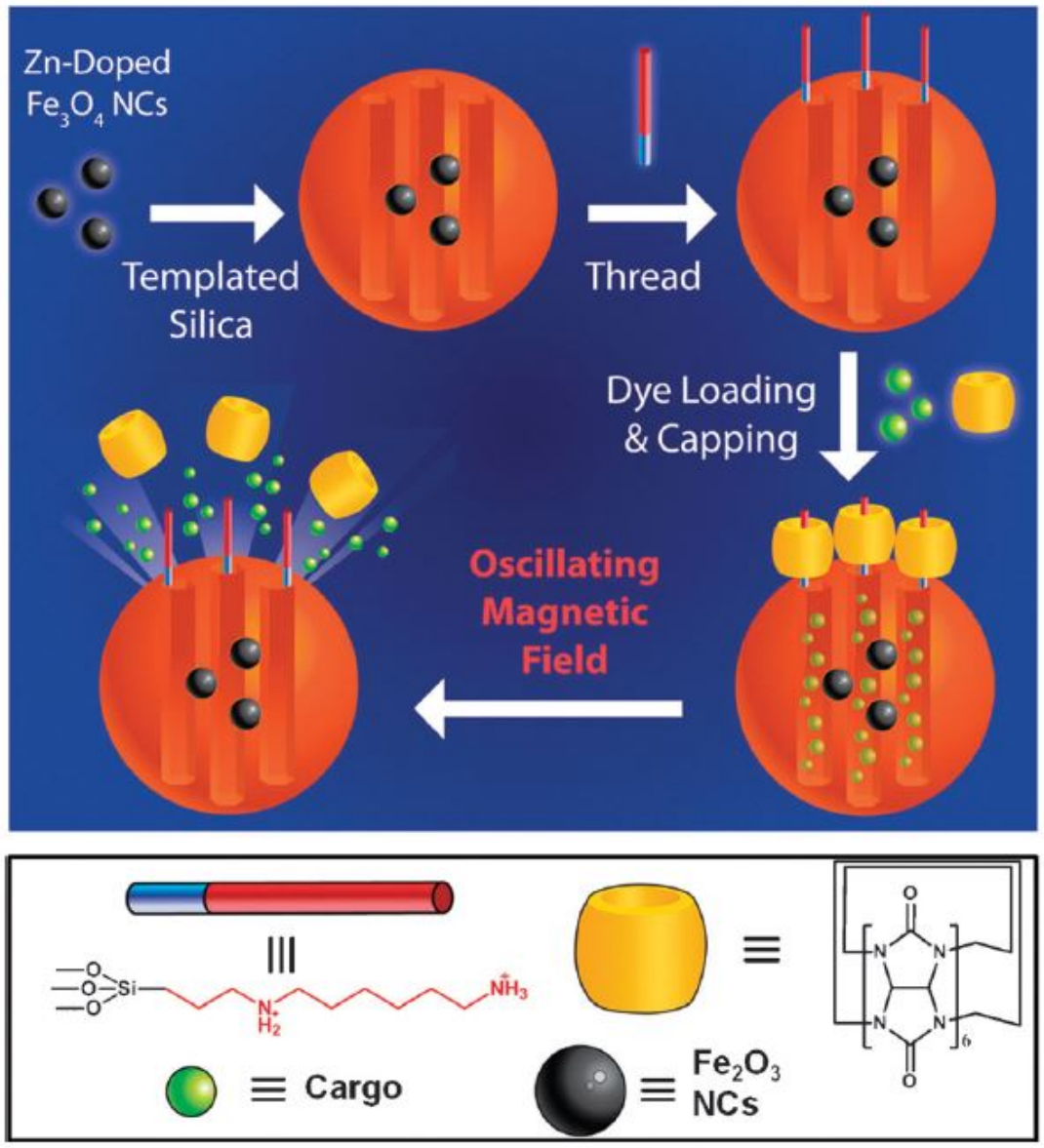

Figure 1.43: Scheme of the dye-loaded magnetic-core MSNPs functionalized with nanovalves that respond to internal heating caused by an oscillating magnetic field. Reprinted from Ref. [154]. Copyright 2012 The Royal Society of Chemistry.

1.5 Conclusion

The past two decades have seen an enormous surge in the applications of nanotechnology to various areas of research, and predominantly in clinical medicine. Nanomaterials, such as liposomes, polymers and porous silicates are being exploited for their capability to carry various therapeutics to the target tissues and organs. On the other end of the spectrum, metallic nanostructures such as magnetic nanoparticles, quantum dots and gold nanoparticles are being vastly employed as molecular imaging probes owing to their unique chemical, physical properties. These advances in nanoscale science and bionanoengineering are thus revolutionizing our understanding and ability to manipulate the complex biological processes. In doing so, these nanotechnology-based approaches are changing the foundations of disease prevention, diagnosis and treatment.

Collectively, nanomaterials have a played a vital role in all fields of research, the key beneficiary being oncology. What is now required is to harness the true potential of these nanomaterials and translate it into improved clinical outcomes. To this end, there has been a thrust in the design and development of multifunctional nanoparticles, which seek to expand on the benefits shown by the first-generation of nanoparticles (eg., Doxil) by adding functionalities which improve the delivery, therapeutic efficacy and ultimately patient outcome. Such multifunctional nanoparticles are being devised to possess stealth-like features, to evade the immune system, targeting moieties for tumor homing, membrane permeable ligands, imaging agents for real-time tracking of these tiny delivery vehicles, endosomal escape and triggered release mechanisms. Such multifunctional nanoparticles can be assembled in a controlled manner using the already available nanomaterials. In doing so, we can achieve orthogonal functionalities within a single nanoplatform, which can then function in an interactive manner to provide invaluable information about disease prevention and diagnosis. Such multifunctional nanotechnologies, hence are well-poised to shift the paradigm of clinical medicine.

1.6 Overview of Dissertation

Nanotechnology, as mentioned earlier has been making positive impacts on nearly every branch of the healthcare industry. The initial research efforts in nanotechnology are now coming close to fruition, with several novel nanoscale therapeutic and diagnostic modalities either under development or in clinical practice today. While the earlier research efforts aimed for improving the already-available therapeutics or diagnostics using nanotechnology-based approaches; recently, the focus has shifted towards engineering multifunctional nanomaterials combining several useful properties in a single nanoparticle, such as targeted delivery of therapeutics; direct visualization of the delivered therapeutics and stimuli-responsive behavior allowing for drug release only under certain endogenous or exogenous conditions. It is hypothesized such nanosized platforms, by virtue of their multi-functionality, can considerably enhance the efficacy of the existing therapeutic and diagnostic regimens and in doing so, make significant advances in the field of developing personalized nanomedicine. Such challenging questions formed the major driving force behind my research in this direction. On the onset of my PhD, I set out to develop multimodal nanoplatforms that are composed of either multiple chemical/nano-structures and can deliver various therapeutics including small molecules, proteins and peptides as well as nucleic acids. Upon developing such nanomaterials, I established their efficacy and versatile by testing them in a variety of cell lines, including brain cancer cells and neural stem cells. Brain cancers are the leading cause of death in terms of brain-related deaths, and are known to be resistant to most conventional therapies, due to their inaccessibility as well as heterogeneity. To this end, nanotechnology has the potential to make significant advances in treatment of brain cancer. On the other hand, stem cells which have shown tremendous potential in regenerative medicine, require specialized techniques to deliver genetic materials in order modulate their differentiation into specialized cell lineages in an efficient yet biocompatible manner.

To this end, my first project focused on developing magnetic core-shell nanoparticles (MCNPs) composed of a magnetic core and a gold plasmonic shell. By combining two

orthogonal elements within the same nanoplatform, these MCNPs possess a number of desirable properties such as near-infrared (NIR) absorption, and photon scattering but also present a relatively inert and facile surface amenable to further functionalization, while preserving the core magnetic properties (such as hyperthermia and MRI). I utilized these MCNPs for magnetically-facilitated delivery of genetic materials (siRNA or plasmid DNA) into stem cells in a highly effective, spatiotemporally controlled, and biocompatible manner. Once delivered to the neural stem cells (NSCs), the MCNPs did not interfere with inherent stem cell properties, such as proliferation and differentiation and hence were found to be biocompatible within the range of concentrations tested. The gold outer-shell enabled us to develop facile surface functionalization, while improving aqueous solubility and stability of the MCNPs. Additionally, the superior magnetic properties of the core allowed us to deliver nanoparticle-biomolecule constructs into the difficult-to-transfect stem cells with high transfection efficiency within significantly shorter incubation times as compared to the conventional lipid-based transfection agents. As a proof-of-concept, we also demonstrated that we could direct the differentiation of NSCs to specific lineages (neurons and oligodendrocytes) by our developed MCNP-based siRNA delivery methods. Additionally, since these MCNPs possess both magnetic and plasmonic properties, they could also be used as dual-mode imaging probes for real-time imaging and tracking of stem cells transfected with MCNPs.

My first project mainly focused on the delivery of RNAi therapeutics to stem cells for directing their differentiation, while my second project was designed to deliver multiple therapeutics using a singular delivery vehicle to cancer cells. The delivery vehicle, termed as DexAM, consisted of a dendritic polyamine backbone conjugated with β-cyclodextrin (β-CD) moieties. The dendritic polyamine, which was cationic in nature, allowed for electrostatic complexation with the negatively charged siRNA while the β-CD moiety allowed for complexation of hydrophobic molecules such as anti-cancer drugs. In this way, I utilized DexAM for targeted simultaneous delivery of both siRNA and anti-cancer drugs to brain cancer cells, as a therapy to inhibit cell proliferation and induce cell apoptosis. As the model siRNA and anti-cancer drugs that I used for this study affected orthogonal signaling pathways, this resulted in a synergistic effect

on apoptosis of brain cancer cells and inhibit the proliferation in brain tumor cells. Dr. Cheoljin Kim, a post-doc in Dr. Ki-Bum Lee's lab and I made equal contributions to this project.

While the previous projects focused mainly on developing nanotechnology platforms for imaging and delivery of therapeutics to cancer and stem cells, it is also essential to monitor the release of therapeutics once they are delivered to cells. To this end, I developed a versatile real-time monitoring strategy based on fluorescent resonant energy transfer (FRET), using mesoporous silica nanoparticles as a nanocarrier for anti-cancer drugs, termed as FRET-MSNs. The FRET-MSNs consisted of (a) mesoporous silica nanoparticles (MSN) as the drug carrier, (b) a β-cyclodextrin-based enzyme-responsive molecular valve blocking the pores, to facilitate drug release only when the disulfide bond is cleaved in the presence of reducing environment, and (c) a FRET donor-acceptor pair of coumarin and fluorescein isothiocyanate (FITC) integrated within the pore-unlocking phenomenon. Such a design allowed for monitoring the release of drugs from the pores in real-time by simply measuring changes in the FRET signal, both in solution as well as in cancer cells. Dr. Jinping Lai, a post-doc in Dr. Ki-Bum Lee's lab and I made equal contributions to this project.

This dissertation provides the details of my work on all projects related to the development of multifunctional nanomaterial-based drug delivery and imaging systems.

Chapter 2

Magneto-plasmonic core-shell nanoparticles for biomolecule delivery and imaging

Nanomedicine, broadly defined as the application of nanoscale materials and measurements toward problems of biomedical importance, has also become a driving force for new concepts in nanoscience and technology. A substantial fraction of this activity is focused on the development of multifunctional nanoparticles (NPs) that can enhance or introduce unique modalities in biomedical imaging, with the extra potential of combining imaging with therapeutic action (also referred to as theranostics). Two types of NPs with particular promise as theranostic agents are plasmon-resonant colloidal gold nanoparticles (AuNPs) and superparamagnetic iron oxide nanoparticles (MNPs), both of which are under active investigation for clinical applications. AuNPs can be prepared in anisotropic forms to support large optical cross sections at near-infrared (NIR) wavelengths and are favored in optical imaging modalities for their high transmitivity through biological tissues. On the other hand, MNPs are useful as T2-weighted contrast agents in magnetic resonance imaging (MRI) and can respond to magnetic field gradients for applications requiring site-specific localization (e.g., magnetofection) or separations (e.g., cell sorting). Both AuNPs and MNPs can also mediate localized hyperthermic effects, and their applications toward tumor cell thermolysis and tissue ablation are now well-documented. Such unique physico-chemical and optical properties make these AuNPs and MNPs attractive candidates for various applications in biomedicine, in particular, as diagnostic and therapeutic agents. The current thrust is to develop multimodal nanoparticles which integrate both magnetic and plasmonic components and hence their functions into a single platform. Such multimodal nanoparticles have obvious benefits for nanomedicine applications, as they can overcome the

limitations of the individual nanoparticles by combining multiple functions or properties not obtainable in individual materials. A practical or generalized approach of integrating plasmonic and magnetic functionalities, is to grow a thin Au shell around the magnetic core, thus imparting an optical modality to the MNPs, which it was lacking earlier. However, there are few reports in the literature demonstrating the synthesis of well-defined multimodal nanoparticles comprising of a magnetic core and a thin gold shell and their applications in biomedicine. This chapter will discuss the development of such multimodal core-shell nanoparticles and their applications to regulating cancer and stem cell fate. The first section that describes the use of multimodal core-shell nanoparticles for stem cell differentiation and imagin has already been published in Angewandte Chemie International Edition [157].

2.1 Multimodal magnetic core-shell nanoparticles for effective stem cell differentiation and imaging

2.1.1 Introduction

Stem cells, owing to their ability to differentiate into specialized cells that can serve a particular function, have enormous potential in the field of regenerative medicine, wherein these stem cell-based therapies can be used to treat a wide range of diseases including diabetes, heart disease, and liver disease [158]. However, the realization of stem cell-based therapies in the clinic is severely hampered by our current inability to achieve the efficient delivery of genetic materials into target cells, which is required to specifically direct differentiation. In particular, with regard to stem cell-based regenerative medicine, it is vital to achieve: i) the highly efficient transfection of targeted cells; ii) biocompatibility, with an emphasis on maintaining a high cell viability without altering migratory and differentiation potential; and iii) non-invasive monitoring for the long-term evaluation of therapy [6]. Currently, the use of virus-mediated delivery results in the highest delivery efficiency (80-90%) for stem cells [159]. However, this method also has a number of harmful effects that limit its clinical applicability including potential cell toxicities, mutagenesis, and the induction of an immune response [113]. To this end, a significant amount of effort has been invested in the development of alternative non-viral delivery methods [160]. In particular, recent studies have demonstrated that magnetic nanoparticles (MNPs) possess a number of advantages that are especially attractive for application to stem cell research [11,161,162]. Typically, MNPs are composed of a magnetic core that can consist of metals or metal oxides, [48] metal alloys, [163] and more recently, doped metals [164]. These MNP cores can then be post-synthetically modified with a biocompatible material (e.g. SiO2, gold, polymer, etc) resulting in a core-shell structure [165–167]. In doing so, this shell can not only act as a hydrophilic layer but also as a platform for the surface functionalization of the MNPs [168]. As a result of its inherent magnetism, the properties of the shell, and the surface functionalization employed, MNPs can possess multifunctionalities including the delivery of nucleic acids such as plasmid DNA (pDNA) and short interfering RNA

(siRNA), magnetically-facilitated delivery, cell targeting, and MRI contrast [169, 170]. In particular, the synthesis of gold coated MNPs can provide a number of additional advantages such near-infrared (NIR) absorption [171, 172], photon scattering, and a relatively inert and facile surface that is amenable to further functionalization, while preserving the core magnetic properties [173]. Herein, we describe the synthesis of well-defined magnetic core-shell nanoparticles (MCNPs), composed of a highly magnetic core surrounded by a thin uniform gold shell and their application for the delivery of genetic materials (siRNA and pDNA) into stem cells in a highly efficient, spatiotemporally controlled, and biocompatible manner (Figure 2.1). Moreover, we demonstrate the utility of the multifunctionalities that are provided by our MCNP system including magnetically-facilitated transfection and dark-field imaging. While numerous studies have previously utilized MNPs as MRI contrast agents and have shown the effectiveness of magnetically facilitated transfection in stem cells, the use of MCNPs to mediate the delivery of genetic materials to stem cells in a highly efficient and biocompatible manner remains to be assessed. To this end, as a proof-of-concept experiment for the genetic manipulation of stem cells using MCNPs and the accompanying differentiation studies, neural stem cells (NSCs) were chosen as they are known to be very sensitive to conventional exogenous lipid-based transfection reagents as well as difficult-to-transfect. Specifically, we hypothesized that we could achieve a significantly higher transfection efficiency for genetic materials without compromising stem cell viability and biological functions (e.g. differentiation) using our MCNP-based magnetically-facilitated delivery. In addition, we hypothesized that the gold shell would provide additional advantages for stem cell-based therapies through the ability to perform dark field imaging, as this would be a simple method with which to confirm the presence of MCNPs within stem cells prior to transplantation or other studies.

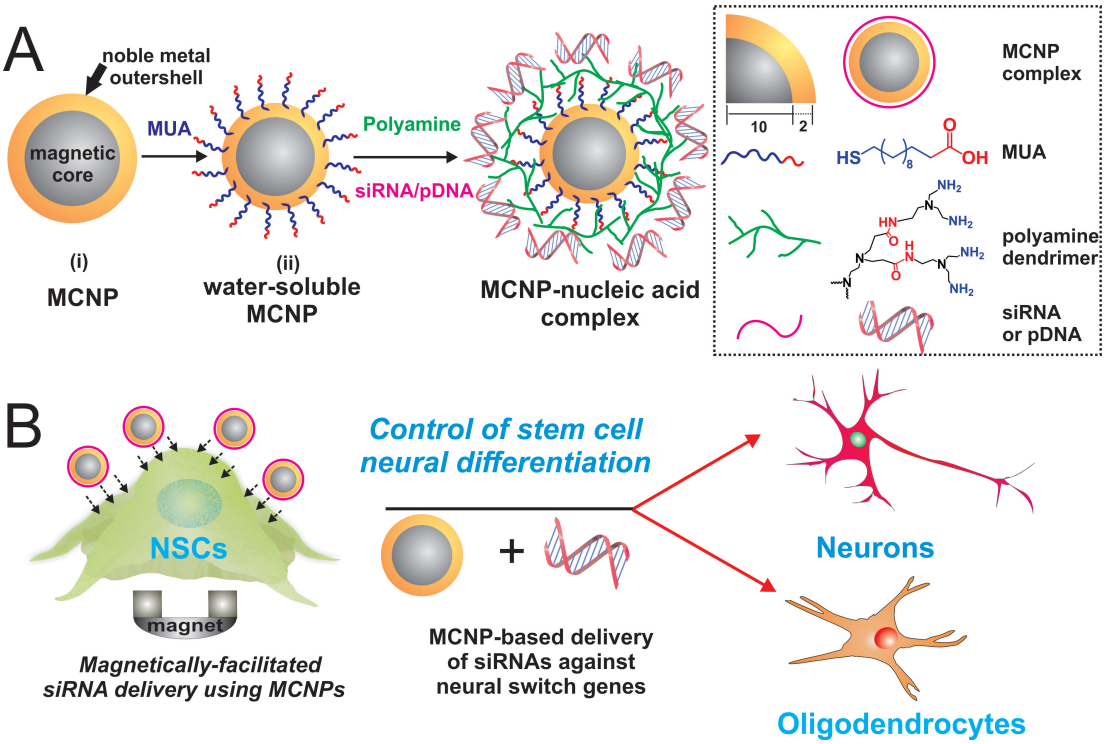

Figure 2.1: (A) Schematic illustration of generating non-water-soluble MCNPs and water-soluble MCNPs. (B) Magnetically-facilitated siRNA delivery using MCNPs to control the differentiation of stem cells. Reprinted from Ref. [157]. Copyright 2013 John Wiley and Sons.

2.1.2 Results and Discussion

Synthesis of magnetic core-shell nanoparticles

For the formation of our MCNPs, we chose doped magnetic nanoparticles ($ZnFe_2O_4$) as our core, since these MNPs have been shown to have a significantly higher magnetic susceptibility and hence can afford improved magnetic properties at much lower concentrations when compared to conventional MNPs [164]. As such, we first synthesized these $ZnFe_2O_4$ NPs via the thermal decomposition of a mixture of metal precursors in the presence of oleic acid as a stabilizer, using a modified synthetic protocol that was previously reported [164]. These $ZnFe_2O_4$ NPs were then coated with a thin layer of Au by reducing hydrogen tetrachloroaurate hydrate ($HAuCl_4.3H_2O$) in a chloroform solution of oleylamine in the presence of $ZnFe_2O_4$ NPs, which resulted in the formation of non-water-soluble MCNPs [52]. These non-water-soluble $ZnFe_2O_4$@Au nanoparticles

were then rendered water-soluble by exchanging their surface oleylamine moieties with 11-mercaptoundecanoic acid (MUA) [174].

Physical characterization of the MCNPs

Initial characterization was performed to confirm that the water-soluble MCNPs retained their magnetic properties and showed a distinct pink coloration, which resembles a gold colloidal solution (Figure 2.2), due to the surface plasmon resonance (SPR) properties of the outer Au shell.

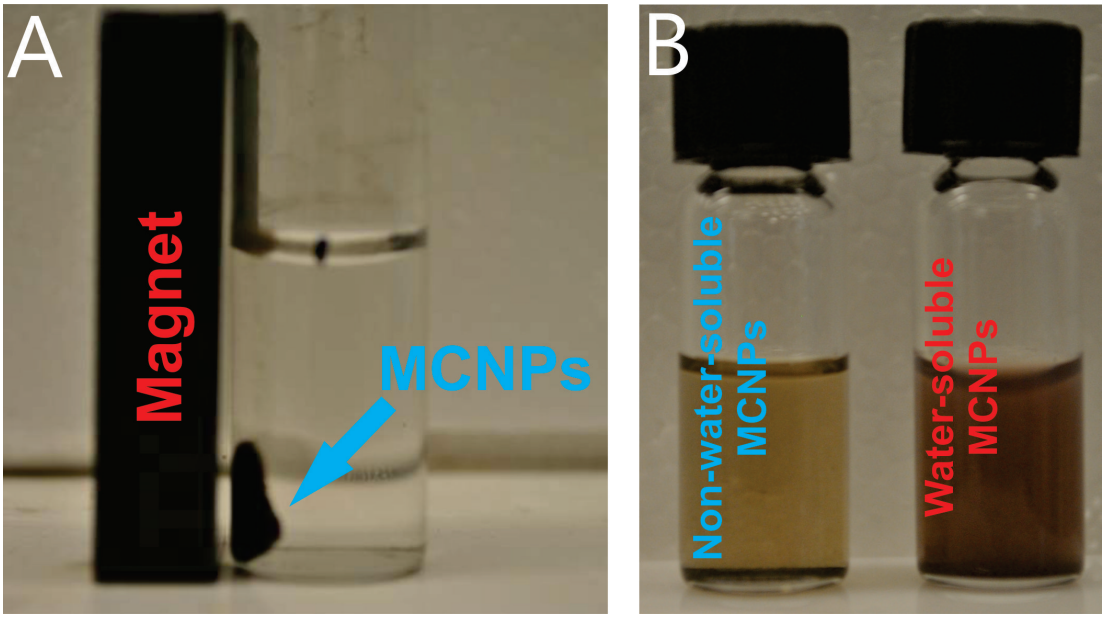

Figure 2.2: (A) Representative picture depicting that the MCNPs dispersed in water are attracted to a magnet. (B) Representative picture of non-water-soluble and water-soluble MCNPs in solution. Please note that the light pink color of water-soluble MCNPs indicates the formation of a gold shell. Reprinted from Ref. [157]. Copyright 2013 John Wiley and Sons.

A detailed characterization of the as-synthesized MCNPs ($ZnFe_2O_4$@Au NPs) was then performed. First, transmission electron microscopy (TEM) analysis revealed that the overall diameter increased from 20 1.2 nm for the $ZnFe_2O_4$ MNPs to 25 2.7 nm for the $ZnFe_2O_4$@Au NPs (Figure 2.3). The lattice fringes in the Au shell can clearly be seen in the High Resolution TEM (HRTEM), and the interfringe spacing was measured to be 0.201 nm, which is the interplane distance of the (200) planes in the face centered

cubic (fcc) Au (Figure 2.3). This indicates that the $ZnFe_2O_4$ nanoparticles are indeed coated with a layer of crystalline Au (2.5 nm). Furthermore, from the HRTEM images, we observed a difference in the contrast between the darker $ZnFe_2O_4$ core and the lighter Au shell. It has been reported that this is attributed to the dominance of the mass contrast over the diffraction contrast, making Au appear lighter in spite of it having a higher electron density than Fe and Zn [175].

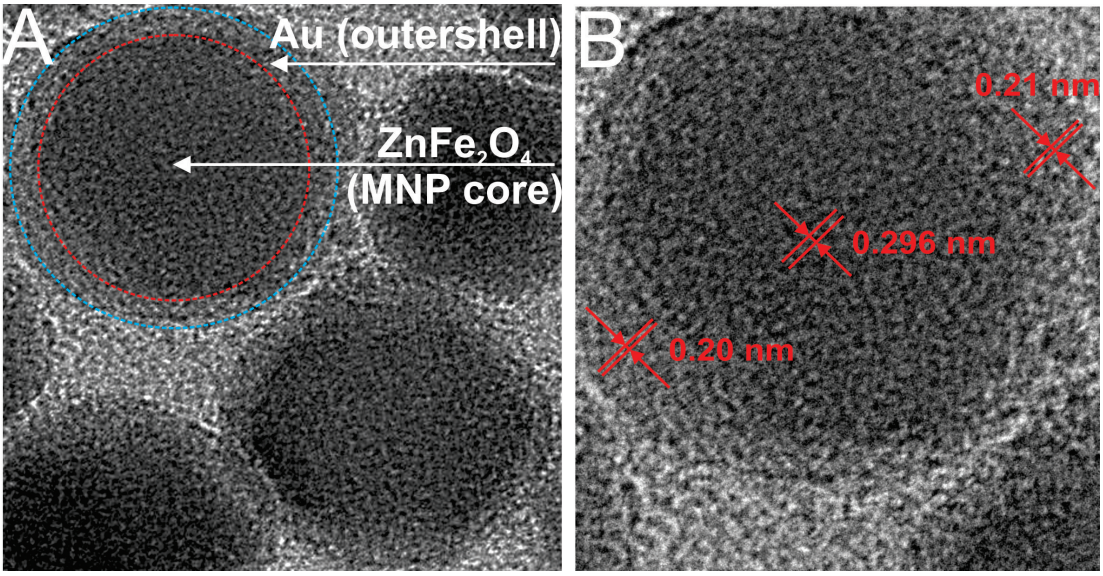

Figure 2.3: (A) TEM image of the MCNPs. Scale bar = 10 nm, B) HRTEM image of a single MCNP. Scale bar = 5 nm. Reprinted from Ref. [157]. Copyright 2013 John Wiley and Sons.

We also confirmed that the MCNPs were composed of Zn, Fe, and Au using Energy Dispersive X-Ray Spectroscopy (EDAX) analysis (Figure 2.4). Finally, from the UV absorption data (Figure 2.4), we clearly observed that the water-soluble MCNPs show a distinct absorption peak at 540 nm, owing to the SPR properties of the water-soluble Au nanostructures. As expected, this peak is not observed in both the core $ZnFe_2O_4$ MNPs and the non-water-soluble $ZnFe_2O_4$@Au NPs coated with oleylamine.

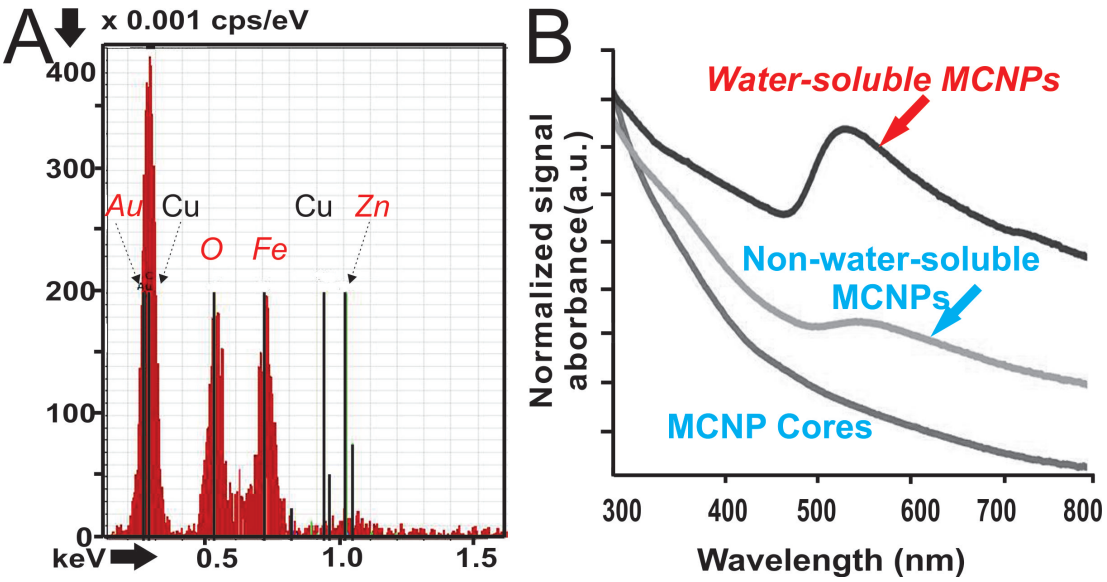

Figure 2.4: (A) EDAX spectra of individual MCNPs, (B) UV-Vis absorption spectra of the MCNP cores, non-water-soluble MCNPs and water-soluble MCNPs. The cores and non-water-soluble MCNPs were dissolved in chloroform before UV-Vis analysis. Reprinted from Ref. [157]. Copyright 2013 John Wiley and Sons.

Preparation of MCNP constructs for gene delivery

To prepare these aforementioned MCNP constructs for the delivery of functional genetic materials such as siRNAs or pDNAs, the water-soluble MCNPs were coated with a cationic polyamine-dendrimer that was previously developed by our group [176] to afford an overall positive charge to the MCNPs. This positive charge facilitated MCNP complexation with negatively charged siRNA or pDNA. In addition, the cationic polyamine-dendrimer has multiple primary amine groups and hence, once the MCNP constructs are internalized, it can act as a proton sponge in the the endosomes, thereby aiding in subsequent endosomal escape of the complexes and protecting the cargo from the deleterious effects of the acidic microenvironment [176]. The hydrodynamic size of the final MCNP constructs was determined to be 70 $\pm$ 2 nm and their net surface charge was found to be +15 mV using dynamic light scattering (DLS) and zeta potential measurements, respectively (Figure 2.5).

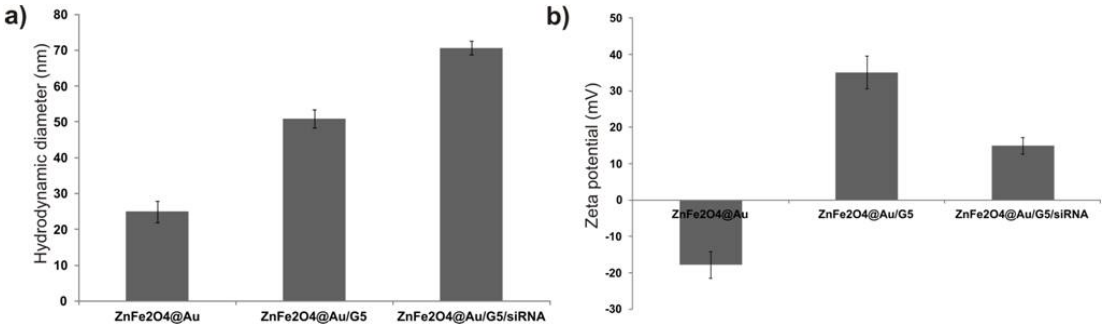

Figure 2.5: (A) Particle size of MCNPs measured at each step of conjugation, (B) Zeta potential of MCNPs measured at each step of conjugation.Reprinted from Ref. [157]. Copyright 2013 John Wiley and Sons.

Optimizing siRNA transfection using MCNP

Once we finished optimizing the synthesis of the MCNP constructs, we tested whether the MCNPs and/or the use of magnetically-facilitated delivery negatively affect the intrinsic ability of NSCs to proliferate and differentiate. To accomplish this, we assessed the proliferation and differentiation capabilities of the NSCs following their exposure to increasing concentrations of MCNPs (2-20 μg/mL) (Figure 2.6) that are complexed with negative control siRNA either in the presence or absence of an external magnetic field (MF), using immunocytochemistry. Based on the expression of proliferation (Ki67) and differentiation (TUJ1 for neurons and GFAP for glial cells) markers, we were able to ascertain that the intrinsic biological functions of the NSCs were unaffected by our MCNPs and the delivery methods employed.

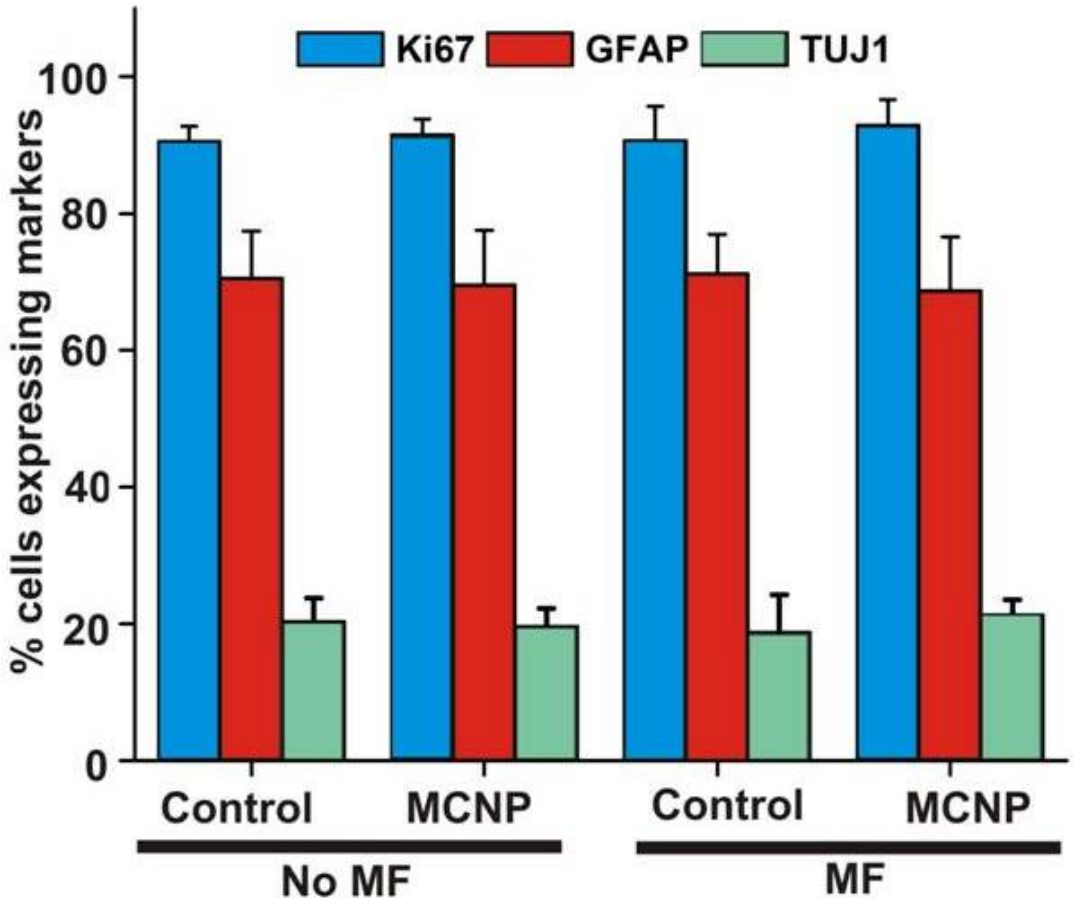

Figure 2.6: Quantification of the expression of proliferation (Ki67) and differentiation (TUJ1-neurons; GFAP- astrocytes) markers following the treatment of NSCs with different concentrations of MCNPs. The MCNPs were complexed with control siRNA (200 nM) before treating the NSCs. Reprinted from Ref. [157]. Copyright 2013 John Wiley and Sons.

Since we confirmed the excellent biocompatibility and non-toxicity of our MCNPs in NSCs, we went ahead and tested the capability of these MCNPs to translocate genetic materials (siRNA or pDNA) into NSC-GFP, which are genetically labeled with green fluorescent protein (GFP), in the presence or absence of an external MF and compared to commercially available transfection agents such as X-tremeGENE. To this end, we first identified the optimal external MF exposure time that results in maximum transfection efficiency while preventing deleterious effects to cell viability (Figure 2.7).

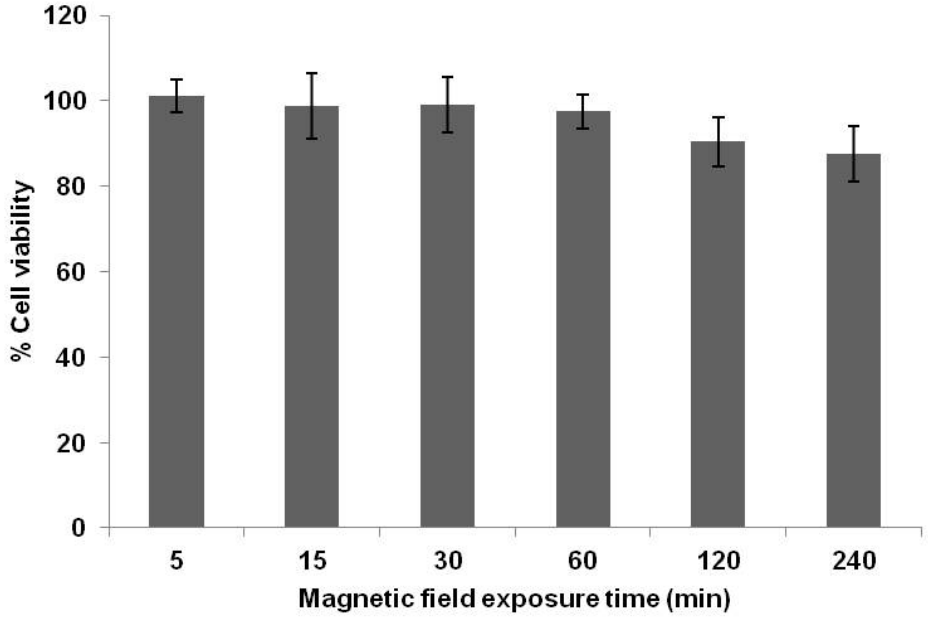

Figure 2.7: Effect of different incubation times on the viability of the NSCs. The neural stem cells were exposed to the magnetic field for different periods of time ranging from 5 min to 4 h, after which the magnetic field was removed. The cells were then incubated for an additional 24 h and their viability was assessed using MTS cell proliferation assay. No nanoparticles were used for this experiment. Reprinted from Ref. [157]. Copyright 2013 John Wiley and Sons.

To accomplish this, we complexed the MCNPs with Cy3-labeled control siRNA (red color, Silencer, Ambion) and incubated these complexes with NSC-GFP in the presence of a MF for increasing periods of time (ranging from 0 to 6 h). After each exposure time point, the NSCs-GFP were washed with DPBS three times to remove untransfected MCNP-siRNA constructs. Using fluorescence microscopy, we observed a sharp increase in the uptake and localization of the tested MCNP-siRNA constructs into the cytoplasm of the NSCs-GFP after the complexes were incubated with the NSCs for only 30 min in the presence of MF, as compared to control (Figure 2.8).

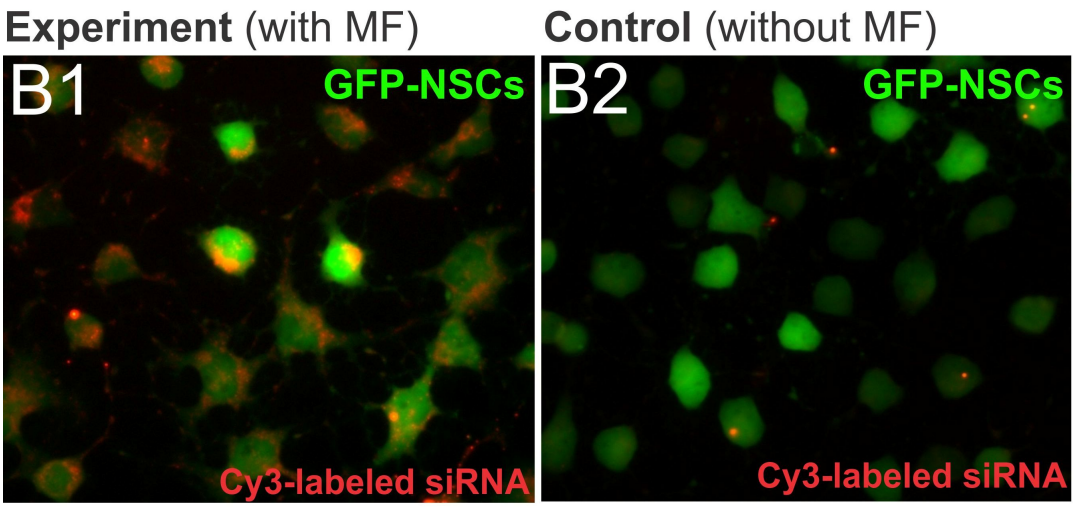

Figure 2.8: Effect of presence (B1) and absence (B2) of MF on uptake of MCNP-Cy-3 labeled siRNA (MCNPs, 5 μg/mL; Cy-3 labeled siRNA, 200 nM) complexes in the NSCs. Reprinted from Ref. [157]. Copyright 2013 John Wiley and Sons.

Upon increasing the time of incubation, we observed a minimal increase in the uptake and localization of MCNP-siRNA constructs (Figure 2.9). As such, we subsequently identified 30 min as the optimum MF exposure time to offset any deleterious effects to the NSC-GFP and used this for all of the following experiments.

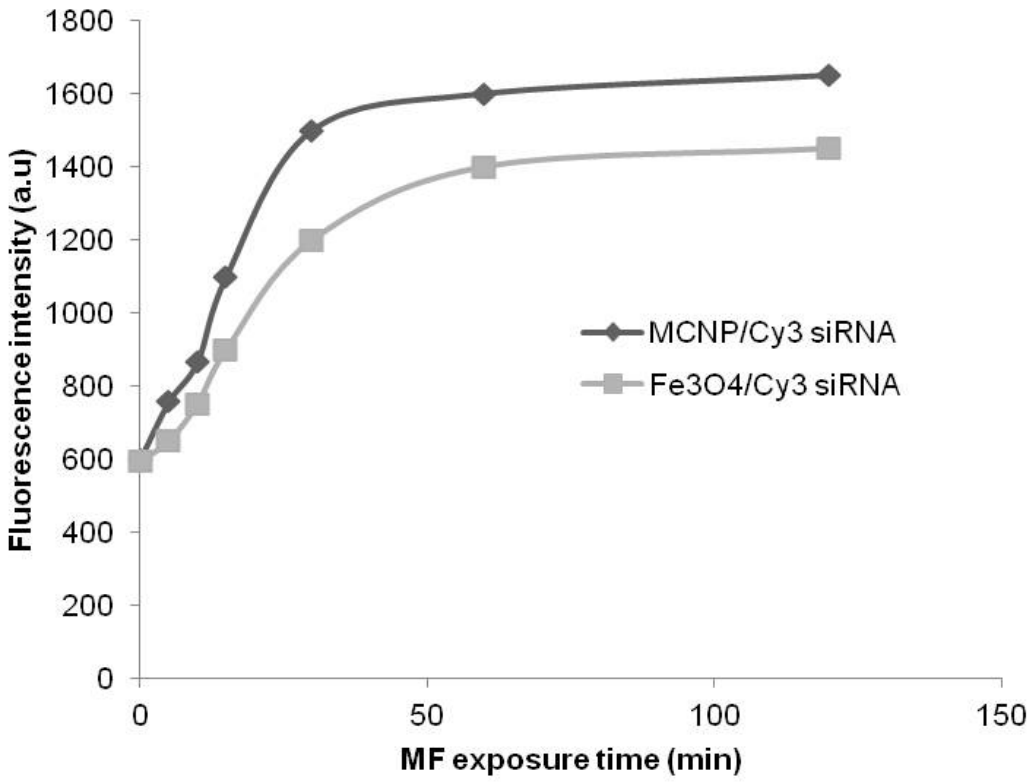

Figure 2.9: Comparison of the uptake of Cy-3 labeled siRNA using MCNP and Fe3O4 NPs into NSCs following exposure to magnetic field (MF) for varying periods of time. The NSCs were incubated with Cy3-labeled siRNA/MCNP (MCNP = 5 μg/mL; Cy-3 siRNA = 200 nM) or Cy3-labeled siRNA/Fe_3O_4 (Fe_3O_4 = 5 μg/mL; Cy-3 siRNA = 200 nM) complexes in the presence of MF for varying periods of time. Thereafter, the NSCs were washed and the uptake of siRNA was measured using fluorescence microscopy. Reprinted from Ref. [157]. Copyright 2013 John Wiley and Sons.

Next, to demonstrate the delivery of functional MCNP-siRNA constructs, we chose siRNA against GFP (siGFP) and optimized the concentrations of MCNP and siGFP to be delivered by varying their respective concentrations and measuring the resulting GFP knockdown efficiency. Once we identified the optimum concentrations of MCNP (5 μg/ mL) and siGFP (200 nM), we compared the knockdown efficiency of MCNPs-based trasfection with that of the commercial transfection agent, X-tremeGENE. Specifically, the X- tremeGENE was complexed with the same concentration of siRNA (200 nM) in the ratio of 3:1 as recommended by the manufacturer. To this end, the MCNP-siGFP and X-tremeGENE-siGFP constructs were incubated with NSCs-GFP for increasing periods of time (from 15 min to 6 h), to first elucidate the correlation between the

incubation time and the transfection efficiency, wherein we used the optimized MF exposure time (30 min) for all conditions. For comparison, we used the recommended incubation time (6 h) for the commercially available transfection reagents (e.g. X-tremeGENE). After each period of incubation, the cells were washed with DPBS three times and further incubated for a period of 72 h, following which we quantified the decrease in the GFP signal intensity of the NSCs. We saw a significant difference in the gene silencing capability of MCNPs in the presence of a MF (55.45 % knockdown, $p < 0.01$) as compared to that in the absence of a MF (36.75% knockdown) (Figure 2.10), when the complexes were incubated for 6 h.

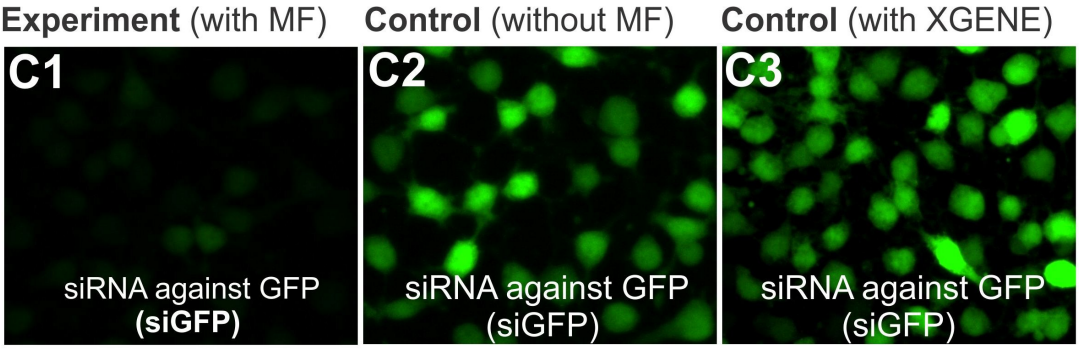

Figure 2.10: Knockdown of GFP fluorescence signal in NSCs treated with MCNPs-siGFP complexes in the presence (C1) or absence (C2) of an external magnetic field. The knockdown efficiency using MCNPs was compared to that using X-TremeGENE (C3) as a positive control. The concentrations of MCNPs and siGFP were 5μg/mL and 200 nM respectively. The amount of X-TremeGENE used was within the manufacturer recommended range. The cells were exposed to the magnetic field for an optimum period of 30 min. Reprinted from Ref. [157]. Copyright 2013 John Wiley and Sons.

Additionally, upon comparison of our magnetically-facilitated delivery with X-GENE based delivery, we observed a remarkable difference in the time-dependent progression curve of the transfection efficiency (Figure 2.11) and in the cytotoxic effects exhibited by the two experimental conditions. In the case of magnetically-facilitated delivery (MCNP-siGFP/MF, Figure 3D), significantly higher levels of GFP knockdown (45.6 % knockdown, $p < 0.01$) were observed after only 15 min of incubation with negligible cytotoxicity (97 % cell viability). Moreover, an additional increase in the gene silencing was seen after increasing the incubation time to 6h (55.45% knockdown). In contrast, negligible GFP knockdown was seen in the case of X-tremeGENE-siGFP complexes

after 15 min of incubation, which gradually increased upon increasing the incubation time, and reaches a plateau (38.95% knockdown) after 6h, however, with significant cytotoxicity (60 % cell viability; $p < 0.01$). From the analysis of the GFP knockdown results, we identified 30 min as the optimum incubation period needed to achieve significant downstream effects from gene delivery using MCNP/MF.

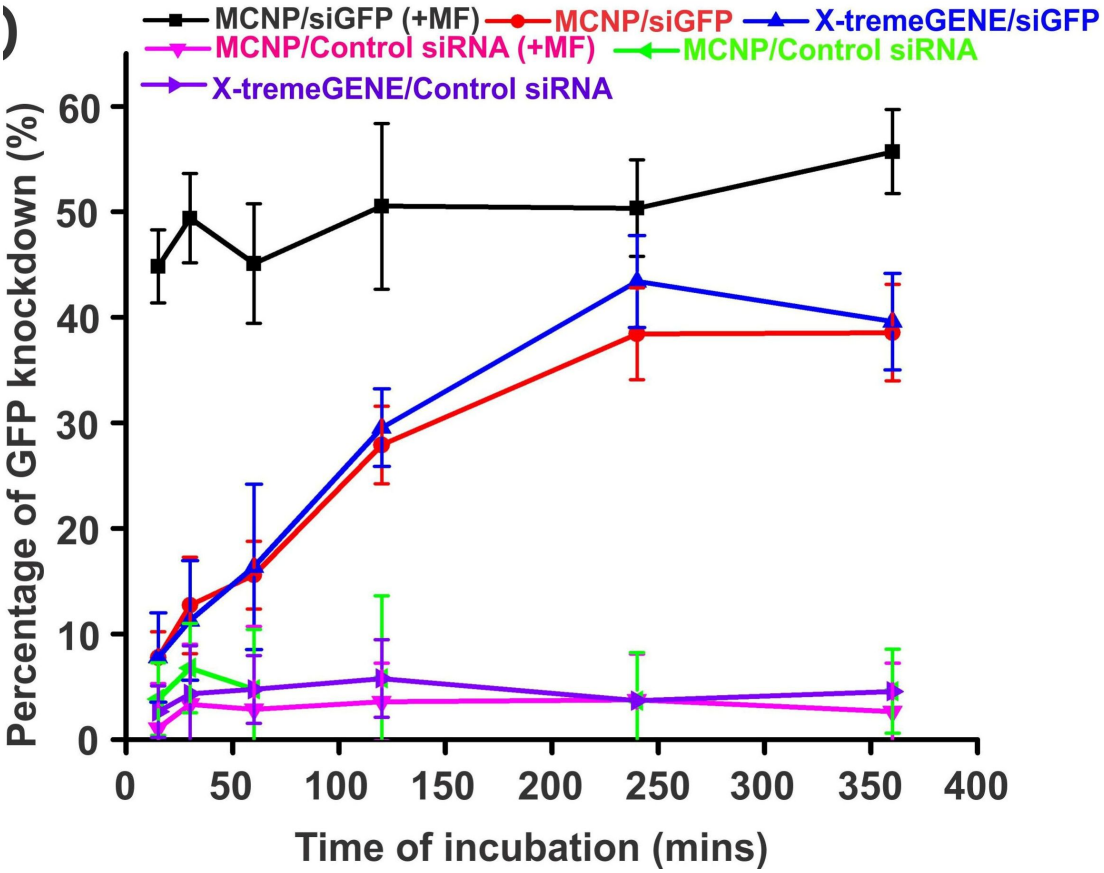

Figure 2.11: Quantification of time-dependent GFP knockdown efficiency in NSCs using MCNPs [w/ or w/o magnetic field (MF)] and X-TremeGENE complexed with either siGFP or control siRNA. The concentrations of MCNPs and siGFP were 5 μg/mL and 200 nM respectively. Reprinted from Ref. [157]. Copyright 2013 John Wiley and Sons.

To see whether we could increase transfection efficiency further, we carried out repeated transfection of the same cell culture (a technique known as multifection [177]) using our MCNP/siGFP constructs and compared the gene-silencing efficiency achieved with multifection to that of a single transfection. We found that we were able to further improve the gene silencing efficiency from 55% (single transfection of MCNP/siGFP) to 65% (multifection of MCNP/siGFP). In the case of X-tremeGENE multifection, we

observed a similar trend of increased GFP knockdown (45% for multifection vs. 38% for single transfection). However, upon comparing their toxicity profiles, the viability of cells multi-transfected with MCNPs only decreased slightly ($p > 0.05$ as compared to control) , while that of X-tremeGENE resulted in significant cell death ($p < 0.01$ as compared to control, Figure 2.12).

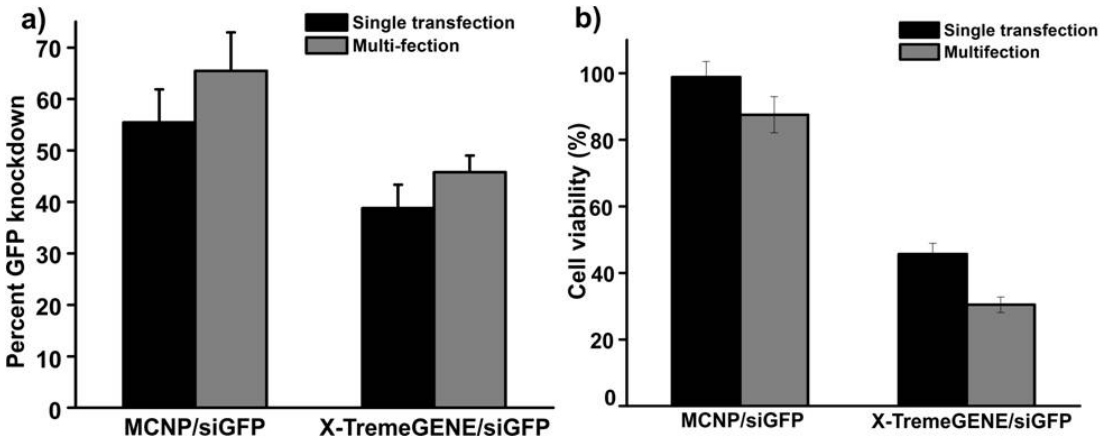

Figure 2.12: Quantification of (a) GFP-knockdown efficiency and (b) cell viability of NSCs treated with MCNP/siGFP or X-TremeGENE/siGFP complexes, either with single transfection or multifection. In case of single transfection, the NSCs were treated with MCNP/siGFP for 30 mins in the presence of MF, and X-TremeGENE/siGFP for 6 hours. The media was changed at the end of treatment. In case of multifection, the same NSCs were treated with MCNP/siGFP or X-TremeGENE/siGFP twice within a 24 h period. Reprinted from Ref. [157]. Copyright 2013 John Wiley and Sons.

Finally, besides siRNA, we also demonstrated the delivery of plasmid DNA (DsRED) to NSC-GFP using our MCNPs under similar experimental conditions as compared to siRNA delivery (Figure 2.13). The magnetically-facilitated delivery of MCNP-DsRED complexes led to significantly higher levels of gene expression in NSCs within a shorter incubation time as compared to delivery of the same complexes in the absence of a MF. Thus, we observed that in spite of shorter-than commonly used incubation times, highly efficient gene deactivation (in the case of siGFP, Figure 2.11) or activation (in the case of DsRED; Figure 2.13) was achieved with negligible toxicity when magnetically-facilitated delivery of MCNP constructs was utilized, which is in contrast to that seen with the positive control experiments using standard transfection agents under the same conditions. However, to achieve comparable levels of knock-down results using the

aforementioned lipid-based transfection methods, we typically needed longer incubation times (>6h), which can significantly induce cytotoxic effects on cells and result in low cell viability (60 % cell viability).

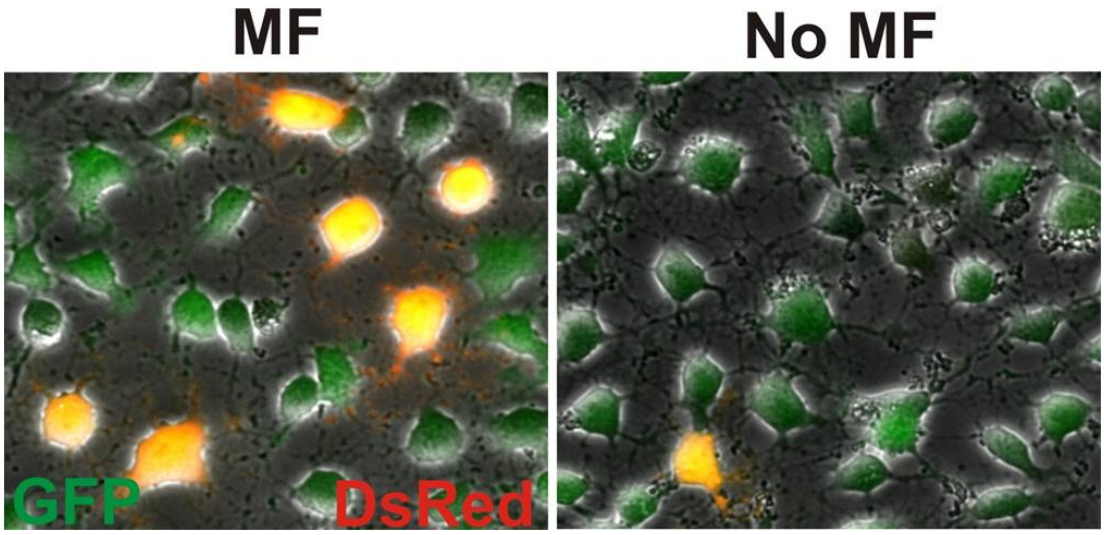

Figure 2.13: The MCNPs (8 μg/mL) were complexed with DsRED (1 μg) and incubated with NSCs in the presence (t = 30 mins) and absence of MF. The expression levels of DsRED were monitored 72h post transfection using fluorescence microscopy. Reprinted from Ref. [157]. Copyright 2013 John Wiley and Sons.

MCNP-mediated siRNA delivery for enhancing neuronal differentiation

Having demonstrated that our MCNPs, in the presence of a MF, can efficiently manipulate gene expression in NSCs without compromising their biological functions, we focused on controlling the neural differentiation of NSCs using our optimized conditions (Figure 4A) in order to demonstrate the utility of our MCNPs for stem cell-based therapies. For this demonstration, we selected functional siRNAs targeting key genes such as CAVEOLIN-1 (siCAV) [178] or SOX9 (siSOX9) [179, 180]. These two genes (CAVEOLIN-1 and SOX9) have already been identified as neural switches that, when inhibited, selectively control the differentiation of NSCs into oligodendrocytes and neurons, respectively. To demonstrate the effective genetic manipulation of NSCs to control their differentiation, the MCNP-siRNA complexes (MCNP, 5 μg/mL; siCAV/siSOX9, 200 nM) were prepared and incubated with NSCs in the presence of a MF (t = 30 min)

as optimized previously. Untreated NSCs and NSCs treated with MCNP-siRNA constructs were characterized and quantified using immunocytochemistry by staining for oligodendrocytes [myelin binding protein (MBP)] and neuron [tubulin (TUJ1)] markers at day 7 after transfection (Figure 2.14).

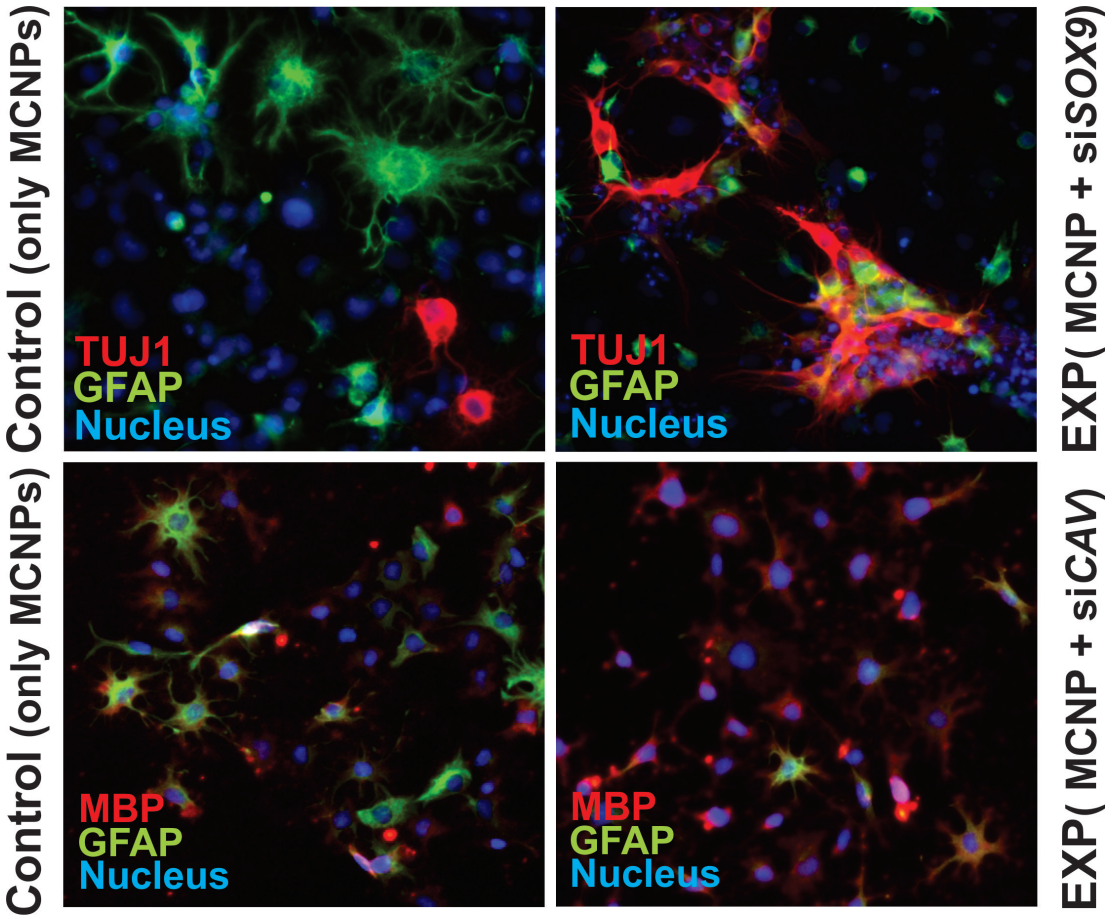

Figure 2.14: Fluorescence microscopy images depicting neuronal (top row) and oligodendrocyte differentiation (bottom row) of the NSCs following delivery of siSOX9 and siCAV respectively using MCNPs. The NSCs were stained with MBP (oligodendrocytes) and GFAP (astrocytes) in the case of MCNP/siCAV treated cells and for TUJ1 (neurons) and GFAP (astrocytes) in case of MCNP/siSOX9 treated cells on day 7 of transfection. The nucleus was stained with Hoechst. Scale bar is 1 μm. Reprinted from Ref. [157]. Copyright 2013 John Wiley and Sons.

From these experiments, we observed a significant increase in the percentage of oligodendrocytes (MBP-positive) and neurons (TUJ1-positive) in the cells treated with siCAV or siSOX9 respectively, as compared to the spontaneous differentiation condition (Figure 2.15, $p < 0.01$ for siCAV and $p < 0.001$ for siSOX9 treatment). Thus, using the

magnetically-facilitated delivery of MCNP-siRNA constructs, we were able to control the differentiation of NSCs to a particular lineage to a significantly greater extent and within shorter incubation periods, as compared to the untreated control NSCs.

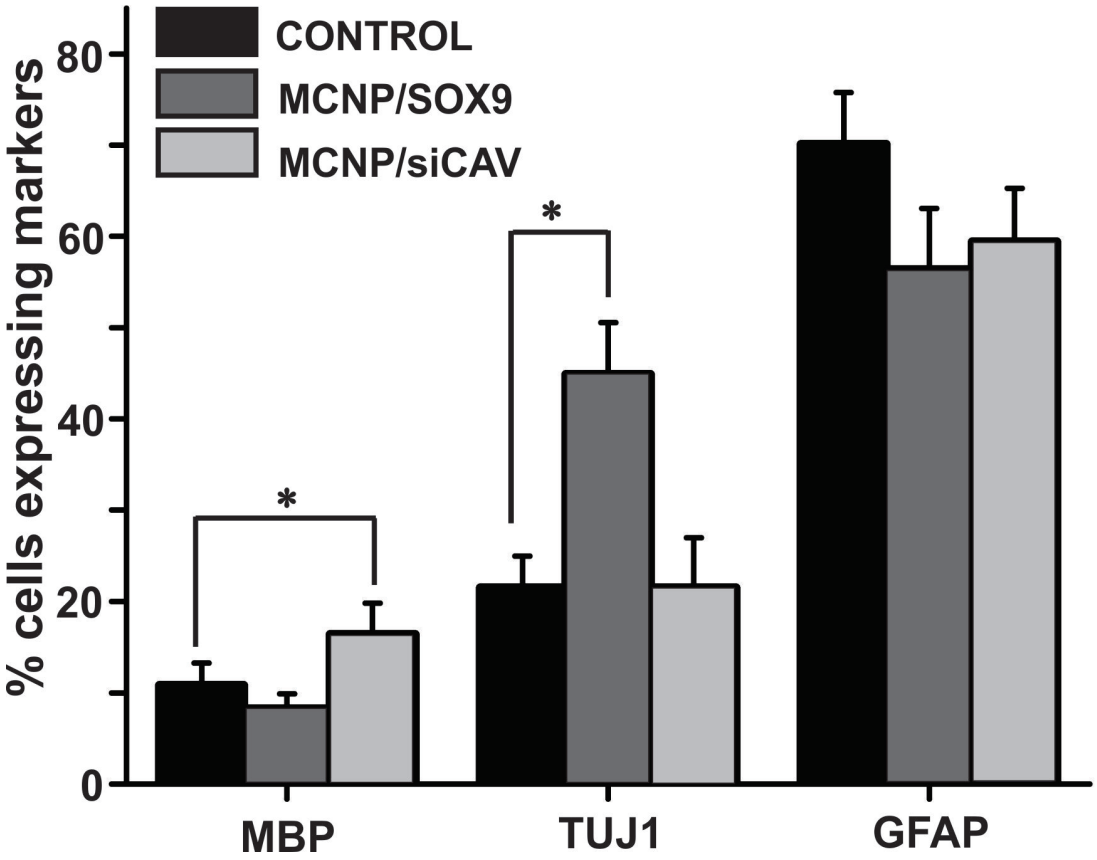

Figure 2.15: Quantification of percent cells expressing neural markers when treated MCNP/siCAV and MCNP/siSOX9 as compared to untreated cells. All results represent the average mean of three independent experiments. Values are represented as mean ± SD. denotes p <0.001 for neuronal differentiation and denotes p< 0.01 for oligodendrocyte differentiation. Reprinted from Ref. [157]. Copyright 2013 John Wiley and Sons.

Noninvasive multimodal imaging in stem cells using MCNPs

Finally, to demonstrate the multifunctional advantages that a gold shell can have for MCNP-based delivery of genetic materials and for stem cell-based therapies, we used dark imaging to confirm the uptake of the MCNPs into NSCs. As our MCNPs possess a thin gold shell and display surface plasmon resonance at 540 nm, they can be used as cellular imaging modalities using simple dark-field microscopy. In particular, gold

nanoparticles are known to scatter visible and infrared light owing to their localized surface plasmons [32, 181]. In addition, they are significantly brighter than chemical fluorophores and do not photobleach, thus making them excellent candidates for biological imaging [179]. To this end, we studied the light scattering properties of our MCNPs complexed with control siRNA, by incubating them with NSCs and then monitored their intracellular uptake using a dark-field microscope. As seen in Figure 2.16, the MCNPs scatter the incident white light more intensely as compared to the control cells. On the other hand, no noticeable change was seen when the cells were incubated with the magnetic core nanoparticles. Thus, besides improving the solubility and affording facile surface functionalization, the gold shell on our MCNPs can also be used as an imaging modality to confirm the localization of MCNPs to stem cells before further study or application. Also, owing to presence of the magnetic core, our MCNPs can afford MRI imaging capability as can be seen from Figure 2.16 providing further advantages for in vivo applications. To evaluate whether our MCNP retain their functions as an MRI contrast agent, we carried out MRI studies using MCNPs in phantom agar gels. Increasing the concentration of the MCNPs from 2 μg/ml to 50 μg/ml, led to a significant reduction in T2, as evident from the decreased signal intensity. Additionally, this decrease was comparable to that of just the core NPs indicating that the Au shell does not negatively affect the MRI contrast of the core. These results, thus demonstrate that our MCNPs could also function as an MRI contrast agent due to shortening of T2 relaxation and higher T2 relaxivity.

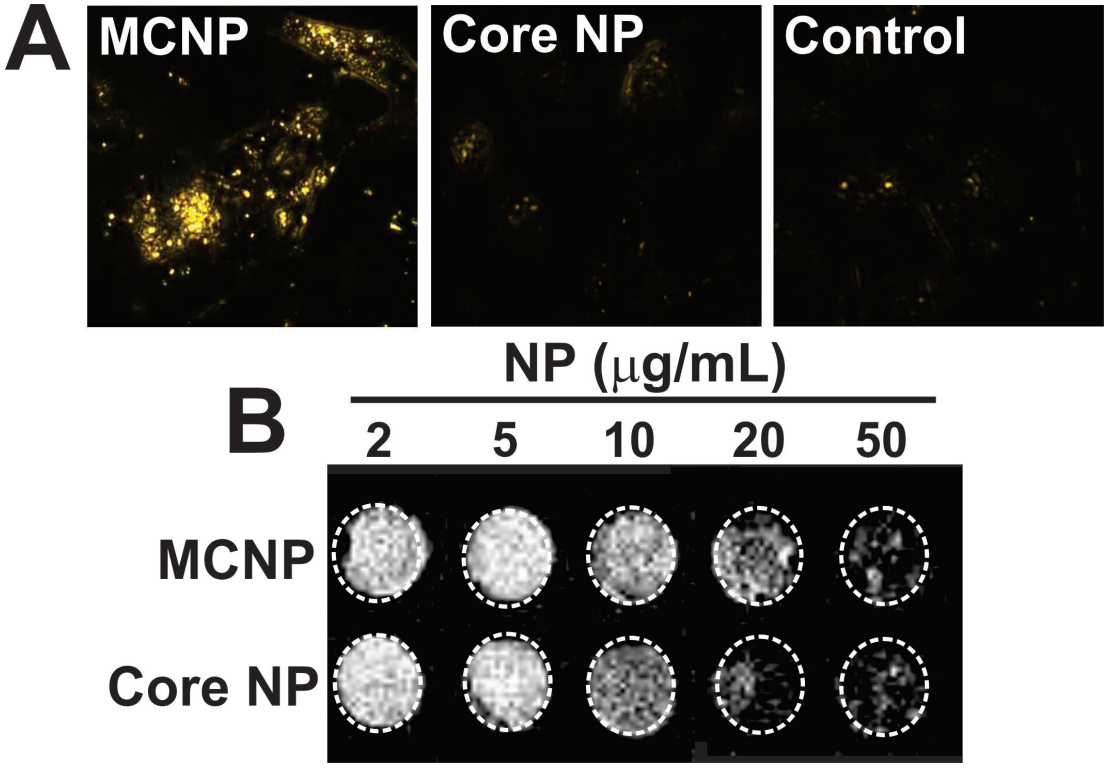

Figure 2.16: (A) Dark-field light scattering images for NSCs treated with MCNPs, Core ($ZnFe_2O_4$) MNPs and untreated NSCs (Control). Please note that the dark-field scattering signals from the core MNP and control experiments come from background signal due to cellular components. Scale bar is 100 nm.(B) Signal intensity T2 weighted MR images of MCNP and Core NPs in phantom agar gel at 2-50 μg/ml concentration at 25 °C. Reprinted from Ref. [157]. Copyright 2013 John Wiley and Sons.

2.1.3 Conclusions

In conclusion, we have synthesized magnetic core-shell nanoparticles (MCNPs) consisting of a highly magnetic $ZnFe_2O_4$ core surrounded by a gold outer-shell ($ZnFe_2O_4$@Au) and utilized them for the genetic manipulation of neural stem cells (NSCs) in a highly efficient, biocompatible, and spatiotemporally controlled manner. As a proof-of-concept for the utility of the MCNPs in the genetic manipulation of stem cells, we also demonstrated that we could direct the differentiation of NSCs to specific lineages (neurons and oligodendrocytes) using our developed MCNPs to delivery siRNA. In particular, while MCNPs have been utilized for the highly efficient labeling of stem cells, this is the first demonstration to utilize MCNPs for the delivery of genetic materials (e.g. siRNA and pDNA) to stem cells. Moreover, these MCNPs hold a number of advantages for

use with stem cells-based applications owing to multifunctionalities that result from the composite of the magnetic core with the gold outer-shell. In particular, we have demonstrated that the gold outer-shell i) enables a facile surface for the functionalization of our MCNPs with a cationic polyamine-dendrimer thereby allowing for the complexation of the MCNs with negatively charged genetic materials, ii) enhances biocompatibility of the MCNP with stem cells, and iii) allows for the use a simple method with which to confirm the presence of MCNPs within stem cells through dark field imaging. In addition, previous studies have shown that a gold outer-shell improves aqueous solubility and long-term stability of the MCNPs. On the other hand, we have demonstrated that the magnetic core of the MCNP i) retains its excellent magnetic properties even after the formation of the gold outer-shell, ii) allows us to deliver nanoparticle-biomolecule constructs into the difficult-to-transfect stem cells with high transfection efficiency and with significantly shorter incubation times as compared to the conventional lipid-based transfection agents, and iii) can be used as an MRI contrast agent, which can be used in the future to track MCNP-transfected stem cells in vivo. Thus, MCNP-based genetic manipulation method can potentially be a powerful tool for stem cell applications.

2.1.4 Materials and Methods

Starting materials, reagents, and solvents were purchased from commercial suppliers (Sigma-Aldrich, Acros, and Fisher) and used as received unless otherwise noted. All reactions were conducted in flame-dried glassware with magnetic stirring under an atmosphere of dry nitrogen.

Synthesis of Zn-doped iron oxide nanoparticles

In a typical experiment for synthesis of the nanoparticles, 300 mg $ZnCl_2$, 400 mg $FeCl_2$ and 3.5 g $Fe(acac)_3$ were mixed in 50 mL of tri-octylamine. To this, 1.2 mL oleic acid was added and refluxed at 300 degrees for an hour in a 250 mL three necked round bottom flask. After one hour, the reaction mixture was cooled down to room temperature and the magnetic nanoparticles were precipitated using ethanol. They were purified by repeated centrifugation and sonication. The as obtained nanoparticles

were then dried overnight under vacuum.

Synthesis of Au coated magnetic nanoparticles

In a typical coating experiment, 243 mg of $HAuCl_4$ in 5 mL chloroform was added to a solution of 10 mg zinc doped iron oxide nanoparticles in chloroform. The $HAuCl_4$ solution was added slowly dropwise to the reaction vial in the presence of oleylamine. The reaction was carried out for 12 hrs. The Au coated nanoparticles were precipitated using ethanol. They were purified by repeated centrifugation and sonication. The core shell nanoparticles were dried under vacuum overnight.

Synthesis of water soluble core shell nanoparticles

For converting the hydrophobic core shell nanoparticles into hydrophilic ones, a ligand exchange reaction was carried out using 11- mercaptoundecanoic acid (MUA). In a typical experiment, 5 g of MUA was dissolved in chloroform and added to a solution containing 40 mg of oleic acid/ oleyl amine coated coreshell nanoparticles. The reaction was carried out at room temperature for 24 hours. The nanoparticles were collected by centrifugation and dried completely. Once dried, they were transferred to water, thereby obtaining an aqueous solution of core shell nanoparticles with desirable concentration.

Synthesis of polyamine dendrimer

A solution of tris(aminoethyl)amine (4.3872 g, 30 mmol) in methanol (25 mL) was added dropwise to a stirred solution of methyl acrylate (19.37 g, 225 mmol) in methanol (25 mL) for 1 h in an ice-water bath. The resulting solution was stirred for 1 h in an ice-water bath and then allowed to warm to room temperature and stirred for further 48 h. The solvent and excess acrylate were removed under reduced pressure using a rotary evaporator. The residue was purified by column chromatography to afford the product (1, hexamethyl-3,3',3",3"',3"",3""'-(2,2',2"-nitrilotris(ethane-2,1-diyl)tris(azanetriyl)) hexapropanoate as a colorless oil. A solution of the above product (2.17 g, 3.3 mmol) in methanol (20 mL) was added dropwise to solution of tris(aminoethyl)amine (7, 5.8 g, 39.6 mol) in methanol (20 mL) and stirred over a

period of 1 h in an ice bath. The resulting solution was allowed to warm to room temperature and stirred for 7 days at room temperature at which time no methyl ester was detectable by NMR spectroscopy. The solvent was removed under reduced pressure using a rotary evaporator and then the excess tris(aminoethyl)amine was removed using an azeotropic mixture of toluene and methanol (90:10 v/v). The remaining toluene was removed by azeotropic distillation using methanol. Finally, the remaining methanol was removed under vacuum. The residue was purified by dialysis and centrifugal filtration to afford the desired product. Finally the product was kept under vacuum to obtain the amino-terminated product (2). To synthesize methyl-ester of 2, a solution of 2 (1.48g, 1.1 mmol) in methanol (5 mL) was added dropwise to a stirred solution of methyl acrylate (2.84 g, 33.0 mmol) in methanol (5 mL) for 1 h in an ice bath. The resulting solution was stirred for 30 min in an ice bath and then for 60 h at room temperature. The volatiles were removed under reduced pressure. The residue was purified by column chromatography using DCM:MeOH (10:1 v/v) to afford the desired product (3) as a yellow oil. Finally,a solution of the methyl ester (3.41g, 1 mmol) in methanol (20 mL) was added dropwise to a stirred solution of tris(aminoethyl)amine (7, 7.02 g, 48 mmol) in methanol (20 mL) over a period of 1 h in an ice bath. The resulting solution was allowed to warm to room temperature and stirred for 7 days at room temperature at which time no methyl ester was detectable by NMR spectroscopy. The solvent was removed under reduced pressure the excess tris(aminoethyl)amine was removed using an azeotropic mixture of toluene:MeOH (90:10 v/v). The product was further purified by washing with anhydrous ether twice, yielding a highly viscous liquid. Finally the product was kept under vacuum to provide the amino-terminated final product (4) as a light yellow liquid.

Quantification of siRNA loading efficiency

The complexes were prepared at various charge ratios by mixing equal volumes of polyamine-coated with siRNA in PBS. Charge ratios (N/P) were calculated as a ratio of the number of primary amines in the polymer, determined from 1H NMR spectra, to the number of anionic phosphate groups in the siRNA. The samples were then incubated

at room temperature for 30 minutes to ensure complex formation. The complexes were prepared at a final siRNA concentration of 0.2 μg of siRNA/100 L of solution. 100 μL of each complex were transferred to a 96-well (black-walled, clear-bottom, non-adsorbing) plate (Corning, NY, USA). A total of 100 μL of diluted PicoGreen dye (1:200 dilution in Tris- EDTA (TE) buffer) was added to each sample. Fluorescence measurements were made after 10 minutes of incubation at room temperature using a M200 Pro Multimode Detector (Tecan USA Inc, NC, USA), at excitation and emission wavelengths of 485 and 535 nm, respectively. All measurements were corrected for background fluorescence from a solution containing only buffer and PicoGreen dye.

Particle size and Zeta potential analysis

Dynamic light scattering (DLS) and Zeta Potential analyses were performed using a Malvern Instruments Zetasizer Nano ZS-90 instrument (Southboro, MA) with reproducibility being verified by collection and comparison of sequential measurements. Nanoparticle/siRNA complexes (siRNA concentration = 330 nM), were prepared using purified water (resistivity = 18.5 MΩ-cm). DLS measurements were performed at a 90° scattering angle at 25°C. Z-average sizes of three sequential measurements were collected and analyzed. Zeta potential measurements were collected at 25°C, and the Z-average potentials following three sequential measurements were collected and analyzed.

Cell culture

Rat neural stem cells (Millipore) were purchased and routinely expanded according to the manufactures protocol. The NSCs were maintained in laminin (Sigma, 20 μg/ml) coated culture dishes pre-coated with poly-L-ornithine (10μg/ml) in DMEM/F-12 media (Invitrogen) supplemented with B-27 (Gibco) and containing L-Glutamine (2 mM, Sigma), and antibiotics penicillin and streptomycin (Invitrogen) in the presence of basic fibroblast growth factor (bFGF-2, 20 ng/ml, Millipore). All cells were maintained at 37°C in humidified 5% CO2 atmosphere.

Magnetically-facilitated delivery of MCNPs

24 h before the magnetically-facilitated delivery of MCNPs, 50,000 NSCs in a volume of 500 uL were seeded into each well of a 24-well plate, so as to attain 80-90% confluency at the time of transfection. For the preparation of MCNP-siRNA constructs, the varying amounts of MCNPs and siRNA solution were gently mixed with DMEM to attain the desired siRNA and MCNP concentration and then incubated at room temperature for 15-30 min. Thereafter the MCNP-siRNA complexes were added to each well to attain the desired final concentration of siRNA/well. Subsequently, the cell culture plates were placed on the Nd-Fe-B magnetic plates (OZ Biosciences, France) for different time periods. After each time period of incubation, the cells were washed with DPBS and the transfection medium was replaced with fresh growth medium.

Cell viability assays

The cellular viability of the NSCs treated with MCNPs was assessed using the standard MTS cell proliferation assay. All experiments were conducted in triplicate and averaged. The quantification of nanoparticle-mediated toxicity was done using MTS assay after incubating the neural stem cells in the presence of varying concentrations (2-20 μg/mL) of only nanoparticles for 48-96 h. The transfected cells were allowed to grow for 48h, after which the cell viability was assessed using the CellTiter 96 AQueous One Solution Cell Proliferation Assay (Promega, Madison, USA) according to the manufacturers recommended protocol. The data is represented as formazan absorbance at 490 nm, considering the control (untreated) cells as 100% viable.

Quantification of knockdown of EGFP expression

Following siRNA treatment, cells were washed with DPBS and fixed with 2-4% formaldehyde solution prior to imaging. The fluorescent and phase contrast images were taken using a Nikon Ti-Eclipsed Inverted Fluorescence microscope (Nikon Instruments, USA). Each image was captured with different channels and focus. Images were processed and overlapped using the NIS-Elements software (Nikon, USA).

Immunocytochemistry

To investigate the extent of differentiation, at Day 6, the basal medium was removed and the cells fixed for 15 minutes in Formalin solution (Sigma) followed by two PBS washes. Cells were permeabilized with 0.1% Triton X-100 in PBS for 10 minutes and non- specific binding was blocked with 5% normal goat serum (NGS, Invitrogen) in PBS for 1 hour at room temperature. To study the extent of neuronal differentiation the primary mouse antibody against TuJ1 (1:500, Covance) was used, for glial differentiation the primary rabbit antibody against GFAP (1:500, Dako) was used and for oligodendrocyte differentiation, the primary mouse antibody against MBP (1:300, Abcam) was used. The fixed samples were incubated overnight at 4°C in solutions of primary antibodies in PBS containing 10% NGS. After washing three times with PBS, the samples were incubated for 1 h at room temperature in solution of anti-mouse secondary antibody labeled with Alexa-Fluor 546 and anti-rabbit secondary antibody labeled with Alexa-Fluor 647 (1:400, Jackson ImmunoResearch), Hoechst (1:500, Invitrogen) in PBS containing 10% NGS to observe neuronal, glial and oligodendral differentiation. The stained samples were imaged using Nikon Ti-Eclipsed Inverted Fluorescence microscope (Nikon Instruments, USA).

Quantification of mechanism of uptake of MCNPs

Our methods included low temperature (4°C, an inhibitory condition for internalization through endocytosis), indomethacin (a specific inhibitor of caveolae-mediated endocytosis), phenylarsine oxide (a specific inhibitor of clathrin-mediated endocytosis) and sodium azide/ 2-deoxy glucose (an inhibitor of all types of energy-dependent transport inside cells). The GFP knockdown efficiency was quantified 72 h post transfection using fluorescence microscopy as described previously.

In vitro Magnetic Resonance Imaging

For MRI studies, 3% (w/v) agar solution containing different amounts of magnetic nanoparticles formulations was prepared by heating agar solution at 80°C for about

20 min and stirring thoroughly to obtain uniform solution, then allowed to cool down to room temperature. These phantom gels were employed to test the in vitro MRI properties. MR images were acquired using 1 Tesla M2 High Performance MRI System (Aspect Magnet Technologies Ltd, Netanya, Israel).

2.2 Magnetic Core-shell Nanoparticle-based Combined Hyperthermia and Peptide Delivery for Enhanced Cancer Cell Apoptosis

2.2.1 Introduction

In addition to being the powerhouse of energy for mammalian cells, mitochondria also plays an important role in regulating cellular death [182, 183]. Permeabilization of the mitochondrial outer membrane - tightly regulated by Bcl-2 family proteins [184] and the subsequent release of apoptogenic factors such as cyto-chrome C, is considered to be a point-of no return in many cascades leading to apoptosis [185]. Hence, the mitochondria is now emerging as a key pharmacological target for cancer therapy [186]. To this end, peptides, which are designed to specifically target as well as permeabilize mitochondria via disruption of protein-protein interactions, that are generally not amenable to small molecules, are considered an attractive option [187, 188]. For example, Ma and his co-workers reported a novel amphipathic tail-anchoring peptide of Bfl-1 (ATAP), which can target the mitochondrial outer membrane specifically, induce permeabilization of the MOM and subsequent release of cytochrome-c, thus triggering potent apoptotic cell death [189]. In addition, the apoptotic efficacy of ATAP was similar or slightly higher than the commonly used BH3 peptides and more importantly, independent of the expression levels of anti-apoptotic Bcl-2 family proteins, unlike the BH3 peptides [190]. Since the levels of Bcl-2 family members are often found to be dysregulated in cancer cells, it was hypothesized that ATAP could hence be a better therapeutic lead as compared to BH3 peptides, owing to its unique mechanism which allows to bypass the Bcl-2-mediated resistance in cancer cells [189, 190]. However, the obvious clinical advantages of ATAP are offset by its poor solubility under physiological conditions, owing to its amphipathic nature; and lack of any tumor targeting capability [188]. To overcome such issues, nanoparticles present an attractive option, as they have been widely explored for drug and gene delivery for numerous biomedical applications [191–193]. In particular, magnetic nanoparticles have shown great potential for use in bioapplications such as imaging, hyperthermia, and drug delivery [40, 194]. The ease of synthesis of these MNPs and their subsequent surface modifications enables

their employment as smart nanomedicines that can incorporate multiple components (e.g. core, shell, surface functionalization) for various functions including cell-targeting, imaging, and therapy [36, 48]. For example, Lee et. al., recently demonstrated the development of novel multimodal magnetic core-shell nanoparticles, composed of a highly magnetic core and a plasmonic gold shell for magnetically-facilitated delivery of siRNA and plasmid DNA to stem cells [157]. The magnetic core of the MNPs enhanced transfection kinetics by allowing for magnetically-facilitated delivery, while the gold shell improved biocompatibility and solubility. Additionally, as these MCNPs comprised of two orthogonal elements, they afforded multimodal imaging capabilities (eg: MRI and dark-field). Hence, such core-shell nanoparticles would be an ideal platform for the target-specific delivery of ATAP to cancer cells. To this end, we describe the development of amphipathic tail anchoring peptide-tethered magnetic core-shell nanoparticles (MCNP-ATAP) for enhanced apoptosis in U87vIII glioblastoma cells (Figure 2.17A). The gold shell of the MCNPs allowed for facile conjugation of the ATAP molecules as well as a tumor targeting peptide (iRGD) which has been shown to selectively home to brain tumors via interactions with nucleopilin and integrin receptors present on these cells, thereby affording tumor targeting capability to our MCNP-ATAP constructs. Additionally, the magnetic core of our MCNPs, when placed in alternating magnetic field, could induce localized hyperthermia, which has been reported to enhance mitochondrial permeabilization as well as directly activate the pro-apoptotic proteins (Bax and Bak) and inhibit anti-apoptotic proteins (Bcl-2, Bcl-xL and MCl-1) of the Bcl-2 family (Figure 2.17B) [195, 196].

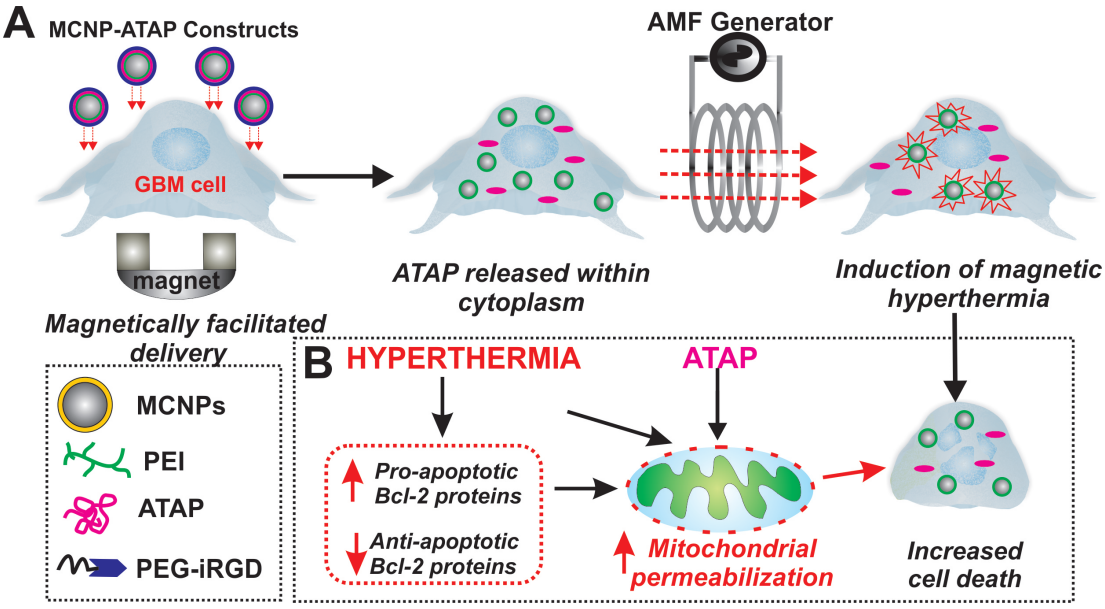

Figure 2.17: (A) Schematic diagram depicting magnetically-facilitated targeted delivery of MCNP-ATAP to brain cancer cells and subsequent application of hyperthermia to induce apoptosis. (B) Mechanism of hyperthermia- and ATAP-mediated apoptosis.

2.2.2 Results and Discussion

Synthesis and characterization of MCNP-ATAP constructs

The citrate-capped magnetic core-shell nanoparticles were synthesized using by making slight modifications to our previously reported method [157, 175]. Thereafter, these citrate-capped MCNPs (10 nm) were coated with branched polyethyleneimine (PEI, Mw = 10 kDa) via electrostatic inter-actions to afford an overall positive charge to the complex. Subsequently, these amine-terminated MCNPs were coupled to the thiol-terminated ATAP moieties via a heterofunctional cross-linker, N-succinimidyl 3-(2-pyridyldithio)propionate (SPDP) to form MCNP-ATAP constructs. Additionally, to improve the overall aqueous solubility of the MCNP-ATAP constructs, thiol-PEG moieties bearing carboxyl endgroups were also conjugated to the MCNPs using the SPDP linker. Furthermore, the carboxyl end-groups of the PEG chains provided a facile handle to attach iRGD for selective delivery of MCNP-ATAP constructs to U87 glioblastoma cells (Figure 2.18).

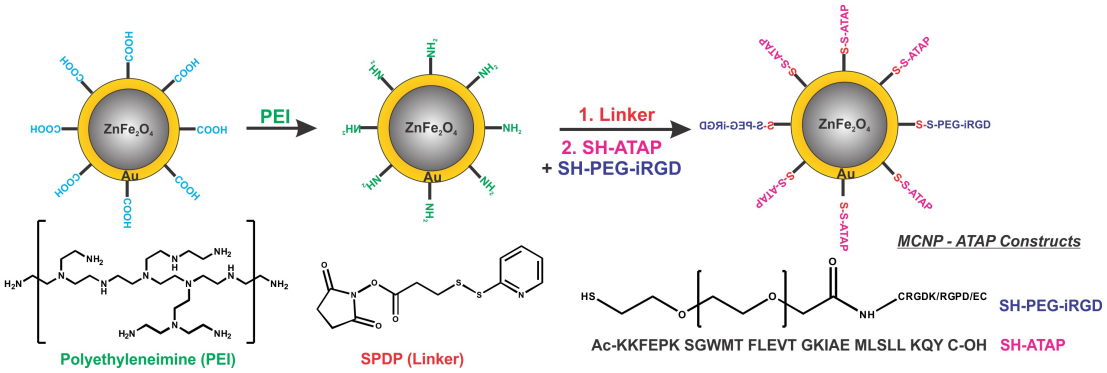

Figure 2.18: Conjugation of ATAP and targeting ligands via a disulfide bond on the surface of MCNPs.

These constructs were then characterized using transmission electron microscopy (Figure 2.19A) and UV-vis spectroscopy (Figure 2.19B). Additionally, the particle diameter and zeta potential of the MCNP-ATAP constructs was measured using dynamic light scattering at each step of conjugation (Figure 2.19C). The final MCNP constructs had a hydrodynamic diameter of 45.61 2.3 nm and were positively charged ($\zeta = +15.1$ mV) to allow for increased cellular uptake. Additionally, the amount of ATAP present on the MCNPs was quantified by measuring the concentration of the unconjugated ATAP moieties present in the supernatant using UV-Vis spectroscopy (SI). Approximately, 50% of the loading amount of ATAP was conjugated on the nanoparticles and it was found that 100 nM ATAP was present per μg of MCNP (10 nm).

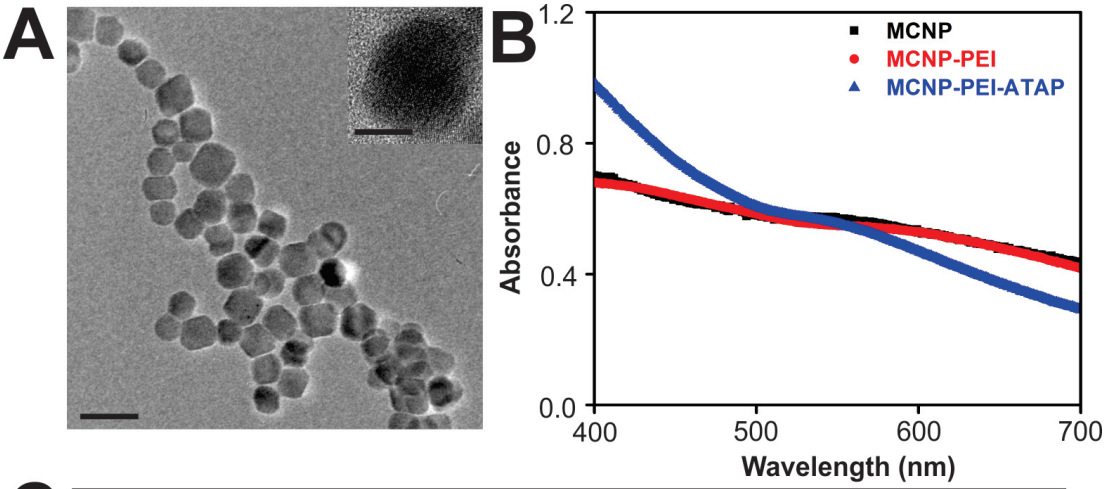

C

Sample	Particle diameter (nm)	Zeta potential (mV)
MCNP	15.41 - 5.8	-15.78
MCNP-PEI	35.7 - 4.6	+20.78
MCNP-PEI-ATAP	46.78 - 8.6	+11.32

Figure 2.19: (A) Transmission electron microscopy and high-resolution transmission electron microscopy (inset) images of MCNP-ATAP constructs. The scale bar is 20 nm (Inset = 5 nm). (B) UV-visible spectroscopy analysis of the MCNPs before and after conjugation of ATAP moieties. (C) Hydrodynamic diameter and zeta potential measurements at each step of formation of MCNP-ATAP constructs

Targeted delivery of MCNP-ATAP constructs

Once the MCNP-ATAP constructs were generated and characterized, we then went on to test their targeted delivery and the subsequent apoptotic efficacy in glioblastoma multiforme cells (U87vIII) overexpressing the mutant epidermal growth factor receptor vIII (EGFRvIII) [80, 176]. The overexpression of EGFRvIII has been implicated in enhancing the tumorigenicity and resistance to radiation and chemotherapy in GBM [197, 198]. As mentioned earlier, ATAP lacks a tumor targeting moiety, thereby restricting its widespread clinical application. Hence, we modified the carboxyl end-groups of the PEG chains, with a targeting ligand, iRGD, which has been reported to

home onto the $\alpha_v\beta_3$ integrin surface receptors present in glioblastoma and other cancer cells [199]. These iRGD-grafted PEG chains were then conjugated on the surface of MCNPs as described earlier (Figure 2.18). Additionally, we conjugated a fluorophore (Alexa Fluor 594) on the surface of MCNPs to make them amenable for visualization using fluorescence microscopy. The iRGD-conjugated MCNPs were incubated with U87vIII and MCF-7 cells, having low integrin expression [**?**], the cells were then washed thrice with PBS to remove any excess MCNPs and thereafter imaged using fluorescence microscopy. As seen in Figure 2.20, U87vIII cells, having higher integrin levels, show significantly higher uptake of the iRGD conjugated MCNPs as compared to MCF-7 cells, which have low levels of integrins. Taken together, these results indicate that by simply conjugating targeting ligands on the surface of the MCNPs, we can adopt a facile approach of conferring tumor targeting capability to the ATAP moieties, without making any structural modifications to ATAP.

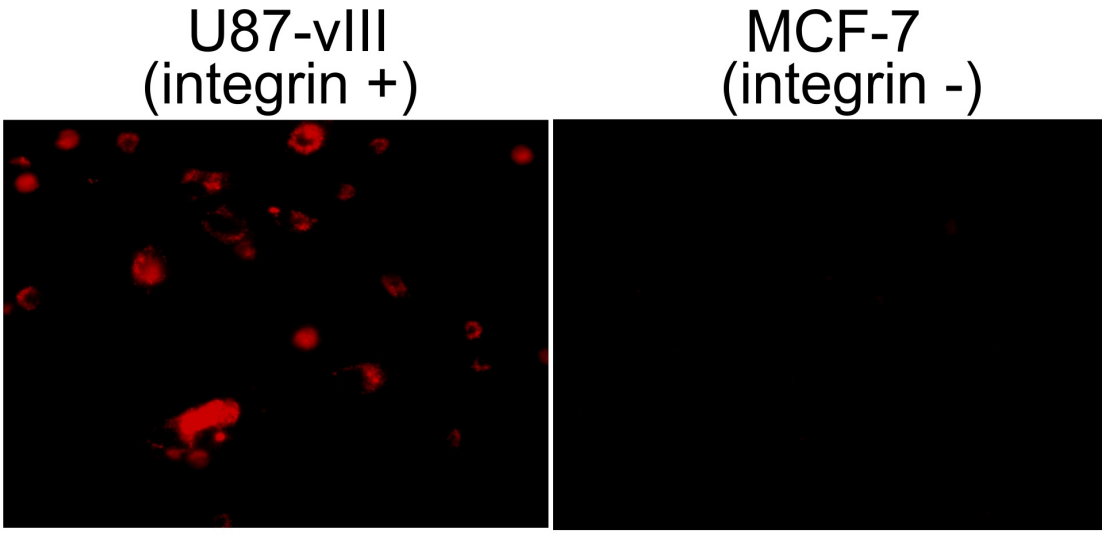

Figure 2.20: Epifluorescent images depicting targeted delivery of iRGD-modified MCNP-ATAP constructs to integrin-positive U87vIII and integrin-negative MCF-7 cells.

Induction of apoptosis in cancer cells using MCNP-ATAP constructs

Thereafter, we tested the apoptotic capability of these targeted MCNPs in glioblastoma cells. Prior to testing MCNP-ATAP constructs, we first tested the effect of varying concentrations of unconjugated ATAP (in DMSO) on viability of U87vIII cells using

the MTS assay. However, unconjugated ATAP had negligible effect on the viability of cells even at significantly higher concentrations (Figure 2.21), owing to its low solubility at physiological conditions.

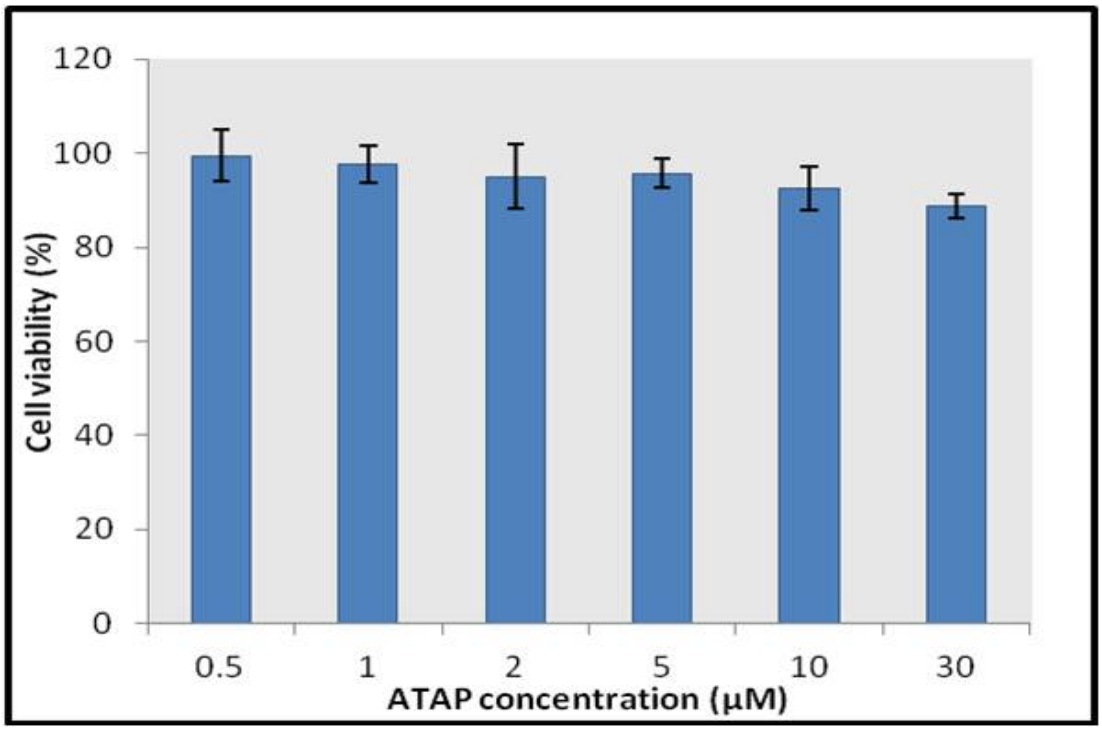

Figure 2.21: The U87vIII cells were incubated with increasing concentrations of ATAP (in DMSO) for 6-8 h and were washed with fresh growth medium after incubation to remove excess ATAP. The viability of the cells was assessed using the MTS proliferation assay 48 h following intial transfection. The final concentration of DMSO (0.01%) was kept constant in all the wells .

We next tested the apoptosis-inducing ability of MCNP-ATAP constructs in U87vIII cells by delivering varying concentrations of MCNP-ATAP constructs to cells using magnetically-facilitated delivery. From Figure 2.22, it can be seen that 30 min exposure to an alternating magnetic field is enough to induce sufficient uptake of dye-labeled MCNP-ATAP constructs. Further increases in the exposure time did not lead to significant changes in the uptake of nanoparticles.

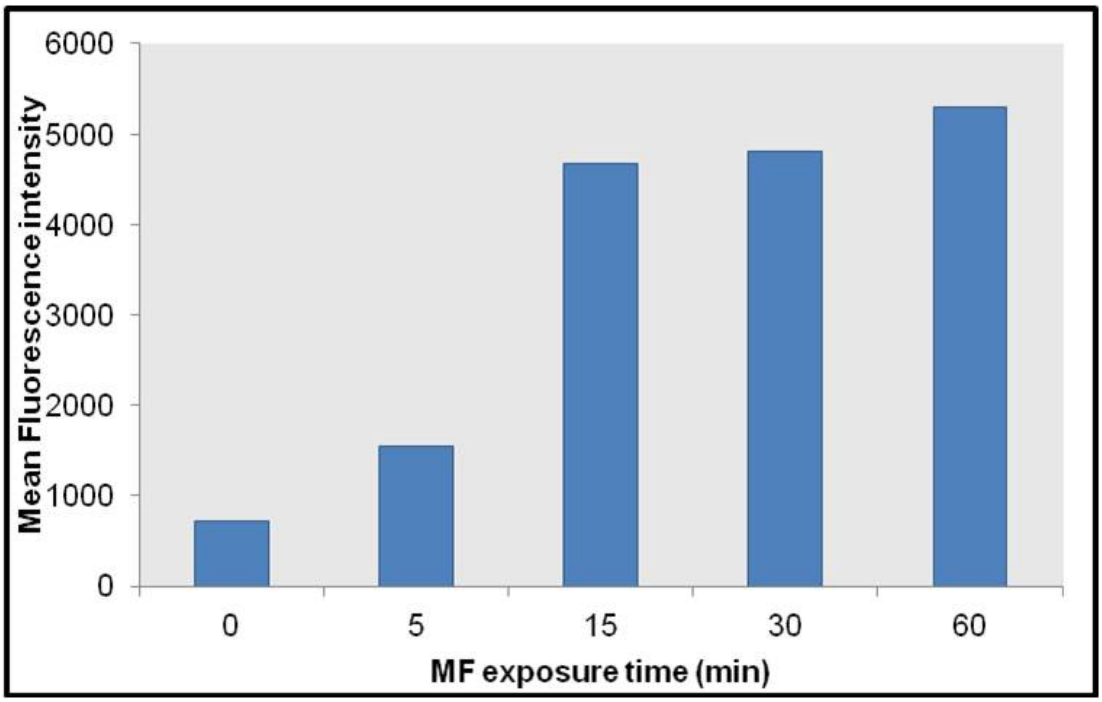

Figure 2.22: The MCNPs were coated with PEI first and then labeled with Alexa-Fluor 594. The U87vIII were incubated with 10 ug/mL MCNPs and exposed to a static magnetic field for increasing periods of time (15-60 min). Following this, the cells were washed with cold PBS and replaced with fresh growth medium. The uptake of MCNPs was measured using fluorescence microscopy.

The viability of the treated cells was then determined using the MTS assay 48 hours post transfection. As can be seem from Figure 2.23, increasing concentrations of MCNP-ATAP constructs led to a significant increase in cell death, as compared to unconjugated ATAP, thus indicating that the potency of ATAP is greatly enhanced when conjugated to MCNPs, possibly due to increase in its aqueous solubility in the presence of PEG molecules.

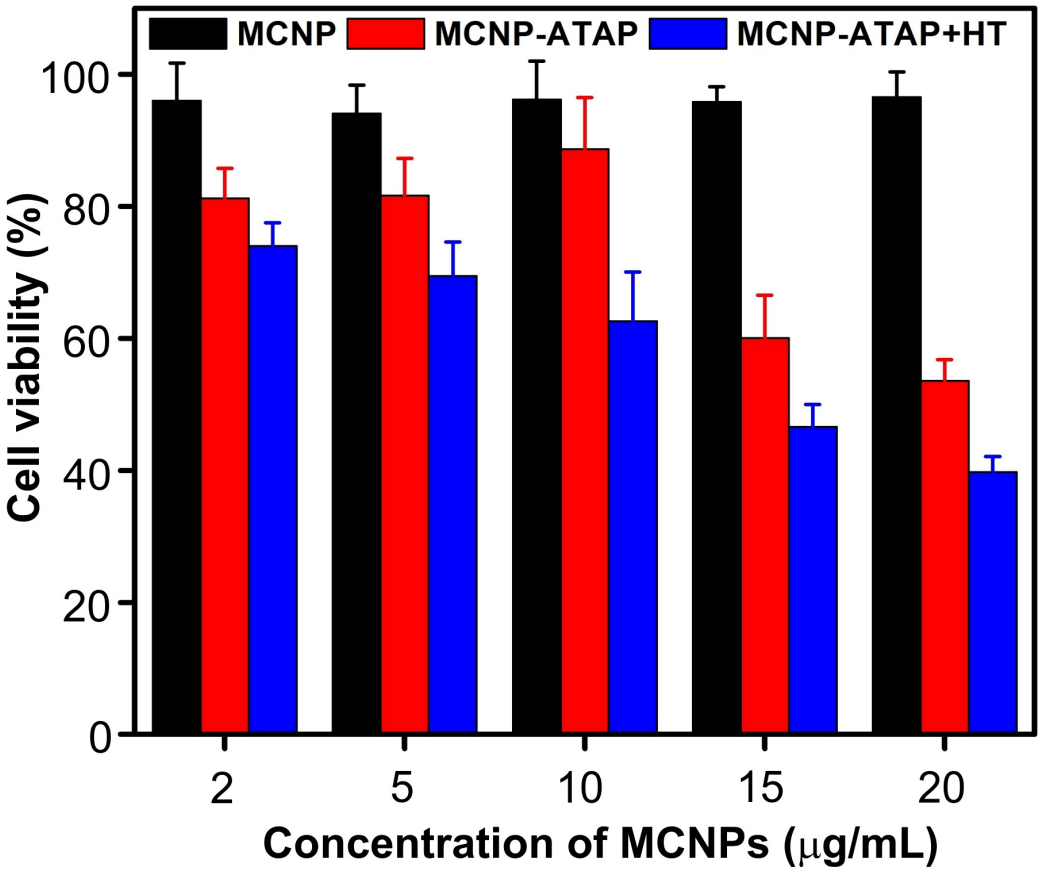

Figure 2.23: Cell viability of U87vIII cells treated with MCNP-ATAP constructs in the presence and absence of hyperthermia, determined 48 h post transfection using MTS-based cell viability assay.

Induction of apoptosis in cancer cells using combined MCNP-mediated ATAP delivery and hyperthermia

As mentioned earlier, our MCNPs could induce localized hyperthermia in the presence of an AMF, which has been shown to further enhance the pro-apoptotic ability of peptides and other therapeutics by directly activating the pro-apoptotic, while inhibiting anti-apoptotic Bcl-2 family members [195, 200] as well as increase the permeabilization of the mitochondrial membrane [201]. Hence, we evaluated the combined effect of MCNP-mediated hyperthermia and ATAP delivery on cancer cell viability. Before testing the combined therapy, we optimized the duration of hyperthermia by ex-posing the cells transfected with MCNPs to either 15, 30, 45 and 60 min of hyperthermia, and found that 45 min of hyperthermia was optimal enough to induce cell death. Thereafter

we tested the combined therapy, by incubating the U87vIII cells with MCNP-ATAP constructs and inducing hyperthermia 24 h post transfection. The cell viability following the combined therapy was determined using an MTS cell viability assay, 48h post transfection. From Figure 2.23, it can be seen that the combined therapy of MCNP-ATAP and hyperthermia caused significant cell death, as compared to either treatment alone.

Effect of combined hyperthermia and MCNP-ATAP therapy on mitochondrial function in cancer cells

In order to confirm that the apoptotic effect of MCNP-ATAP constructs was caused as a result of mitochondrial dysfunction, we investigated the loss of mitochondrial membrane potential ($\Delta\psi$m), which occurs as a result of mitochondrial dysfunction and is regarded as a hallmark for apoptosis, using a flow-cytometry based JC-1 assay [183]. From Figure 2.24, it can be seen that there is no obvious change in the mitochondrial membrane potential in the U87 cells treated with MCNPs alone, as is evident from the formation of red J-aggregates (96.0%) with minimal green fluorescence (2.6%). However, when the U87 cells are treated with MCNP-ATAP, there is a dramatic increase in the green fluorescence (JC-1 monomer in the cytoplasm, 25.7%), coupled with a decrease in red fluorescence (normal mitochondria, 67.0%). This suggests that the MCNP-mediated delivery of ATAP resulted in mitochondrial dysfunction and eventually apoptosis. Furthermore, when hyperthermia is induced in cells treated with MCNP-ATAP, it causes even higher increase in the green fluorescence (38.1%; as compared to 25.7% seen with MCNP-ATAP), thus suggesting the additive effect of hyperthermia (HT) on the mitochondrial-regulated apoptosis caused by ATAP.

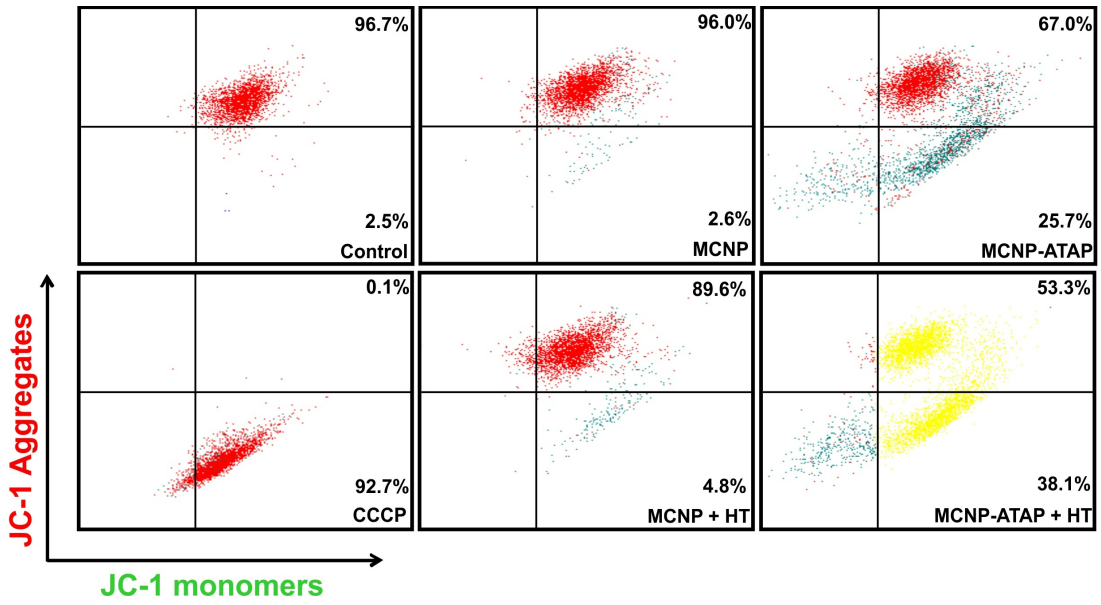

Figure 2.24: Flow cytometry-based JC-1 assay as a measure of mitochondrial depolarization induced by MCNP-ATAP constructs. The top right quadrant indicates normal mitochondria (healthy cells, red fluorescence); whereas the bottom right quadrant indicates depolarized mitochondria (apoptotic cells, green fluorescence).

To further quantify the ATAP-induced mitochondria-dependent apoptosis of U87 cells, we conducted a flow cytometry-based Annexin V-FITC/PI assay (Figure 2.25). It can be seen that the combined treatment of MCNP-mediated ATAP and hyperthermia (MCNP-ATAP+HT) showed the highest percentage of apoptotic cells (38.3%), as compared to the individual treatments, MCNP-ATAP only and MCNP-induced hyperthermia.

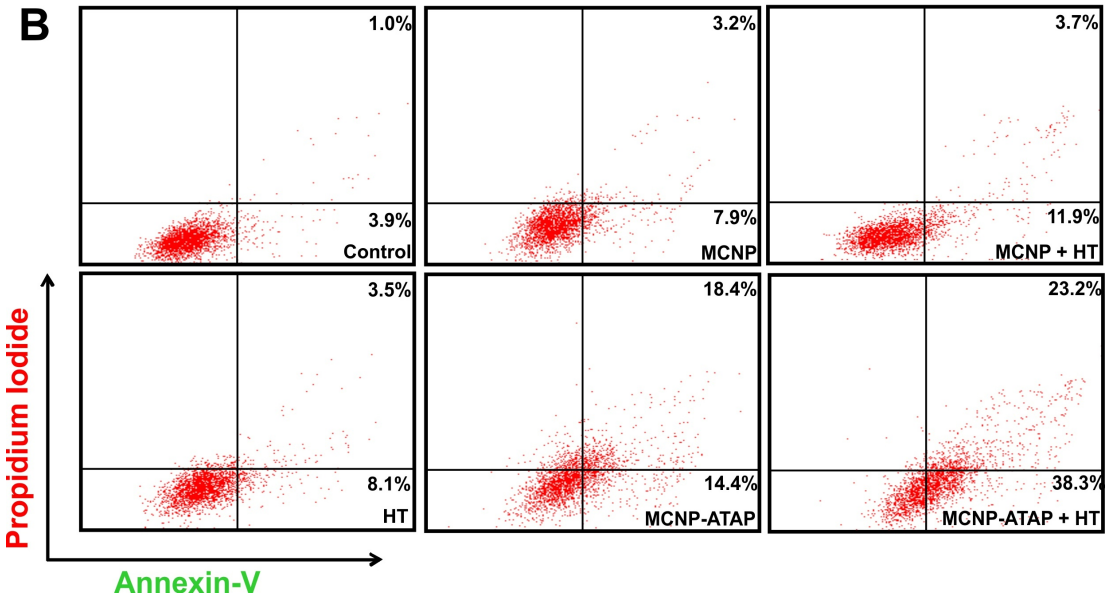

Figure 2.25: Flow cytometry-based Annexin-V-FITC/PI assay indicating percentage of early and late apoptotic cells in case of each treatment. The bottom right quadrant indicates early apoptotic cells (Annexin-V +/PI-); whereas the top right quadrant indicates late apoptotic cells (Annexin-V +/ PI +)

Conclusions

Taken together, our MCNP-based combined approach of delivering a mitochondrial targeting peptide, ATAP as well as inducing localized hyperthermia can lead to significant apoptosis in glioblastoma cells, as a result of their synergistic effect on mitochondrial dysfunction. By modifying these MCNPs with PEG molecules and targeting ligands such as iRGD, we were able to overcome the issues hampering the obvious benefits of ATAP as a cancer therapeutic, namely poor aqueous solubility and lack of tumor homing capacity. Our MCNPs, not only provided a platform for tethering different biomolecules on their surface, but also imparted active functionalities (i.e. hyperthermia and magnetically-facilitated delivery) owing to their unique composition. Additionally, our nanoparticle platform can also afford non-invasive imaging capabilities, such as MRI (due to the mag-netic core) and dark-field imaging (due to gold shell). Such orthogonal imaging capabilities can allow for non-invasive tracking of the MCNPs within either cancer and stem cells and hence afford different kinds of information owing to their complementary nature.

2.2.3 Materials and Methods

Starting materials, reagents, and solvents were purchased from commercial suppliers (Sigma-Aldrich, Acros, and Fisher) and used as received unless otherwise noted. All reactions were conducted in flame-dried glassware with magnetic stirring under an atmosphere of dry nitrogen

Synthesis of Zn-doped iron oxide nanoparticles

In a typical experiment for synthesis of the nanoparticles, 300 mg $ZnCl_2$, 400 mg $FeCl_2$ and 3.5 g $Fe(acac)_3$ were mixed in 50 mL of tri-octylamine. To this, 1.2 mL oleic acid was added and refluxed at 300 degrees for an hour in a 250 mL three necked round bottom flask. After one hour, the reaction mixture was cooled down to room temperature and the magnetic nanoparticles were precipitated using ethanol. They were purified by repeated centrifugation and sonication. The as obtained nanoparticles were then dried overnight under vacuum.

Synthesis of Au coated magnetic nanoparticles

In a typical coating experiment, 2.5 mg zinc doped iron oxide nanoparticles in chloroform were added to 10 mL tri-n-octylamine and heated in order to evaporate the chloroform. After the solution, cooled down to room temperature, 15 μL of gold stock solution (5 mg $HAuCl_4$ in 300 μL ethyl acetate) was added slowly dropwise to the reaction vial followed by 0.306 μL of 1-dodecanethiol. The reaction mixture was heated to 150 °C and kept at this temperature for 4 h. The Au coated nanoparticles were precipitated using ethanol. They were purified by repeated centrifugation and sonication. The core shell nanoparticles were dried under vacuum overnight.

Synthesis of water soluble core shell nanoparticles

For converting the hydrophobic core shell nanoparticles into hydrophilic ones, a ligand exchange reaction was carried out by sonicating the hydrophobic MCNPs in the presence of trisodium citrate and TMAOH. In a typical experiment, the particles were suspended

in a minimal amount of chloroform and added to 5mL of 1M TMAOH containing 0.06g of trisodium citrate. A few drops of acid were added to ensure slightly acidic conditions. The resulting suspension was sonicated on a probe type sonicator for 30 minutes. The resulting solution was purified by multiple rounds of magnetic decantation.

Formation of MCNP-ATAP complexes

To obtain PEI coated MNPs, the water soluble MNPs from above were first diluted with DPBS to reach a final concentration of 0.1 mg/mL. Afterwards, excess 10 kDa branched PEI (Sigma Aldrich) was added drop wise (1 mg/mL). After spinning overnight, the PEI coated MNPs were filtered a using centrifugal filter unit (EMD Millipore, 10,000 MW).

Particle size and Zeta potential analysis

Dynamic light scattering (DLS) and Zeta Potential analyses were performed using a Malvern Instruments Zetasizer Nano ZS-90 instrument (Southboro, MA) with reproducibility being verified by collection and comparison of sequential measurements. Nanoparticle/siRNA complexes (siRNA concentration = 330 nM), were prepared using purified water (resistivity = 18.5 MΩ-cm). DLS measurements were performed at a 90° scattering angle at 25°C. Z-average sizes of three sequential measurements were collected and analyzed. Zeta potential measurements were collected at 25°C, and the Z-average potentials following three sequential measurements were collected and analyzed.

Cell culture

U87-EGFRvIII cells were cultured in the DMEM (Dulbeccos modified Eagles medium) with high glucose (Invitrogen), 10% Fetal Bovine Serum (FBS), 1% streptomycin-penicillin, 1% glutamax (Invitrogen), and hygromycin B (30 μg/ml). MCF-7 cells were cultured in DMEM/F-12 with 10% Fetal Bovine Serum (FBS), 1% streptomycin-penicillin, and 1% glutamax (Invitrogen).

Magnetically-facilitated delivery of MCNPs

24 h before the magnetically-facilitated delivery of MCNPs, 2 X 10^5 cells in a volume of 500 uL were seeded into each well of a 24-well plate, so as to attain 80-90% confluency at the time of transfection. For the transfection of MCNP-ATAP constructs, the varying amounts of MCNP-ATAP constructs were gently mixed with OptiMEM and then were added to each well to obtain the desired MCNP-ATAP concentration per well. Subsequently, the cell culture plates were placed on the Nd-Fe-B magnetic plates (OZ Biosciences, France) for 15 mins. Following this, the cells were transferred back to the incubator and the media was replaced with growth medium after 1-2 h of additional incubation

Cell viability assays

The percentage of viable cells was determined by MTS assay following standard protocols described by the manufacturer. All experiments were conducted in triplicate and averaged. 48h after initial transfection, the cells were incubated with MTS for 1-1.5 h. The data is represented as formazan absorbance at 490 nm, considering the control (untreated) cells as 100% viable.

Targeted delivery

High integrin expressing U87-EGFRvIII and low integrin expressing MCF-7 cells were cultured in 24- well plates, at a density of 5 x 10^4 cells per well. For the delivery of iRGD-modified MCNP-ATAP complexes, media was exchanged with serum free DMEM media. The cells were incubated in the iRGD-modified MCNP-ATAP complexes for 6-8 h. Fluorescence images were taken after replacing the serum-free media with regular media.

Magnetic Hyperthermia

24 h after seeding cells as described above, varying concentrations (5-20 μg/mL) of MCNP-ATAP constructs were prepared in OptiMEM (Life Technologies) and added to

each well. Subsequently, the cell culture plates were exposed to magnetofection for 15 minutes as described above. The culture plates were placed back into the incubator for 1 hour and afterwards, the cells were washed with DPBS and the transfection medium was replaced with fresh growth medium. 24 h after transfection, cells were washed with DPBS, trypsinized, and exposed to an alternating magnetic field (5 kA/m, 300 kHz) for the desired amount of time. Thereafter, fresh media was added to the treated cells and the cells were plated back into 12-well plates.

Measurement of mitochondrial membrane potential

Mitochondrial stability was assessed by fluorescence microscopy after incubation with 5,59,6,69-tetrachloro-1,19,3,39-tetraethylbenzimidoazolylcarbocyanino iodide (JC-1) as per manufacturer's recommended protocol. Briefly, the cells were analyzed using flow cytometry-based JC-1 assay 48h after initial transfection. The cells were trypsinized, resuspended in warm DPBS and incubated with JC-1 (2μM) for 15-30 mins at 37°Cand 5% CO2. Thereafter the cells were centrifuged, resuspended in 500 uL PBS and analysed immediately on a flow cytometer (GalliosTM, Beckman Coulter, Inc.) with 488 nm excitation using emission filters appropriate for Alexa Fluor 488 dye (520 nm) and R-phycoerthyrin (590 nm). Standard compensation was performed using the carbonyl cyanide 3-chlorophenylhydrazone (CCCP)-treated cells as positive control. Untreated cells (no MCNP and no ATAP) were used as negative controls.

Apoptosis assay

To assay apoptosis using Annexin V-FLUOS and Propidium Iodide staining (Roche), 48 hours after initial transfection, 10^6 cells were prepared in 1 mL of PBS with 10% FBS in each test tube. After centrifugation, cells were resuspended in 100 μL Annexin V Binding Buffer (ice-cold) and Annexin V-FLUOS and Propidium Iodide (PI) were added following the manufacturers recommendation. Samples were incubated in the dark for 15 minutes at room temperature. Finally, 400 μL of additional ice-cold Annexin V Binding Buffer was added and the samples were kept on ice, under foil until analysis using flow cytometry (GalliosTM, Beckman Coulter, Inc). Early apoptotic cells with

exposed phosphatidylserine but intact cell membranes bound to Annexin V-FITC but excluded propidium iodide. Cells in necrotic or late apoptotic stages were labeled with both Annexin V-FITC and propidium iodide.

Chapter 3

Simultaneous delivery of small molecules and siRNA using cyclodextrin-tethered polyamines for cancer therapy

In previous chapter, we developed novel nanomaterial-based advanced molecular imaging and diagnostic probes for imaging of cancer and stem cells. In this chapter we will see the application of nanotechnology for the purpose of drug delivery and in particular, for the delivery of multiple anticancer therapeutics and siRNA into brain cancer cells. We will then see the synergistic effects of different drugs on increasing the apoptosis of brain cancer cells by the down regulation of key oncogenic signaling pathways. Finally, we will review the emerging impact of novel nanomaterials in cancer biology and how they can circumvent the current issues in cancer treatment from a clinical viewpoint.

3.1 Synergistic Induction of Apoptosis in Brain Cancer cells by Targeted Co-delivery of siRNA and Anticancer Drugs

3.1.1 Introduction

Advances in the field of chemical genetics and molecular cell biology have triggered a surge in development of genetic manipulation based therapies for cancer [202]. Such genetic manipulation methods typically rely on either the traditional small molecule/ protein modalities [203] or the newly discovered RNA interference (RNAi) based modalities [31], each having their own advantages and disadvantages. For example, RNAi therapeutics can provide attractive solutions to the major shortcomings of the conventional therapeutics, including difficulty in lead identification and complex synthesis of small organic molecules and proteins, and potentially can be applicable to all molecular targets for cancer therapy [204]. However, RNAi-based therapeutics, such as small interfering RNA (siRNA) and micro RNA (miRNA), are inherently antagonistic and their downstream effects (i.e., gene silencing) are delayed, compared to those of conventional small molecule/ protein-based therapeutics [205]. Additionally, owing to their short serum half-life and poor cellular uptake, successful clinical application of siRNA requires appropriate chemical modifications and better delivery vehicles to overcome the numerous cellular barriers [31]. On the other hand, small organic molecules can act as both antagonists and agonists for molecular targets and their drug effects can be much faster than siRNA with minimal problems during their intracellular uptake [204]. Hence, from a biological perspective, it would be beneficial to combine the advantages of these therapeutic modalities to potentially enhance their individual efficacy. For example, it was recently demonstrated that simultaneous delivery of siRNA against multidrug resistance genes in cancer cells led to the enhanced efficacy of the codelivered anticancer drugs [20, 206] These studies demonstrate that it would be desirable to target multiple oncogenic signaling elements using different therapeutic modalities for cooperative effect, especially considering the molecular heterogeneity of tumors.

In this section we describe the use of organic dendrimer-based platforms for the co-delivery of siRNA and small molecule drugs in order to elicit a synergistic effect

on inhibiting the proliferation of brain tumor cells (Figure 3.1). This work has been already publisehd in Molecular Pharmaceutics [176].

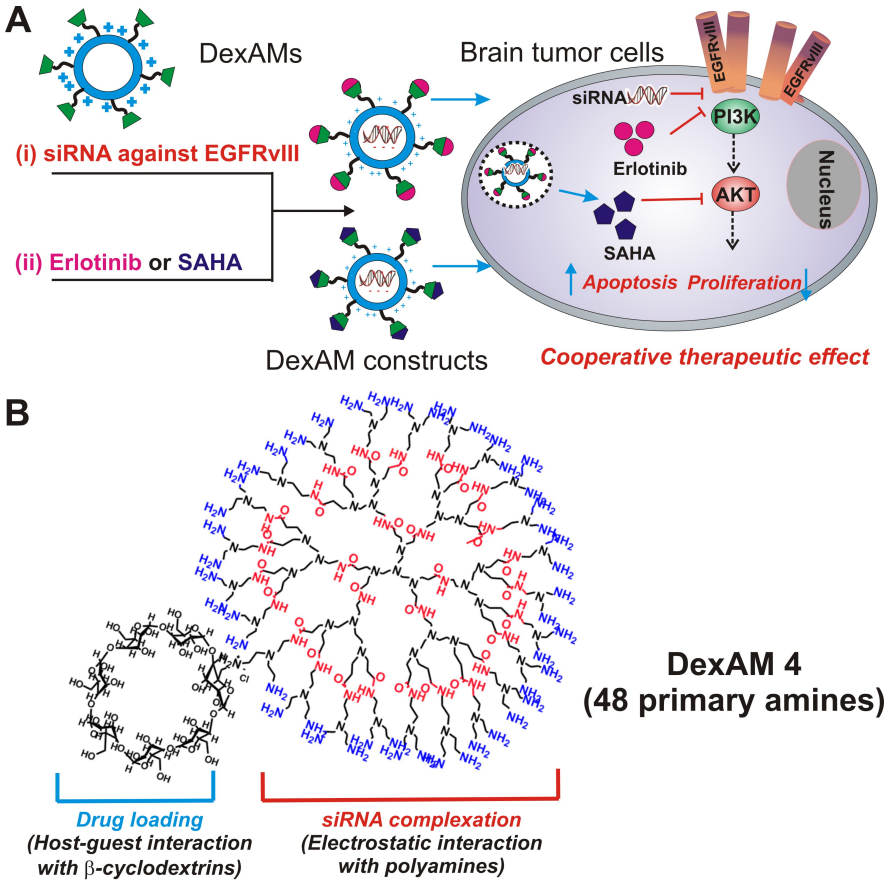

Figure 3.1: Schematic diagram showing the application of DexAM for co-delivery of drugs and siRNA to brain tumor cells. (A) DexAM molecule is complexed with siRNA via electrostatic interactions with the polyamine backbone and the small molecule via encapsulation within the β-cyclodextrin and delivered to brain cancer cells. (B) Chemical structure of the delivery vehicle. Reprinted from Ref. [176]. Copyright 2011 American Chemical Society.

In the past, dendrimers have been utilized to carry a variety of small molecule pharmaceuticals and nucleic acids (DNA, siRNA and miRNA) to several tumor cells. However, most of the dendrimer-based drug carriers are known to be extremely cytotoxic to cells. Hence, in order to address the aforementioned need for non-cytotoxic cooperative chemotherapeutics, herein we describe the synthesis of a multifunctional delivery platform consisting of a dendritic polyamine backbone conjugated with β-cyclodextrin (β-CD) moieties [henceforth referred to as DexAMs] and its application

for target-specific co-delivery of two orthogonal chemotherapeutic molecules (siRNA and anti-cancer drug). We hypothesize that co-delivery of siRNA and anticancer drugs will have a cooperative therapeutic effect against the target oncogenic signaling pathway (EGFRvIII-PI3K/AKT), resulting in the selective induction of apoptosis in brain tumor cells (Figure 3.1). Additionally, conjugation of targeting ligands against receptors overexpressed in brain cancer cells (EGFR), would allow for selective uptake of our complexes into glioblastoma cells, thereby minimizing toxic side effects on normal cells.

3.1.2 Results and Discussion

In order to achieve the dual delivery of these molecules, the delivery platform (termed DexAM) consists of a dendritic polyamine linked with β-cyclodextrins (β-CD). In this way, the positively-charged polyamine backbone was used to complex the negatively-charged siRNA molecules, while the β-CD increased the solubility of the hydrophobic small molecule by encapsulation in the inner cavity. As a proof-of-concept, we first assessed the efficiency of RNAi by examining the suppression of green fluorescent protein (GFP) in brain tumor cells that were genetically modified to express GFP. Based on the GFP knockdown studies, we then used the optimized conditions to simultaneously deliver the siRNA against the EGFRvIII oncogene in combination with specific anti-cancer drugs (affecting different signaling pathways) to achieve a synergistic inhibition of tumor cell proliferation. By maintaining minimal cytotoxicity with high delivery efficiency of multiple molecules of interest, our study provides a reliable methodology to enhance the efficacy of traditional chemotherapeutic agents.

DexAM: structure and synthesis

In our study, we developed a synthetic methodology to generate a series of highly water soluble dendritic polyamine compounds conjugated to β-cyclodextrin (β-CD) molecules. The DexAM molecule was synthesized using multistep solution-phase and solid-phase synthesis, we generated a series of highly water-soluble dendritic polyamine compounds conjugated to one or more β-cyclodextrin (β-CD), referred to as DexAMs, with higher yield and purity as compared to reported syntheses (Figure 3.2a).

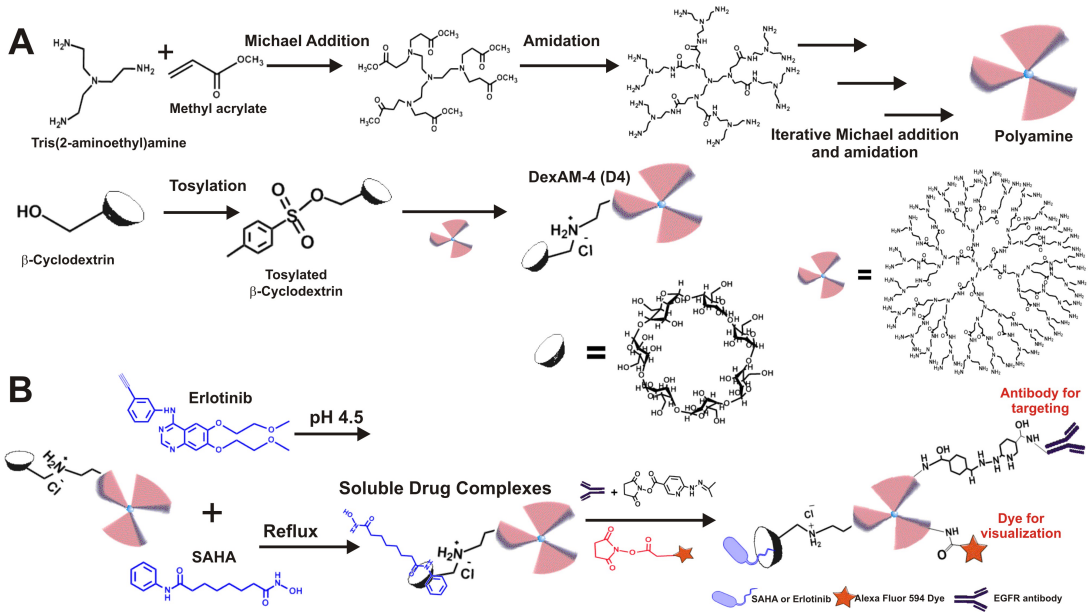

Figure 3.2: General Scheme for the synthesis of DexAM. The polyamine backbone is initially synthesized by the iterative Michael addition of tris(2-aminoethyl)amine and methyl acrylate, followed by amidation. Tosylated β-cyclodextrin is then used to form the final DexAM molecule. (B) Inclusion of drugs (Erlotinib and SAHA) and conjugation of antibodies to DexAMs. Reprinted from Ref. [176]. Copyright 2011 American Chemical Society.

The first step for synthesizing DexAM involved generating a dendritic polyamine backbone by Michael addition of tris(2-aminoethyl) amine and methyl acrylate, followed by amidation of the amino esters generated after Michael addition. The use of tris(2-amino ethyl) amine as the core initiator yielded higher surface amine groups and hence more compact dendrimers as compared to the reported synthetic methods (for e.g. ethylenediamine, ammonia) for PAMAM dendrimers [115]. The conjugation of β-cyclodextrin to the polyamine backbone involved tosylation of β-cyclodextrin, followed by nucleophilic addition with amine group. Compared to the previously reported protocol [207], where tosyl chloride was used for regioselective tosylation of β-cyclodextrin resulting in very low yields, we improved the synthetic yield ($\sim$ 50%) and purity by using tosyl-imidazole, instead of tosyl chloride, under reflux conditions to generate 6-mono-tosylated β-cyclodextrin. In the final step, polyamine backbone was conjugated to tosylated-CD via nucleophilic addition to generate cyclodextrin conjugated polyamines resulting in a 25-fold increase in the aqueous solubility of CD (>50 g/100

mL) as compared to that of CD alone (<1.8 g/100 mL), owing to generation of an aminium salt.

Inclusion of anticancer drugs into DexAM

The first component of our delivery vehicle - β-CD - has been extensively used in pharmaceutical applications to improve solubility of hydrophobic moieties, such as anticancer drugs [208]. Many anticancer drugs are known to have poor aqueous solubility, thereby necessitating the use of toxic organic solvents like dimethylsulfoxide (DMSO), which can be detrimental in biological applications [209]. The presence of β-CD in our DexAM moiety and the optimized drug loading would not only prevent the use of such toxic solvents but also improve the water-solubility of CD- drug complex for the optimal cellular uptake and drug efficacy. In our study, two hydrophobic anticancer drugs [Erlotinib and suberoylanilide hydroxamic acid (SAHA)] were synthesized and loaded into the β-CD cavity by using our optimized protocols (Figure 3.2b) [210, 211]. These drugs have already shown some promising results for GBM therapy, but have met with limited success since they require higher doses and longer exposures, which may lead to increased toxic side-effects. By utilizing the pH-dependent solubility of erlotinib, we could load drug up to almost 50% of the molar ratio of β-CD, resulting in a significant increase in its aqueous solubility (178 mg/100 mL) [212,213]. Similarly, we complexed SAHA with β-CD under reflux conditions to obtain highly water-soluble SAHA-CD complexes (solubility $\sim$175 mg/100 mL) [214].

siRNA complexation efficiency of DexAM

The second component of our DexAMs - dendritic polyamine backbone provides a positive surface charge which can interact electrostatically with the negatively charged nucleic acids, condensing them into cationic complexes (known as polyplexes), thus facilitating their intracellular uptake and endosomal escape [113]. However, these primary/tertiary amines are also responsible for cytotoxicity by interacting with the cellular components and interfering in the cellular processes [215]. Our synthetic methods enabled us to precisely control the number of primary amine head groups from 4 to 48

leading to four different generations of DexAMs molecules (D1-D4), thereby allowing us to achieve an optimal balance between cytotoxicity and complexation ability. We assessed the capability of our four different generations of DexAMs (D1-D4) to spontaneously form complexes with the negatively charged siRNA using a well-established dye exclusion assay (Picogreen Assay, Molecular Probes, Invitrogen). As the number of amine groups increased from DexAM-1 (D1, 4 primary amines) to DexAM-4 (D4, 48 primary amines), the amount of free/unbound siRNA decreased correspondingly at a given DexAM concentration (Figure 3.3).

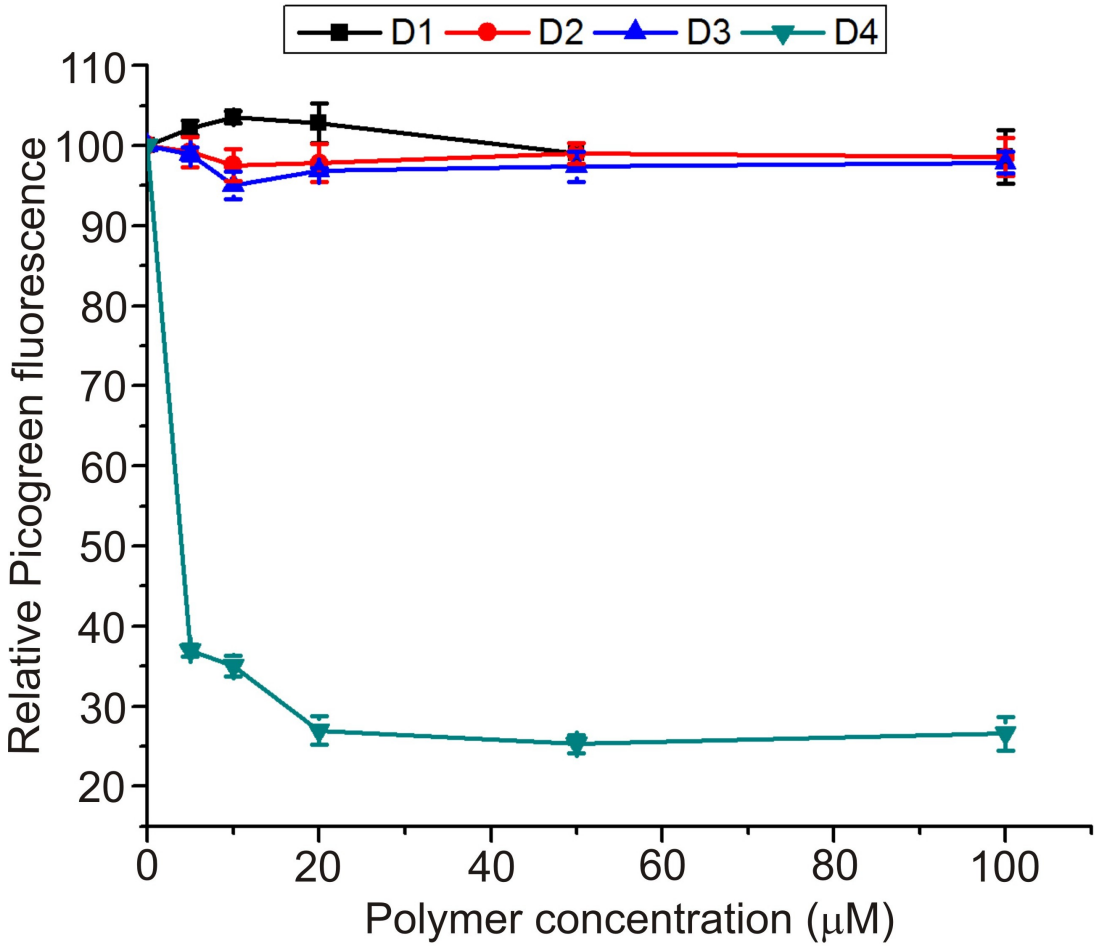

Figure 3.3: siRNA complexation efficiency of different DexAMs measured by Picogreen dye exclusion assay (Absorption = 480 nm, Emission = 520 nm). Reprinted from Ref. [176]. Copyright 2011 American Chemical Society.

Since we found that the complexation ability of DexAM-4 is higher than that of the other generations with minimal cytotoxicity, we proceeded with using DexAM-4 for the

subsequent experiments. Additionally, the hydrodynamic diameters of the resultant polyplexes could be controlled from 250 to 400 nm with polydispersity index of 0.8-1.0 by increasing the polymer concentration (Figure 3.4a). The zeta potentials of the resulting polyplexes were in the range of 8-10 mV at pH 7.4 (Figure 3.4b), demonstrating the cationic nature of the polyplexes.

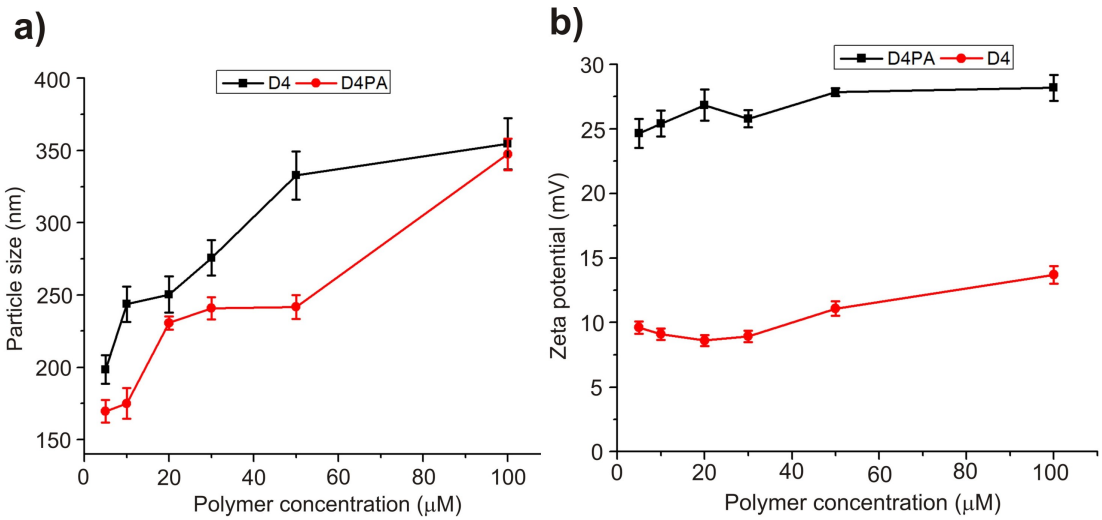

Figure 3.4: Comparison of particle diameters (a) and zeta potentials (b) of polyamines with and without cyclodextrins. The results are an average of three independent experiments and their respective standard errors. Reprinted from Ref. [176]. Copyright 2011 American Chemical Society.

GFP knockdown efficiency of DexAM

The optimization of gene silencing with our DexAM construct and assessment of knockdown efficiency was first performed by measuring the suppression of green florescent protein (GFP) in U87 brain cancer cells, which were genetically modified to constitutively express GFP (U87-EGFP). Varying concentrations of the DexAM molecule was mixed with a given amount of GFP siRNA (100 pmol) to form the DexAM-siRNA complexes.The decrease of green fluorescence intensity due to siRNA-mediated EGFP silencing was monitored over a time-period of 48-96h to quantify the knockdown efficiency of our DexAM/siRNA constructs.

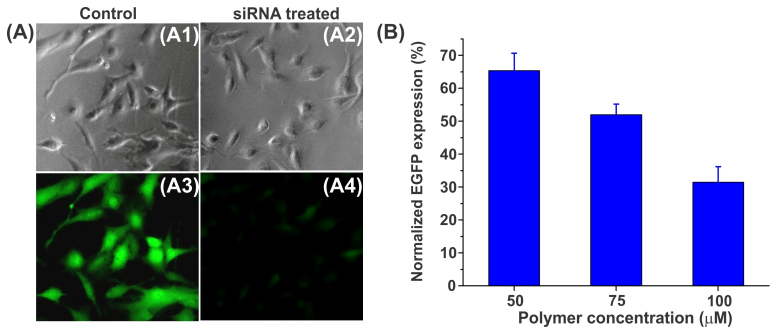

Figure 3.5: Delivery of DexAM-siRNA for GFP knockdown in U87-EGFP cells. (A) Phase contrast (A1, A2) and fluorescent (A3, A4) images showing siRNA-mediated decrease in green fluorescence in treated and control (untreated) U87-EGFP cells. (B) Quantitative comparison of the percentage of GFP knockdown in U87-EGFP cells with varying concentrations of DexAM at 3 d. The results are expressed as mean of three independent experiments (n=3). Reprinted from Ref. [176]. Copyright 2011 American Chemical Society.

Approximately, 70% of the U87-EGFP cells showed no EGFP signal after 96 h of siRNA treatment as compared to the control cells at a polymer concentration of 100 μM (Figure 3.5) with negligible cytotoxicity (∼95 % cell viability). In parallel, we compared the transfection efficiency and the corresponding cytotoxicity of our delivery platform with that of the commercially available transfection agent (Xtremegene) under the same condition, in which Xtremegenebased transfection demonstrated similar levels of EGFP knockdown (∼70 % knockdown efficiency), albeit with significant toxicity (∼30 % cell viability) (Figure 3.6).

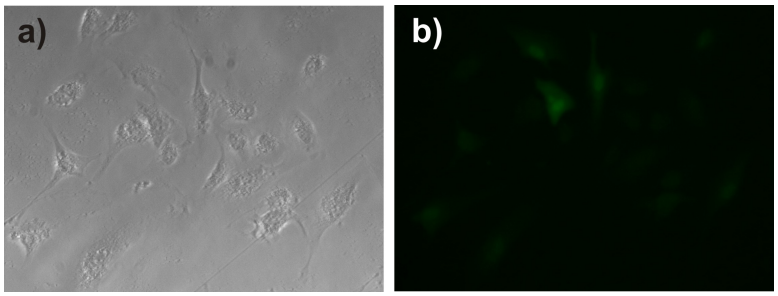

Figure 3.6: Delivery of siRNA using XtremeGene for GFP knockdown in U87-EGFP cells. Phase contrast (a) and fluorescent (b) images of siRNA-mediated EGFP gene silencing using Xtremegene. U87-EGFP cells were incubated with Xtremegene-siRNA polyplexes for 12h and analyzed 96h post transfection using fluorescence microscopy. The polyplexes were formed at a ratio of 1:2 of siRNA to Xtremegene in serum-free media. Reprinted from Ref. [176]. Copyright 2011 American Chemical Society.

DexAM is non-cytotoxic and biocompatible

While we achieved a remarkable knockdown efficiency with the DexAM-siRNA constructs, maintaining high cellular viability was equally important. Cytotoxicity of the DexAM molecules was assessed using MTS assay. First we confirmed the effect of β-CD moiety on cytotoxicity of DexAMs by comparing the cytotoxicity of the DexAM (containing CD) to that of the DexAM without CD. Our cytotoxicity assay data clearly shows that the DexAM constructs with CD show significantly less cytotoxicity as compared to those without CD (Figure 3.7a). We believe this is due to the presence of CDs on a polycationic backbone in DexAM, which can potentially reduce non-specific binding of the DexAM constructs with proteins or cellular structures [215–217]. We also compared the cytotoxicity of our DexAMs with the commercially available transfection agents, Polyethyleneimine (PEI), Lipofectamine 2000 (LF) and Xtremegene (Xgene) at the recommended concentrations for transfection, and found that those agents were significantly more cytotoxic at those concentrations as compared to DexAMs (Figure 3.7b).

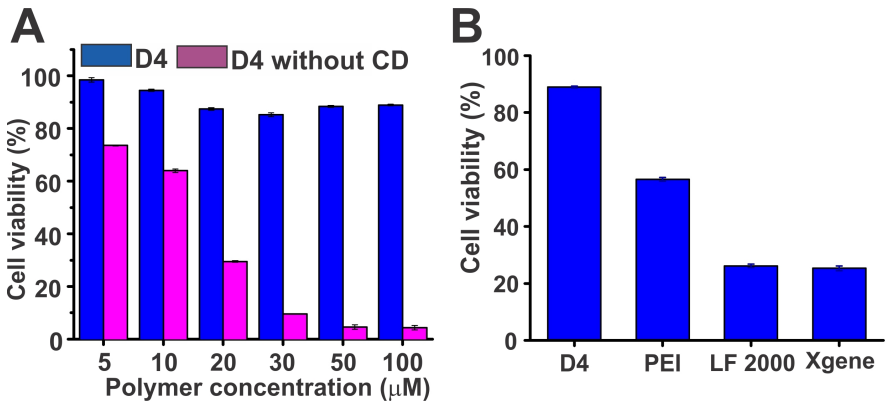

Figure 3.7: DexAM cytotoxicity in U87-EGFP cells. (A) Effect of cyclodextrin grafting on polymer-mediated toxicity. (B) Comparison of toxicities of DexAM-4 with commercially used transfection agents at optimized concentrations of delivery agent and siRNA. (LF 2000 - Lipofectamine 2000 and Xgene - Xtremegene). The percentage of viable cells was estimated using MTS assay following incubation of cells with the DexAM for 72 h. The data was obtained as absorbance of water-soluble formazan at 490 nm, following incubation with only DexAMs for 72 h. The fluorescence for treated samples was normalized to that of untreated controls. Reprinted from Ref. [176]. Copyright 2011 American Chemical Society.

Targeted delivery of siRNA using DexAM

In addition to efficient translocation of siRNA across the cell membrane with minimal cytotoxicity, successful therapeutic application of siRNA also requires the siRNA to interact with the RNAi machinery within a target cell, thereby minimizing off-target effects [218]. Brain tumor cells, particularly glioblastoma cells, are known to present high levels of epidermal growth factor receptors (EGFRs) on their cell surface, thus making it a specific biomarker for cell-specific delivery towards brain tumor cells [219]. For targeted delivery to glioblastoma cells, we modified our DexAM-4 with appropriate ratios of EGFR antibodies (DexAM-4:EGFR-Ab = 1:5) and incubated them in U87 (glioblastoma cell line, target cells) and other less-tumorigenic PC-12 cells (control cells) which tend to have low levels of expression of EGFRs. The DexAM-4 constructs were also labeled with a fluorescent dye (Alexa Fluor-594) to monitor their intracellular uptake using fluorescence microscopy. From our data we could see that EGFR-antibody modified DexAM-4 were selectively translocated into U87 (target glioblastoma cells) with high efficiency as compared to the PC-12 (control cells) (Figure 3.8).

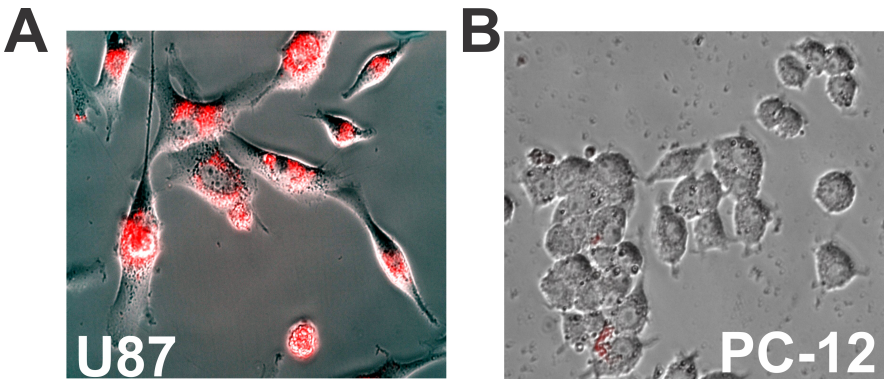

Figure 3.8: Targeted delivery of DexAMs modified with EGFR antibodies in (A) highly-tumorigenic U87-EGFP cells and (B) less-tumorigenic PC-12 cells. Reprinted from Ref. [176]. Copyright 2011 American Chemical Society.

Codelivery of anti-cancer drugs and siRNA using DexAM into glioblastoma cells

The key advantage of our delivery platform is its versatility in delivering both negatively charged nucleic acids (via complexation with the cationic polyamine backbone)

and hydrophobic small molecules (via complexation within the β-CD cavity). Having demonstrated the efficient gene silencing capability of DexAM by delivering siRNA against GFP, we focused on using our delivery vehicle for targeting key oncogenic signaling pathways (e.g. EGFRvIII-(phoshphatidylinositol-3-kinase) PI3K/AKT) to achieve a cooperative chemotherapeutic effect. Tumors harbor multiple dysregulated signaling pathways, thus limiting the clinical utility of single target agents [220]. Hence, combining approaches targeting multiple oncogenic elements, using a single delivery platform, can not only increase the likelihood of blocking tumor survival and metastasis, as compared to individual treatments, but also simplify clinical applications. For this purpose, we focused on developing a combined therapeutic approach based on siRNA and anti-cancer cancer drugs targeting oncogenic pathways in glioblastoma multiforme (GBM). We aimed at down-regulating the EGFRvIII-PI3K/AKT pathway, implicated in the proliferation and apoptosis of brain tumor cells, by delivering siRNA against epidermal growth factor receptor variant III (EGFRvIII), which is known to enhance the tumorigenicity of GBM [80, 221, 222]. However, due to tumor molecular heterogeneity, only siRNA-based down-regulation of a single oncogenic target (EGFRvIII) may not be efficacious. Histone deacetylase (HDAC) inhibitors like suberoylanilide hydroxamic acid (SAHA) and EGFR tyrosine kinase inhibitors like erlotinib have been reported to enhance the efficacy of other EGFR antagonists [220, 223].

To this end, we used either SAHA or Erlotinib for co-delivery with siRNA against EGFRvIII oncogene to deactivate the target signaling pathway in a selective and efficient manner. Our hypothesis is that combination of anti-cancer drugs against complementary therapeutic targets with siRNA therapeutics against EGFRvIII would have a cooperative effect on induction of apoptosis in brain tumor cells. To test this hypothesis, we initially compared the anti-proliferative capability of anti-cancer drugs (SAHA and Erlotinib) and siRNA against EGFRvIII in glioblastoma cells, either individually or in combination by using cell viability assay (Figure 3.9a). From the data, we could clearly observe a cooperative inhibition of glioblastoma cell proliferation when SAHA (5 μM)was co-delivered with the siRNA (200 nM; polymer concentration 100 μM), as compared to treating the cells with only SAHA at the same concentration (5 μM). This

can be attributed to the fact that SAHA is known to significantly enhance the efficacy of agents targeting EGFR signaling pathway by modulating several indirect downstream targets, which in turn are key regulators of EGFR pathways. Similarly, co-delivery of erlotinib (30 μM) and siRNA (200 nM) also inhibited tumor cell proliferation to a higher extent (Figure 3.9a).

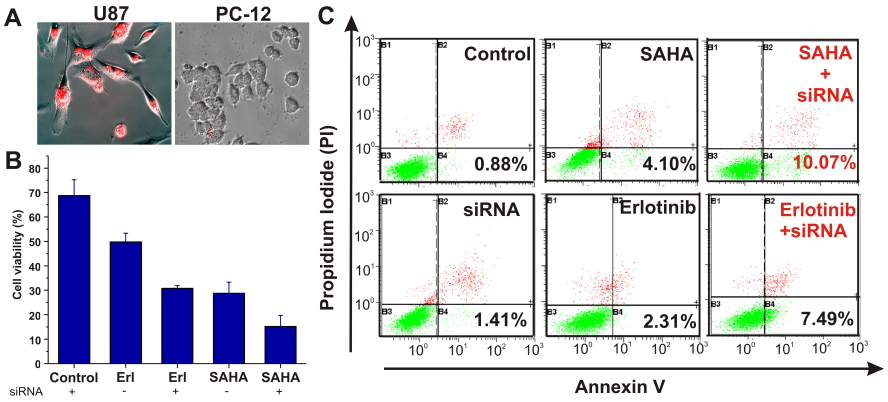

Figure 3.9: Cooperative effect of anticancer drugs and siRNA on glioblastoma cells. (A) Targeted delivery of EGFR- conjugated DexAM-4 constructs to U87 and PC-12 cells. The DexAM-4 constructs were labelled with Alexa Fluor-594 dye to enable monitoring of their uptake.(B) Viability of glioblastoma cells following individual treatments and co-delivery of drugs and siRNA, based upon MTS assay.C) Flow cytometry based Annexin-V/PI assay demonstrating the apoptotic effect of combined and individual siRNA and drug treatments. Percentages represent Annexin-V-positive (apoptotic cells). For all experiments, the polymer concentration was kept constant (100 μM), wherease the concentrations of SAHA, Erlotinib and siRNA were 5 μM, 30 μM and 200 nM respectively. Reprinted from Ref. [176]. Copyright 2011 American Chemical Society.

Additionally, we also monitored the effect of co-delivery of both siRNA and anticancer drugs on inducing cell death in glioblastoma cells using the apoptosis assay (Annexin-V/Propidium Iodide assay). Significantly higher proportion of cell population treated with both siRNA and SAHA were Annexin-V-FITC-positive as compared to the individual treatments as well as untreated cells. These results indicate greater induction of apoptosis in cells treated with both siRNA and SAHA, as compared to those with only SAHA and only siRNA treatment (Figure 3.9b). A similar trend in the cooperative induction of apoptosis was seen in case of combined erlotinib/siRNA treatment (Figure 3.9C). We also found that complexation of SAHA and erlotinib within the CD cavity improved their aqueous solubility and hence increased their potency,

measured as IC_{50} values, by approximately 2-fold as compared to its DMSO solution (Figure 3.10).

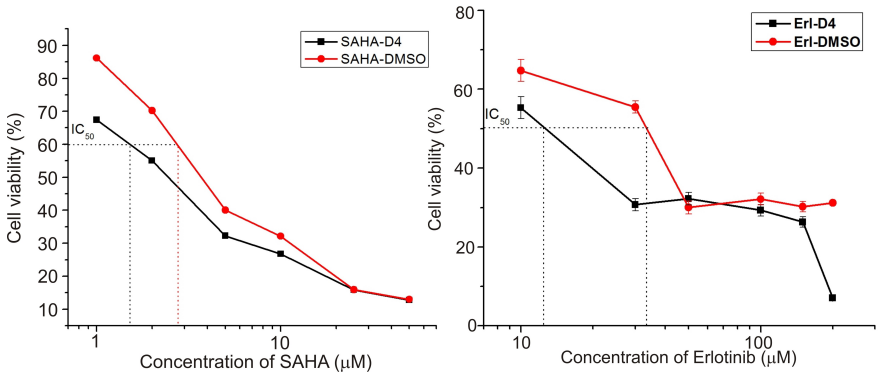

Figure 3.10: Dose response curves for Erlotinib and SAHA in U87-EGFRvIII cells. For cell viability studies, SAHA and Erlotinib were dissolved in DMSO as well as complexed within cyclodextrin moiety of DexAM-4. Cell viability is represented as the absorbance of the formazan product formed, with that of control (untreated) cells considered as 100%. The data represents mean of three independent experiments. Reprinted from Ref. [176]. Copyright 2011 American Chemical Society.

Thus, these results show the cooperative effect on selectively inducing the apoptosis of brain tumor cells by the right combination of siRNA and anti-cancer drugs and the capability of our delivery molecules (DexAMs) for target-specific delivery and improved chemotherapeutic efficacy.

3.1.3 Conclusions

Overall, introduction of exogenous nucleic acids combined with small molecules using our DexAM platform represents a powerful approach for manipulating cancer cell apoptosis. Our synthetic techniques afforded facile manipulation of the polymer structure to achieve efficient transfection with minimal polymer-mediated cytotoxicity. The strategy of co-delivering anti-cancer drug with therapeutic siRNA is particularly advantageous for *in vivo* applications, so that both the moieties are delivered to the target cells using a single delivery platform. Our versatile delivery platform can also be used to co-deliver different kinds of small molecules and nucleic acids to regulate cancer cell fate such as proliferation, migration and apoptosis by targeting multiple signaling pathways. Collectively, our DexAM-based co-delivery strategy has significant potential for

cancer therapy as well as regulating cell fate by modulating key signaling cascades. With the increasing interest in achieving precise control over delivery of anticancer drugs, our DexAM delivery system serves as a step towards bridging the gap between basic science and clinically-relevant treatment strategies. While we have demonstrated the application of our DexAM platform for the simultaneous delivery of siRNAs and hydrophobic small molecules into brain cancer cells, potentially, our approach and methodology can be extended towards introducing exogenous siRNA combined with small molecules into other mammalian cells such as stem cells to direct cellular processes like differentiation and self renewal, which in turn would be beneficial for applications such as tissue engineering and regenerative medicine.

3.1.4 Materials and Methods

β-cyclodextrin, tosylimidazole, di-tert-butyl dicarbonate, tris(aminoethyl) amine, methyl acrylate, 6,7-dimethoxyquinazolone, aniline and amberlite IRA 900 were obtained from Sigma-Aldrich and used as received unless otherwise noted. 6-hydrazinonicotinamide and 4-formylbenzamide were from SoluLinK. Other chemicals and solvents were of analytical reagent grade. All reactions were conducted in flame-dried glassware with magnetic stirring under an atmosphere of dry nitrogen. Reaction progress was monitored by analytical thin layer chromatography (TLC) using 250 m silica gel plates (Dynamic Absorbents F-254). Visualization was accomplished with UV light and potassium permanganate stain, followed by heating. Proton nuclear magnetic resonance (^{1}H NMR) spectra were recorded on either a Varian-300 instrument (300 MHz), Varian-400 instrument (400 MHz) or a Varian-500 instrument (500 MHz). Chemical shifts of the compounds are reported in ppm relative to tetramethylsilane (TMS) as the internal standard. Data are reported as follows: chemical shift, integration, multiplicity (s=singlet, d=doublet, t=triplet, q=quartet, br=broad, m=multiplet), and coupling constants (Hz).

Detailed synthesis of DexAM 1 (with 4 amines)

(Figure 3.11)

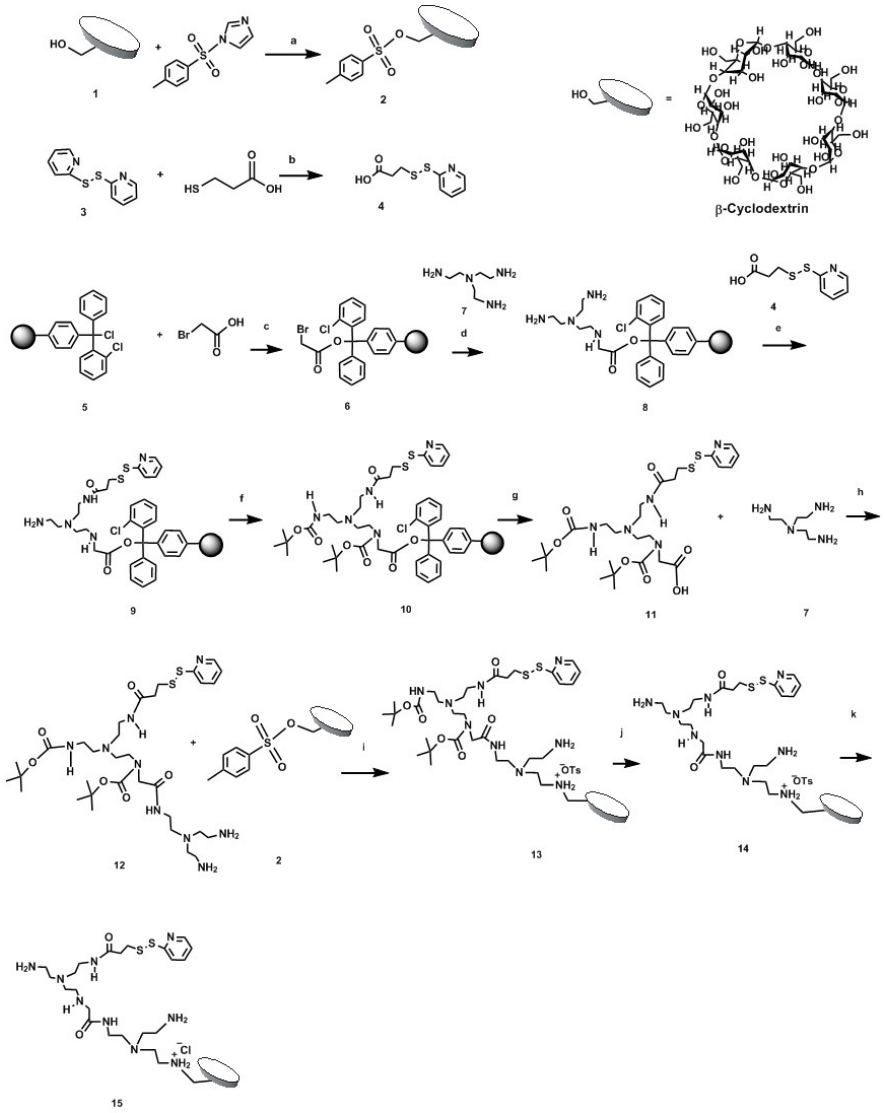

Figure 3.11: Synthesis of DexAM 1. a) ddH_2O, RT, 4 h / 1 % NaOH, 10min/NH_4Cl, b) AcOH, EtOH, RT, 12 h, c) DIEA, DCM; d) DMF, RT, 2 h, e) DCC, DMAP, DCM, 0°C, 30 min/DMF, RT, 10 h, f) Di-tert-butyl dicarbonate, DIEA, DCM, RT, 24 h, g) CF_3CH_2OH, DCM; h) DCC, DMAP, DMSO, 0°C, 30 min/RT, 24 h, i) DMF, 90°C, 48 h, j) TFA:DCM (50:50 v/v); k) Amberlite IRA 900. Reprinted from Ref. [176]. Copyright 2011 American Chemical Society.

Synthesis of mono-tosylated cyclodextrin (2)

β-cyclodextrin (6, 8.75 g, 7.71 mmol) and tosylimidazole (2.22g, 10.0 mmol) was dissolved in 88 ml deionized water. The solution was vigorously stirred for 4 h at room temperature. Aqueous NaOH solution (1% (w/v), 10.0 ml) was gradually added to the solution and stirred for an additional 10 min. The insoluble solid was filtered off and the filtrate was collected. The filtrate was neutralized to pH=7.0 using NH_4Cl to induce precipitation. The precipitate was then collected by filtration, washed with cold water (25 ml X 3) and with acetone (25 ml X 4). The solid was dried in a drying oven at 60°C under vacuum (10 mm Hg) overnight to yield 2 as a white solid (4.5 g, 51% yield). ^{1}H NMR (300 MHz, DMSO-d6), δ 7.72 (d, J=8.4 Hz, 2H), 7.41 (d, J = 8.4 Hz, 2H), 5.60-5.89 (m, 14H), 4.75-4.81 (m, 7H), 4.15-4.62 (m, 6H), 3.45-3.72 (m, 28H), 3.15-3.47 (m, 24H), 2.41 (s, 3H). MS (m/z): calculated, 1,279 for $C_{49}H_{76}O_{37}Na$; found, 1,311.5 for $[M + Na]^+$.

Synthesis of 2-pyridyl-2-carboxyethyl disulfide (4)

2,2'-Bipyridyl disulfide (3, 1 g, 4.54 mmol) was dissolved in 15 mL of ethanol (99.5%) followed by addition of 0.4 mL of glacial acetic acid. The solution was vigorously stirred and 0.24 g (2.27 mmol) of 3-mercaptopropionic acid in 5 mL of ethanol was added dropwise. The reaction mixture was stirred at room temperature for 12 h. The excess solvent was then removed under reduced pressure. The resulting oily product mixture was dissolved in 3 mL of hexane/ether (80:20, v/v %). The product was purified by column chromatography using silica gel. The pyridine-2-thione eluted as a yellow band. The desired product (4, 2-pyridyl-2-carboxyethyl disulfide) was collected, and the solvent was removed by evaporation. The residual acetic acid was removed under high vacuum. Isolated yield = 0.4 g (82.2%, based on 0.24 g of the 3-mercaptopropionic acid starting material). ^{1}H NMR (300 MHz, $CDCl_3$), δ 2.68-2.73 (t, J =7.20 Hz, 2H), 3.02-3.06 (t, J = 6.90 Hz, 2H), 7.20-7.25 (t, J = 5.0 Hz, 1H), 7.78-7.87 (t, J = 7.2 Hz, 2H), 8.39-8.41 (d, J = 4.8 Hz, 1H). MS (m/z): calculated, 207.01 for $C_8H_9NO_2Na_2$; found, 238.28 for $[M + Na]^+$.

Anchorage of the Acidic Function to the Polymeric Support

Briefly, o-chlorotrityl chloride resin (5, 5 g, 1.2 mmol of Cl/g of resin from Fisher

Chemicals) was placed in the solid-phase synthesis vessel (100mL) and 50 mL of CH_2Cl_2 was added, followed by bromoacetic acid (1.05 g, 7 mmol) and DIEA (0.95 ml, 7.5 mmol). The flask was shaken on a horizontal gyrorotatory shaker for 3 h at room temperature. The solution was filtered and the functionalized resin beads (6) were washed three times with CH_2Cl_2, iPrOH and MeOH followed by drying under a stream of nitrogen.

Reaction of the Polyamine with the Bromoacetyl Resins (8)

Tris(2-aminoethyl)amine (7, 10-fold molar excess) were dissolved in 50 mL of DMF, added to the vessel containing the functionalized resin beads (6) and shaken for 2 h. The reaction was monitored using the ninhydrin test. The product (8) was filtered, washed with CH_2Cl_2 and iPrOH (20 mL each) and then finally washed with CH_2Cl_2.

Attachment of a disulfide linker to the polyamine on the resin (9)

To a suspension of pyridyl-2-carboxyethyl disulfide (4.65 g, 3.00 mmol) inCH_2Cl_2 (15 mL), DCC (0.93 g, 4.50 mmol, 1.5 eq) and dimethylamino pyridine (36.65 mg, 0.3mmol, 0.1 eq) were added at 0°C and stirred at the same temperature for 30 min. This mixture was added to the vessel containing compound 8 and shaken for 10 h at room temperature.

Protection of the amine groups of the functionalized polyamine on the solid support (10)

Di-tert-butyl dicarbonate (5.51 mL, 24 mmol) and DIEA (4.35 mL, 25 mmol) were dissolved in CH_2Cl_2 (15 mL) and added to 9; the reaction was left overnight at room temperature under shaking. The product (10) was filtered, washed with CH_2Cl_2, iPrOH and MeOH and finally dried under a stream of nitrogen. The protection of the amine groups was confirmed using the ninhydrin test, which was found to be negative.

Synthesis of 11-(tert-butoxycarbonyl)-2,2-dimethyl-4-oxo-8-(2-(3-(pyridin-2-yldisulfanyl) propanamido)ethyl)-3-oxa-5,8,11-triazatridecan-13-oic acid (11)

The Boc-protected resin (10) was placed in a 100 mL solid phase vessel. A solution containing 25 mL of dichloromethane and 25 mL of CF_3COOH was added to it and shaken for 2 h at room temperature. The solution was filtered and the resin washed with 100 mL of CH_2Cl_2. The organic fractions were collected and the solvent

evaporated. The crude products were purified by flash chromatography on SiO_2. The fractions containing the products were identified by TLC and characterized using mass spectroscopy and NMR. TLC (CH_2Cl_2:MeOH, 90:10 v/v): R_f =0.65; ^{1}H NMR (400 MHz, DMSO-d6) δ 1.3 (s, 18H), 2.32 (m, J = 6.5 Hz, 8H), 2.66 (t, J =7 Hz, 2H), 3.46 (m, J =7 Hz, 4H), 3.74 (t, 2H), 4.3 (s, 2H), 7.10-7.20 (t, J = 5.0 Hz,1H), 7.26(t, J= 5.0 Hz, 1H), 7.60-7.68 (t, J = 7.2 Hz, 2H), 8.44-8.56 (d, J = 4.8 Hz, 1H). MS (m/z): calculated, 593.26 for $C_{26}H_{43}N_5O_7Na_2$; found, 624.77 for $[M + Na]^+$.

DCC coupling to obtain (12)

To 11 (601.8 mg, 1.00 mmol) in DMSO (10 mL), DCC (309.5 mg, 1.50 mmol, 1.5 eq) and DMAP (0.1 eq, 12.22 mg) were added at 0°C and stirred for 30 mins. Tris-(aminoethyl) amine (7) was added dropwise to the solution and stirred for 30 mins. The mixture was then allowed to stir for 24 h at room temperature. DMSO was then removed under reduced pressure. The product (12) was purified by column chromatography using silica gel. Yield: 80%; TLC ($CHCl_3$:MeOH, 90:10 v/v): R_f =0.4; ^{1}H NMR (400 MHz, DMSO-d6) δ 1.0-1.4 (m, 4H), 1.5 (s, 18H), 1.8 (m, J = 6.5 Hz, 14H), 2.00 (m, J =7 Hz, 8H), 3.5 (m, J =7 Hz, 6H), 4.0 (s, 2H), 7.10-7.20 (t, J = 5.0 Hz,1H), 7.26(t, J= 5.0 Hz, 1H), 7.60-7.68 (t, J = 7.2 Hz, 2H), 8.44-8.56 (d, J = 4.8 Hz, 1H). MS (m/z): calculated, 721.40 for $C_{32}H_{59}N_9O_6Na_2$; found, 752.99 for $[M + Na]^+$.

Synthesis of water-soluble CD polyamine (13)

Tosylated CD (2, 1.29 g, 1 mmol) and the Boc-protected polyamine (12, 730 mg, 1 mmol) were dissolved in DMF (10 mL) in a 25-mL one-necked round-bottomed flask, equipped with a Liebigs condenser and a stir bar. The flask was degassed and purged with nitrogen. The mixture was stirred and refluxed at 90°C for 48 h. The reaction mixture was cooled down to room temperature and the product was precipitated out by the addition of acetone (20 ml). The precipitate was collected by filtration, washed with acetone and dried overnight at 60°C in a vacuum oven (10 mm Hg) to yield 13 as a brown solid (1.3g, 91% yield). ^{1}H NMR (400 MHz, DMSO-d6) δ 1.0-1.4 (m, 4H), 1.5 (s, 18H), 1.8 (m, J = 6.5 Hz, 14H), 2.00 (m, J =7 Hz, 8H), 3.153.47 (m, 24H), 3.453.72 (m, 28H), 3.5 (m, J =7 Hz, 6H), 4.0 (s, 2H), 4.15-4.62 (m, 6H), 4.75-4.81 (m, 7H),

5.60-5.89 (m, 14H), 7.10-7.20 (t, J = 5.0 Hz,1H), 7.26(t, J= 5.0 Hz, 1H), 7.2 (d, J=8.4, 2H), 7.5 (d, J=8.4, 2H), 7.60-7.68 (t, J = 7.2 Hz, 2H), 8.448.56 (d, J = 4.8 Hz, 1H).

Deprotection of N-Boc amines by TFA (14)

The Boc-protected products (13) were deprotected using trifluoroacetic acid:DCM (1:1) for 1 h. The solvent was evaporated and the solid washed with acetone. The solid was dried overnight at 60°C in a vacuum oven (10 mm Hg) to yield 14 as a brown solid (1.2g, 95% yield). ^{1}H NMR (400 MHz, DMSO-d6) δ 1.0-1.4 (m, 4H), 1.8 (m, J = 6.5 Hz, 14H), 2.00 (m, J =7 Hz, 8H), 3.153.47 (m, 24H), 3.453.72 (m, 28H), 3.5 (m, J =7 Hz, 6H), 4.0 (s, 2H), 4.15-4.62 (m, 6H), 4.75-4.81 (m, 7H), 5.60-5.89 (m, 14H), 7.10-7.20 (t, J = 5.0 Hz,1H), 7.26(t, J= 5.0 Hz, 1H), 7.2 (d, J=8.4, 2H), 7.5 (d, J=8.4, 2H), 7.60-7.68 (t, J = 7.2 Hz, 2H), 8.44-8.56 (d, J = 4.8 Hz, 1H). $[M + H]^+$=1819.94.

Anion exchange reaction (15)

CD Polyamine tosylate (14, 1.4 g, 1 mmol) was dissolved in 40 mL deionized water. A 50 mL solid-phase synthesis vessel was packed with Amberlite IRA-900 ion-exchange resin to about half the vessel volume. The solution was transferred into the solid phase vessel. After 1 h, the eluent was collected and the water distilled off under reduced pressure using a vacuum pump. The solid residue was dried overnight at 60°C in a vacuum oven (10 mm Hg) to yield 15 as a brown solid. Yield: (1.15g, 95% yield); ^{1}H NMR (400 MHz, DMSO-d6) δ 1.0-1.4 (m, 4H), 1.8 (m, J = 6.5 Hz, 14H), 2.00 (m, J =7 Hz, 8H), 3.15-3.47 (m, 24H), 3.45-3.72 (m, 28H), 3.5 (m, J =7 Hz, 6H), 4.0 (s, 2H), 4.15-4.62 (m, 6H), 4.75-4.81 (m, 7H), 5.60-5.89 (m, 14H), 7.10-7.20 (t, J = 5.0 Hz,1H), 7.26(t, J= 5.0 Hz, 1H), 7.60-7.68 (t, J = 7.2 Hz, 2H), 8.44-8.56 (d, J = 4.8 Hz, 1H). $[M + H]^+$=1684.20.

Detailed synthesis of DexAM 2 (with 8 amines)

(Figure 3.12)

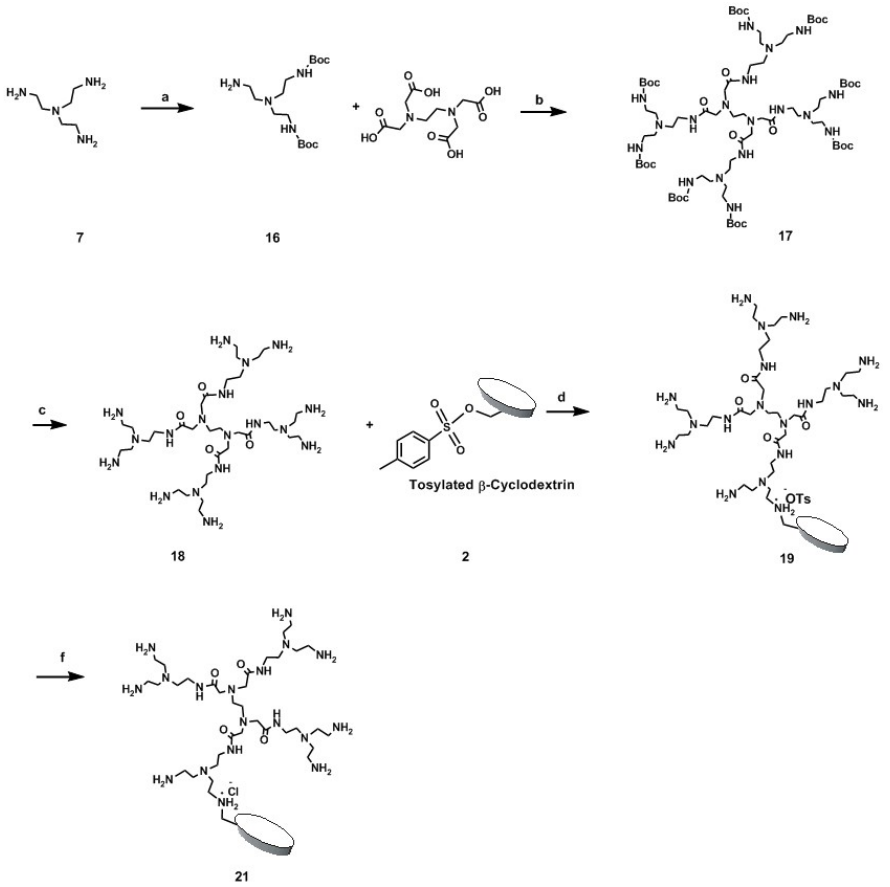

Figure 3.12: Synthesis of DexAM 2. a) DCC, DMAP, DCM, MeOH, b) DCC, DMAP, DCM, MeOH, c) TFA:DCM (50:50 v/v), d) DMF, 90°C, 48h, e) DMSO, RT, 24 h, f) Amberlite IRA900. Reprinted from Ref. [176]. Copyright 2011 American Chemical Society.

Bis-[2-(tert-butoxycarbonylamino)ethyl]-(2-aminoethyl)amine (16)

Tris(2-aminoethyl) amine (7, 14.6 g, 100mmol) was dissolved in 40 mL of dry CH_2Cl_2 and cooled to 0°C. A solution of di-tert-butyl dicarbonate (44.11 mL, 200 mmol) in 50 mL dry CH_2Cl_2 was added dropwise over 1h. The mixture was stirred at room temperature for 24 h. After removal of the solvent under reduced pressure, the remaining yellow oil was dissolved in ethyl acetate and washed twice with 0.5 N NaOH. The aqueous phase was diluted with brine and re-extracted with ethyl acetate. The combined organic phases were dried over $MgSO_4$ and the solvent removed under reduced pressure. The crude products were purified by flash chromatography on SiO_2. The fractions containing the desired product were identified by TLC and characterized by mass spectroscopy and NMR. The product (16) was isolated as a pale-yellow oil. Yield: (18.02 g, 52%); TLC (CH_2Cl_2:MeOH, 90:10 v/v): $R_f = 0.65$; ^{1}H NMR (DMSO-d6) δ 1.37 (s, 18 H), 2.38-2.44 (m, 6 H), 2.49-2.54 (m, 2 H), 2.95 (d, 4 H), 5.30 (s, 2 H). MS (m/z): calculated, 346.26 for $C_{16}H_{34}N_4O_4$; found, 369.46 for $[M + Na]^+$.

Synthesis of 4-armed Boc-protected amines

To EDTA (2.93g, 10.0 mmol) in CH_2Cl_2 (45 ml), DCC (9.9g, 48 mmol, 4.8 eq) and DMAP (0.4 eq, 489.0 mg, 4mmol) were added at 0°C and allowed to stir for 1 h. This solution was then added to 16 in MeOH (15ml) and stirred for 24 h at room temperature. Yield: (12.85g, 60%); TLC (CH_2Cl_2/MeOH, 90:10 v/v): $R_f = 0.4$; ^{1}H NMR (DMSO-d6, 400 MHz): δ 1.37 (s, 18 H), 1.00-1.49 (m, 16H), 1.8 (s, 4H), 2.40-2.85 (m, 40H), 3.00 (s, 8H), 3.45-3.55 (m, 8H), 8.20 (s, 4H). MS (m/z): calculated, 1605.08 for $C_{74}H_{144}N_{18}O_{20}$; found, 1629.03 for $[M + Na]^+$.

Deprotection of N-Boc amines by TFA to obtain polyamine of DexAM 2 (18)

To 4 arm-boc-protected amines (17, 1.6g, 1mmol), 40% TFA in dichloromethane (10 ml) was added. After 3 h, the reaction mixture was concentrated to give 18 as clear oil. The solvent was evaporated and the crude products were purified by flash chromatography on SiO_2 to obtain 18. Yield: (772.92 mg, 96%); TLC CH_2Cl_2/MeOH, 9:1): $R_f = 0.1$; ^{1}H NMR (DMSO-d6, 400 MHz): δ 1.00-1.49 (m, 16H), 1.8 (s, 4H), 2.40-2.85 (m, 40H), 3.00 (s, 8H), 3.45-3.55 (m, 8H), 8.20 (s, 4H). MS (m/z): calculated, 804.66 for $C_{34}H_{80}N_{18}O_4$; found, 828.11 for $[M + Na]^+$.

Synthesis of water-soluble CD-polyamine tosylate (19)

Tosylated cyclodextrin (2, 2.58 g, 2 mmol) and amine (18, 1.61g, 2 mmol) was dissolved in DMF (10 mL) in a 25-ml one-necked round-bottomed flask equipped with Liebigs condenser and a stir bar. The flask was degassed and purged with nitrogen. The mixture was stirred and refluxed at 90°C for 48 h. The reaction mixture was cooled down to room temperature and the product precipitated out by the addition of acetone (20 ml). The precipitate was collected by filtration, washed with acetone and dried overnight at 60°C in a vacuum oven (10 mm Hg) to yield 19 as a brown solid. Yield: (3.77g, 90%); ^{1}H NMR (DMSO-d6, 400 MHz): δ 1.00-1.49 (m, 16H), 1.8 (s, 4H), 2.40-2.85 (m, 40H), 2.41 (s, 3H), 3.00 (s, 8H), 3.15-3.47 (m, 24H), 3.45-3.55 (m, 8H), 3.45-3.72 (m, 28H), 4.15-4.62 (m, 6H), 4.75-4.81 (m, 7H), 5.60-5.89 (m, 14H), 7.2 (d, J=8.4, 2H), 7.5 (d, J=8.4, 2H), 8.0 (s, 4H). $[M + H]^+ = 2095.29$.

Anion exchange reaction for obtaining DexAM 2 (20)

CD-polyamine tosylate (19, 2.2g, 1 mmol) was dissolved in 40 mL deionized water. A 50 mL solid-phase synthesis vessel was packed with Amberlite IRA-900 ion-exchange resin to about half the vessel volume. The solution was transferred into the solid phase vessel. After 1 h, the eluent was collected and the water was distilled off under reduced pressure using a vacuum pump. The solid residue was dried overnight at 60°C in a vacuum oven (10 mm Hg) to yield 20 as a brown solid. Yield: (2.05g, 95%); ^{1}H NMR (DMSO-d6, 400 MHz): δ 1.00-1.49 (m, 16H), 1.8 (s, 4H), 2.40-2.85 (m, 40H), 2.41 (s, 3H), 3.00 (s, 8H), 3.15-3.47 (m, 24H), 3.45-3.55 (m, 8H), 3.45-3.72 (m, 28H), 4.15-4.62 (m, 6H), 4.75-4.81 (m, 7H), 5.60-5.89 (m, 14H), 7.10-7.20 (t, J = 5.0 Hz,1H), 7.26(t, J= 5.0 Hz, 1H), 7.607.68 (t, J = 7.2 Hz, 2H), 8.2 (s, 4H), 8.44-8.56 (d, J = 4.8 Hz, 1H). $[M + H]^+ = 2156.82$.

Detailed synthesis of DexAM 3 (with 12 amines)

(Figure 3.13)

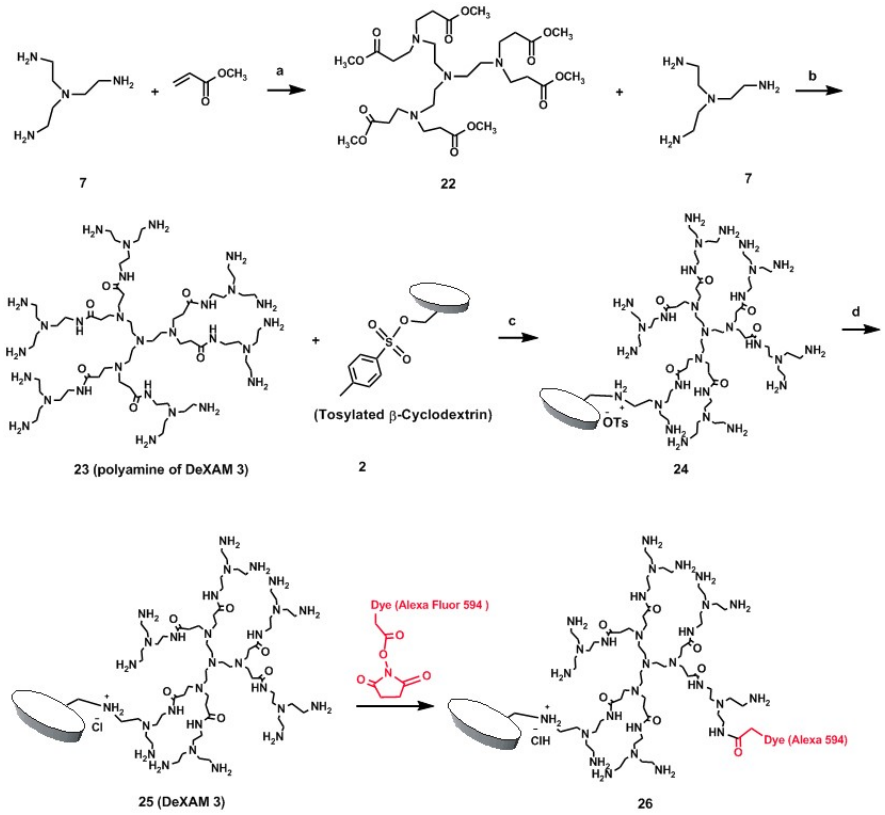

Figure 3.13: Synthesis of DexAM 3. a) MeOH, 0°C, 1h/ RT, 48 h, b) MeOH, 0°C, 1 h, RT, 7 days, c) DMF, 90°C, 48 h, d) Amberlite IRA900. Reprinted from Ref. [176]. Copyright 2011 American Chemical Society.

Synthesis of Hexamethyl-3,3',3",3"',3"",3""'-(2,2',2"-nitrilotris(ethane-2,1-diyl)tris (azanetriyl))hexapropanoate (22)

A solution of tris(aminoethyl)amine (7, 4.3872g, 30 mmol) in methanol (25 mL) was added dropwise to a stirred solution of methyl acrylate (19.37 g, 225 mmol) in methanol (25 mL) for 1 h in an ice-water bath. The resulting solution was stirred for 1 h in an ice-water bath and then allowed to warm to room temperature and stirred for further 48 h. The solvent and excess acrylate were removed under reduced pressure using a rotary evaporator. The residue was purified by column chromatography to afford the product (22) as a colorless oil. Yield: (16.88 g, 85%). ^{1}H NMR (300 MHz, $CDCl_3$): δ 2.44 (t, J=6.9 Hz, 12H), 2.49 (s, J=6 Hz, 12H), 2.74 (t, J=6.9 Hz, 12H), 3.67 (s, 18H). MS (m/z): calculated, 662.37 for $C_{30}H_{54}N_4O_{12}$; found, 685.76 for $[M + Na]^+$.

3,3',3",3"',3"",3""'-(2,2',2"-nitrilotris(ethane-2,1-diyl)tris(azanetriyl))hexakis(N-2-(bis(2-aminoethyl)amino)ethyl)propanamide) (23)

A solution of 22 (2.17 g, 3.3 mmol) in methanol (20 mL) was added dropwise to solution of tris(aminoethyl)amine (7, 5.8 g, 39.6 mol) in methanol (20 mL) and stirred over a period of 1 h in an ice bath. The resulting solution was allowed to warm to room temperature and stirred for 7 days at room temperature at which time no methyl ester was detectable by NMR spectroscopy. The solvent was removed under reduced pressure using a rotary evaporator and then the excess tris(aminoethyl)amine was removed using an azeotropic mixture of toluene and methanol (90:10 v/v). The remaining toluene was removed by azeotropic distillation using methanol. Finally, the remaining methanol was removed under vacuum. The residue was purified by dialysis and centrifugal filtration to afford the desired product. Finally the product was kept under vacuum to obtain the amino-terminated product as colorless oil (23, Yield: 4.4 g, 99%). ^{1}H NMR (300 MHz, $CDCl_3$): δ 1.25 (s, J=6.0 Hz, 24H), 2.44 (t, J=6.9 Hz, 12H), 2.48 (m, J=8 Hz, 72H), 2.74 (t, J=6.9 Hz, 12H), 3.25 (t, 12H), 8.0 (s, 6H). MS (m/z): calculated, 1347.14 for $C_{60}H_{138}N_{28}O_6$; found, 1370.0391 for $[M + Na]^+$.

Synthesis of water-soluble CD-polyamine tosylate (24)

Tosylated cyclodextrin (2, 2.58 g, 2 mmol) and the polyamine (23, 2.694g, 2 mmol) were dissolved in DMF (10 mL) in a 25 mL one-necked round-bottomed flask equipped

with Liebigs condenser and a stir bar. The flask was degassed and purged with nitrogen. The mixture was stirred and refluxed at 90°C for 48 h. The reaction mixture was cooled down to room temperature and product precipitated out by the addition of acetone (20 mL). The precipitate was collected by filtration, washed with acetone and dried overnight at 60°C in a vacuum oven (10 mm Hg) to yield 24 as a brown solid (Yield: 4.75g, 90%). ^{1}H NMR (300 MHz, DMSO-d6), δ 1.25 (s, J=6.0 Hz, 24H), 2.41 (s, 3H), 2.44 (t, J=6.9 Hz, 12H), 2.48 (m, J=8 Hz, 72H), 2.74 (t, J=6.9 Hz, 12H), 3.15-3.47 (m, 24H), 3.25 (t, 12H), 3.45-3.72 (m, 28H), 4.15-4.62 (m, 6H), 4.75-4.81 (m, 7H), 5.60-5.89 (m, 14H), 7.21 (d, J = 8.4 Hz, 2H), 7.52 (d, J=8.4 Hz, 2H), 8.0 (s, 6H). MS (m/z): [M + H]$^+$ = 2638.09.

Anion exchange reaction for obtaining DexAM3 or D3 (25)

CD-polyamine tosylate (24, 2.637g, 1 mmol) was dissolved in 40 mL deionized water. A 50 mL solid-phase synthesis vessel was packed with Amberlite IRA-900 ion-exchange resin to about half the vessel volume. The solution was transferred into the solid phase vessel. After 1 h, the eluent was collected and the water was distilled off under reduced pressure using a vacuum pump. The solid residue was dried overnight at 60°C in a vacuum oven (10 mm Hg) to yield 25 as a brown solid. Yield: (2.376g, 95% yield). ^{1}H NMR (300 MHz, DMSO-d6), 1.25 (s, J=6.0 Hz, 24H), 2.41 (s, 3H), 2.44 (t, J=6.9 Hz, 12H), 2.48 (m, J=8 Hz, 72H), 2.74 (t, J=6.9 Hz, 12H), 3.15-3.47 (m, 24H), 3.25 (t, 12H), 3.45-3.72 (m, 28H), 4.15-4.62 (m, 6H), 4.75-4.81 (m, 7H), 5.60-5.89 (m, 14H), 8.0 (s, 6H). [M + H]$^+$ = 2502.35.

Detailed synthesis of DexAM 4 (with 48 amines)

(Figure 3.14)

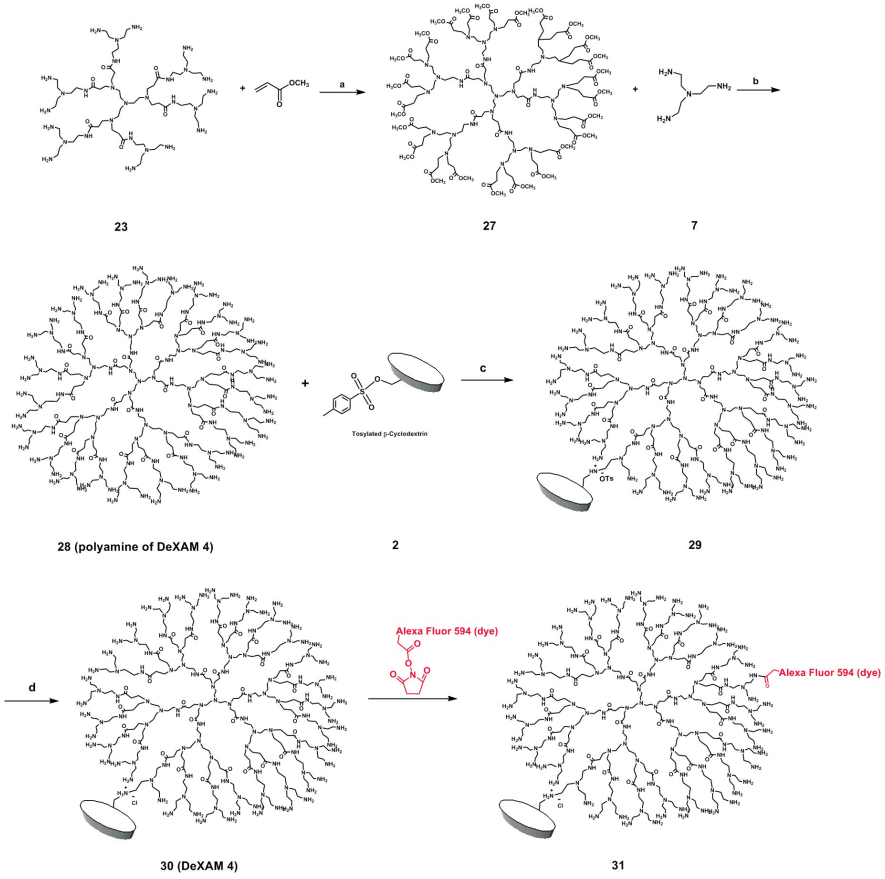

Figure 3.14: Synthesis of DexAM 4. Synthesis of DexAM 4, a) MeOH, 0°C, 1h/ RT, 48 h, b) MeOH, 0°C, 1 h, RT, 7 days, c) DMF, 90°C, 48 h, d) Amberlite IRA900. Reprinted from Ref. [176]. Copyright 2011 American Chemical Society.

Synthesis of methyl ester of 23 (27)

A solution of 23 (1.48g, 1.1 mmol) in methanol (5 mL) was added dropwise to a stirred solution of methyl acrylate (2.84 g, 33.0 mmol) in methanol (5 mL) for 1 h in an ice bath. The resulting solution was stirred for 30 min in an ice bath and then for 60 h at room temperature. The volatiles were removed under reduced pressure. The residue was purified by column chromatography using DCM:MeOH (10:1 v/v) to afford the desired product (27) as a yellow oil. Yield: (3.41 g, 91%); ^{1}H NMR (300 MHz, $CDCl_3$): δ 2.44 (t, J=6.9 Hz, 12H), 2.49 (s, J=6 Hz, 12H), 2.74 (t, J=6.9 Hz, 12H), 3.67 (s, 18H). MS (m/z): calculated, 3433.03 for $C_{158}H_{284}N_{26}O_{54}Na$; M/z found 3435.08 for [M

+ Na]$^+$.

Synthesis of the polyamine of DexAM 4 (28)

A solution of ester 27 (3.41g, 1 mmol) in methanol (20 mL) was added dropwise to a stirred solution of tris(aminoethyl) amine (7, 7.02 g, 48 mmol) in methanol (20 mL) over a period of 1 h in an ice bath. The resulting solution was allowed to warm to room temperature and stirred for 7 days at room temperature at which time no methyl ester was detectable by NMR spectroscopy. The solvent was removed under reduced pressure the excess tris(aminoethyl) amine was removed using an azeotropic mixture of toluene:MeOH (90:10 v/v). The product was further purified by washing with anhydrous ether twice, yielding a highly viscous liquid. Finally the product was kept under vacuum to provide the amino-terminated final product (28) as a light yellow liquid. Yield (6.1 g, 99%); ^{1}H NMR (300 MHz, $CDCl_3$): δ 1.25 (s, J=6.0 Hz, 24H), 2.44 (t, J=6.9 Hz, 12H), 2.48 (m, J=8 Hz, 72H), 2.74 (t, J=6.9 Hz, 12H), 3.25 (t, 12H), 8.0 (s, 6H). MS (m/z): calculated, 6174.06 for $C_{276}H_{618}N_{124}O_{30}Na$; M/z found 6177.66 for [M + Na]$^+$.

Synthesis of water-soluble CD-Polyamine tosylate (29)

Tosylated CD (2, 1.29g, 1mmol) and polyamine of DexAM 4 (28, 6.1g, 1 mmol) were dissolved in DMF (10 mL) in a 25 mL one-necked round-bottomed flask equipped with Liebigs condenser and a stir bar. The flask was degassed and purged with nitrogen. The mixture was stirred and refluxed at 90°C for 48 h. The reaction mixture was cooled down to room temperature and product precipitated out by the addition of acetone (20 mL). The precipitate was collected by filtration, washed with acetone and dried overnight at 60°C in a vacuum oven (10 mm Hg) to yield 29 as a brown solid. Yield: (6.6g, 89%); ^{1}H NMR (300 MHz, DMSO-d6), δ 1.25 (s, J=6.0 Hz, 24H), 2.41 (s, 3H), 2.44 (t, J=6.9 Hz, 12H), 2.48 (m, J=8 Hz, 72H), 2.74 (t, J=6.9 Hz, 12H), 3.153.47 (m, 24H), 3.25 (t, 12H), 3.45-3.72 (m, 28H), 4.15-4.62 (m, 6H), 4.75-4.81 (m, 7H), 5.60-5.89 (m, 14H), 7.21 (d, J = 8.4 Hz, 2H), 7.52 (d, J=8.4 Hz, 2H), 8.0 (s, 6H). [M + H]$^+$ = 7444.84 or 8733.01

Anion exchange reaction for obtaining DexAM 4 or D4 (30)

CD-polyamine tosylate (29, 3.72g, 0.5 mmol) was dissolved in 40 mL deionized

water. A 50 mL solid-phase synthesis vessel was packed with Amberlite IRA-900 ion-exchange resin to about half the vessel volume. The solution was transferred into the solid phase vessel. After 1 h, the eluent was collected and the water was distilled off under reduced pressure using a vacuum pump. The solid residue was dried overnight at 60°C in a vacuum oven (10 mm Hg) to yield 30 as a brown solid. Yield: (3.47g, 95%); ^{1}H NMR (300 MHz, DMSO-d6), δ 1.25 (s, J=6.0 Hz, 24H), 2.41 (s, 3H), 2.44 (t, J=6.9 Hz, 12H), 2.48 (m, J=8 Hz, 72H), 2.74 (t, J=6.9 Hz, 12H), 3.153.47 (m, 24H), 3.25 (t, 12H), 3.453.72 (m, 28H), 4.154.62 (m, 6H), 4.754.81 (m, 7H), 5.605.89 (m, 14H), 8.0 (s, 6H). $[M + H]^+ = 7309.10$ or 8462.53.

Conjugation of Alexa-Fluor® dye to DexAM 4 (31)

Alexa-Fluor®-594 dye (100 nM, Molecular Probes) and DeXAM 4 (30, 100 nM) were dissolved in PBS buffer solution (0.5 mL). The reaction mixture was allowed to vortex for 5 minutes. After being vortexed, the mixture was shaken at room temperature for 3 h.

Synthesis of erlotinib

(Figure 3.15

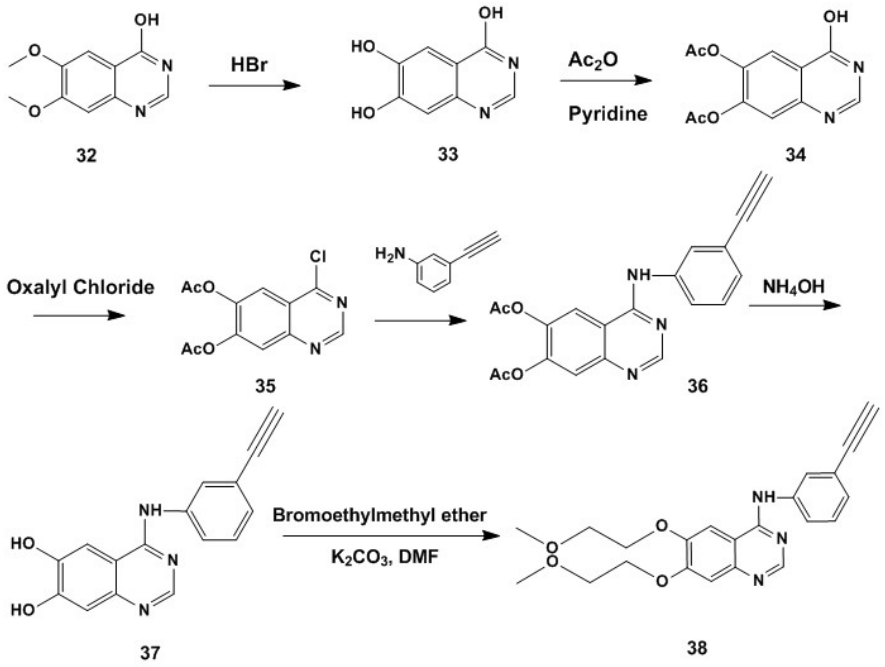

Figure 3.15: Synthesis of Erlotinib. Reprinted from Ref. [176]. Copyright 2011 American Chemical Society.

The EGFR tyrosine kinase inhibitor N-(3-ethynylphenyl)-6,7-bis(2-methoxyethoxy) quinazolin-4-amine (commonly known as Erlotinib) was synthesized using previously reported protocols albeit with slight modifications. Briefly, 5.0 g of the 6,7-dimethoxy quinazolone (32) was suspended in concentrated HBr and refluxed under nitrogen to obtain 33 as a white solid. This was then suspended in 23 mL of acetic anhydride in presence of 200 μL of pyridine. The reaction mixture was refluxed under nitrogen for 3 h and the acetic anhydride/acetic acid was removed in vacuo to yield the diacetate (34) in 91% yield. The diacetate was converted to the chloro derivative (35) by reacting it with oxalyl chloride which was then reacted with 3-ethynylaniline to yield 36 as an off-white solid. The product was converted to the dihydroxy derivative (37) by hydrolysis using conc. NH_4OH. 37 was dissolved in 10 mL of dry DMF followed by the addition of 11.4 g of K_2CO_3. Potassium Iodide (2 g) and bromomethylethyl ether (3.5 g) were added to the above solution and stirred overnight at 45°C. The solvent was removed

in vacuo, dissolved in DCM, washed with water and dried over $MgSO_4$. The solvent was evaporated to obtain the product (38) as a brown solid. Yield: (3.56g, 95%); ^{1}H NMR ($CDCl_3$) δ 8.60 (s, 1H), 7.96 (w, 1H), 7.85 (s, 1H), 7.70-7.76 (m, 1H), 7.42-7.36 (m, 3H), 7.12 (s, 1H), 4.13-4.21 (m, 4H), 3.73-3.78 (m, 4H), 3.40 (s, 3H), 3.08 (s, 1H)

Synthesis of suberoylanilide hydroxamic acid (SAHA)

(Figure 3.16

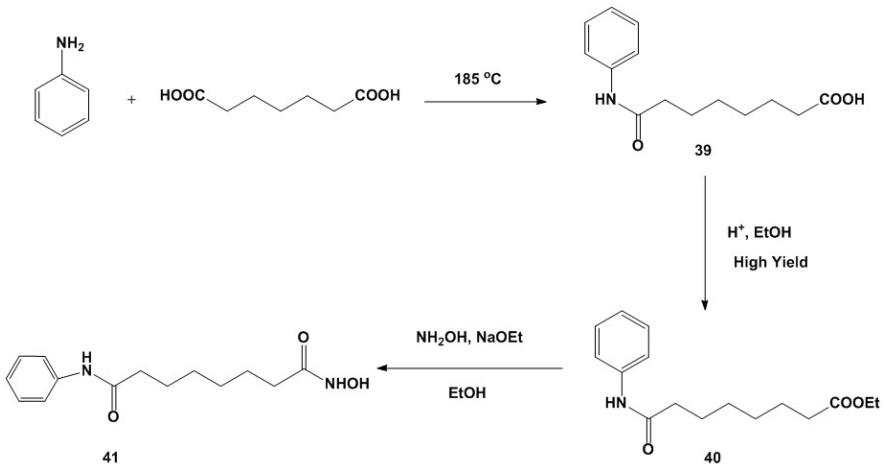

Figure 3.16: Synthesis of SAHA. Reprinted from Ref. [176]. Copyright 2011 American Chemical Society.

The histone deacetylase inhibitor suberoylanilide hydroxamic acid (SAHA) was synthesized according to previously reported methods. Briefly, freshly distilled aniline (4.09 g, 0.044 mol) and suberic acid (6.96 g, 0.040 mol) were heated at 185-190°C for 10 min to yield suberanilic acid (39) as a white solid in 41% yield. This was then converted to the methyl ester (40) by refluxing with methanol for 22 h. Hydroxylamine hydrochloride (2.17 g, 0.0312 mol) was dissolved in 15 mL of ethanol in a 50 mL flask equipped with magnetic stirring and an addition funnel. Solid methyl suberanilate (4.10 g, 0.0156 mol) was added, which dissolved readily. followed by the addition of sodium methoxide solution. The reaction was mixture for stirred for 26 h at room temperature and then rinsed with 100 mL of water where most of it dissolved. Glacial acetic acid (4.0 g) was added with stirring. The resulting heavy precipitate was filtered, rinsed with water, then slurried with another 75 mL of water, filtered, and rinsed again. The solid was

dried at room temperature, affording the product (41) as a white solid. Yield: (1.82 g, 47%); MP = 159-160.5°C; ^{1}H NMR (DMSO-d6) δ 10.33 (s, 11H), 9.84 (s, 11H), 8.66 (s, 11H), 7.57 (d, J = 7.61, 2H), 7.27 (t, J = 7.2, 2H), 7.00 (t, J = 7.4, 1H), 2.27 (t, J = 7.61, 2H), 1.92 (t, J = 7.4, 2H), 1.56 (p, J = 6.7, 2H), 1.47 (p, J = 6.21, 2H), 1.26 (m, 4H)

Inclusion of erlotinib and SAHA into DexAM

(Figure 3.17

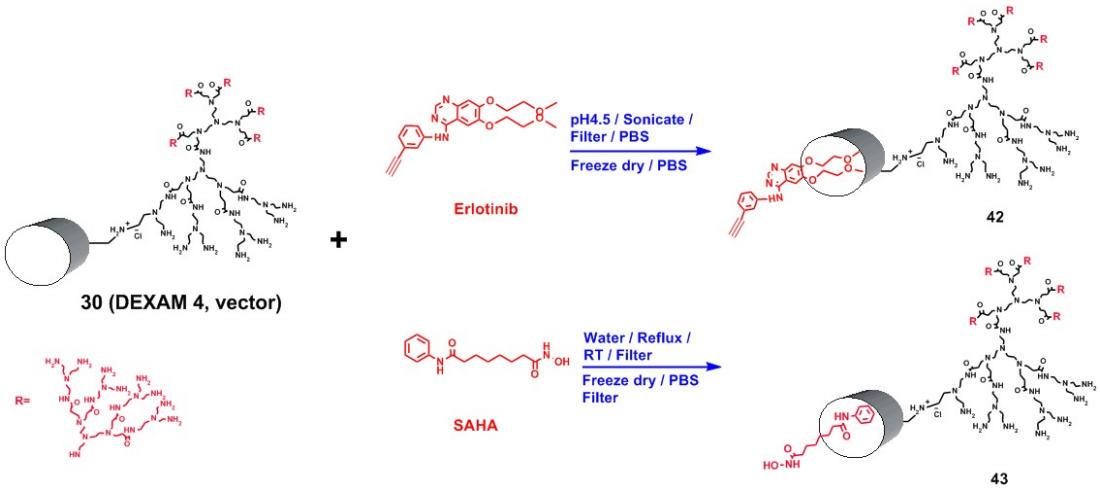

Figure 3.17: Inclusion of Erlotinib and SAHA into DexAM. Reprinted from Ref. [176]. Copyright 2011 American Chemical Society.

Formation of Erlotinib-DexAM 4 inclusion complex (42) Erlotinib (5mg, 13 μmol) was dissolved in 10 mL of acetate buffer (pH=4.5). The erlotinib solution was added to vials containing pure DexAM 4 (26 μmol). The contents of the vials were vortexed for 10 min, sonicated for 30 min and stirred vigorously for 8 h. The resulting complex was freeze-dried. Thereafter, 200 μL of PBS was added to the DexAM complex (10 μmol) and allowed to stand at room temperature to dissolve for a few minutes. The solution was then filtered and purified using an appropriate molecular weight cut-off (MWCO) centrifugal filter (Millipore, Billerica, MA, USA).

Formation of SAHA-DexAM 4 inclusion complex (43) Suberoylanilide hydroxamic acid (SAHA) was solubilized in 2 molar equivalents of DexAMs in distilled water.

Briefly, 8 mg of SAHA was added to a solution of 370mg of DexAM 4 in 3 mL of water, heated until fully dissolved, stirred for 8 h, and then rapidly cooled on ice to room temperature. This solution was filtered and freeze-dried. Thereafter, 200 μL PBS was added to DexAM complex (10 μmol) and allowed to stand at room temperature to dissolve for a few minutes. Finally, the complex was purified through by centrifugal filtration using an appropriate MWCO membrane. DexAM-SAHA solutions of various concentrations were prepared by maintaining the molar ratio between SAHA and DexAMs.

Antibody conjugation to DexAM 4 complexes

(Figure 3.18)

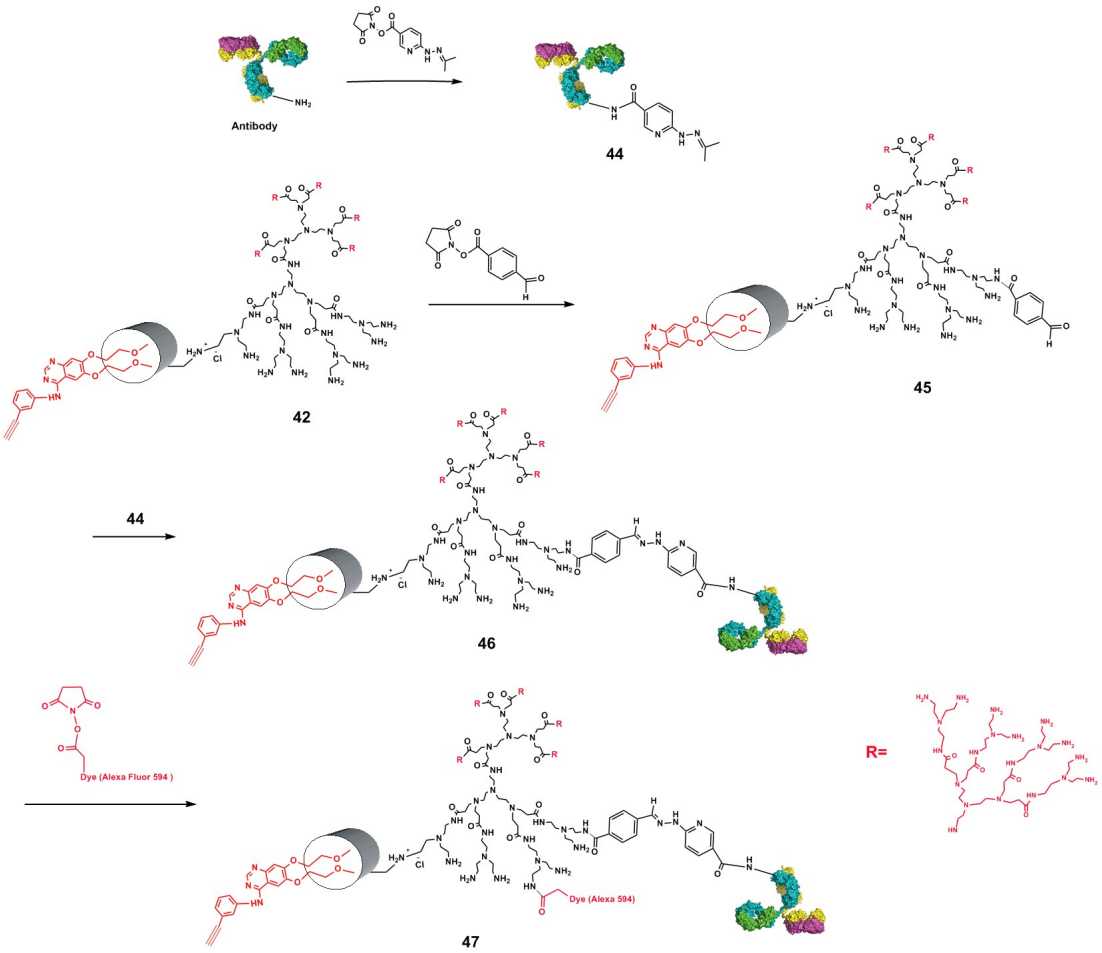

Figure 3.18: Conjugation of EGFR antibody to DeXAM 4 complexes. Reprinted from Ref. [176]. Copyright 2011 American Chemical Society.

Functionalization of antibody with 6-hydrazinonicotinamide (44) 6-hydrazinonicotinamide (HyNic), an aromatic hydrazine was attached to the amine group of antibody. Briefly, 6-hydrazinonicotinamide (11 nM, HyNic, SoluLinK) and EGFR Antibody (10 nM) were mixed in 2 mL of buffer (pH = 6.0) and vortexed for 5 minutes. After being vortexed, the mixture was shaken at room temperature for 2 h.

Functionalization of DexAM with 4-formylbenzamide (45) 4-formylbenzamide (4-FB), an aromatic aldehyde was linked to the amine group of DeXAMs. Briefly, 4-FB (11 nM, SoluLinK) and DeXAM 4 (10 nM) were dissolved in 2 mL buffer (pH = 6.0) and the reaction mixture vortexed for 5 minutes. After being vortexed, the mixture was shaken at room temperature for 2 h.

Antibody conjugation to DexAMs (46) 44 and 45 were vortexed together for a few minutes at room temperature thereby leading to the formation of a stable bis-aryl hydrazone bond between the antibody and DexAM 4 (46). A similar conjugation strategy was used for attaching the antibody to DexAM 4-SAHA complex (43)

Conjugation of Alexa Fluor®-594 dye to antibody-modified DexAMs (47) Alexa Fluor-594 (100 nM. Molecular Probes, Invitrogen) and EGFR antibody-conjugated DexAM 4 (46, 100 nM) were dissolved in PBS buffer solution (0.5mL) and vortexed for 5 minutes. After being vortexed, the mixture was shaken for 2 h at room temperature.

Formation of polyplexes between siRNA and DexAM

(Figure 3.19)

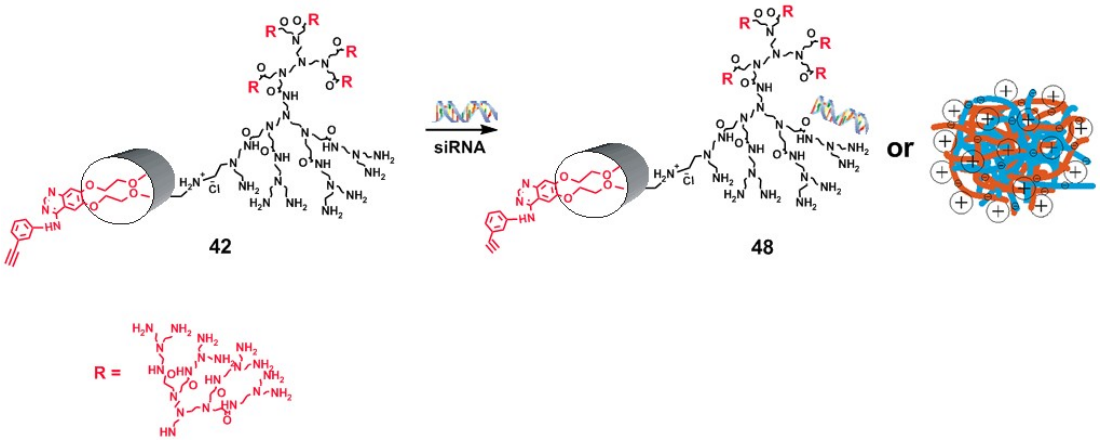

Figure 3.19: Polyplex formation of DexAM and siRNA. Reprinted from Ref. [176]. Copyright 2011 American Chemical Society.

DexAM/siRNA complexes were prepared by adding equal volumes of DexAM solution (DexAM dissolved in dH_2O) and siRNA (dissolved in water) at varying different concentrations. The resultant solution was then incubated for 30 min at room temperature before transfection. The GFP siRNA sequence was: Antisense 5'- GGCUACGUCC AGGAGCGCACC-3', Sense - 5'-phosphate-UGCGCUCCUGGACGUAGCCUU-3'. The U87-EGFR-vIII siRNA sequence was: Antisense - 5'-GAAAGGUAAUUAUGUGGUGUU-3', Sense - 5'-phosphate-UUCUUUCCAUUAAUACACCAC-5'.

Quantification of siRNA loading efficiency

The complexes were prepared at various charge ratios by mixing equal volumes of DexAM with siRNA in PBS. Charge ratios (N/P) were calculated as a ratio of the number of primary amines in the polymer, determined from ^{1}H NMR spectra, to the number of anionic phosphate groups in the siRNA. The samples were then incubated at room temperature for 30 minutes to ensure complex formation. The complexes were prepared at a final siRNA concentration of 0.2 μg of siRNA/100 μL of solution. 100 μL of each complex were transferred to a 96-well (black-walled, clear-bottom, non-adsorbing) plate (Corning, NY, USA). A total of 100 μL of diluted PicoGreen dye (1:200 dilution in Tris- EDTA (TE) buffer) was added to each sample. Fluorescence measurements were made after 10 minutes of incubation at room temperature using a

M200 Pro Multimode Detector (Tecan USA Inc, NC, USA), at excitation and emission wavelengths of 485 and 535 nm, respectively. All measurements were corrected for background fluorescence from a solution containing only buffer and PicoGreen dye.

Particle size and Zeta potential analysis

Dynamic light scattering (DLS) and Zeta Potential analyses were performed using a Malvern Instruments Zetasizer Nano ZS-90 instrument (Southboro, MA) with reproducibility being verified by collection and comparison of sequential measurements. Polymer/siRNA complexes (siRNA concentration = 330 nM) at different polymer concentrations, were prepared using purified water (resistivity = 18.5 MΩ cm). DLS measurements were performed at a 90°C scattering angle at 25°C. Z-average sizes of three sequential measurements were collected and analyzed. Zeta potential measurements were collected at 25°C, and the Z-average potentials following three sequential measurements were collected and analyzed.

Cell culture

Cells were cultured in the following growth media: DMEM (Dulbeccos modified Eagles medium) with high glucose (Invitrogen), 10% Fetal Bovine Serum (FBS), 1% streptomycin-penicillin, 1% glutamax (Invitrogen), and selection markers, G418 (100 μg/ml) and hygromycin B (30 μg/ml) for U87-EGFP and U87-EGFRvIII respectively. PC-12 cells were cultured in DMEM with 10% horse serum, 5% FBS and 1% streptomycin penicillin. For the knockdown experiment and targeted delivery, passaged cells were prepared to 40-60% confluency in 24-well plates. For the knockdown experiment, targeted delivery and cell viability assay, media was exchanged with serum-free basal media (500 μl) and siRNA-DexAM solution (50 μl) was added after 20-30 minutes. After incubation for 12 hours, media was exchanged with normal media. Fluorescence measurement and cellular assays were performed after 48-96 hours from the starting point.

Cytotoxicity assays

The percentage of viable cells was determined by MTS assay following standard protocols described by the manufacturer. All experiments were conducted in triplicate and averaged. The quantification of polymer-mediated toxicity was done using MTS assay after incubating the glioblastoma cells in the presence of varying concentrations of only polymer vehicle for 48-96 h. The data is represented as formazan absorbance at 490 nm, considering the control (untreated) cells as 100% viable.

Quantification of knockdown of EGFP expression

Following siRNA treatment, cells were washed with DPBS and fixed with 2-4% paraxformaldehyde solution prior to imaging. For the fluorescence, DIC, and phase contrast images were obtained using the Zeiss Axio observer inverted epifluorescence microscope. Each image was captured with different channels and focus. Images were processed and overlapped using Image-Pro (Media Cybernetics) and ImageJ (NIH).

Targeted delivery

Highly tumorigenic U87-EGFP cells and low-tumorigenic PC-12 cells were cultured in 24- well plates, at a density of 5 x 10^4 cells per well. For PC-12 cells, the normal growth media was DMEM (with high glucose, Invitrogen), 5% horse serum, 10% FBS, 1% Glutamax, and 1% penicillin-streptomycin. For the delivery of EGFR-Ab conjugated DexAM polyplexes, media was exchanged with serum free DMEM media. The cells were incubated in the Ab-conjugated polyplex medium for 6-8 h. Fluorescence images were taken after replacing the serum-free media with regular media.

Apoptosis assay

Cells were harvested by trypsinization and stained using an Annexin-V FITC Apoptosis Detection kit (Roche, Cambridge, MA) according to the manufacturers protocol. The stained cells were immediately analyzed by flow cytometry (FACScan; Becton Dickinson, Franklin Lake, NJ). Early apoptotic cells with exposed phosphatidylserine

but intact cell membranes bound to Annexin V-FITC but excluded propidium iodide. Cells in necrotic or late apoptotic stages were labeled with both Annexin-V-FITC and propidium iodide.

Chapter 4

Mesoporous silica nanoparticles for Real-time Monitoring of Drug release in Cancer cells

The previous two chapters focused on the design and development of novel nanoscale delivery vehicles which can not only deliver various kinds of therapeutics in an efficient and target specific manner, but can also impart imaging capabilities to these delivery vehicles. However, it is equally important to monitor the release of these therapeutic moieties upon administration at *in vitro* or *in vivo* level. Hence, it becomes necessary to incorporate release-monitoring strategies within the nanoplatform, such that it can enable spatiol and temporal resolution of drug release in real-time. The following chapter discusses the development of one such versatile strategy for monitoring of drug release intracellularly. This work has been already publised in ACS Nano [18].

4.1 Versatile fluorescence resonance energy transfer-based mesoporous silica nanoparticles for real-time monitoring of stimuli-responsive drug release

4.1.1 Introduction

It has been known that diseased/injured microenvironments release different biological cues and follow abnormal regulatory cycles, when compared to physiologically normal cells and tissues [224–226]. Such dynamic microenvironmental conditions require scientists to develop more effective nanomaterial-based drug delivery systems (DDSs) having the following attributes: i) they can deliver multiple drugs such as organic small molecules, proteins, peptides, DNA, and RNAi molecules without any physicochemical alterations to drug structure, [97, 154, 227, 228] ii) they can modulate the drug-release profile in response to external or internal stimuli for enhancing therapeutic efficacy and minimizing side-effects of drug treatment, [229–234] and iii) they can monitor the drug release in real time for investigating accumulation of the drugs at the targeted area [235–239]. In this regard, mesoporous silica nanoparticles (MSNs) have excellent potential as DDSs owing to their unique porous structure, tunable pore size, biocompatibility, ease of surface functionalization, and overall versatility [136,240]. The hexagonal-ordered pore network within these MSNs allows for entrapping drugs within these pores by simple diffusion. Additionally, the pores can be functionalized with molecular valves designed to trigger the release of the entrapped drugs in the presence of external or internal stimuli including light, [241–244] temperature, [245–247] pH, [155,248–251] and biomolecules [252–256]. While there have been numerous reports on the design and development of stimuli-responsive MSNs for drug delivery, development of strategies for real-time monitoring of drug release inside the targeted cells is still in its nascent stage. The most widely used amongst these strategies include using fluorescent dyes/drugs as a model cargo system, [235–237, 241–244] or conjugating the drugs with caged dyes [238, 239]. However, such strategies come with their own limitations such as difficulty in correlating the release of the fluorescent model dye to that of the actual drug molecules; restricting the usage of fluorescent drugs like doxorubicin as

model cargoes, although most of the current drug candidates are non-fluorescent; and possibility of affecting the therapeutic efficacy of the drug owing to structural changes required for conjugation of dyes. Such challenges in investigating the release of drug in complex cellular microenvironments necessitate the development and integration of a real-time monitoring system within the stimuli-responsive nanomaterial-based DDSs.

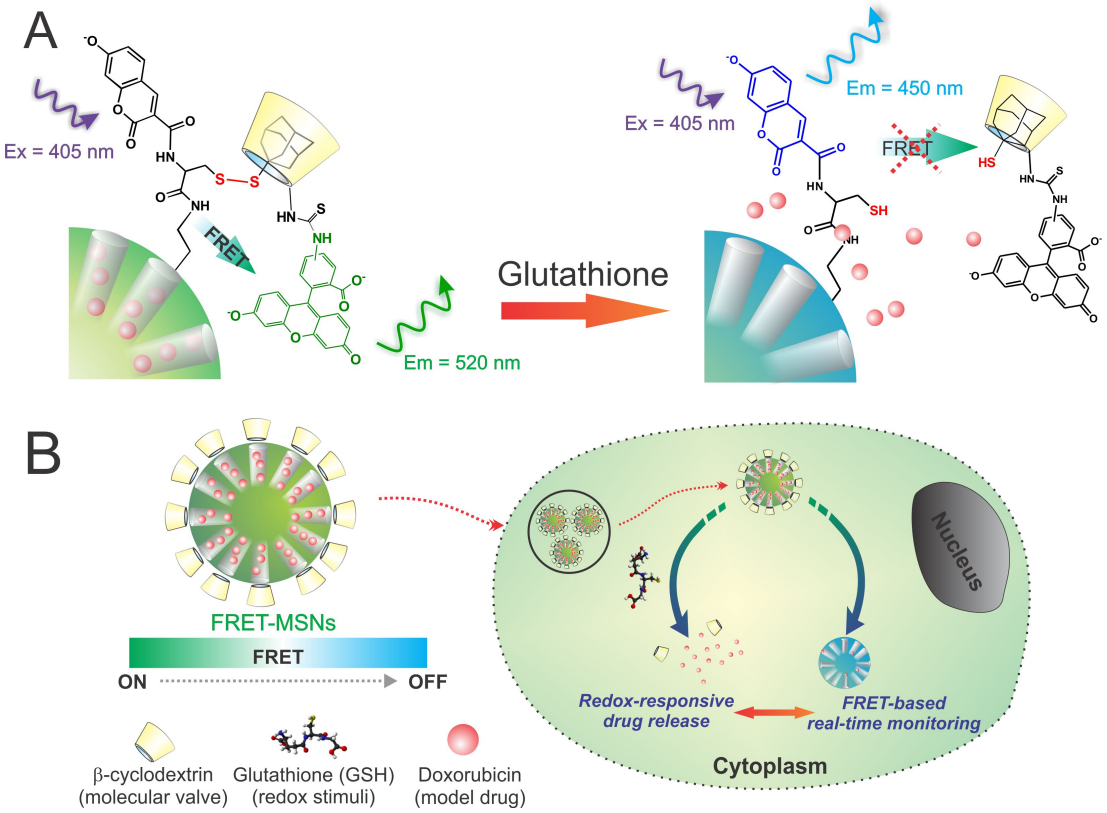

Figure 4.1: (A) The coumarin-labeled cysteine on the surface of the FRET-MSNs act as a donor and the FITC-β-CD act as an acceptor, thereby forming a FRET system when the disulfide bond is intact (left). When disulfide bond is cleaved in the presence of redox stimuli, glutathione, the FITC-β-CD, which also acts as the molecular valve, is removed from the surface of the MSNs, thereby the FRET between coumarin and FITC is abolished. (B) The delivery of encapsulated cargo is selectively triggered in the presence of the redox-stimuli, glutathione which is found in significantly higher amounts in the cytoplasm of cancer cells and the concomitant change of FRET signal can be used to report the uncaging event and estimate the dosing amount of drug. Reprinted from Ref. [18]. Copyright 2013 American Chemical Society.

To address the aforementioned issues, herein we describe the synthesis and development of a redox-responsive fluorescent resonance energy transfer based MSN drug

delivery system (henceforth referred to as FRET-MSN), which enables real-time monitoring (based upon the FRET signal) of redox-responsive drug release occurring in the presence of glutathione found in significantly higher levels in the cancer cells (Figure 4.1) [257–259]. Fluorescence resonance energy transfer (or Frster resonance energy transfer, FRET) is a well-established energy transfer process between two fluorophores which is very sensitive to changes at nanometer-scale (typically less than 10 nm) in the donor-to-acceptor separation distance [260]. This unique feature of FRET can potentially be an ideal tool to monitor delicate interactions between nanomaterial-based DDSs and external/internal stimuli [261, 262].As illustrated in Figure 4.1, our FRET-based real-time monitoring platform is comprised of four components: (i) coumarin (donor)-tethered MSNs as the drug carriers, (ii) fluorescein isothiocyanate (FITC, acceptor)-attached β-cyclodextrin (β-CD) as the molecular cap to entrap the drugs within the MSNs, (iii) disulfide linkage as the redox-responsive trigger to release the entrapped drug molecules, and (iv) FRET donor-acceptor pair of coumarin and FITC for monitoring drug release in real time. Under non-reducing conditions (e.g. without glutathione), [80] the intact disulfide bond supports formation of a donor-acceptor complex between the coumarin-attached MSN and the FITC-β-CD molecular cap, thereby creating a FRET system. At this stage (FRET ON), the coumarin and FITC moieties are in close proximity on the MSN surface and the FRET-MSNs display an emission peak at 520 nm (correlated to energy transfer from coumarin to FITC), when they are excited at 405 nm (the excitation wavelength of coumarin). However, in the presence of a reducing environment (e.g. with glutathione), the disulfide bond can be cleaved, [80] causing the removal of the FITC-β-CD cap from the MSNs, thereby unlocking the pores and releasing the cargo within. Upon cleavage of the disulfide bond, the FITC-β-CD diffuses away from the MSN surface, hence the FRET between coumarin and FITC is abolished (FRET OFF), and the MSNs display emission at 450 nm (characteristic of coumarin) when excited at 405 nm. Since the on/off change in FRET signal is regulated by molecular structures within our platform and correlated to the unlocking event, we can monitor and quantify the drug release process, by measuring the change of FRET

signal. By monitoring the FRET signal on the nanoparticles in real-time, we can visualize the release of any drug molecules, without relying on the drugs optical properties, thereby extending the application of our FRET-MSNs to many drug molecules without compromising their efficacy.

4.1.2 Results and Discussion

Synthesis and characterization of the FRET-MSNs

The generation of our FRET-MSN-based drug delivery system began with the synthesis of MCM-41 type MSNs via condensation of tetraethylorthosilicate (TEOS) in the presence of a cetyltrimethylammonium bromide (CTAB) micelle template [263] (Figure 4.2). These MSNs were then functionalized with 3-aminopropyltriethoxysilane (APTES) and grafted with N-Boc-cysteine via an amide bond. The thiol group of cysteine was conjugated with 1-adamantanethiol to form an redox-responsive disulfide bond, while the amine group was further labeled with 3-carboxy-7-hydroxyl-coumarin (CHC) to obtain the functional CHC-MSNs.

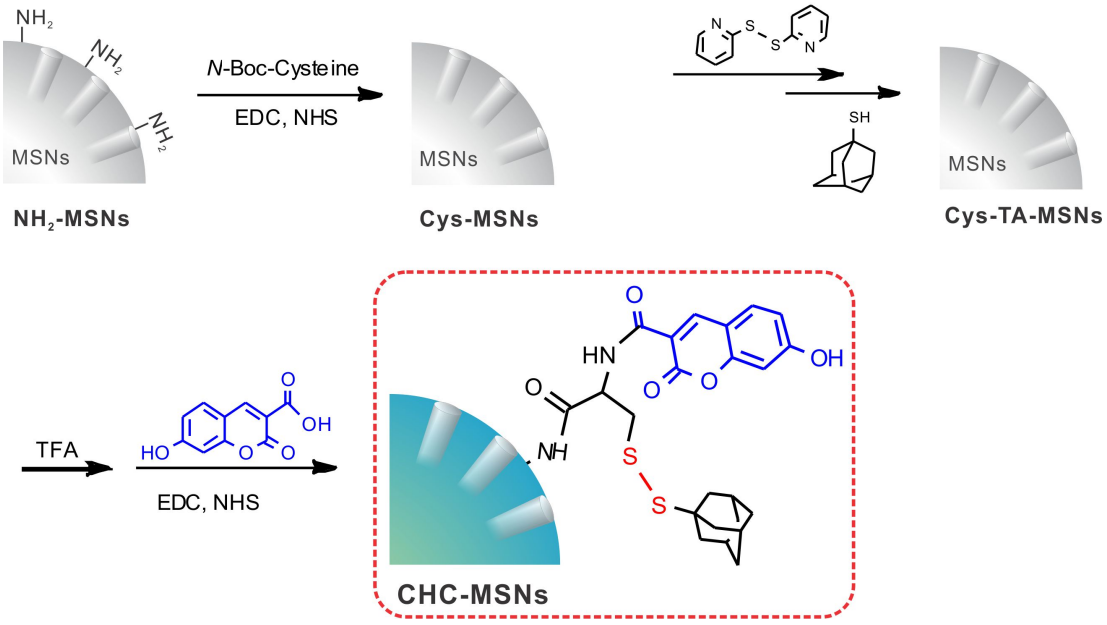

Figure 4.2: Schematic illustration of the synthesis of CHC-labeled MSNs. The CHC moiety acts as the FRET donor in our FRET-MSNs. Reprinted from Ref. [18]. Copyright 2013 American Chemical Society.

Using transmission electron microscopy (TEM), we affirmed that the CHC-MSNs still retain the characteristics of MCM-41 type of MSNs, such as their spherical particle shape, having an average diameter of 100 nm 14 nm (n = 100) and hexagonally packed mesoporous structures. This was also substantiated by N_2 adsorption isotherms which demonstrated that the CHC-MSNs have a Burnauer-Emmett-Teller (BET)-surface area of 398 m^2g^{-1} and a narrow Barrett-Joyner-Halenda (BJH) pore-size distribution (average pore diameter = 2.3 nm) (Figure 4.3).

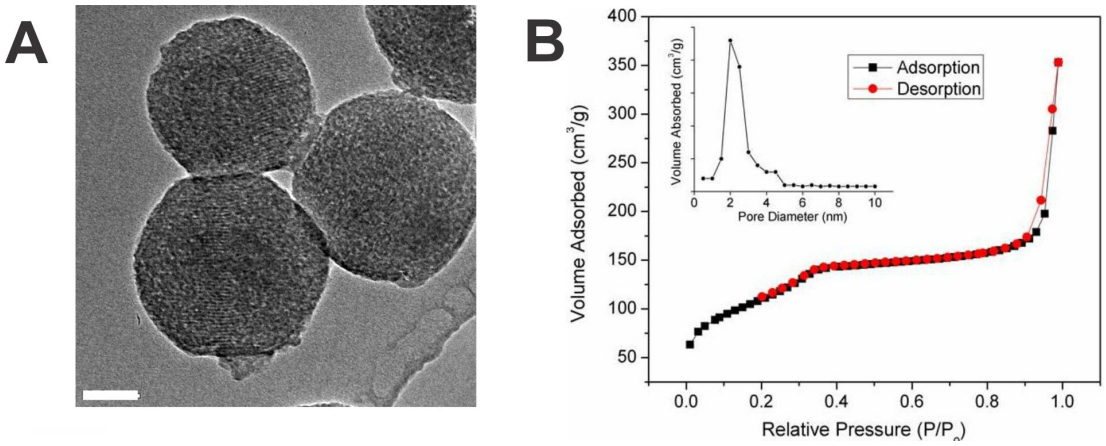

Figure 4.3: (A) TEM image of CHC-MSNs. Scale bar is 50 nm. TEM image confirms that CHC-MSNs retain characteristics typical of MCM-41 type nanoparticles. (B) N_2 adsorption-desorption isotherms of the prepared CHC-MSNs. The inset figure shows the pore diameter distribution of the CHC-MSNs. Reprinted from Ref. [18]. Copyright 2013 American Chemical Society.

In addition, the cysteine functionalized MSNs show a characteristic Raman peak of free thiol group [264] at 2550 cm^{-1} (Figure 4.4, top curve). However, after conjugation with 1-adamantanethiol via a disulfide bond, this characteristic free thiol peak disappeared, which confirmed the formation of a disulfide bond. The UV-Vis absorption and fluorescence emission of CHC-MSNs, demonstrate the successful conjugation of CHC to the MSN surface and indicates that the CHC-moiety can act as the energy donor for FITC. Together with the FTIR characterization of CHC-MSNs, these results demonstrated the successful construction of CHC-MSNs (Figure 4.4).

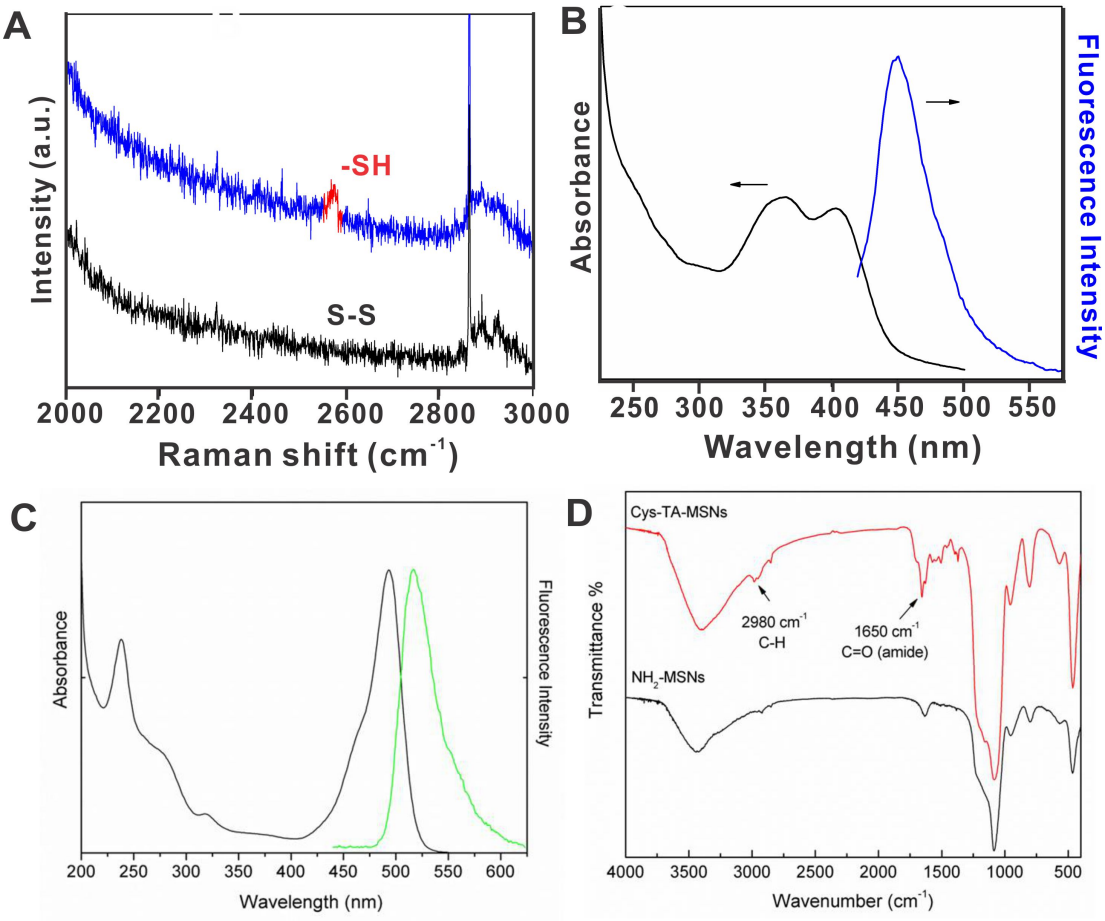

Figure 4.4: (A) Raman spectra confirming the formation of a disulfide bond, following conjugation with 1-adamantane thiol. The top curve indicates the free thiol (-SH) moiety on the surface of CHC MSNs, prior to conjugation with 1-adamantanethiol. Following conjugation, no free -SH groups are observed as shown in the bottom curve, thus indicating successful formation of disulfide bond. (B) UV-visible absorbance and emission spectra for CHC-MSNs. The CHC moiety in the CHC-MSNs absorbs maximally at 405 nm and emits light corresponding to 450 nm, thereby acting as a FRET donor for FITC. (C) UV-Vis absorption and fluorescence spectrum of FITC-β-CD. (D) FT-IR spectrum of the as prepared MSNs. Reprinted from Ref. [18]. Copyright 2013 American Chemical Society.

Assembly of a Donor-Acceptor FRET Model

The synthesis of FRET-MSNs was then followed by the combination of the CHC-MSNs with FITC-β-CD via host-guest complexation between FITC-β-CD and adamantane moiety [265] present on CHC-MSNs. As shown earlier, the coumarin moiety in CHC-MSNs can be excited by absorbing light with a wavelength of 405 nm, resulting in

emission of light in the range of 430-480 nm. When the disulfide bond is intact (Figure 4.1), the coumarin moiety in CHC-MSNs upon excitation at 405 nm will act as a photon donor for the FITC-β-CD which absorbs maximally at 480 nm (Figure 4.4). We observed that the addition of FITC-β-CD lead to a decrease in blue fluorescence (450 nm) and an increase in green fluorescence (520 nm), which was also reflected in a significant change of the color of the solution from blue to green, sufficiently distinct to be identified via naked eye (Figure 4.5).

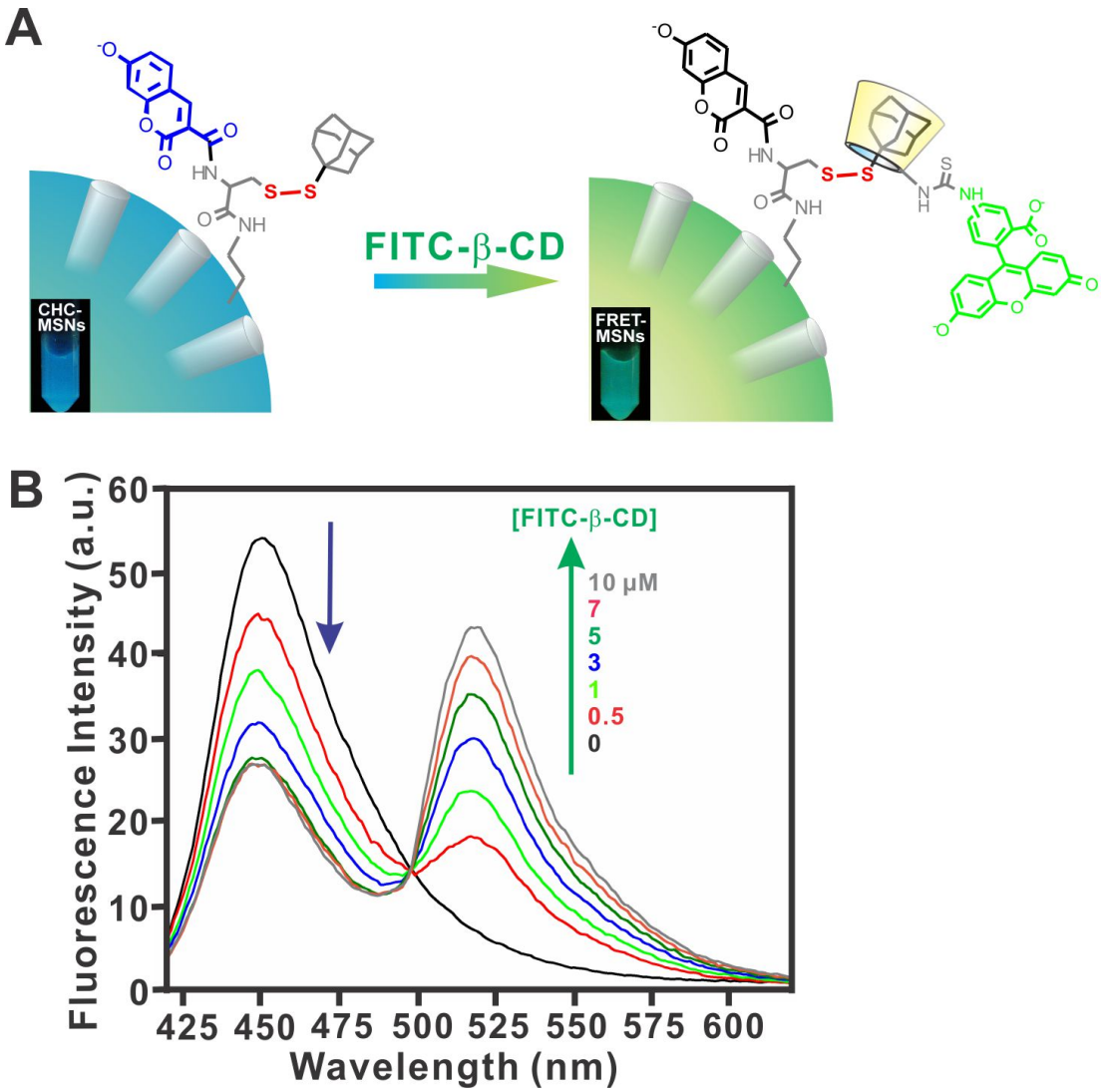

Figure 4.5: (A) Schematic diagram indicating the assembly of FRET-MSNs, upon addition of FITC-β-CD to CHC-MSNs. (B) Changes in blue (450 nm) and green (520 nm) fluorescence upon addition of increasing concentrations of FITC-β-CD to the CHC-MSNs dispersed in pH7.4 PBS, indicating formation of FRET-MSNs (FRET ON). Reprinted from Ref. [18]. Copyright 2013 American Chemical Society.

As seen in Figure 4.5, further increases in the concentration of FITC-β-CD quenched the blue fluorescence maximally. Additionally, the ratio of relative fluorescence intensities (FRET signal R, where R = F520nm / F450nm) reached a value of 1.25 at a concentration of 3 μM for FITC-β-CD for a fixed concentration of CHC MSNs (10 μgmL-1), which indicated the assembly of FITC-β-CD to the MSN surface reached a saturation point. Further addition of FITC-β-CD beyond the saturation point only led to an increase in the FITC fluorescence with negligible quenching of coumarin fluorescence, presumably due to the direct excitation of FITC at 405 nm [260]. When these nanoparticles were isolated from the solution and redispersed in PBS (pH 7.4), they displayed dual emission peaks at 450 nm and 520 nm upon excitation at 405 nm (Figure 4.6). Collectively, these results demonstrated that FITC-β-CD can assemble onto the surface of the CHC-MSN surface through the formation of inclusion complex with 1-adamantanethiol, thereby inducing a donor-acceptor FRET system.

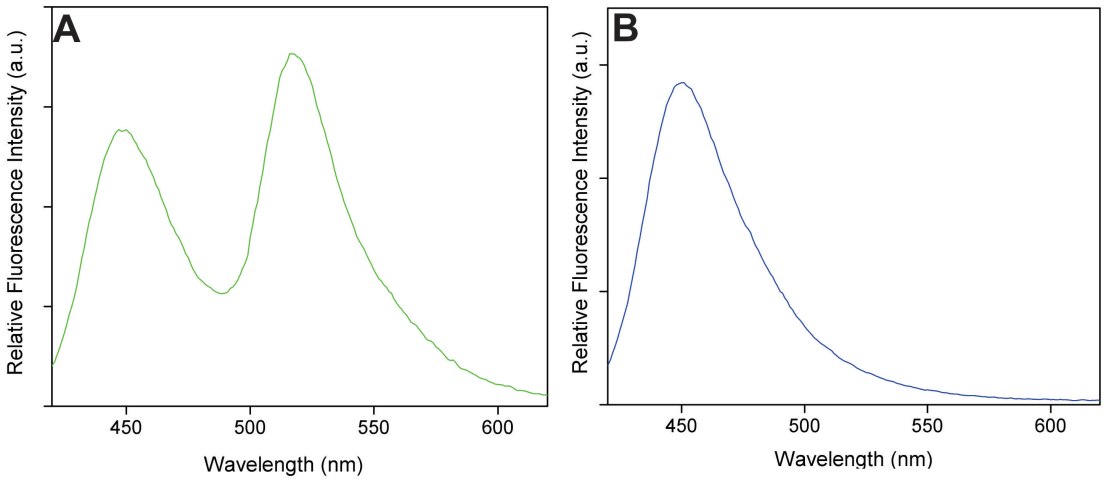

Figure 4.6: (A) Dual emission peaks corresponding to both coumarin (450 nm) and FITC (520 nm) emission when the FRET-MSNs are excited using coumarin's excitation wavelength (i.e 405 nm). This result confirms the presence of an intact FRET donor-acceptor pair on the surface of FRET-MSNs in the absence of any reducing stimuli. (B) A single emission peak corresponding to coumarin (450 nm) is seen when the FRET-MSNs are treated with gutathione (GSH, 5 mM) for 10 mins and then excited using coumarin's excitation wavelength (i.e. 405 nm). Reprinted from Ref. [18]. Copyright 2013 American Chemical Society.

Redox-Responsive Behavior of FRET-MSNs

The redox-responsive property of the FRET-MSNs was examined by observing the changes in FRET signal in the presence of glutathione (GSH) which mimics the intracellular reducing environment Figure 4.7. Addition of increasing concentrations of GSH (0.1 - 5 mM) to a buffered solution of FRET-MSNs induced a decrease in the green fluorescence (520 nm) accompanied by recovery of blue fluorescence (450 nm) upon excitation at 405 nm. This strongly indicated the cleavage of disulfide bond and the removal of the FRET acceptor, FITC-β-CD. Accordingly, the color of the solution changed from green to blue under UV lamp (365 nm) (Figure 4.7, inset). Fluorescence spectrum of the isolated nanoparticles after redispersing in PBS (pH 7.4) revealed that these nanoparticles only show the emission at 450 nm (Figure 4.6). Based on these results, we can confirm the redox-responsive behavior of our FRET-MSNs, which results in a concomitant change in the FRET signal.

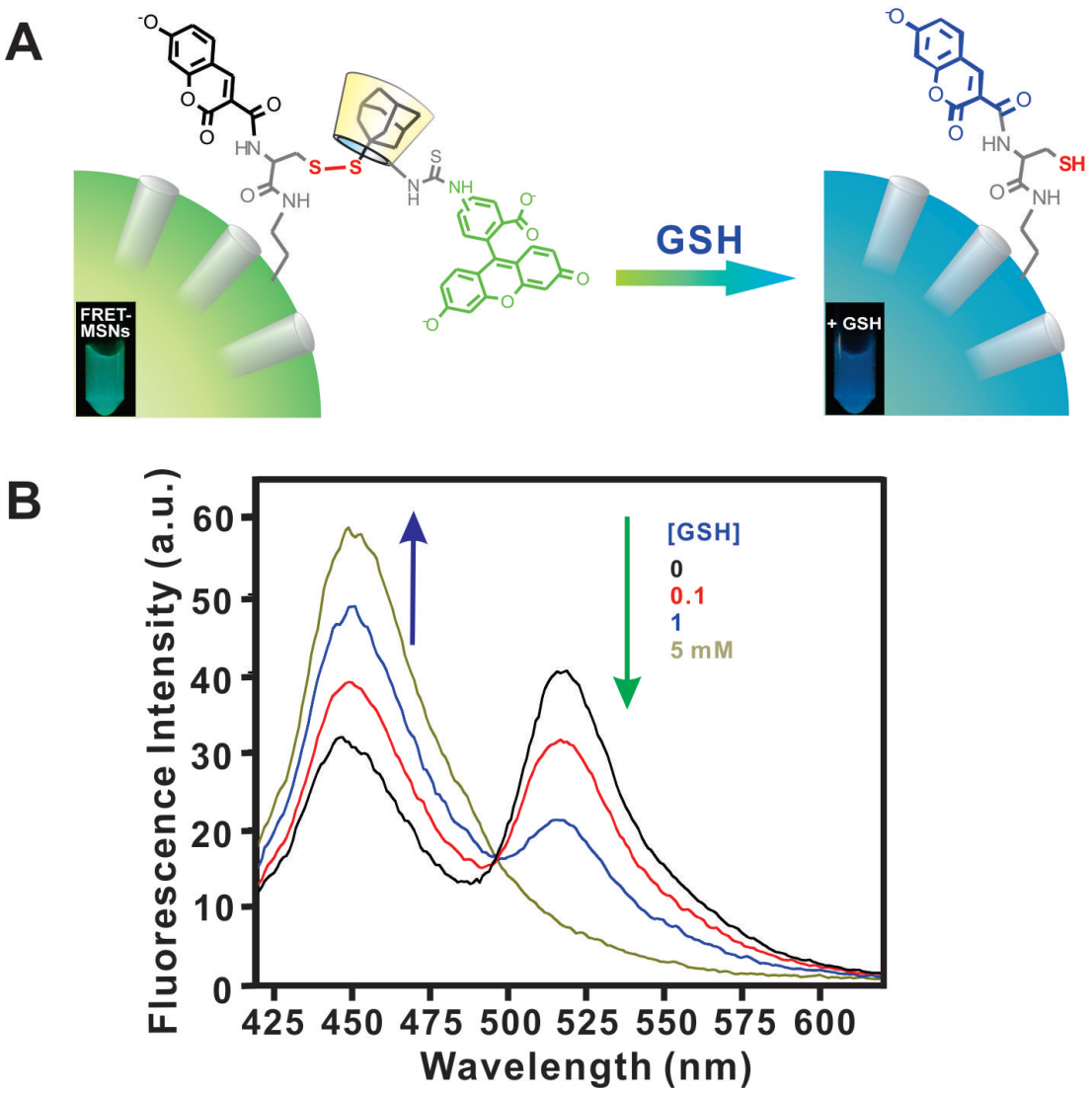

Figure 4.7: (A) Schematic diagram indicating cleavage of disulfide bond (right), following treatment of FRET-MSNs with Glutathione (GSH). Inset figures show the corresponding change in color of the nanoparticle solution under UV lamp (365 nm).(B) Changes in blue (450 nm) and green (520 nm) fluorescence upon addition of increasing GSH concentrations to FRET-MSNs dispersed in pH7.4 PBS, indicating cleavage of disulfide bond (FRET OFF). Reprinted from Ref. [18]. Copyright 2013 American Chemical Society.

Correlating Drug Release from FRET-MSNs to the FRET signal

Once we confirmed the redox-responsive gating behavior of our FRET-MSNs, our next step was to utilize their FRET properties for monitoring the drug release from the pores. Since the modulation of FRET is integrated within the uncapping event, we hypothesize

that the corresponding change in the FRET signal can be utilized for monitoring the drug release on a temporal level (Figure 4.8).

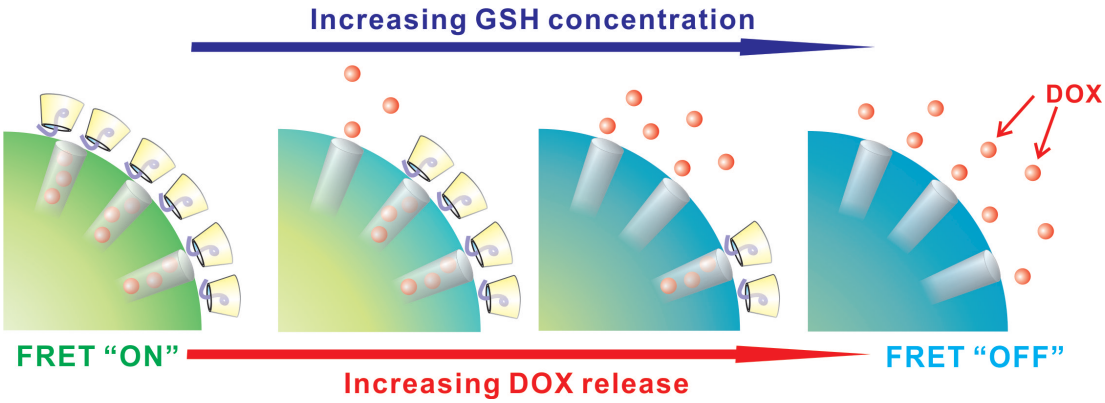

Figure 4.8: Scheme showing the release of DOX at different concentrations of GSH and the corresponding change in FRET signal as well color of FRET-MSNs. Reprinted from Ref. [18]. Copyright 2013 American Chemical Society.

To demonstrate this, we chose doxorubicin (DOX) as our model cargo, which was loaded into the pores of MSNs by first mixing aqueous buffered solutions of CHC-MSNs and DOX for 12 h. Thereafter, the pores were capped with FITC-β-CD and the final product (DOX-loaded FRET-MSNs) was isolated by centrifugation after repeated washing. The amount of DOX loaded into the pores of FRET-MSNs was determined to be 41.3 mg DOX/g of FRET-MSNs. It should be noted that the DOX-loaded FRET-MSNs were well-dispersed in aqueous solutions, owing to the presence of hydrophilic β-CD moieties on their surface, which can be exploited for the delivery of hydrophobic cargoes, like anti-cancer drugs [176]. To investigate the capping efficiency, DOX-loaded FRET-MSNs were dispersed in PBS (pH 7.4) and the absorbance of the released DOX in the absence of GSH was first monitored. As shown in Figure 4.9, negligible release of DOX was observed over a period of 24 h, indicating that the FRET-MSNs remain intact in the absence of GSH. In contrast, the release profiles of DOX in the presence of varying concentrations of GSH depict an increase in the percent DOX released as time progressed. Thus, we can see that the percent DOX released from the FRET-MSNs was dependent on GSH concentration, wherein concentrations of 0.1 mM or higher lead to significantly faster and greater release of DOX.

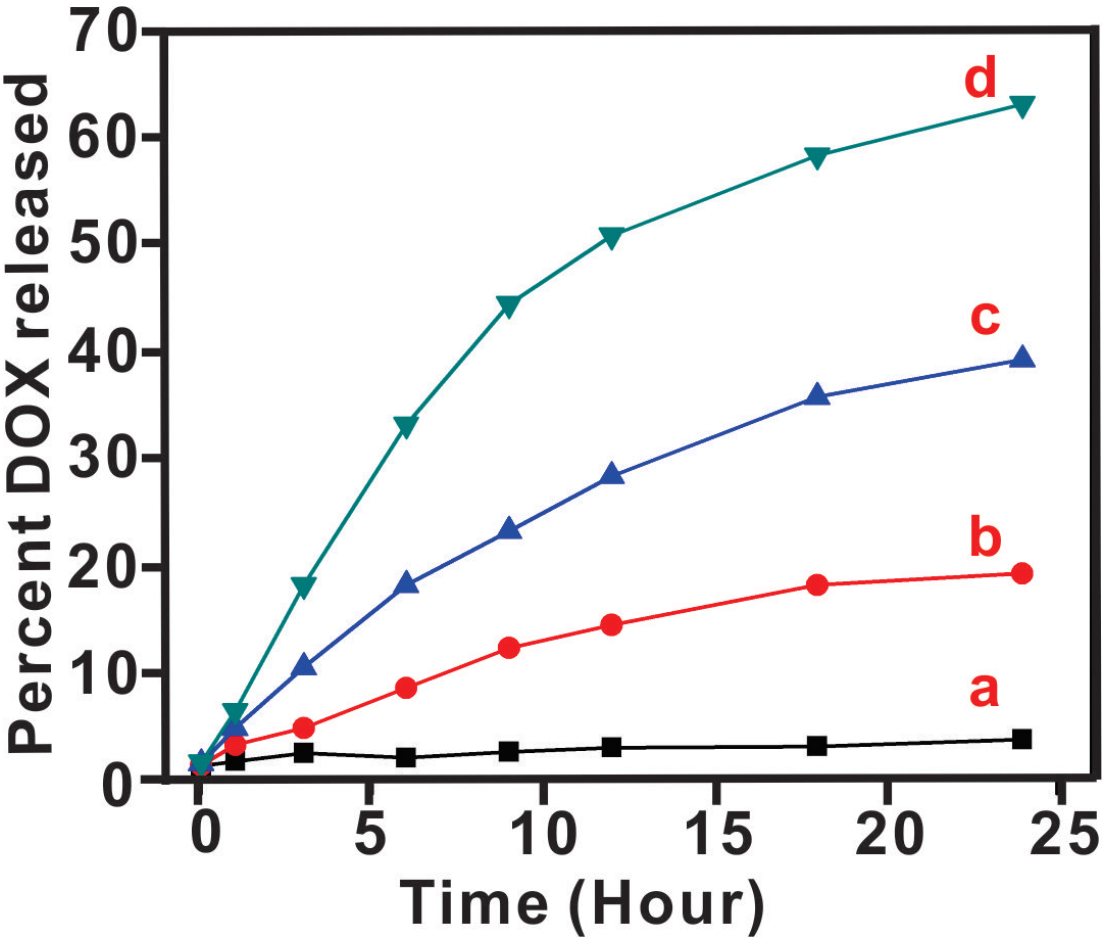

Figure 4.9: Percent DOX released from the FRET-MSNs at different time points following treatment with increasing concentrations of GSH. a = no GSH, b = 0.1 mM GSH, c = 1 mM GSH and d = 5 mM GSH. Reprinted from Ref. [18]. Copyright 2013 American Chemical Society.

Since the release of DOX only occurs when the pores are unlocked as a consequence of FITC-β-CD diffusing away from the FRET-MSNs, we also observed a corresponding change in the FRET signal R. As shown in Figure 4.10, addition of GSH (0.1 mM) to Dox-loaded FRET-MSNs induced a relatively slow time-dependent decrease in FRET signal over a period of 3 h, while higher concentrations of GSH lead to faster decrease in the FRET signal, reaching a minimal value of R within 1 h at 5 mM concentration of GSH. These GSH-concentration induced changes in FRET signal remained constant over a period of 24 h, at which the release of DOX also reached a plateau. From this data (t = 24 h), a correlation between the amount of DOX released and FRET signal R was obtained (Figure 4.10), which strongly suggested that the FRET-MSNs have the

capability of monitoring the drug release in real-time.

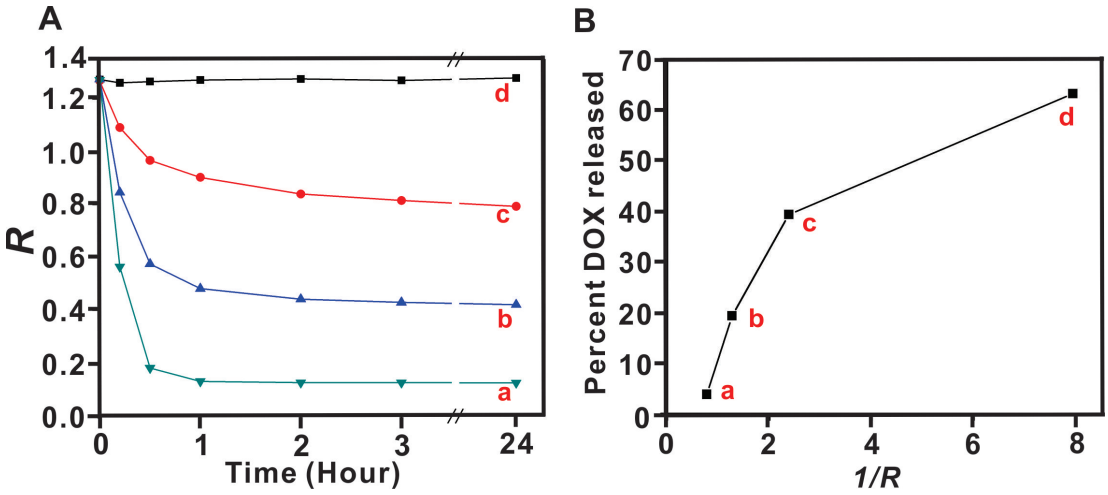

Figure 4.10: (A) Change in FRET signal R at different time points following treatment of FRET-MSNs with increasing concentrations of GSH. (B) Correlation between percent DOX released and change in FRET signal R (plotted as 1/R) at 24 h after GSH treatment. (a = no GSH, b = 0.1 mM GSH, c = 1 mM GSH and d = 5 mM GSH). Reprinted from Ref. [18]. Copyright 2013 American Chemical Society.

Observing FRET Change in Cancer Cells Using FRET-MSNs

Prior to using the FRET-MSNs for cellular studies, we identified a range of concentrations within which the FRET-MSNs demonstrated minimal cytotoxicity (Figure 4.11). Using a cell proliferation assay, we found that concentrations lower than 20 μgmL-1 induced negligible cytotoxicity in HeLa cells and hence for all of our experiments, we utilized FRET-MSNs within this concentration range.

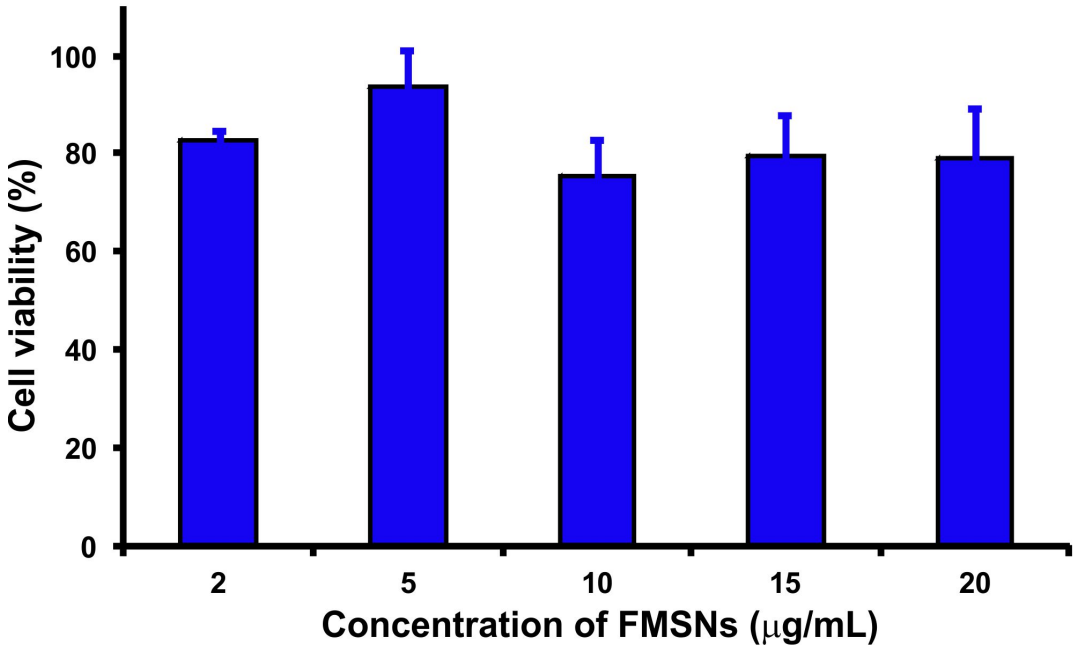

Figure 4.11: Percent cell viability of HeLa cells following treatment with increasing concentrations of FRET-MSNs. The cell viability was analyzed 48 h after treatment with FRET-MSNs using CellTiter 96 AQueous One Solution Cell Proliferation Assay (MTS). All experiments were done in triplicates and the average and standard deviation for each condition are represented. Reprinted from Ref. [18]. Copyright 2013 American Chemical Society.

To investigate the change in FRET signal following uptake and localization of FRET-MSNs in mammalian cells, we incubated the FRET-MSNs with cervical cancer cells (HeLa) and observed the change in FRET signal over extended periods of time (0 to 24 h) using confocal fluorescence microscopy. As seen in Figure 4.12 (top left), at time t = 0 h, blue-green spots were visible in the perinuclear region of HeLa cells when they were excited using 405 nm light, indicating intact FRET-MSNs with the FRET signal ON. From the emission spectrum (Figure 4.12, top right), we can see that these spots show lower blue emission, but stronger green emission thus confirming that most of the FRET-MSNs were in the "FRET ON" stage at this time-point. However, at approximately t = 24 h, an increase in the blue fluorescence intensity and a corresponding decrease in the green fluorescence intensity (Figure 4.12, bottom left) were observed when the cells were excited using 405 nm light. This was consistent with our expectation as the cleavage of disulfide bond would lead to the removal of FITC-β-CD

cap, thereby leading to the recovery of the blue fluorescence intensity (Figure 4.12, bottom right). These results demonstrated that we were able to monitor the change in the intracellular FRET signal over a period of time by using confocal microscopy.

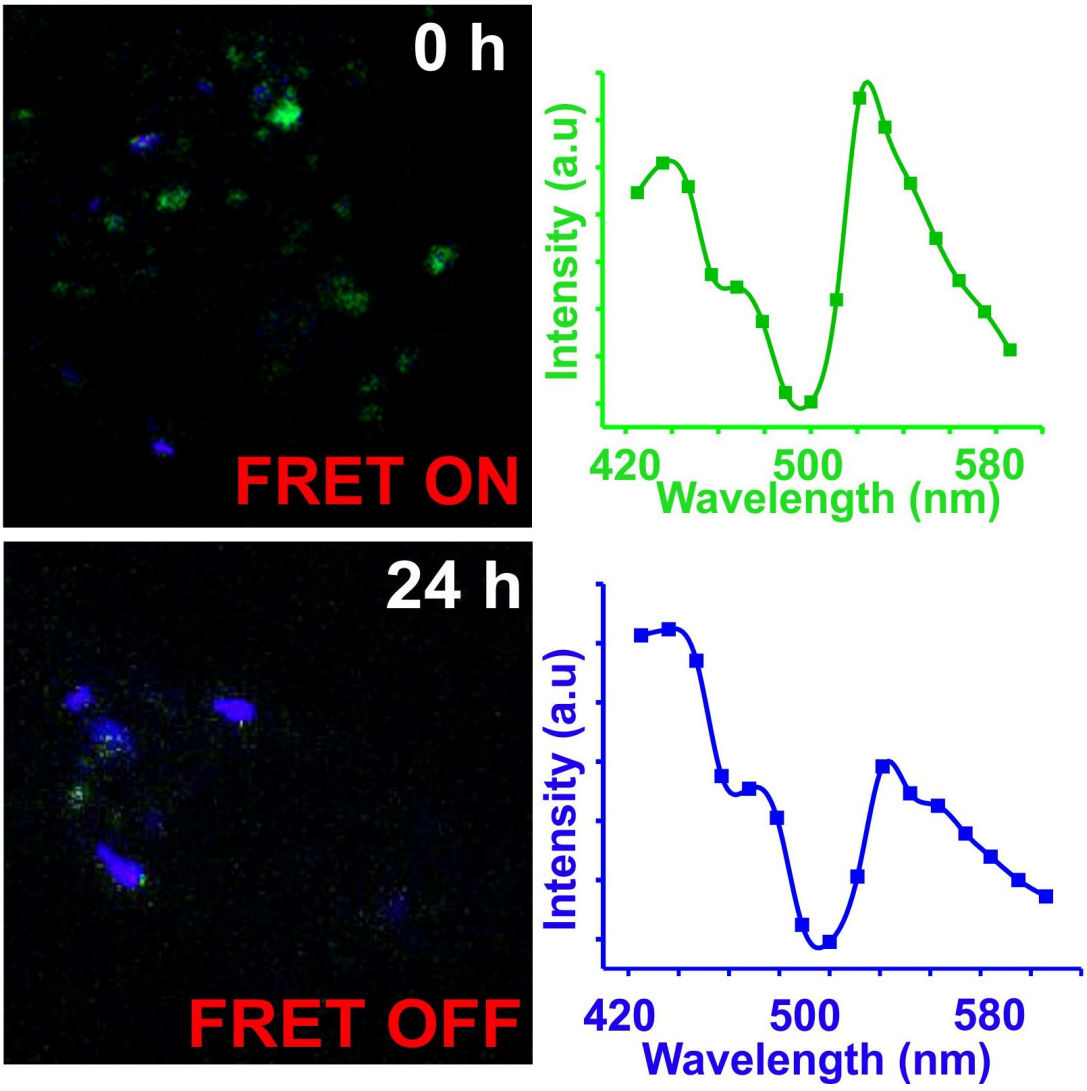

Figure 4.12: Confocal microscopy images (Left panel) depicting the change in FRET signal in HeLa cells treated with FRET-MSNs at different time points. Right panel shows the corresponding change in the average fluorescence intensities, when the cells were excited with 405 nm light. Scale bar is 1 μm. Reprinted from Ref. [18]. Copyright 2013 American Chemical Society.

As shown earlier, we have already demonstrated that our FRET-MSNs can respond to the presence of exogenous GSH by releasing the entrapped cargo with concurrent change in the FRET signal. However, in order to demonstrate this in mammalian

cells, we used thioctic acid (TA, a GSH synthesis enhancer, 10 μM) [266] and N-ethylmaleimide (NEM, a GSH scavenger, 5 μM) [267,268] to modulate the intracellular GSH concentration. The HeLa cells were incubated with TA and NEM, 10 min prior to incubating with the FRET-MSNs and were subsequently analyzed using fluorescence microscopy. As depicted in Figure 4.13, we observed a clear enhancement in the characteristic coumarin emission at 450 nm for the cells treated with TA in FRET channel (Ex = 405 nm), coupled with increased FITC fluorescence in FITC channel (Ex = 488 nm), indicating that higher number of the molecular valves (FITC-β-CD) were being removed from the surface of FRET-MSNs due to increased intracellular GSH concentration and were subsequently diffused into the cytoplasm. On the contrary, a distinct punctate blue-green fluorescence in FRET channel, indicating FRET ON, was seen in the perinuclear region in case of cells treated with NEM. Since NEM decreases intracellular GSH concentration, there will be negligible cleavage and subsequent release of FITC-β-CD, hence resulting in the FRET being ON.

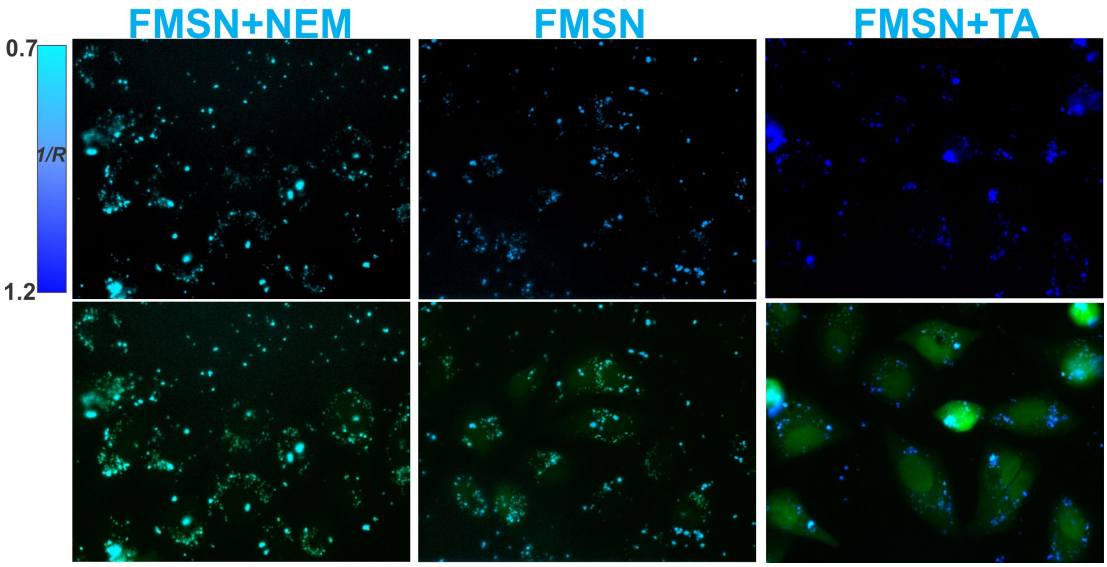

Figure 4.13: Fluorescence microscopy images showing the change in the fluorescence intensity (FRET channel, 405 nm excitation, top panel, and the merged images with FITC channel which used 488 nm as excitation, bottom panel) upon varying intracellular GSH concentration of HeLa cells, prior to treatment with FRET-MSNs. Cells treated with N-ethyl maleimide (NEM, 5 μM) present low levels of GSH, thereby FRET signal is on; whereas, the cells treated with thiotic acid (TA, 10 μM) have increased GSH levels and hence the FRET is turned off. The bar (top left corner) indicates the correlation between FRET signal R and the color of the FRET-MSNs seen in the top panel. Scale bar is 5 μm. Reprinted from Ref. [18]. Copyright 2013 American Chemical Society.

Monitoring Drug Release in Real-time in Cancer Cells Using FRET-MSNs

However, it is important to demonstrate if we can correlate this change in the FRET signal with the corresponding drug release and its downstream therapeutic efficacy. To prove this, we treated HeLa cells with TA and NEM to modulate the cytoplasmic GSH concentration prior to the addition of DOX-loaded FRET-MSNs, and the viability of HeLa cells was monitored 24 h after treatment (Figure 4.14). As seen in Figure 4.14A, quantitative analysis of the relative intensities of coumarin emission (Ex = 405 nm. Em = 450 nm) also showed a similar trend of increasing coumarin emission as the intracellular GSH concentration increased. Based on these results, we were also able to confirm that the release of the molecular gate (FITC-β-CD) occurred in response to the redox stimuli, GSH present in millimolar levels in the cytoplasm of cancer cells [257–259]. The change in intracellular GSH concentration will result in a change in the

extent of disulfide bond cleavage, which shall be displayed as a change in the FRET signal R as well as the amount of DOX released. Since the amount of DOX released from the nanoparticles influences the viability of cells, we can then correlate the change in FRET signal with the cell viability. As expected, the presence of TA, which increased the intracellular GSH concentration, led to an increase in the unlocking of pores which was associated with a decrease in the cell viability as well as an decrease in the FRET signal, R (thus 1/R increases as seen inFigure 4.14B, FRET OFF). In contrast, when the cells were pre-treated with the GSH scavenger, NEM, we observed an increase in the cell viability as well as a increase in the FRET signal ratio, R (thus 1/R decreases as seen in Figure 4.14B, FRET ON). These results demonstrated the ability of our proposed FRET-MSNs based DDS in real-time monitoring drug release and reporting cell viability.

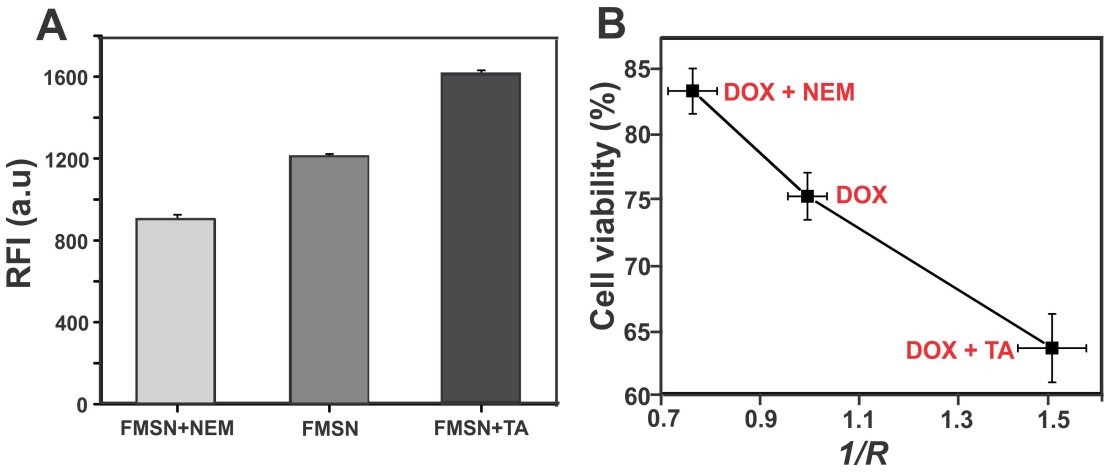

Figure 4.14: (A) Quantitative comparison of the relative fluorescence intensities (RFI, Em = 450 nm, Ex = 405 nm), of the HeLa cells treated with TA and NEM. (D) Correlation between FRET signal R and cell viability, when the HeLa cells were treated with DOX loaded FRET-MSNs at varying GSH concentrations. Reprinted from Ref. [18]. Copyright 2013 American Chemical Society.

4.1.3 Conclusions

In summary, we have successfully demonstrated the formation of redox-responsive fluorescent MSNs, comprised of an integrated FRET-based real-time monitoring system, which enabled tracking the release of the payload from the pores of the MSNs in real-time, by measuring the change in the FRET signal. We have shown a good correlation

between the change in the FRET signal and the extent of drug released at different GSH concentrations both at the solution level as well as inside the cells. The advantage of our platform is that it can be extended to any cargo, fluorescent or non-fluorescent, as the molecular structures responsible for real-time monitoring are integrated within the unlocking mechanism present on the nanoparticle, and hence, we do not need to rely on the optical properties of the drug or a model dye. As such, we can monitor the release of the cargo on a temporal level, even if the drug is non-fluorescent, thus demonstrating the versatility of our platform. Additionally, no structural modification of the drug is required as the donor-acceptor pair is integrated within the nanoparticles, thereby preserving the drug efficacy. Numerous studies have demonstrated significantly higher intracellular glutathione concentrations in cancer cells as compared to normal cells, we can expect our FRET-MSNs to release the biomolecules more selectively in cancer cells. However, we can expect to extend the applications of the FRET-MSNs to any trigger such as pH or temperature by making appropriate structural modifications, since the FRET signal only depends on the donor-acceptor pair. Thus, we can envision our real-time monitoring system would provide a unique and universal strategy for overcoming the challenges encountered in the tracking (location) and monitoring (time) of drug release over extended periods of time and shows great potential for bio-applications, such as the investigation of cancer stem cells and effective therapies against them. However, a more advanced real-time monitoring system should also possess the capability of achieving direct monitoring of the release kinetics of drugs. Hence, we will explore additional avenues for enabling our FRET-MSNs to precisely monitor the kinetics of drug release as our future goals.

4.1.4 Materials

All chemicals were purchased from Sigma-Aldrich or TCI Chemical and used as received.

Synthesis of FRET-MSNs

(a) NH_2-MSNs. In a typical synthesis procedure, 28 mg of sodium hydroxide and 100 mg of cetyl trimethyammonium bromide (CTAB) in sequence were completely dissolved

into 50 mL of deionized water under vigorous stirring at 80 °C. After the solution became clear, 0.5 mL of TEOS was added dropwise in 10 min. After 3 hours, 20 L of APTES was added and the vigorous stirring was continued for 20 h, and then milk-white as-synthesized materials were collected by centrifugation. In order to remove the surfactant, the as-synthesized materials were refluxed in a solution consisting of 50 mL ethanol and 0.5 mL hydrochloric acid (36-38%) for 12 hours, centrifuged and finally washed several times with methanol. The final products were dried for 12 h at 120 °C in vacuum. (b) Cys-MSNs. To a solution of N-Boc-cysteine (22 mg) and N-hydroxysuccinimide (NHS, 25 mg) in 5 mL anhydrous DMF at 0 °C, 1-ethyl-3-(3-dimethylaminopropyl)carbodiimide hydrochloride (EDC•HCl, 31 mg) was added. The solution was stirred at 0 °C for 30 min and recovered to room temperature for additional 4 hours. Then 100 mg of NH_2-MSNs in 5 mL DMF solution was added slowly and the mixture was keep stirring overnight under N_2. The nanoparticles were collected by centrifugation and washed several times with DMF and methanol, and finally dried in vacuum to obtain Cys-MSNs. (c) Cys-TA-MSNs. A solution of Cys-MSNs (80 mg) in 5 mL methanol was added dropwise into a solution of 2,2-dithiodipyridine (0.1 g) in methanol/pH7.4 PBS solution (v/v, 10 mL/1.5 mL). The mixture was stirred at room temperature overnight and the nanoparticles were collected by centrifugation, washed thrice with methanol and finally redispersed in 10 mL methanol. 1-adamantanethiol (0.1 g) in 2 mL methanol was then added to the above solution and the mixture was stirred overnight at room temperature under $N_2$2 atmosphere. The Cys-TA-MSNs were collected by centrifugation, washed several times with methanol, and then dried under vacuum. (d) CHC-MSNs. 5 mL DCM solution of Cys-TA-MSNs (60 mg) was cooled to 0 °C for 30 min and then 2 mL trifluoroacetic acid (TFA) were added. The mixture was stirred at 0 °C for 30 min and then recovered to room temperature for an additional 3 hours. Then 10 mL of methanol was added to dilute the mixture. The nanoparticles were collected by centrifugation and washed several times with methanol, dried in vacuum, and finally redispersed in 5 mL anhydrous DMF. To a solution of 7-hydroxycoumarin-3-carboxylic acid (100 mg) and NHS (80 mg) in 5 mL anhydrous DMF at 0 °C, 70 mg of EDC•HCl were added. The solution was stirred at 0 °C for 30

min and recovered to room temperature for an additional 4 hours. Then, the 5 mL of DMF solution consisting of TFA-treated Cys-TA-MSN nanoparticles was added slowly to the solution and the mixture was keep for stirring overnight. The nanoparticles were collected by centrifugation and washed several times with DMF and methanol, and then finally dried in vacuum to obtain the CHC-MSNs. (e) FITC-β-CD. Mono-6-deoxy-6-amino--cyclodextrin (NH2-β-CD) was first synthesized by a previously reported method [207]. 1H NMR (300 MHz, D2O): δ 4.97 (s, 7H), 3.74-3.88 (m), 3.38-3.56 (m), 3.08 (d, 1H, J = 14.2 Hz), 2.84 (dd, 1H, J1 = 7.0 Hz, J2 = 14.1 Hz). ESI-MS m/z 1132.3 [M-H]-. 38 mg FITC, 10 mg DMAP and 0.1 g NH2-β-CD were added into 5 mL anhydrous DMF and the solution was stirred overnight at room temperature under N_2. 10 mL acetone was added to the solution and the precipitate was collected and washed with acetone several times. ESI-MS m/z 1521.9 $[M-H]_-$, 761.3 $[M-2H]/2_-$.

Characterization of FRET-MSNs

UV-vis absorption spectra were recorded on a Varian Cary 50 spectrophotometer. Fluorescence spectra were recorder on a Varian Cary Eclipse fluorescence spectrophotometer. FT-IR spectra were collected on an Avatar Nicolet FT-IR330 spectrometer. Raman spectrum characterizations were performed on Laser Raman, Renishaw inVia Raman microscope. 1H NMR was acquired on Varian 400MHz NMR spectrometer. ESI-MS was collected on Finnigan LCQTM DUO LC/MS spectrometer. Transmission electron microscopy (TEM) was performed on a Topcon 002B electron microscope at 200 kV. Sample preparation was carried out by placing a drop of the freshly prepared colloidal solution on a carbon-coated copper grid and allowing the solution to evaporate. Nitrogen adsorption-desorption measurements were performed on a Micromeritics Tristar-3000 surface area analyzer at 196°C. The sample was dried at 200°C for 3 h before analysis. The Burnauer-Emmett-Teller (BET) specific surface areas were calculated using the first 10 experimental data points. Pore volumes were determined from the amount of N_2 adsorbed at the single point $P/P_0 = 0.98$.

Cell culture

HeLa cells were used for FRET-MSNs. HeLa cells were cultured in DMEM supplemented with 10% FBS and 1% streptomycin-penicillin. For the delivery experiment, passaged cells were prepared to 40-60% confluency in 24-well plates. After 24 h of plating, media was exchanged with serum-free basal media (500 μL) and FRET-MSNs/ X-tremeGENE complexes (50 μL) were added. After incubation for 6 hours, media was exchanged with normal growth medium. Fluorescence measurements were performed after 0-24 h after transfection.

Imaging of FRET-MSNs

At different time points following transfection, the cells were imaged using fluorescent microscopy. The effect of GSH concentration on the FRET signal was studied using the eplifluorescence microscopy. For this purpose, the fluorescent and phase contrast images were obtained using the Nikon T2500 inverted epifluorescence microscope. Each image was captured with different channels and focus. Images were processed and overlapped using Image-Pro (Media Cybernetics) and ImageJ (NIH). In order to monitor and quantify the change in FRET signal in vitro, confocal imaging was done using Zeiss LSM 510-META confocal microscope equipped with an Axiovert 200 inverted Scope.

Chapter 5

Conclusions and Perspectives

As can be seen from the earlier chapters, nanotechnology has had a tremendous and revolutionizing effect in the field of cancer therapy, molecular imaging and regenerative medicine. In combination with the advances made in cancer biology as well as stem cell biology, these nanotechnology-based approaches are expected to increase exponentially in the future as a result of increasing federal and corporate expenditure. What remains to be seen, however is the wide-spread commercialization of these technological advances. There are still several issues in terms of cost-benefit ratio, long-term toxicity concerns and regulatory considerations, that need to be overcome prior to their extensive use in the clinic. This thesis has demonstrated a few examples of developing multimodal or multifunctional nanoparticles for regulating cancer and stem cell fate, that are designed to overcome a few, if not all the above mentioned issues pertaining to nanomaterials.

In chapter 2, the design and generation of magnetic core-shell nanoparticles for cancer and stem cell applications was discussed . These core-shell nanoparticles were composed of a magnetic core and plasmonic shell and as a result, possessed multimodal capabilities (magnetic and plasmonic). In the initial part of this chapter, these nanoparticles were utilized for controlling the differentiation of neural stem cells and their real-time imaging. To this end, the magnetic core of these nanoparticles afforded magnetically- facilitated delivery of therapeutics leading to enhanced stem cell differentiation and minimal toxicity. The gold shell, on the other hand improved biocompatibility and provided a facile surface for tethering different therapeutics on the surface. Hence we were able to induce differentiation of stem cells into neurons and oligodendrocytes in a facile and efficient manner, while not compromising the inherent

stem cell characteristics. Additionally, dual mode imaging (MRI and dark-field imaging) was possible due to the multi-composite nature of these nanoparticles. In the later part of the chapter, the above-mentioned nanoparticles were then utilized for cancer therapy. Again, the gold shell allowed for facile conjugation of apoptotic peptides and targeting ligands on the surface of the nanoparticles, which led to improved solubility and efficacy of the peptides. The magnetic core, in addition to improving the delivery of the peptides via magnetically-facilitated delivery, also induced localized hyperthermia in the presence of an alternating magnetic field. Thus we were able to develop multifunctional nanoparticles which not only enabled effective delivery of therapeutics, but also enabled real-time imaging and concomittant hyperthermia to improve the overall therapeutic efficacy.

In chapter 3, we focused on the development of a cyclodextrin-tethered dendritic polymer vehicle (DexAMs) for simultaneous delivery of RNAi therapeutics and anticancer drugs. Since the DexAM moiety comprised of two different nanocarriers - dendrimers and cyclodextrins, we were able to co-deliver two different payloads using a singular vehicle specifically and efficiently to brain cancer cells. Additionally, since cyclodextrin moieties present in DexAM can encapsulate a wide majority of the hydrophobic drugs available commercially, this can preclude the use of toxic organic solvents for the administration of these drugs in the clinic. The siRNA used in this model study targeted EGFRvIII, a key oncogene known to be responsible for the dysregulated proliferation and migration of many types of cancer, and particularly brain cancer. The delivery of two different payloads targeting orthogonal signaling pathways led to a synergistic effect on brain cancer cell apoptosis.

Finally, in chapter 4, we designed a real-time monitoring system for drug release from nanoparticles in cells, based on fluorescence resonance energy transfer (FRET) mechanism. The FRET mechanism was based on the change in the emission profile of a donor-acceptor dye pair of coumarin and fluorescein isothiocyanate (FITC). To this end, we utilized mesoporous silica nanoparticles (MSNs) as a drug carrier and integrated a FRET-based monitoring system within the stimuli-responsive molecular valves blocking the release of the drugs from the pores of the MSNs. The molecular

valves were so designed to release the anti-cancer drugs trapped within the pores, only in the presence of excess glutathione encountered in the cytoplasm of cancer cells. The release of the molecular valves and subsequent release of entrapped drugs led a change in the FRET signal, thus enabling real-time monitoring of drug release both in solution and in cancer cells. Also, while we utilized a redox-responsive molecular valve as a model system, our platform is versatile enough to be extended to any stimuli and any cellular platform by making simple changes in the structural design.

This work has been truly novel and has the potential of being extended to clinical applications on its own or in combination with the other therapeutic strategies being employed currently. I hope that the research I have conducted helps to further this field of nanotechnology and nanomedicine.

References

[1] R. P. Feynman, "Theres plenty of room at the bottom," *Eng. Sci. (Caltech)*, vol. 23, pp. 22–36, 1960.

[2] D. F. Emerich and C. G. Thanos, "Nanotechnology and medicine," *Expert Opin Biol Ther*, vol. 3, no. 4, pp. 655–63, 2003.

[3] K. K. Jain, "Nanodiagnostics: application of nanotechnology in molecular diagnostics," *Expert Review of Molecular Diagnostics*, vol. 3, no. 2, pp. 153–161, 2003.

[4] J. Freitas, Robert A., "What is nanomedicine?," *Nanomedicine : nanotechnology, biology, and medicine*, vol. 1, no. 1, pp. 2–9, 2005.

[5] K. Riehemann, S. W. Schneider, T. A. Luger, B. Godin, M. Ferrari, and H. Fuchs, "Nanomedicine–challenge and perspectives," *Angew Chem Int Ed Engl*, vol. 48, no. 5, pp. 872–97, 2009.

[6] A. Solanki, J. D. Kim, and K.-B. Lee, "Nanotechnology for regenerative medicine: nanomaterials for stem cell imaging," *Nanomedicine*, vol. 3, no. 4, pp. 567–578, 2008.

[7] O. C. Farokhzad and R. Langer, "Nanomedicine: developing smarter therapeutic and diagnostic modalities," *Adv Drug Deliv Rev*, vol. 58, no. 14, pp. 1456–9, 2006.

[8] Y. Dang, Y. L. Zhang, L. Fan, H. C. Chen, and M. C. Roco, "Trends in worldwide nanotechnology patent applications: 1991 to 2008," *Journal of Nanoparticle Research*, vol. 12, no. 3, pp. 687–706, 2010.

[9] M. G. Harisinghani, J. Barentsz, P. F. Hahn, W. M. Deserno, S. Tabatabaei, C. H. van de Kaa, J. de la Rosette, and R. Weissleder, "Noninvasive detection of clinically occult lymph-node metastases in prostate cancer," *New England Journal of Medicine*, vol. 348, no. 25, pp. 2491–U5, 2003.

[10] D. W. Bartlett and M. E. Davis, "Insights into the kinetics of sirna-mediated gene silencing from live-cell and live-animal bioluminescent imaging," *Nucleic Acids Research*, vol. 34, no. 1, pp. 322–333, 2006.

[11] L.-Y. Chien, J.-K. Hsiao, S.-C. Hsu, M. Yao, C.-W. Lu, H.-M. Liu, Y.-C. Chen, C.-S. Yang, and D.-M. Huang, "In vivo magnetic resonance imaging of cell tropsim, trafficking mechanism, and therapeutic impact of human mesenchymal stem cells in a murine glioma model," *Biomaterials*, vol. 32, no. 12, pp. 3275–3284, 2011.

[12] M. Bruchez, M. Moronne, P. Gin, S. Weiss, and A. P. Alivisatos, "Semiconductor nanocrystals as fluorescent biological labels," *Science*, vol. 281, no. 5385, pp. 2013–2016, 1998.

[13] X. Bai, S. J. Son, S. Zhang, W. Liu, E. K. Jordan, J. A. Frank, T. Venkatesan, and S. B. Lee, "Synthesis of superparamagnetic nanotubes as mri contrast agents and for cell labeling," *Nanomedicine*, vol. 3, no. 2, pp. 163–174, 2008.

[14] M. F. Kircher, U. Mahmood, R. S. King, R. Weissleder, and L. Josephson, "A multimodal nanoparticle for preoperative magnetic resonance imaging and intraoperative optical brain tumor delineation," *Cancer Res*, vol. 63, no. 23, pp. 8122–5, 2003.

[15] L. Brannon-Peppas and J. O. Blanchette, "Nanoparticle and targeted systems for cancer therapy," *Adv Drug Deliv Rev*, vol. 56, no. 11, pp. 1649–59, 2004.

[16] D. W. Bartlett and M. E. Davis, "Impact of tumor-specific targeting and dosing schedule on tumor growth inhibition after intravenous administration of sirna-containing nanoparticles," *Biotechnology and Bioengineering*, vol. 99, no. 4, pp. 975–985, 2008.

[17] N. C. Bellocq, S. H. Pun, G. S. Jensen, and M. E. Davis, "Transferrin-containing, cyclodextrin polymer-based particles for tumor-targeted gene delivery," *Bioconjugate Chemistry*, vol. 14, no. 6, pp. 1122–1132, 2003.

[18] J. Lai, B. P. Shah, E. Garfunkel, and K. B. Lee, "Versatile fluorescence resonance energy transfer-based mesoporous silica nanoparticles for real-time monitoring of drug release," *Acs Nano*, vol. 7, no. 3, pp. 2741–50, 2013.

[19] V. P. Torchilin, "Multifunctional nanocarriers," *Advanced Drug Delivery Reviews*, vol. 58, no. 14, pp. 1532–1555, 2006.

[20] A. M. Chen, M. Zhang, D. G. Wei, D. Stueber, O. Taratula, T. Minko, and H. X. He, "Co-delivery of doxorubicin and bcl-2 sirna by mesoporous silica nanoparticles enhances the efficacy of chemotherapy in multidrug-resistant cancer cells," *Small*, vol. 5, no. 23, pp. 2673–2677, 2009.

[21] J. Cheon and J.-H. Lee, "Synergistically integrated nanoparticles as multimodal probes for nanobiotechnology," *Accounts of Chemical Research*, vol. 41, no. 12, pp. 1630–1640, 2008.

[22] R. Langer, "Drug delivery and targeting," *Nature*, vol. 392, no. 6679, pp. 5–10, 1998.

[23] R. Duncan, "The dawning era of polymer therapeutics," *Nat Rev Drug Discov*, vol. 2, no. 5, pp. 347–60, 2003.

[24] K. C. Li, S. D. Pandit, S. Guccione, and M. D. Bednarski, "Molecular imaging applications in nanomedicine," *Biomed Microdevices*, vol. 6, no. 2, pp. 113–6, 2004.

[25] T. M. Allen, "Ligand-targeted therapeutics in anticancer therapy," *Nat Rev Cancer*, vol. 2, no. 10, pp. 750–63, 2002.

[26] R. K. Jain, "The next frontier of molecular medicine: delivery of therapeutics," *Nat Med*, vol. 4, no. 6, pp. 655–7, 1998.

[27] M. Ferrari, "Cancer nanotechnology: opportunities and challenges," *Nat Rev Cancer*, vol. 5, no. 3, pp. 161–71, 2005.

[28] E. K. Chow and D. Ho, "Cancer nanomedicine: from drug delivery to imaging," *Sci Transl Med*, vol. 5, no. 216, p. 216rv4, 2013.

[29] S. K. Sahoo and V. Labhasetwar, "Nanotech approaches to drug delivery and imaging," *Drug Discov Today*, vol. 8, no. 24, pp. 1112–20, 2003.

[30] J. W. Park, "Liposome-based drug delivery in breast cancer treatment," *Breast Cancer Res*, vol. 4, no. 3, pp. 95–9, 2002.

[31] D. H. Kim and J. J. Rossi, "Strategies for silencing human disease using rna interference," *Nature Reviews Genetics*, vol. 8, no. 3, pp. 173–184, 2007.

[32] C. J. Murphy, A. M. Gole, J. W. Stone, P. N. Sisco, A. M. Alkilany, E. C. Goldsmith, and S. C. Baxter, "Gold nanoparticles in biology: Beyond toxicity to cellular imaging," *Accounts of Chemical Research*, vol. 41, no. 12, pp. 1721–1730, 2008.

[33] H. B. Na, I. C. Song, and T. Hyeon, "Inorganic nanoparticles for mri contrast agents," *Advanced Materials*, vol. 21, no. 21, pp. 2133–2148, 2009.

[34] S. S. Li, H. He, Q. C. Jiao, and P. H. Chuong, "Applications of carbon nanotubes in drug and gene delivery," *Progress in Chemistry*, vol. 20, no. 11, pp. 1798–1803, 2008.

[35] A. Bianco, K. Kostarelos, and M. Prato, "Applications of carbon nanotubes in drug delivery," *Current Opinion in Chemical Biology*, vol. 9, no. 6, pp. 674–679, 2005.

[36] M. Liong, J. Lu, M. Kovochich, T. Xia, S. G. Ruehm, A. E. Nel, F. Tamanoi, and J. I. Zink, "Multifunctional inorganic nanoparticles for imaging, targeting, and drug delivery," *Acs Nano*, vol. 2, no. 5, pp. 889–896, 2008.

[37] L. Y. T. Chou, K. Ming, and W. C. W. Chan, "Strategies for the intracellular delivery of nanoparticles," *Chemical Society Reviews*, vol. 40, no. 1, pp. 233–245, 2011.

[38] C. Sun, J. S. H. Lee, and M. Zhang, "Magnetic nanoparticles in mr imaging and drug delivery," *Advanced Drug Delivery Reviews*, vol. 60, no. 11, pp. 1252–1265, 2008.

[39] C. Corot, P. Robert, J. M. Idee, and M. Port, "Recent advances in iron oxide nanocrystal technology for medical imaging," *Advanced Drug Delivery Reviews*, vol. 58, no. 14, pp. 1471–1504, 2006.

[40] Q. A. Pankhurst, J. Connolly, S. K. Jones, and J. Dobson, "Applications of magnetic nanoparticles in biomedicine," *Journal of Physics D-Applied Physics*, vol. 36, no. 13, pp. R167–R181, 2003.

[41] C. Corot, K. G. Petry, R. Trivedi, A. Saleh, C. Jonkmanns, J. F. Le Bas, E. Blezer, M. Rausch, B. Brochet, P. Foster-Gareau, D. Baleriaux, S. Gaillard, and V. Dousset, "Macrophage imaging in central nervous system and in carotid atherosclerotic plaque using ultrasmall superparamagnetic iron oxide in magnetic resonance imaging," *Investigative Radiology*, vol. 39, no. 10, pp. 619–625, 2004.

[42] D. Yoo, J. H. Lee, T. H. Shin, and J. Cheon, "Theranostic magnetic nanoparticles," *Acc Chem Res*, vol. 44, no. 10, pp. 863–74, 2011.

[43] A. Akbarzadeh, M. Samiei, and S. Davaran, "Magnetic nanoparticles: preparation, physical properties, and applications in biomedicine," *Nanoscale Res Lett*, vol. 7, no. 1, p. 144, 2012.

[44] A. K. Gupta and M. Gupta, "Synthesis and surface engineering of iron oxide nanoparticles for biomedical applications," *Biomaterials*, vol. 26, no. 18, pp. 3995–4021, 2005.

[45] S. E. McNeil, "Nanotechnology for the biologist," *J Leukoc Biol*, vol. 78, no. 3, pp. 585–94, 2005.

[46] L. Frullano and T. J. Meade, "Multimodal mri contrast agents," *J Biol Inorg Chem*, vol. 12, no. 7, pp. 939–49, 2007.

[47] O. Veiseh, J. W. Gunn, and M. Zhang, "Design and fabrication of magnetic nanoparticles for targeted drug delivery and imaging," *Adv Drug Deliv Rev*, vol. 62, no. 3, pp. 284–304, 2010.

[48] T. Hyeon, "Chemical synthesis of magnetic nanoparticles," *Chemical Communications*, no. 8, pp. 927–934, 2003. Times Cited: 610.

[49] R. S. Molday and D. MacKenzie, "Immunospecific ferromagnetic iron-dextran reagents for the labeling and magnetic separation of cells," *J Immunol Methods*, vol. 52, no. 3, pp. 353–67, 1982.

[50] S. Lee, S. Kim, J. Choo, S. Y. Shin, Y. H. Lee, H. Y. Choi, S. Ha, K. Kang, and C. H. Oh, "Biological imaging of hek293 cells expressing plc gamma 1 using surface-enhanced raman microscopy," *Analytical Chemistry*, vol. 79, no. 3, pp. 916–922, 2007.

[51] S. H. Sun, H. Zeng, D. B. Robinson, S. Raoux, P. M. Rice, S. X. Wang, and G. X. Li, "Monodisperse mfe2o4 (m = fe, co, mn) nanoparticles," *Journal of the American Chemical Society*, vol. 126, no. 1, pp. 273–279, 2004.

[52] C. Xu and S. Sun, "Monodisperse magnetic nanoparticles for biomedical applications," *Polymer International*, vol. 56, no. 7, pp. 821–826, 2007.

[53] J.-H. Lee, Y.-M. Huh, Y.-w. Jun, J.-w. Seo, J.-t. Jang, H.-T. Song, S. Kim, E.-J. Cho, H.-G. Yoon, J.-S. Suh, and J. Cheon, "Artificially engineered magnetic nanoparticles for ultra-sensitive molecular imaging," *Nature Medicine*, vol. 13, no. 1, pp. 95–99, 2007.

[54] M. A. Willard, L. K. Kurihara, E. E. Carpenter, S. Calvin, and V. G. Harris, "Chemically prepared magnetic nanoparticles," *International Materials Reviews*, vol. 49, no. 3-4, pp. 125–170, 2004.

[55] R. Weissleder, A. Bogdanov, E. A. Neuwelt, and M. Papisov, "Long-circulating iron-oxides for mr-imaging," *Advanced Drug Delivery Reviews*, vol. 16, no. 2-3, pp. 321–334, 1995.

[56] M. G. Harisinghani and R. Weissleder, "Sensitive, noninvasive detection of lymph node metastases," *Plos Medicine*, vol. 1, no. 3, pp. 202–209, 2004.

[57] W. S. Enochs, G. Harsh, F. Hochberg, and R. Weissleder, "Improved delineation of human brain tumors on mr images using a long-circulating, superparamagnetic iron oxide agent," *Jmri-Journal of Magnetic Resonance Imaging*, vol. 9, no. 2, pp. 228–232, 1999.

[58] P. Varallyay, G. Nesbit, L. L. Muldoon, R. R. Nixon, J. Delashaw, J. I. Cohen, A. Petrillo, D. Rink, and E. A. Neuwelt, "Comparison of two superparamagnetic viral-sized iron oxide particles ferumoxides and ferumoxtran-10 with a gadolinium chelate in imaging intracranial tumors," *American Journal of Neuroradiology*, vol. 23, no. 4, pp. 510–519, 2002.

[59] C. A. Taschner, S. G. Wetzel, M. Tolnay, J. Froehlich, A. Merlo, and E. W. Radue, "Characteristics of ultrasmall superparamagnetic iron oxides in patients with brain tumors," *American Journal of Roentgenology*, vol. 185, no. 6, pp. 1477–1486, 2005.

[60] Y. E. L. Koo, G. R. Reddy, M. Bhojani, R. Schneider, M. A. Philbert, A. Rehemtulla, B. D. Ross, and R. Kopelman, "Brain cancer diagnosis and therapy with nanoplatforms," *Advanced Drug Delivery Reviews*, vol. 58, no. 14, pp. 1556–1577, 2006.

[61] P. Cherukuri, E. S. Glazer, and S. A. Curleya, "Targeted hyperthermia using metal nanoparticles," *Advanced Drug Delivery Reviews*, vol. 62, no. 3, pp. 339–345, 2010.

[62] V. S. Kalambur, E. K. Longmire, and J. C. Bischof, "Cellular level loading and heating of superparamagnetic iron oxide nanoparticles," *Langmuir*, vol. 23, no. 24, pp. 12329–12336, 2007.

[63] B. Samanta, H. Yan, N. O. Fischer, J. Shi, D. J. Jerry, and V. M. Rotello, "Protein-passivated fe3o4 nanoparticles: low toxicity and rapid heating for thermal therapy," *Journal of Materials Chemistry*, vol. 18, no. 11, pp. 1204–1208, 2008.

[64] M. Faraday *Philos. Trans. R. Soc. London*, vol. 147, pp. 145–181, 1857.

[65] M. C. Daniel and D. Astruc, "Gold nanoparticles: Assembly, supramolecular chemistry, quantum-size-related properties, and applications toward biology, catalysis, and nanotechnology," *Chemical Reviews*, vol. 104, no. 1, pp. 293–346, 2004.

[66] X. Huang, P. K. Jain, I. H. El-Sayed, and M. A. El-Sayed, "Gold nanoparticles: interesting optical properties and recent applications in cancer diagnostic and therapy," *Nanomedicine*, vol. 2, no. 5, pp. 681–693, 2007.

[67] X. Huang, P. K. Jain, I. H. El-Sayed, and M. A. El-Sayed, "Plasmonic photothermal therapy (pptt) using gold nanoparticles," *Lasers in Medical Science*, vol. 23, no. 3, pp. 217–228, 2008.

[68] X. H. Huang, I. H. El-Sayed, W. Qian, and M. A. El-Sayed, "Cancer cell imaging and photothermal therapy in the near-infrared region by using gold nanorods," *Journal of the American Chemical Society*, vol. 128, no. 6, pp. 2115–2120, 2006.

[69] S. Lal, S. E. Clare, and N. J. Halas, "Nanoshell-enabled photothermal cancer therapy: Impending clinical impact," *Accounts of Chemical Research*, vol. 41, no. 12, pp. 1842–1851, 2008.

[70] L. He, M. D. Musick, S. R. Nicewarner, F. G. Salinas, S. J. Benkovic, M. J. Natan, and C. D. Keating, "Colloidal au-enhanced surface plasmon resonance for ultrasensitive detection of dna hybridization," *Journal of the American Chemical Society*, vol. 122, no. 38, pp. 9071–9077, 2000.

[71] J. J. Storhoff, R. Elghanian, R. C. Mucic, C. A. Mirkin, and R. L. Letsinger, "One-pot colorimetric differentiation of polynucleotides with single base imperfections using gold nanoparticle probes," *Journal of the American Chemical Society*, vol. 120, no. 9, pp. 1959–1964, 1998.

[72] E. Boisselier and D. Astruc, "Gold nanoparticles in nanomedicine: preparations, imaging, diagnostics, therapies and toxicity," *Chemical Society Reviews*, vol. 38, no. 6, pp. 1759–1782, 2009.

[73] D. Yelin, D. Oron, S. Thiberge, E. Moses, and Y. Silberberg, "Multiphoton plasmon-resonance microscopy," *Optics Express*, vol. 11, no. 12, pp. 1385–1391, 2003.

[74] C. X. Zhang, Y. Zhang, X. Wang, Z. M. Tang, and Z. H. Lu, "Hyper-rayleigh scattering of protein-modified gold nanoparticles," *Analytical Biochemistry*, vol. 320, no. 1, pp. 136–140, 2003.

[75] S. W. Bishnoi, C. J. Rozell, C. S. Levin, M. K. Gheith, B. R. Johnson, D. H. Johnson, and N. J. Halas, "All-optical nanoscale ph meter," *Nano Letters*, vol. 6, no. 8, pp. 1687–1692, 2006.

[76] Q. Hu, L.-L. Tay, M. Noestheden, and J. P. Pezacki, "Mammalian cell surface imaging with nitrile-functionalized nanoprobes: Biophysical characterization of aggregation and polarization anisotropy in sers imaging," *Journal of the American Chemical Society*, vol. 129, no. 1, pp. 14–15, 2007.

[77] J. Kneipp, H. Kneipp, B. Wittig, and K. Kneipp, "One- and two-photon excited optical ph probing for cells using surface-enhanced raman and hyper-raman nanosensors," *Nano Letters*, vol. 7, no. 9, pp. 2819–2823, 2007.

[78] A. P. Alivisatos, "Semiconductor clusters, nanocrystals, and quantum dots," *Science*, vol. 271, pp. 933–937, 1996.

[79] A. M. Smith, H. W. Duan, A. M. Mohs, and S. M. Nie, "Bioconjugated quantum dots for in vivo molecular and cellular imaging," *Advanced Drug Delivery Reviews*, vol. 60, no. 11, pp. 1226–1240, 2008.

[80] J. J. Jung, A. Solanki, K. A. Memoli, K. Kamei, H. Kim, M. A. Drahl, L. J. Williams, H. R. Tseng, and K. Lee, "Selective inhibition of human brain tumor cells through multifunctional quantum-dot-based sirna delivery," *Angewandte Chemie-International Edition*, vol. 49, no. 1, pp. 103–107, 2010.

[81] X. Michalet, F. F. Pinaud, L. A. Bentolila, J. M. Tsay, S. Doose, J. J. Li, G. Sundaresan, A. M. Wu, S. S. Gambhir, and S. Weiss, "Quantum dots for live cells, in vivo imaging, and diagnostics," *Science*, vol. 307, no. 5709, pp. 538–544, 2005.

[82] W. C. Chan, D. J. Maxwell, X. Gao, R. E. Bailey, M. Han, and S. Nie, "Luminescent quantum dots for multiplexed biological detection and imaging," *Current Opinion in Biotechnology*, vol. 13, no. 1, pp. 40–6, 2002.

[83] C. B. Murray, D. J. Norris, and M. G. Bawendi, "Synthesis and characterization of nearly monodisperse cde (e = s, se, te) semiconductor nanocrystallites," *Journal of the American Chemical Society*, vol. 115, no. 19, pp. 8706–8715, 1993.

[84] B. O. Dabbousi, J. RodriguezViejo, F. V. Mikulec, J. R. Heine, H. Mattoussi, R. Ober, K. F. Jensen, and M. G. Bawendi, "(cdse)zns core-shell quantum dots: Synthesis and characterization of a size series of highly luminescent nanocrystallites," *Journal of Physical Chemistry B*, vol. 101, no. 46, pp. 9463–9475, 1997.

[85] R. G. Xie, U. Kolb, J. X. Li, T. Basche, and A. Mews, "Synthesis and characterization of highly luminescent cdse-core cds/zn0.5cd0.5s/zns multishell nanocrystals," *Journal of the American Chemical Society*, vol. 127, no. 20, pp. 7480–7488, 2005.

[86] J. K. Jaiswal, H. Mattoussi, J. M. Mauro, and S. M. Simon, "Long-term multiple color imaging of live cells using quantum dot bioconjugates," *Nature Biotechnology*, vol. 21, no. 1, pp. 47–51, 2003.

[87] N. Gaponik, D. V. Talapin, A. L. Rogach, K. Hoppe, E. V. Shevchenko, A. Kornowski, A. Eychmuller, and H. Weller, "Thiol-capping of cdte nanocrystals: An alternative to organometallic synthetic routes," *Journal of Physical Chemistry B*, vol. 106, no. 29, pp. 7177–7185, 2002.

[88] D. Gerion, F. Pinaud, S. C. Williams, W. J. Parak, D. Zanchet, S. Weiss, and A. P. Alivisatos, "Synthesis and properties of biocompatible water-soluble silica-coated cdse/zns semiconductor quantum dots," *Journal of Physical Chemistry B*, vol. 105, no. 37, pp. 8861–8871, 2001.

[89] B. Dubertret, P. Skourides, D. J. Norris, V. Noireaux, A. H. Brivanlou, and A. Libchaber, "In vivo imaging of quantum dots encapsulated in phospholipid micelles," *Science*, vol. 298, no. 5599, pp. 1759–1762, 2002.

[90] B. Ballou, B. C. Lagerholm, L. A. Ernst, M. P. Bruchez, and A. S. Waggoner, "Noninvasive imaging of quantum dots in mice," *Bioconjugate Chemistry*, vol. 15, no. 1, pp. 79–86, 2004.

[91] L. Josephson, M. F. Kircher, U. Mahmood, Y. Tang, and R. Weissleder, "Near-infrared fluorescent nanoparticles as combined mr/optical imaging probes," *Bioconjugate Chemistry*, vol. 13, no. 3, pp. 554–560, 2002.

[92] M. K. So, C. J. Xu, A. M. Loening, S. S. Gambhir, and J. H. Rao, "Self-illuminating quantum dot conjugates for in vivo imaging," *Nature Biotechnology*, vol. 24, no. 3, pp. 339–343, 2006.

[93] M. E. Akerman, W. C. W. Chan, P. Laakkonen, S. N. Bhatia, and E. Ruoslahti, "Nanocrystal targeting in vivo," *Proceedings of the National Academy of Sciences of the United States of America*, vol. 99, no. 20, pp. 12617–12621, 2002.

[94] W. B. Cai, D. W. Shin, K. Chen, O. Gheysens, Q. Z. Cao, S. X. Wang, S. S. Gambhir, and X. Y. Chen, "Peptide-labeled near-infrared quantum dots for imaging tumor vasculature in living subjects," *Nano Letters*, vol. 6, no. 4, pp. 669–676, 2006.

[95] K. Narayanan, S. K. Yen, Q. Q. Dou, P. Padmanabhan, T. Sudhaharan, S. Ahmed, J. Y. Ying, and S. T. Selvan, "Mimicking cellular transport mechanism in stem cells through endosomal escape of new peptide-coated quantum dots," *Scientific reports*, vol. 3, 2013.

[96] W. B. Cai and X. Y. Chen, "Nanoplatforms for targeted molecular imaging in living subjects," *Small*, vol. 3, no. 11, pp. 1840–1854, 2007.

[97] J. Zhou, Z. Liu, and F. Y. Li, "Upconversion nanophosphors for small-animal imaging," *Chemical Society Reviews*, vol. 41, no. 3, pp. 1323–1349, 2012.

[98] F. Wang, D. Banerjee, Y. Liu, X. Chen, and X. Liu, "Upconversion nanoparticles in biological labeling, imaging, and therapy," *Analyst*, vol. 135, no. 8, pp. 1839–1854, 2010.

[99] J.-C. Boyer, L. A. Cuccia, and J. A. Capobianco, "Synthesis of colloidal upconverting nayf4 : Er3+/yb3+ and tm3+/yb3+ monodisperse nanocrystals," *Nano Letters*, vol. 7, no. 3, pp. 847–852, 2007.

[100] J. C. Boyer, F. Vetrone, L. A. Cuccia, and J. A. Capobianco, "Synthesis of colloidal upconverting nayf4 nanocrystals doped with er3+, yb3+ and tm3+, yb3+ via thermal decomposition of lanthanide trifluoroacetate precursors," *Journal of the American Chemical Society*, vol. 128, no. 23, pp. 7444–7445, 2006.

[101] F. Wang, Y. Han, C. S. Lim, Y. Lu, J. Wang, J. Xu, H. Chen, C. Zhang, M. Hong, and X. Liu, "Simultaneous phase and size control of upconversion nanocrystals through lanthanide doping," *Nature*, vol. 463, no. 7284, pp. 1061–1065, 2010.

[102] M. Yu, F. Li, Z. Chen, H. Hu, C. Zhan, H. Yang, and C. Huang, "Laser scanning up-conversion luminescence microscopy for imaging cells labeled with rare-earth nanophosphors," *Analytical Chemistry*, vol. 81, no. 3, pp. 930–935, 2009.

[103] Q. Chen, X. Wang, F. Chen, Q. Zhang, B. Dong, H. Yang, G. Liu, and Y. Zhu, "Functionalization of upconverted luminescent nayf4: Yb/er nanocrystals by folic acid-chitosan conjugates for targeted lung cancer cell imaging," *Journal of Materials Chemistry*, vol. 21, no. 21, pp. 7661–7667, 2011.

[104] G. Chen, T. Y. Ohulchanskyy, W. C. Law, H. Agren, and P. N. Prasad, "Monodisperse naybf4: Tm3+/nagdf4 core/shell nanocrystals with near-infrared to near-infrared upconversion photoluminescence and magnetic resonance properties," *Nanoscale*, vol. 3, no. 5, pp. 2003–2008, 2011.

[105] J. Ryu, H.-Y. Park, K. Kim, H. Kim, J. H. Yoo, M. Kang, K. Im, R. Grailhe, and R. Song, "Facile synthesis of ultrasmall and hexagonal nagdf4: Yb3+, er3+ nanoparticles with magnetic and upconversion imaging properties," *Journal of Physical Chemistry C*, vol. 114, no. 49, pp. 21077–21082, 2010.

[106] L.-Q. Xiong, Z.-G. Chen, M.-X. Yu, F.-Y. Li, C. Liu, and C.-H. Huang, "Synthesis, characterization, and in vivo targeted imaging of amine-functionalized rare-earth up-converting nanophosphors," *Biomaterials*, vol. 30, no. 29, pp. 5592–5600, 2009.

[107] Z. F. Liu, F. Wang, and X. Y. Chen, "Integrin alpha(v)beta(3)-targeted cancer therapy," *Drug Development Research*, vol. 69, no. 6, pp. 329–339, 2008.

[108] Q. Q. Zhan, J. Qian, H. J. Liang, G. Somesfalean, D. Wang, S. L. He, Z. G. Zhang, and S. Andersson-Engels, "Using 915 nm laser excited tm3+/er3+/ho3+-doped naybf4 upconversion nanoparticles for in vitro and deeper in vivo bioimaging without overheating irradiation," *Acs Nano*, vol. 5, no. 5, pp. 3744–3757, 2011.

[109] L. Xiong, Z. Chen, Q. Tian, T. Cao, C. Xu, and F. Li, "High contrast upconversion luminescence targeted imaging in vivo using peptide-labeled nanophosphors," *Analytical Chemistry*, vol. 81, no. 21, pp. 8687–8694, 2009.

[110] X.-F. Yu, Z. Sun, M. Li, Y. Xiang, Q.-Q. Wang, F. Tang, Y. Wu, Z. Cao, and W. Li, "Neurotoxin-conjugated upconversion nanoprobes for direct visualization of tumors under near-infrared irradiation," *Biomaterials*, vol. 31, no. 33, pp. 8724–8731, 2010.

[111] L. Cheng, C. Wang, X. X. Ma, Q. L. Wang, Y. Cheng, H. Wang, Y. G. Li, and Z. Liu, "Multifunctional upconversion nanoparticles for dual-modal imaging-guided stem cell therapy under remote magnetic control," *Advanced Functional Materials*, vol. 23, no. 3, pp. 272–280, 2013.

[112] J. A. Hubbell and A. Chilkoti, "Nanomaterials for drug delivery," *Science*, vol. 337, no. 6092, pp. 303–305, 2012.

[113] D. W. Pack, A. S. Hoffman, S. Pun, and P. S. Stayton, "Design and development of polymers for gene delivery," *Nature Reviews Drug Discovery*, vol. 4, no. 7, pp. 581–593, 2005.

[114] E. R. Gillies and J. M. J. Frechet, "Dendrimers and dendritic polymers in drug delivery," *Drug Discovery Today*, vol. 10, no. 1, pp. 35–43, 2005.

[115] D. A. Tomalia, H. Baker, J. Dewald, M. Hall, G. Kallos, S. Martin, J. Roeck, J. Ryder, and P. Smith, "A new class of polymer: starburst-dendritic macromolecules," *Polymer Journal*, vol. 17, pp. 117–132, 1985.

[116] R. Esfand and D. A. Tomalia, "Poly(amidoamine) (pamam) dendrimers: from biomimicry to drug delivery and biomedical applications," *Drug Discovery Today*, vol. 6, no. 8, pp. 427–436, 2001. Times Cited: 681.

[117] N. Malik, R. Wiwattanapatapee, R. Klopsch, K. Lorenz, H. Frey, J. W. Weener, E. W. Meijer, W. Paulus, and R. Duncan, "Dendrimers: Relationship between structure and biocompatibility in vitro, and preliminary studies on the biodistribution of i-125-labelled polyamidoamine dendrimers in vivo," *Journal of Controlled Release*, vol. 65, no. 1-2, pp. 133–148, 2000.

[118] C. J. Hawker and J. M. J. Frechet, "Preparation of polymers with controlled molecular architecture - a new convergent approach to dendritic macromolecules," *Journal of the American Chemical Society*, vol. 112, no. 21, pp. 7638–7647, 1990.

[119] M. J. Liu, K. Kono, and J. M. J. Frechet, "Water-soluble dendritic unimolecular micelles: Their potential as drug delivery agents," *Journal of Controlled Release*, vol. 65, no. 1-2, pp. 121–131, 2000.

[120] J. Haensler and F. C. Szoka, "Polyamidoamine cascade polymers mediate efficient transfection of cells in culture," *Bioconjugate Chemistry*, vol. 4, no. 5, pp. 372–379, 1993.

[121] C. Rudolph, J. Lausier, S. Naundorf, R. H. Muller, and J. Rosenecker, "In vivo gene delivery to the lung using polyethylenimine and fractured polyamidoamine dendrimers," *Journal of Gene Medicine*, vol. 2, no. 4, pp. 269–278, 2000.

[122] Y. Harada, M. Iwai, S. Tanaka, T. Okanoue, K. Kashima, H. Maruyama-Tabata, H. Hirai, E. Satoh, J. Imanishi, and O. Mazda, "Highly efficient suicide gene expression in hepatocellular carcinoma cells by epstein-barr virus-based plasmid vectors combined with polyamidoamine dendrimer," *Cancer Gene Therapy*, vol. 7, no. 1, pp. 27–36, 2000.

[123] J. F. G. A. Jansen, E. M. M. Debrabandervandenberg, and E. W. Meijer, "Encapsulation of guest molecules into a dendritic box," *Science*, vol. 266, no. 5188, pp. 1226–1229, 1994.

[124] J. F. G. A. Jansen, E. W. Meijer, and E. M. M. Debrabandervandenberg, "The dendritic box - shape-selective liberation of encapsulated guests," *Journal of the American Chemical Society*, vol. 117, no. 15, pp. 4417–4418, 1995.

[125] C. Kojima, K. Kono, K. Maruyama, and T. Takagishi, "Synthesis of polyamidoamine dendrimers having poly(ethylene glycol) grafts and their ability to encapsulate anticancer drugs," *Bioconjugate Chemistry*, vol. 11, no. 6, pp. 910–917, 2000.

[126] N. Malik, E. G. Evagorou, and R. Duncan, "Dendrimer-platinate: a novel approach to cancer chemotherapy," *Anti-Cancer Drugs*, vol. 10, no. 8, pp. 767–776, 1999.

[127] R. X. Zhuo, B. Du, and Z. R. Lu, "In vitro release of 5-fluorouracil with cyclic core dendritic polymer," *Journal of Controlled Release*, vol. 57, no. 3, pp. 249–257, 1999.

[128] K. Kono, M. Liu, and J. M. Frechet, "Design of dendritic macromolecules containing folate or methotrexate residues," *Bioconjug Chem*, vol. 10, no. 6, pp. 1115–21, 1999.

[129] J. Sudimack and R. J. Lee, "Targeted drug delivery via the folate receptor," *Advanced Drug Delivery Reviews*, vol. 41, no. 2, pp. 147–162, 2000.

[130] A. Quintana, E. Raczka, L. Piehler, I. Lee, A. Myc, I. Majoros, A. K. Patri, T. Thomas, J. Mule, and J. R. Baker, "Design and function of a dendrimer-based therapeutic nanodevice targeted to tumor cells through the folate receptor," *Pharmaceutical Research*, vol. 19, no. 9, pp. 1310–1316, 2002.

[131] M. Vallet-Regi, A. Ramila, R. P. del Real, and J. Perez-Pariente, "A new property of mcm-41: Drug delivery system," *Chemistry of Materials*, vol. 13, no. 2, pp. 308–311, 2001.

[132] M. Vallet-Regi, "Ordered mesoporous materials in the context of drug delivery systems and bone tissue engineering," *Chemistry-a European Journal*, vol. 12, no. 23, pp. 5934–5943, 2006.

[133] Y. Zhao, B. G. Trewyn, I. I. Slowing, and V. S. Y. Lin, "Mesoporous silica nanoparticle-based double drug delivery system for glucose-responsive controlled release of insulin and cyclic amp," *Journal of the American Chemical Society*, vol. 131, no. 24, pp. 8398–+, 2009.

[134] B. Moulari, D. Pertuit, Y. Pellequer, and A. Lamprecht, "The targeting of surface modified silica nanoparticles to inflamed tissue in experimental colitis," *Biomaterials*, vol. 29, no. 34, pp. 4554–4560, 2008.

[135] C. Altaner and V. Altanerova, "Stem cell based glioblastoma gene therapy," *Neoplasma*, vol. 59, no. 6, pp. 756–60, 2012.

[136] F. Tang, L. Li, and D. Chen, "Mesoporous silica nanoparticles: synthesis, biocompatibility and drug delivery," *Adv Mater*, vol. 24, no. 12, pp. 1504–34, 2012.

[137] N. J. Halas, "Nanoscience under glass: The versatile chemistry of silica nanostructures," *Acs Nano*, vol. 2, no. 2, pp. 179–183, 2008.

[138] V. Biju, "Chemical modifications and bioconjugate reactions of nanomaterials for sensing, imaging, drug delivery and therapy," *Chemical Society Reviews*, vol. 43, no. 3, pp. 744–764, 2014.

[139] C. T. Kresge, M. E. Leonowicz, W. J. Roth, J. C. Vartuli, and J. S. Beck, "Ordered mesoporous molecular-sieves synthesized by a liquid-crystal template mechanism," *Nature*, vol. 359, no. 6397, pp. 710–712, 1992.

[140] H. P. Lin and C. Y. Mou, "Structural and morphological control of cationic surfactant-templated mesoporous silica," *Accounts of Chemical Research*, vol. 35, no. 11, pp. 927–935, 2002.

[141] M. T. Anderson, J. E. Martin, J. G. Odinek, and P. P. Newcomer, "Effect of methanol concentration on ctab micellization and on the formation of surfactant-templated silica (sts)," *Chemistry of Materials*, vol. 10, no. 6, pp. 1490–1500, 1998.

[142] S. Huh, J. W. Wiench, J. C. Yoo, M. Pruski, and V. S. Y. Lin, "Organic functionalization and morphology control of mesoporous silicas via a co-condensation synthesis method," *Chemistry of Materials*, vol. 15, no. 22, pp. 4247–4256, 2003.

[143] J. Lu, M. Liong, J. I. Zink, and F. Tamanoi, "Mesoporous silica nanoparticles as a delivery system for hydrophobic anticancer drugs," *Small*, vol. 3, no. 8, pp. 1341–1346, 2007.

[144] J. Gu, S. Su, Y. Li, Q. He, F. Zhong, and J. Shi, "Surface modification-complexation strategy for cisplatin loading in mesoporous nanoparticles," *Journal of Physical Chemistry Letters*, vol. 1, no. 24, pp. 3446–3450, 2010.

[145] A. Nieto, F. Balas, M. Colilla, M. Manzano, and M. Vallet-Regi, "Functionalization degree of sba-15 as key factor to modulate sodium alendronate dosage," *Microporous and Mesoporous Materials*, vol. 116, no. 1-3, pp. 4–13, 2008.

[146] A. Sood and R. Panchagnula, "Peroral route: An opportunity for protein and peptide drug delivery," *Chemical Reviews*, vol. 101, no. 11, pp. 3275–3303, 2001.

[147] S. Hudson, J. Cooney, and E. Magner, "Proteins in mesoporous silicates," *Angewandte Chemie-International Edition*, vol. 47, no. 45, pp. 8582–8594, 2008.

[148] I. Slowing, B. G. Trewyn, and V. S. Y. Lin, "Mesoporous silica nanoparticles for intracellular delivery of membrane-impermeable proteins," *Journal of the American Chemical Society*, vol. 129, no. 28, pp. 8845–8849, 2007.

[149] F. Torney, B. G. Trewyn, V. S. Y. Lin, and K. Wang, "Mesoporous silica nanoparticles deliver dna and chemicals into plants," *Nature Nanotechnology*, vol. 2, no. 5, pp. 295–300, 2007.

[150] D. R. Radu, C. Y. Lai, K. Jeftinija, E. W. Rowe, S. Jeftinija, and V. S. Y. Lin, "A polyamidoamine dendrimer-capped mesoporous silica nanosphere-based gene transfection reagent," *Journal of the American Chemical Society*, vol. 126, no. 41, pp. 13216–13217, 2004.

[151] I. Y. Park, I. Y. Kim, M. K. Yoo, Y. J. Choi, M. H. Cho, and C. S. Cho, "Mannosylated polyethylenimine coupled mesoporous silica nanoparticles for receptor-mediated gene delivery," *International Journal of Pharmaceutics*, vol. 359, no. 1-2, pp. 280–287, 2008.

[152] T. A. Xia, M. Kovochich, M. Liong, H. Meng, S. Kabehie, S. George, J. I. Zink, and A. E. Nel, "Polyethyleneimine coating enhances the cellular uptake of mesoporous silica nanoparticles and allows safe delivery of sirna and dna constructs," *Acs Nano*, vol. 3, no. 10, pp. 3273–3286, 2009.

[153] X. Li, Q. R. Xie, J. X. Zhang, W. L. Xia, and H. C. Gu, "The packaging of sirna within the mesoporous structure of silica nanoparticles," *Biomaterials*, vol. 32, no. 35, pp. 9546–9556, 2011.

[154] J. M. Li, Y. Y. Wang, M. X. Zhao, C. P. Tan, Y. Q. Li, X. Y. Le, L. N. Ji, and Z. W. Mao, "Multifunctional qd-based co-delivery of sirna and doxorubicin to hela cells for reversal of multidrug resistance and real-time tracking," *Biomaterials*, vol. 33, no. 9, pp. 2780–2790, 2012.

[155] S. Angelos, N. M. Khashab, Y. W. Yang, A. Trabolsi, H. A. Khatib, J. F. Stoddart, and J. I. Zink, "ph clock-operated mechanized nanoparticles," *Journal of the American Chemical Society*, vol. 131, no. 36, pp. 12912–12914, 2009.

[156] C. R. Thomas, D. P. Ferris, J. H. Lee, E. Choi, M. H. Cho, E. S. Kim, J. F. Stoddart, J. S. Shin, J. Cheon, and J. I. Zink, "Noninvasive remote-controlled release of drug molecules in vitro using magnetic actuation of mechanized nanoparticles," *Journal of the American Chemical Society*, vol. 132, no. 31, pp. 10623–10625, 2010.

[157] B. Shah, P. T. Yin, S. Ghoshal, and K.-B. Lee, "Multimodal magnetic coreshell nanoparticles for effective stem-cell differentiation and imaging," *Angewandte Chemie-International Edition*, vol. 52, pp. 6190–6195, 2013.

[158] T. Reya, S. J. Morrison, M. F. Clarke, and I. L. Weissman, "Stem cells, cancer, and cancer stem cells," *Nature*, vol. 414, no. 6859, pp. 105–111, 2001.

[159] X. Y. Zhang, V. F. La Russa, L. Bao, J. Kolls, P. Schwarzenberger, and J. Reiser, "Lentiviral vectors for sustained transgene expression in human bone marrow-derived stromal cells," *Mol Ther*, vol. 5, no. 5 Pt 1, pp. 555–65, 2002.

[160] L. Ferreira, J. M. Karp, L. Nobre, and R. Langer, "New opportunities: The use of nanotechnologies to manipulate and track stem cells," *Cell Stem Cell*, vol. 3, no. 2, pp. 136–146, 2008.

[161] C. Sapet, N. Laurent, A. de Chevigny, L. Le Gourrierec, E. Bertosio, O. Zelphati, and C. Beclin, "High transfection efficiency of neural stem cells with magnetofection," *Biotechniques*, vol. 50, no. 3, pp. 187–189, 2011.

[162] S. I. Jenkins, M. R. Pickard, N. Granger, and D. M. Chari, "Magnetic nanoparticle-mediated gene transfer to oligodendrocyte precursor cell transplant populations is enhanced by magnetofection strategies," *Acs Nano*, vol. 5, no. 8, pp. 6527–6538, 2011.

[163] J. K. Park, J. Jung, P. Subramaniam, B. P. Shah, C. Kim, J. K. Lee, J. H. Cho, C. Lee, and K. B. Lee, "Graphite-coated magnetic nanoparticles as multimodal imaging probes and cooperative therapeutic agents for tumor cells," *Small*, vol. 7, no. 12, pp. 1647–1652, 2011.

[164] J. T. Jang, H. Nah, J. H. Lee, S. H. Moon, M. G. Kim, and J. Cheon, "Critical enhancements of mri contrast and hyperthermic effects by dopant-controlled magnetic nanoparticles," *Angewandte Chemie-International Edition*, vol. 48, no. 7, pp. 1234–1238, 2009.

[165] L. Y. Wang, H. Y. Park, S. I. I. Lim, M. J. Schadt, D. Mott, J. Luo, X. Wang, and C. J. Zhong, "Core@shell nanomaterials: gold-coated magnetic oxide nanoparticles," *Journal of Materials Chemistry*, vol. 18, no. 23, pp. 2629–2635, 2008.

[166] J. Huang, L. H. Bu, J. Xie, K. Chen, Z. Cheng, X. G. Li, and X. Y. Chen, "Effects of nanoparticle size on cellular uptake and liver mri with polyvinylpyrrolidone-coated iron oxide nanoparticles," *Acs Nano*, vol. 4, no. 12, pp. 7151–7160, 2010.

[167] W. R. Zhao, J. L. Gu, L. X. Zhang, H. R. Chen, and J. L. Shi, "Fabrication of uniform magnetic nanocomposite spheres with a magnetic core/mesoporous silica shell structure," *Journal of the American Chemical Society*, vol. 127, no. 25, pp. 8916–8917, 2005.

[168] S. Laurent, D. Forge, M. Port, A. Roch, C. Robic, L. V. Elst, and R. N. Muller, "Magnetic iron oxide nanoparticles: Synthesis, stabilization, vectorization, physicochemical characterizations, and biological applications," *Chemical Reviews*, vol. 108, no. 6, pp. 2064–2110, 2008.

[169] R. G. Chaudhuri and S. Paria, "Core/shell nanoparticles: Classes, properties, synthesis mechanisms, characterization, and applications," *Chemical Reviews*, vol. 112, no. 4, pp. 2373–2433, 2012.

[170] H. Y. Zhang, M. Y. Lee, M. G. Hogg, J. S. Dordick, and S. T. Sharfstein, "Gene delivery in three-dimensional cell cultures by superparamagnetic nanoparticles," *Acs Nano*, vol. 4, no. 8, pp. 4733–4743, 2010.

[171] H. Wang, K. J. Chen, S. T. Wang, M. Ohashi, K. I. Kamei, J. Sun, J. H. Ha, K. Liu, and H. R. Tseng, "A small library of dna-encapsulated supramolecular nanoparticles for targeted gene delivery," *Chemical Communications*, vol. 46, no. 11, pp. 1851–1853, 2010.

[172] Y. D. Jin, C. X. Jia, S. W. Huang, M. O'Donnell, and X. H. Gao, "Multifunctional nanoparticles as coupled contrast agents," *Nature Communications*, vol. 1, 2010.

[173] C. Xu, J. Xie, D. Ho, C. Wang, N. Kohler, E. G. Walsh, J. R. Morgan, Y. E. Chin, and S. Sun, "Au-fe3o4 dumbbell nanoparticles as dual-functional probes," *Angewandte Chemie-International Edition*, vol. 47, no. 1, pp. 173–176, 2008.

[174] S. Guo, Y. Huang, Q. Jiang, Y. Sun, L. Deng, Z. Liang, Q. Du, J. Xing, Y. Zhao, P. C. Wang, A. Dong, and X.-J. Liang, "Enhanced gene delivery and sirna silencing by gold nanoparticles coated with charge-reversal polyelectrolyte," *Acs Nano*, vol. 4, no. 9, pp. 5505–5511, 2010.

[175] I. Robinson, L. D. Tung, S. Maenosono, C. Waelti, and N. T. K. Thanh, "Synthesis of core-shell gold coated magnetic nanoparticles and their interaction with thiolated dna," *Nanoscale*, vol. 2, no. 12, pp. 2624–2630, 2010.

[176] C. Kim, B. P. Shah, P. Subramaniam, and K. B. Lee, "Synergistic induction of apoptosis in brain cancer cells by targeted codelivery of sirna and anticancer drugs," *Molecular pharmaceutics*, vol. 8, no. 5, pp. 1955–1961, 2011.

[177] M. R. Pickard, P. Barraud, and D. M. Chari, "The transfection of multipotent neural precursor/stem cell transplant populations with magnetic nanoparticles," *Biomaterials*, vol. 32, no. 9, pp. 2274–84, 2011.

[178] Y. Li, W.-M. Lau, K.-F. So, Y. Tong, and J. Shen, "Caveolin-1 inhibits oligodendroglial differentiation of neural stem/progenitor cells through modulating beta-catenin expression," *Neurochemistry International*, vol. 59, no. 2, pp. 114–121, 2011.

[179] M. Wegner and C. C. Stolt, "From stem cells to neurons and glia: a soxist's view of neural development," *Trends in Neurosciences*, vol. 28, no. 11, pp. 583–588, 2005.

[180] A. Solanki, S. Shah, P. T. Yin, and K.-B. Lee, "Nanotopography-mediated reverse uptake for sirna delivery into neural stem cells to enhance neuronal differentiation," *Scientific reports*, vol. 3, pp. 1553–1553, 2013.

[181] M. A. El-Sayed, "Some interesting properties of metals confined in time and nanometer space of different shapes," *Accounts of Chemical Research*, vol. 34, no. 4, pp. 257–264, 2001.

[182] D. R. Green and G. Kroemer, "The pathophysiology of mitochondrial cell death," *Science*, vol. 305, no. 5684, pp. 626–629, 2004.

[183] D. R. Green and J. C. Reed, "Mitochondria and apoptosis," *Science*, vol. 281, no. 5381, pp. 1309–1312, 1998.

[184] X. Luo, I. Budihardjo, H. Zou, C. Slaughter, and X. D. Wang, "Bid, a bcl2 interacting protein, mediates cytochrome c release from mitochondria in response to activation of cell surface death receptors," *Cell*, vol. 94, no. 4, pp. 481–490, 1998.

[185] J. Yang, X. S. Liu, K. Bhalla, C. N. Kim, A. M. Ibrado, J. Y. Cai, T. I. Peng, D. P. Jones, and X. D. Wang, "Prevention of apoptosis by bcl-2: Release of cytochrome c from mitochondria blocked," *Science*, vol. 275, no. 5303, pp. 1129–1132, 1997.

[186] N. Hail, "Mitochondria: A novel target for the chemoprevention of cancer," *Apoptosis*, vol. 10, no. 4, pp. 687–705, 2005.

[187] E. Jacotot, A. Deniaud, A. Borgne-Sanchez, Z. Touat, J. P. Briand, M. Le Bras, and C. Brenner, "Therapeutic peptides: Targeting the mitochondrion to modulate apoptosis," *Biochimica Et Biophysica Acta-Bioenergetics*, vol. 1757, no. 9-10, pp. 1312–1323, 2006.

[188] J. E. Constance and C. S. Lim, "Targeting malignant mitochondria with therapeutic peptides," *Ther Deliv*, vol. 3, no. 8, pp. 961–79, 2012.

[189] J. K. Ko, K. H. Choi, Z. Pan, P. H. Lin, N. Weisleder, C. W. Kim, and J. Ma, "The tail-anchoring domain of bfl1 and hccs1 targets mitochondrial membrane permeability to induce apoptosis," *Journal of Cell Science*, vol. 120, no. 16, pp. 2912–2923, 2007. Ko, Jae-Kyun Choi, Kyoung-Han Pan, Zui Lin, Peihui Weisleder, Noah Kim, Chul-Woo Ma, Jianjie.

[190] J. K. Ko, K. H. Choi, J. Peng, F. He, Z. Zhang, N. Weisleder, J. L. Lin, and J. J. Ma, "Amphipathic tail-anchoring peptide and bcl-2 homology domain-3 (bh3) peptides from bcl-2 family proteins induce apoptosis through different mechanisms," *Journal of Biological Chemistry*, vol. 286, no. 11, pp. 9038–9048, 2011.

[191] C. C. Berry and A. S. G. Curtis, "Functionalisation of magnetic nanoparticles for applications in biomedicine," *Journal of Physics D-Applied Physics*, vol. 36, no. 13, pp. R198–R206, 2003.

[192] D. A. Giljohann, D. S. Seferos, W. L. Daniel, M. D. Massich, P. C. Patel, and C. A. Mirkin, "Gold nanoparticles for biology and medicine," *Angewandte Chemie-International Edition*, vol. 49, no. 19, pp. 3280–3294, 2010.

[193] M. Goldberg, R. Langer, and X. Jia, "Nanostructured materials for applications in drug delivery and tissue engineering," *Journal of Biomaterials Science-Polymer Edition*, vol. 18, no. 3, pp. 241–268, 2007.

[194] J. R. McCarthy and R. Weissleder, "Multifunctional magnetic nanoparticles for targeted imaging and therapy," *Advanced Drug Delivery Reviews*, vol. 60, no. 11, pp. 1241–1251, 2008.

[195] A. E. Salah-Eldin, S. Inoue, S. E. Tsukamoto, H. Aoi, and M. Tsuda, "An association of bcl-2 phosphorylation and bax localization with their functions after hyperthermia and paclitaxel treatment," *International Journal of Cancer*, vol. 103, no. 1, pp. 53–60, 2003.

[196] Y. G. Shellman, W. R. Howe, L. A. Miller, N. B. Goldstein, T. R. Pacheco, R. L. Mahajan, S. M. LaRue, and D. A. Norris, "Hyperthermia induces endoplasmic reticulum-mediated apoptosis in melanoma and non-melanoma skin cancer cells," *Journal of Investigative Dermatology*, vol. 128, no. 4, pp. 949–956, 2008.

[197] I. K. Mellinghoff, M. Y. Wang, I. Vivanco, D. A. Haas-Kogan, S. J. Zhu, E. Q. Dia, K. V. Lu, K. Yoshimoto, J. H. Y. Huang, D. J. Chute, B. L. Riggs, S. Horvath, L. M. Liau, W. K. Cavenee, P. N. Rao, R. Beroukhim, T. C. Peck, J. C. Lee, W. R. Sellers, D. Stokoe, M. Prados, T. F. Cloughesy, C. L. Sawyers, and P. S. Mischel, "Molecular determinants of the response of glioblastomas to egfr kinase inhibitors," *New England Journal of Medicine*, vol. 353, no. 19, pp. 2012–2024, 2005.

[198] M. Nagane, A. Levitzki, A. Gazit, W. K. Cavenee, and H. J. S. Huang, "Drug resistance of human glioblastoma cells conferred by a tumor-specific mutant epidermal growth factor receptor through modulation of bcl-x-l and caspase-3-like proteases," *Proceedings of the National Academy of Sciences of the United States of America*, vol. 95, no. 10, pp. 5724–5729, 1998.

[199] L. Agemy, D. Friedmann-Morvinski, V. R. Kotamraju, L. Roth, K. N. Sugahara, O. M. Girard, R. F. Mattrey, I. M. Verma, and E. Ruoslahti, "Targeted nanoparticle enhanced proapoptotic peptide as potential therapy for glioblastoma," *Proceedings of the National Academy of Sciences of the United States of America*, vol. 108, no. 42, pp. 17450–17455, 2011.

[200] L. J. Pagliari, T. Kuwana, C. Bonzon, D. D. Newmeyer, S. Tu, H. M. Beere, and D. R. Green, "The multidomain proapoptotic molecules bax and bak are directly activated by heat," *Proc Natl Acad Sci U S A*, vol. 102, no. 50, pp. 17975–80, 2005.

[201] E. H. A. Nijhuis, S. Le Gac, A. A. Poot, J. Feijen, and I. Vermes, "Bax-mediated mitochondrial membrane permeabilization after heat treatment is caspase-2 dependent," *International Journal of Hyperthermia*, vol. 24, no. 4, pp. 357–365, 2008.

[202] F. Mac Gabhann, B. H. Annex, and A. S. Popel, "Gene therapy from the perspective of systems biology," *Current Opinion in Molecular Therapeutics*, vol. 12, no. 5, pp. 570–577, 2010.

[203] I. Collins and P. Workman, "New approaches to molecular cancer therapeutics," *Nature Chemical Biology*, vol. 2, no. 12, pp. 689–700, 2006.

[204] D. Bumcrot, M. Manoharan, V. Koteliansky, and D. W. Y. Sah, "Rnai therapeutics: a potential new class of pharmaceutical drugs," *Nature Chemical Biology*, vol. 2, no. 12, pp. 711–719, 2006.

[205] D. Castanotto and J. J. Rossi, "The promises and pitfalls of rna-interference-based therapeutics," *Nature*, vol. 457, no. 7228, pp. 426–433, 2009.

[206] C. H. Zhu, S. Jung, S. B. Luo, F. H. Meng, X. L. Zhu, T. G. Park, and Z. Y. Zhong, "Co-delivery of sirna and paclitaxel into cancer cells by biodegradable cationic micelles based on pdmaema-pcl-pdmaema triblock copolymers," *Biomaterials*, vol. 31, no. 8, pp. 2408–2416, 2010.

[207] W. Tang and S. C. Ng, "Facile synthesis of mono-6-amino-6-deoxy-alpha-, beta-, gamma-cyclodextrin hydrochlorides for molecular recognition, chiral separation and drug delivery," *Nature Protocols*, vol. 3, no. 4, 2008.

[208] K. Uekama, F. Hirayama, and T. Irie, "Cyclodextrin drug carrier systems," *Chemical Reviews*, vol. 98, no. 5, pp. 2045–2076, 1998.

[209] M. E. Brewster and T. Loftsson, "Cyclodextrins as pharmaceutical solubilizers," *Advanced Drug Delivery Reviews*, vol. 59, no. 7, pp. 645–666, 2007.

[210] P. Knesl, D. Roseling, and U. Jordis, "Improved synthesis of substituted 6,7-dihydroxy-4-quinazolineamines: Tandutinib, erlotinib and gefitinib," *Molecules*, vol. 11, no. 4, pp. 286–297, 2006. Knesl, Petr Roeseling, Dirk Jordis, Ulrich.

[211] J. C. Stowell, R. I. Huot, and L. Vanvoast, "The synthesis of n-hydroxy-n'-phenyoctanediamide and its inhibitory effect on proliferation of axc rat prostate cancer cells," *Journal of Medicinal Chemistry*, vol. 38, no. 8, pp. 1411–1413, 1995.

[212] Y. H. P. Lee, S. Sathigari, Y. J. J. Lin, W. R. Ravis, G. Chadha, D. L. Parsons, V. K. Rangari, N. Wright, and R. J. Babu, "Gefitinib-cyclodextrin inclusion complexes: physico-chemical characterization and dissolution studies," *Drug Development and Industrial Pharmacy*, vol. 35, no. 9, pp. 1113–1120, 2009.

[213] A. N. Khramov and J. A. Stenken, "Enhanced microdialysis recovery of some tricyclic antidepressants and structurally related drugs by cyclodextrin-mediated transport," *Analyst*, vol. 124, no. 7, pp. 1027–1033, 1999.

[214] E. Hockly, V. M. Richon, B. Woodman, D. L. Smith, X. B. Zhou, E. Rosa, K. Sathasivam, S. Ghazi-Noori, A. Mahal, P. A. S. Lowden, J. S. Steffan, J. L. Marsh, L. M. Thompson, C. M. Lewis, P. A. Marks, and G. P. Bates, "Suberoylanilide hydroxamic acid, a histone deacetylase inhibitor, ameliorates motor deficits in a mouse model of huntington's disease," *Proceedings of the National Academy of Sciences of the United States of America*, vol. 100, no. 4, pp. 2041–2046, 2003.

[215] S. H. Pun, N. C. Bellocq, A. J. Liu, G. Jensen, T. Machemer, E. Quijano, T. Schluep, S. F. Wen, H. Engler, J. Heidel, and M. E. Davis, "Cyclodextrin-modified polyethylenimine polymers for gene delivery," *Bioconjugate Chemistry*, vol. 15, no. 4, pp. 831–840, 2004.

[216] M. E. Davis, "Non-viral gene delivery systems," *Current Opinion in Biotechnology*, vol. 13, no. 2, pp. 128–131, 2002.

[217] J. D. Heidel, S. W. Hu, X. F. Liu, T. Triche, and M. E. Davis, "Cyclodextrin-containing polycations (cdps) for in vivo delivery of sirna," *Abstracts of Papers of the American Chemical Society*, vol. 227, pp. 208–BIOT, 2004.

[218] D. M. Dykxhoorn, D. Palliser, and J. Lieberman, "The silent treatment: sirnas as small molecule drugs," *Gene Therapy*, vol. 13, no. 6, pp. 541–552, 2006.

[219] A. B. Heimberger, D. Suki, D. Yang, W. M. Shi, and K. Aldape, "The natural history of egfr and egfrviii in glioblastoma patients," *Journal of Translational Medicine*, vol. 3, 2005.

[220] C. J. Lai, R. Bao, X. Tao, J. Wang, R. Atoyan, H. Qu, D. G. Wang, L. Yin, M. Samson, J. Forrester, B. Zifcak, G. X. Xu, S. DellaRocca, H. X. Zhai, X. Cai, W. E. Munger, M. Keegan, C. V. Pepicelli, and C. G. Qian, "Cudc-101, a multitargeted inhibitor of histone deacetylase, epidermal growth factor receptor, and human epidermal growth factor receptor 2, exerts potent anticancer activity," *Cancer Research*, vol. 70, no. 9, pp. 3647–3656, 2010.

[221] J. A. Engelman, "Targeting pi3k signalling in cancer: opportunities, challenges and limitations," *Nature Reviews Cancer*, vol. 9, no. 8, pp. 550–562, 2009.

[222] P. X. Liu, H. L. Cheng, T. M. Roberts, and J. J. Zhao, "Targeting the phosphoinositide 3-kinase pathway in cancer," *Nature Reviews Drug Discovery*, vol. 8, no. 8, pp. 627–644, 2009.

[223] C. A. Learn, T. L. Hartzell, C. J. Wikstrand, G. E. Archer, J. N. Rich, A. H. Friedman, H. S. Friedman, D. D. Bigner, and J. H. Sampson, "Resistance to tyrosine kinase inhibition by mutant epidermal growth factor receptor variant iii contributes to the neoplastic phenotype of glioblastoma multiforme," *Clinical Cancer Research*, vol. 10, no. 9, pp. 3216–3224, 2004.

[224] P. Vaupel, F. Kallinowski, and P. Okunieff, "Blood-flow, oxygen and nutrient supply, and metabolic microenvironment of human-tumors - a review," *Cancer Research*, vol. 49, no. 23, pp. 6449–6465, 1989.

[225] D. Sidransky, "Emerging molecular markers of cancer," *Nature Reviews: Cancer*, vol. 2, no. 3, pp. 210–219, 2002.

[226] D. A. Tennant, R. V. Duran, and E. Gottlieb, "Targeting metabolic transformation for cancer therapy," *Nature Reviews: Cancer*, vol. 10, no. 4, pp. 267–277, 2010.

[227] J. A. Shen, Q. Yin, L. L. Chen, Z. W. Zhang, and Y. P. Li, "Co-delivery of paclitaxel and survivin shrna by pluronic p85-pei/tpgs complex nanoparticles to

overcome drug resistance in lung cancer," *Biomaterials*, vol. 33, no. 33, pp. 8613–8624, 2012.

[228] X. B. Xiong and A. Lavasanifar, "Traceable multifunctional micellar nanocarriers for cancer-targeted co-delivery of mdr-1 sirna and doxorubicin," *Acs Nano*, vol. 5, no. 6, pp. 5202–5213, 2011.

[229] W. C. Huang, S. H. Hu, K. H. Liu, S. Y. Chen, and D. M. Liu, "A flexible drug delivery chip for the magnetically-control led release of anti-epileptic drugs," *Journal of Controlled Release*, vol. 139, no. 3, pp. 221–228, 2009.

[230] A. Klaikherd, C. Nagamani, and S. Thayumanavan, "Multi-stimuli sensitive amphiphilic block copolymer assemblies," *Journal of the American Chemical Society*, vol. 131, no. 13, pp. 4830–4838, 2009.

[231] C. D. Lux, S. Joshi-Barr, T. Nguyen, E. Mahmoud, E. Schopf, N. Fomina, and A. Almutairi, "Biocompatible polymeric nanoparticles degrade and release cargo in response to biologically relevant levels of hydrogen peroxide," *Journal of the American Chemical Society*, vol. 134, no. 38, pp. 15758–15764, 2012.

[232] D. Schmaljohann, "Thermo- and ph-responsive polymers in drug delivery," *Advanced Drug Delivery Reviews*, vol. 58, no. 15, pp. 1655–1670, 2006.

[233] A. D. Wong, M. A. DeWit, and E. R. Gillies, "Amplified release through the stimulus triggered degradation of self-immolative oligomers, dendrimers, and linear polymers," *Advanced Drug Delivery Reviews*, vol. 64, no. 11, pp. 1031–1045, 2012.

[234] J. Nakanishi, H. Nakayama, T. Shimizu, H. Ishida, Y. Kikuchi, K. Yamaguchi, and Y. Horiike, "Light-regulated activation of cellular signaling by gold nanoparticles that capture and release amines," *Journal of the American Chemical Society*, vol. 131, no. 11, pp. 3822–+, 2009.

[235] A. Jana, K. S. P. Devi, T. K. Maiti, and N. D. P. Singh, "Perylene-3-ylmethanol: Fluorescent organic nanoparticles as a single-component photoresponsive nanocarrier with real-time monitoring of anticancer drug release," *Journal of the American Chemical Society*, vol. 134, no. 18, pp. 7656–7659, 2012.

[236] M. H. Lee, J. Y. Kim, J. H. Han, S. Bhuniya, J. L. Sessler, C. Kang, and J. S. Kim, "Direct fluorescence monitoring of the delivery and cellular uptake of a cancer-targeted rgd peptide-appended naphthalimide theragnostic prodrug," *Journal of the American Chemical Society*, vol. 134, no. 30, pp. 12668–12674, 2012.

[237] K. Ock, W. I. Jeon, E. O. Ganbold, M. Kim, J. Park, J. H. Seo, K. Cho, S. W. Joo, and S. Y. Lee, "Real-time monitoring of glutathione-triggered thiopurine anticancer drug release in live cells investigated by surface-enhanced raman scattering," *Analytical Chemistry*, vol. 84, no. 5, pp. 2172–2178, 2012.

[238] S. Santra, C. Kaittanis, O. J. Santiesteban, and J. M. Perez, "Cell-specific, activatable, and theranostic prodrug for dual-targeted cancer imaging and therapy," *Journal of the American Chemical Society*, vol. 133, no. 41, pp. 16680–16688, 2011.

[239] R. Weinstain, E. Segal, R. Satchi-Fainaro, and D. Shabat, "Real-time monitoring of drug release," *Chemical Communications*, vol. 46, no. 4, pp. 553–555, 2010.

[240] T. Asefa and Z. M. Tao, "Biocompatibility of mesoporous silica nanoparticles," *Chemical Research in Toxicology*, vol. 25, no. 11, pp. 2265–2284, 2012.

[241] W. J. Fang, J. Yang, J. W. Gong, and N. F. Zheng, "Photo- and ph-triggered release of anticancer drugs from mesoporous silica-coated pd@ag nanoparticles," *Advanced Functional Materials*, vol. 22, no. 4, pp. 842–848, 2012.

[242] D. P. Ferris, Y. L. Zhao, N. M. Khashab, H. A. Khatib, J. F. Stoddart, and J. I. Zink, "Light-operated mechanized nanoparticles," *Journal of the American Chemical Society*, vol. 131, no. 5, pp. 1686–+, 2009.

[243] C. J. Lai, R. Bao, X. Tao, J. Wang, R. Atoyan, H. Qu, D. G. Wang, L. Yin, M. Samson, J. Forrester, B. Zifcak, G. X. Xu, S. DellaRocca, H. X. Zhai, X. Cai, W. E. Munger, M. Keegan, C. V. Pepicelli, and C. G. Qian, "Cudc-101, a multitargeted inhibitor of histone deacetylase, epidermal growth factor receptor, and human epidermal growth factor receptor 2, exerts potent anticancer activity," *Cancer Research*, vol. 70, no. 9, pp. 3647–3656, 2010.

[244] Q. N. Lin, Q. Huang, C. Y. Li, C. Y. Bao, Z. Z. Liu, F. Y. Li, and L. Y. Zhu, "Anticancer drug release from a mesoporous silica based nanophotocage regulated by either a one- or two-photon process," *Journal of the American Chemical Society*, vol. 132, no. 31, pp. 10645–10647, 2010.

[245] C. Y. Liu, J. Guo, W. L. Yang, J. H. Hu, C. C. Wang, and S. K. Fu, "Magnetic mesoporous silica microspheres with thermo-sensitive polymer shell for controlled drug release," *Journal of Materials Chemistry*, vol. 19, no. 27, pp. 4764–4770, 2009.

[246] M. Ma, H. R. Chen, Y. Chen, X. Wang, F. Chen, X. Z. Cui, and J. L. Shi, "Au capped magnetic core/mesoporous silica shell nanoparticles for combined photothermo-/chemo-therapy and multimodal imaging," *Biomaterials*, vol. 33, no. 3, pp. 989–998, 2012.

[247] B. S. Tian and C. Yang, "Thermo-sensitive poly(n-isopropylacrylamide)/mesoporous silica nanocomposites as controlled delivery carriers: Loading and release behaviors for drug ibuprofen," *Journal of Nanoscience and Nanotechnology*, vol. 11, no. 3, pp. 1871–1879, 2011.

[248] C. Park, K. Oh, S. C. Lee, and C. Kim, "Controlled release of guest molecules from mesoporous silica particles based on a ph-responsive polypseudorotaxane motif," *Angewandte Chemie-International Edition*, vol. 46, no. 9, pp. 1455–1457, 2007.

[249] S. Angelos, Y. W. Yang, K. Patel, J. F. Stoddart, and J. I. Zink, "ph-responsive supramolecular nanovalves based on cucurbit[6]uril pseudorotaxanes," *Angewandte Chemie-International Edition*, vol. 47, no. 12, pp. 2222–2226, 2008.

[250] C. H. Lee, S. H. Cheng, I. P. Huang, J. S. Souris, C. S. Yang, C. Y. Mou, and L. W. Lo, "Intracellular ph-responsive mesoporous silica nanoparticles for the controlled

release of anticancer chemotherapeutics," *Angewandte Chemie-International Edition*, vol. 49, no. 44, pp. 8214–8219, 2010.

[251] R. Liu, Y. Zhang, X. Zhao, A. Agarwal, L. J. Mueller, and P. Y. Feng, "ph-responsive nanogated ensemble based on gold-capped mesoporous silica through an acid-labile acetal linker," *Journal of the American Chemical Society*, vol. 132, no. 5, pp. 1500–+, 2010.

[252] N. Singh, A. Karambelkar, L. Gu, K. Lin, J. S. Miller, C. S. Chen, M. J. Sailor, and S. N. Bhatia, "Bioresponsive mesoporous silica nanoparticles for triggered drug release," *Journal of the American Chemical Society*, vol. 133, no. 49, pp. 19582–19585, 2011.

[253] E. Climent, A. Bernardos, R. Martinez-Manez, A. Maquieira, M. D. Marcos, N. Pastor-Navarro, R. Puchades, F. Sancenon, J. Soto, and P. Amoros, "Controlled delivery systems using antibody-capped mesoporous nanocontainers," *Journal of the American Chemical Society*, vol. 131, no. 39, pp. 14075–14080, 2009.

[254] E. Climent, R. Martinez-Manez, F. Sancenon, M. D. Marcos, J. Soto, A. Maquieira, and P. Amoros, "Controlled delivery using oligonucleotide-capped mesoporous silica nanoparticles," *Angewandte Chemie-International Edition*, vol. 49, no. 40, pp. 7281–7283, 2010.

[255] C. Park, H. Kim, S. Kim, and C. Kim, "Enzyme responsive nanocontainers with cyclodextrin gatekeepers and synergistic effects in release of guests," *Journal of the American Chemical Society*, vol. 131, no. 46, pp. 16614–+, 2009.

[256] A. Popat, B. P. Ross, J. Liu, S. Jambhrunkar, F. Kleitz, and S. Z. Qiao, "Enzyme-responsive controlled release of covalently bound prodrug from functional mesoporous silica nanospheres," *Angewandte Chemie-International Edition*, vol. 51, no. 50, pp. 12486–12489, 2012.

[257] G. K. Balendiran, R. Dabur, and D. Fraser, "The role of glutathione in cancer," *Cell Biochemistry and Function*, vol. 22, no. 6, pp. 343–52, 2004.

[258] R. Cheng, F. Feng, F. H. Meng, C. Deng, J. Feijen, and Z. Y. Zhong, "Glutathione-responsive nano-vehicles as a promising platform for targeted intracellular drug and gene delivery," *Journal of Controlled Release*, vol. 152, no. 1, pp. 2–12, 2011.

[259] Y. C. Wang, F. Wang, T. M. Sun, and J. Wang, "Redox-responsive nanoparticles from the single disulfide bond-bridged block copolymer as drug carriers for overcoming multidrug resistance in cancer cells," *Bioconjugate Chemistry*, vol. 22, no. 10, pp. 1939–1945, 2011.

[260] J. Lakowicz, *Principles of Fluorescence Spectroscopy*. Springer, third edition ed., 2006.

[261] V. Bagalkot, L. Zhang, E. Levy-Nissenbaum, S. Jon, P. W. Kantoff, R. Langer, and O. C. Farokhzad, "Quantum dot - aptamer conjugates for synchronous cancer imaging, therapy, and sensing of drug delivery based on bi-fluorescence resonance energy transfer," *Nano Letters*, vol. 7, no. 10, pp. 3065–3070, 2007.

[262] Y. P. Ho, H. H. Chen, K. W. Leong, and T. H. Wang, "Evaluating the intracellular stability and unpacking of dna nanocomplexes by quantum dots-fret," *J Control Release*, vol. 116, no. 1, pp. 83–9, 2006.

[263] Q. J. He, J. M. Zhang, J. L. Shi, Z. Y. Zhu, L. X. Zhang, W. B. Bu, L. M. Guo, and Y. Chen, "The effect of pegylation of mesoporous silica nanoparticles on nonspecific binding of serum proteins and cellular responses," *Biomaterials*, vol. 31, no. 6, pp. 1085–1092, 2010.

[264] A. M. Sauer, A. Schlossbauer, N. Ruthardt, V. Cauda, T. Bein, and C. Brauchle, "Role of endosomal escape for disulfide-based drug delivery from colloidal mesoporous silica evaluated by live-cell imaging," *Nano Letters*, vol. 10, no. 9, pp. 3684–3691, 2010.

[265] J. Szejtli, "Introduction and general overview of cyclodextrin chemistry," *Chemical Reviews*, vol. 98, no. 5, pp. 1743–1754, 1998.

[266] R. Deng, X. Xie, M. Vendrell, Y.-T. Chang, and X. Liu, "Intracellular glutathione detection using mno2-nanosheet-modified upconversion nanoparticles," *Journal of the American Chemical Society*, vol. 133, no. 50, pp. 20168–20171, 2011.

[267] W. Gao, R. Langer, and O. C. Farokhzad, "Poly(ethylene glycol) with observable shedding," *Angewandte Chemie International Edition*, vol. 49, no. 37, pp. 6567–6571, 2010.

[268] J. Yang, H. Chen, I. R. Vlahov, J.-X. Cheng, and P. S. Low, "Evaluation of disulfide reduction during receptor-mediated endocytosis by using fret imaging," *Proceedings of the National Academy of Sciences of the United States of America*, vol. 103, no. 37, pp. 13872–13877, 2006.